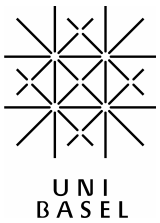

Atomistic Simulations of Transition Metal Catalyzed Reactions Using Specialized Force Fields and Quantum Mechanical Methods

Inauguraldissertation

zur

Erlangung der Würde eines Doktors der Philosophie

vorgelegt der

Philosophisch-Naturwissenschaftlichen Fakultät

der Universität Basel

von

Franziska D. Hofmann

aus Basel (Schweiz)

Basel, 2014

Genehmigt von der Philosophisch-Naturwissenschaftlichen Fakultät auf Antrag von:

Prof. Dr. Markus Meuwly

Prof. Dr. Andreas Pfaltz

Basel, den 10. Dezember 2013

Prof. Dr. Jörg Schibler

Dekan

ISBN 978-3-033-04410-4

Preface

Computers are incredibly fast, accurate and stupid.
People are incredibly slow, inaccurate and remarkable.
Together they are an inconceivable force.

- *Albert Einstein* -

Ich bin von der Wissenschaft tief beeindruckt.
Ohne sie gäbe es nicht all diese wunderbaren Dinge,
mit denen wir uns heute herumschlagen dürfen.

- *Sidney Harris* -

Acknowledgements

I am very grateful to my supervisors Prof. Markus Meuwly and Prof. Andreas Pfaltz for providing me the framework for an intensive and fruitful doctoral study at the University of Basel. I appreciated their guidance and their support in all scientific fields and the inspiring discussions throughout my PhD. Their shared experiences were very supportive and will remain as an important influence in my further career. Another thank you goes to Prof. Stefan Willitsch for chairing the defense.

It was more than a pleasure to work with our group members: Stephan Lutz, Tristan Bereau, Juan Carlos Castro Palacio, Lixian Zhang, Pierre-Andre Cazade, Florent Hédin, Myung Won Lee, Juvenal Yosa Reyes, Prashant Gupta, Ana Patricia Gamiz-Hernandez, Christian Kramer, Manuela Utzinger, Tobias Schmidt, Michael Göllner, Jing Huang, Vijay Solomon Rajadurai, Franziska Schmid, Nuria Plattner, Sabyashachi Mishra, Marek Orzechowski, Zhen-Hao Xu, Akshaya Kumar Das and Ganna Berezovska.
A special thanks goes to Maurus Schmid for his scientific support and for joyful moments during the entire PhD time. I also want to point out the fantastic team work with Jaroslaw Szymczak, Tibor Nagy and Michael Devereux concerning shared projects and Maksym Soloviov for an amusing time while sharing an office together. The group was like a family with an incredible team spirit, thanks for the great time!

I am especially thankful to Jaroslav Padevet, Tibor Nagy and Matthias Maywald for revising my thesis. Many thanks also go to Mirco Ropic for sharing his knowledge in graphical and scripting concerns and to Carmen Hunkeler for her proofreading and extensive moral support. A special thanks goes to Stephan Steinmann for his continuous motivation, his scientific support and for having a pleasant time during our studies. I also want to thank Karin Kisiala, Cristina Riera, Kerstin Albiez, Fabienne Müller, Anne-Christin Meyer-Gerspach, Johanna Wittek, Natalie Mäeder, Annette Bahlinger, Isabell Syga,

Acknowledgements

Sarah Diesslin, Gerhard Zimmermann and Irmtraud Hofmann for their amicable support;)

I want to dedicate this Thesis to Ömchen (Gertrud Zimmermann, *6.8.1921 - †31.1.2013). She was always very enthusiastic and excited about this dissertation, sadly, she passed away too early to witness the end of my PhD.

Contents

Abstract

In this thesis, we utilized current computational methods for exploring molecular architectures and dynamical properties of metal-catalyzed reactions. The importance of transition metals (TM) in catalysis was our motivation to work on the development of new empirical force fields and their applications.

TM specialized force fields provide the possibility to characterize complex geometries and relate them to their reactivity. Therefore, we parametrized the VALBOND TRANS force field by refining non-bonded parameters for a large test set of octahedral iridium(III) compounds. The optimized force field allowed a successful ranking of lowest-energy diastereomers and the performance of subsequent molecular dynamic (MD) simulations. Inspired by the natural process of the photosynthesis, Ir-catalysts are also relevant for the light-induced artifical oxidation of water leading to the synthesis of dioxygen. Using parameterized force fields, we studied the role of half-sandwich iridium complexes in different proposed reaction mechanisms. The applied force fields could help to understand catalytic cycles and to establish a basis to guide experimental screenings of new effective catalysts. TM complexes are also key components in harvesting solar energy which encouraged us to investigate the function of relevant compounds such as ruthenium-tris-(2,2'-bipyridine). Its electronic excitation led to a non-equilibrium system in which excess energy was redistributed to the surrounding solvent. The determined energy transfer to the solvent and the vibrational signatures of the surrounding water supplied an explanation for experimental findings [1,2].

Part I.

Introduction

1. Introduction

The growing availability of computational methods and the fast development of computing resources established the framework for sophisticated studies of chemical reactions. Moreover, the evaluation of physical and chemical properties on a computational level allows a deeper understanding of experimental findings. The value of computational methods to explore molecular architectures and dynamics of chemical reactions is well established by the pioneering work of Warshel[3,4], Coulson[5] and others[6,7]. Applied methodologies for such purposes can be divided into two main fields: The quantum mechanics (QM) where *ab initio* or density functional theory (DFT) methods are frequently used and the molecular mechanics (MM), usually represented by empirical force fields (FF). Both are powerful tools to analyze e.g. the conformational space of transition metal catalysts[8–11] and the reactions they mediate[12–16].

Transition metal (TM) catalysts have proven to be highly efficient in the preparation of enantiomerically pure compounds[17,18]. Therefore, this work focuses on the development of new force fields to model such organometallic complexes in terms of their geometries, relative energies, and in a next step also to facilitate the determination of their reaction barriers. Only few force fields are well parametrized to adequately treat metal containing systems, and at the current state, there is a lack of established FF-based methods which can perform expensive MD simulations. The importance of TM-complexes and the general procedure to derive metal force fields from DFT data is described in **Chapter 2**.

DFT is a powerful instrument to collect geometrical and energetical reference data. Although experimental data are supposed to be more reliable, they are rather inhomogeneous or even not available, while computational data provide a convenient alternative as they are rapidly accessible. The QM methods are outlined in **Chapter 3** to understand differences in common *ab initio* methods and in applied DFT functionals with existing basis sets. Additionally, several well-known DFT-failures are outlined in this section related to the current state of research. Some of these mentioned DFT drawbacks may have an

impact on our studies as they are mainly based on DFT calculations. Having a high accuracy of QM data is therefore beneficial to the quality of our generated force field and even directly linked to mechanistic studies which are purely based on QM calculations. An overview of the relevant MM methods, namely force fields, are also given in **Chapter 3**. A distinction in *generalized* and *specialized* force fields helps to classify their different types and to centralize the applications which can be treated with either approach. As one of the generalized approaches, the CHARMM force field[19], is emphasized more extensively as this method is constantly used within this work. It is also listed which drawbacks can arise from the usage of empirical force fields related to the current state of research and how to overcome these issues. Further, it is referred to metal specialized force fields playing a crucial role in modelling the complex transition metal catalysts. An overview of such specialized FF is given, including a more detailed report of the frequently used SIBFA[20], LFMM[21] and VALBOND[22,23] force fields. Within this work, the extended VALBOND TRANS force field is used, where additional terms for the trans effect provide a tailor-made solution for our research purposes. The multi-state adiabatic reactive molecular dynamics (MS-ARMD)[24] method based on a force field is also described. This surface-crossing algorithm enables to model bond breakage and bond formation, hence it allows to follow a chemical reaction while molecules are in gas phase or in a solvated environment. **Chapter 3** is completed with a description of several fitting algorithms which are relevant for the refinement of parameters to develop new force fields.

The development of new metal specialized force fields for atomistic simulations requires a careful refinement procedure to obtain transferable parameters. The fitting process for the empirical VALBOND TRANS force field, based on the valence bond theory (VB-theory)[25] is outlined in **Chapter 4**. This force field accounts for octahedral Ir(III) complexes with different coordinating groups including chiral N,P-ligands which are important for asymmetric catalysis. Parameters were fitted to QM data with the least-square fitting program I-NoLLS[26,27] to set up a robust force field. This allows to identify the energy-lowest diastereomers and to carry out subsequent molecular dynamics. The refinement of non-bonded parameters for a single Ir(III) complex is presented, followed by an extended training set of three related complexes. The inclusion of four diverse complexes (36 diasteromers) in the refinement provided a set of transferable parameters across different molecular architectures. Test compounds were used to validate the obtained parameters and to ensure a high degree of transferability. The additional adjustment of bonded parameters further revealed a suitable match of our FF to QM/MD data. The force field described here is a first step towards the investigation of Ir-mediated reactions

and facilitates the development of new catalysts.

Ir-catalysts in combination with catalyst precursors are also known to be highly efficient for the oxidation of water[28]. This artificial reaction to produce dioxygen is a pendant to one of the most substantial processes in nature. The role of half-sandwich iridium complexes is studied in **Chapter 5** where a powerful tool is applied which couples the CHARMM force field with the multi-state adiabatic reactive molecular dynamic (MS-ARMD)[24] approach. A parameter refinement for reactants, products and intermediate states is illustrated to describe different reaction mechanisms which were already proposed by DFT calculations[28]. (Non)-bonded parameters were fitted with a simplex algorithm for a later elucidation of the essential oxygen-oxygen bond formation at an atomistic resolution. Quantum methods are too prohibitive to determine rate constants for several catalysts, they are rather used as a reference to set up multiple force fields corresponding to different states of the reaction pathway. A correct determination of barrier heights permits the screening of various iridium catalysts to evaluate their potency and to allow a mechanistic study in an explicit-solvated environment.

The importance of a realistic solvated system is even more pronounced by exploring the solvent shells around photoexcited transition metal complexes. The excitation of different metal complexes is a key concept in the area of solar-energy research. In **Chapter 6**, the structural dynamics of solvated ruthenium-tris-(2,2'-bipyridine) after excitation is illustrated[29] to further explore the redistribution of excess energy to the surrounding solvent. The VALBOND TRANS force field is used to follow the electronic excitation by monitoring the time-dependent solvent response. It reveals that the solvent structure relaxes towards the equilibrium state on a sub-picosecond time scale. During the excitation process, the increased dynamics in the inner solvation sphere was analyzed by the determination of the solvent residence time and rotational reorientation times. An investigation of the different degrees of freedom (DoF) also provided a time range in which the energy transfer to the solvent appeared. Additional computed infrared spectrum (IR) of water and the $[Ru^{II}(bpy)_3]^{2+}$ complex validated the adequate set up of the underlying force field by comparing those data with experimental results. Obtained results from these MM simulations are comparable with more expensive QM/MM methods and therefore the method offers a suitable alternative where averaging over hundreds of independent trajectories becomes feasible. This approach paves the way for the investigation of several other TM complexes such as $[Fe^{II}(bpy)_3]^{2+}$.

1. Introduction

A pure QM-based study for an asymmetric hydrogenation reaction with iridium-phosphinooxazoline (Ir-PHOX) catalysts is outlined in the **Appendix**. Again, the importance of TM catalysts is investigated to contribute to a long debate about the mechanistic ambiguity of involved Ir(I)/(III) or Ir(III)/(V) species. The study is based on a remarkable experimental work[30] which reported an inversion of the diastereoselectivity triggered by a small structural change in the PHOX-ligand. To explain this unusual behavior we examined all proposed mechanisms[31–35] computationally to suggest the most plausible reaction pathway in terms of kinetical aspects. The chapter reports that a hydrogenation mechanism involving Ir(I)/(III) species can qualitatively explain the change in selectivity while the Ir(III)/(V) mechanism does not correlate with the experimentally observed ratio of diastereomers. Therefore, the ester functionalized alkene as a substrate played a decisive role, as its coordination to the metal center led to different activation barriers. This can explain the similar barrier heights for the Ir(I)/(III) and Ir(III)/(V) mechanism, but also the more stabilized transition states of the Ir(III)/(V) mechanism if the order of transferred hydrogen is reversed. The investigation of this system in an explicit solvated environment is now feasible with a developed iridium specialized force field which was outlined in a previous chapter. It provides the basis for future work in the field of asymmetric hydrogenations within in a more realistic framework.

2. Background

2.1. Organometallic Complexes

Recent developments in molecular mechanic (MM) methods paved the way for deriving molecular geometries of organometallic complexes, energies and various other properties[36,37]. In the MM approach, electrons are neglected, one rather uses the relationship of molecular geometries and their corresponding potential by applying an empirical approach. The classical treatment, on an atomistic level, allows even to handle large bio-molecular systems while the MM approach keeps its high speed and simplicity. However, the treatment of organometallic complexes is not trivial. Depending on the derived force field, the performance can be superior over low-level quantum mechanical (QM) methods[38] or even qualitatively equal to expensive *ab initio* methods[39]. However, MM methods have their limitations, they strongly depend on the chosen reference system which can suffer from the availability of experimental data or from a dependence on empirical parameters. The quality of the underlying MM model is characterized by the quality of derived parameters and by their transferability to other molecular systems. Different "atom types" are assigned to such parameters, defining a specific element which builds the basic unit in common force fields. Depending on the chemical environment of the element, multiple atom types are introduced. The number of atom types is also dependent on the diversity of the model compound, on the availability of reference data, and on the desired target accuracy. Organometallic complexes pose new challenges to assign a proper atom type as a single transition metal (TM) can adopt different oxidation and spin states as well as the corresponding coordination pattern. The availability of such transferable parameters enables the application of force fields to a wide range of substances, but to capture more specific structures (e.g. metal complexes) several force field extensions and refinements are necessary.

2.1.1. Force Field Parametrization

Molecular mechanic force fields such as CHARMM[40] are frequently used for atomistic simulations of condensed-matter systems. For such simulations an - ideally transferable - set of force field parameters is required for computing meaningful observables. This requires a careful choice of reference data and elaborate approaches to derive feasible parameters. For instance, applied electrostatics can depend heavily on the chosen concept of charge assignment. It can play an essential role if the assignment is done either by fragment matching[41], by contributions from bond incremental charges[42,43], or by using geometrical aspects as it is done for polarizable FFs[44]. Such decisive aspects also appear for the determination of other parameters and are even more pronounced if the underlying quantity is not an observable.

The aim of a parametrization, regardless which reference data are considered, is to fit the model as close as possible to the training set. To obtain transferable parameters, it is of major importance to include diverse data into the training set. Fitting with a diverse set of test compounds allows to compute parameters which can be also applied to similar systems. However, the diversity should be limited to related compounds so that it remains possible to describe the entire training set with a sufficient accuracy. Therefore, structural features and energies, which can be split into conformational energies e.g. for different diastereomers and distorted energies arising from electronically influenced or strained compounds, should not vary too widely.

Experimental and QM data are both a source of reference data while the experimentally obtained information are normally preferred as they are realistic and usually not biased. However, the common procedure to refine parameters uses data obtained form gas phase experiments, which cannot be directly applied as the most TM complexes were studied in the condensed phase. High level QM calculations are often used as they can overcome a lack of inhomogeneous experimental data. Their suitability to FF parameters[42,45] is another advantage (more in Chapter 3, DFT section) where the relevant position of the nuclei can be determined easily. In contrast, X-ray crystallographic data determine the points of maximal electron-density which can be problematic especially for hydrogen as the density is normally not centered on the nucleus[46]. However, structural data obtained from X-ray analysis are inevitable in the validation of FFs[47]. Each force field is based on a different source of data: either it is largely based on QM calculations such as CHARMM[48], on mainly experimental gas phase data as for MM2[49],

or it uses a combination as it was implemented in CFF93[50]. In general, the reference data should be weighted according to their quality before a detailed evaluation of the data is carried out[46]. Before a fitting procedure can be started, the determination of a set of primary parameters is required.

The refinement of FF parameters demands a well chosen set of initial parameters to avoid that the fit takes either too long, or depending on the fitting algorithm (see Chapter 4), is trapped in a local minimum. Initial values can be obtained from several sources and require a careful consideration of the underlying purpose. The most common source of structural data is X-ray crystallography, if such experiments for a certain compound are available. Especially for (ligand-metal) bonds and angles it is a reliable source and partially also for torsional angles. Long-range interactions including interatomic distances can also be obtained, but those data require some down scaling for longer distances[51]. Force field bond lengths correlate with a potential energy minimum, therefore, accurate values can be also obtained by taking vibrational analysis[52] into account. This data are also relevant to determine e.g. force constants of a bond where several conformational energy data are investigated. Such vibrational data can be obtained by infrared spectroscopy (IR), Raman or other methods giving information about potential energy surfaces (PES)[53] and of course by QM calculations[47,54]. The estimation of primary data for the electrostatics is rather limited to QM-derived point charges, dipoles or higher order multipoles[55]. In accordance with the underlying system, the applied schemes of charge assignment should be selected carefully as each assignment has its own weakening. An initial set of vdW parameters for small compounds can be as well obtained by high-level QM calculations[56,57], but usually they are taken from X-ray diffraction data[58]. In general, if numerous reference values are available from which initial parameters can be received, the initial value should be set close to the averaged value.

A quick validation of the chosen initial parameter set can be carried out by comparing e.g. reference bond lengths with calculated bond lengths of the training set (or energies). If a correlation coefficient is far from 1.0, the primary parameters should be corrected until a reliable correlation is found. An estimated set of initial parameters, an adequate training set and the corresponding functional form of the force field are necessary for the refinement of parameters to their optimal magnitude. Different fitting algorithms (see Chapter 3) can be applied depending on the investigated quantities, the linear dependency or higher correlated dependency of the parameters and on their amount.

A fitting algorithm can be coupled with a MM-method which evaluates the quality of different refinement cycles. For this purpose, a valence bond theory[25]-inspired extension of a conventional force field is taken in this work to treat metal-containing complexes. The VALBOND FF[22,23,59–61] is specialized for such a purpose. For the majority of molecular mechanic methods the specification of a topology is one of the first steps. Among others, a decision has to be made which atoms are connected by localized bonds and which are treated with non-bonded interactions. For MM approaches, localized bonds (formed by an overlap of hybrid orbitals) are better described by valence bond theory (VB-theory) than by molecular orbital theory (MO-theory) where linear combinations of atomic orbitals are used to form delocalized bonds. For this reason, the power or the strength of bond formation has a strong angular dependence and ask for precise definition of angle bending terms. Such an angle bending term is implemented in the metal specialized VALBOND force field[22,23,59–61].

2.1.2. Valence Bond Theory

The *valence bond theory* (VB-theory) goes back to 1928 where Linus Pauling established the description of covalent binding. He stated that a covalent bond is formed between two atoms by the interaction of two unpaired electrons[62]. He showed how atomic orbitals overlap to form a stable molecule and established the definition of resonance[63]. The overlap of two s-orbitals can form a σ-bond as well as the overlap of one s-orbital and one p-orbital pointing in z-direction (along the bond axis). An overlap of two p-orbitals along the z-axis also results in a σ-bond, but the overlap of parallel p-orbitals forms a π-bond[25]. This pioneering idea was inspired by the early work of Frankland who introduced the valence concept[64] and Kekule who extended the valence concept to carbon atoms[65]. A further invention was made by Van't Hoff and Le Bel who introduced the stereochemistry and proposed a tetrahedral arrangement for a carbon atom[66], which was further refined for inorganic complexes by Werner[67]. Using Lewis structures[68] completed the basis for the valence bond theory. In 1927, Heitler and London performed calculations on the H_2 molecule which was the first wave-mechanical treatment of a valence bond[69].

The prediction of correct geometries however was only possible by the implementation of hybridization which is the concept of mixing atomic orbitals (AO) to form hybrid orbitals. Without the concept of mixing atomic orbitals to form hybrid orbitals the VB-theory would not predict the correct bonding pattern of methane as illustrated in Fig. 2.1.

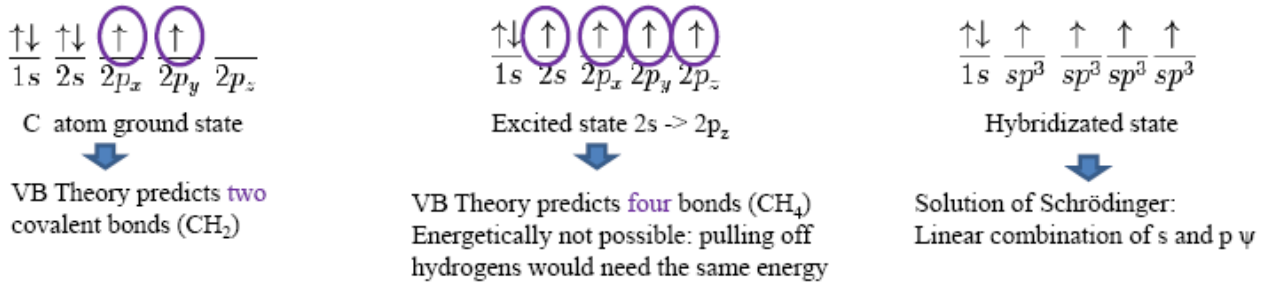

Figure 2.1.: Concept of mixing atomic orbitals to form hybrid orbitals to describe chemical bonding.

The hybrid orbitals consist of underlying atomic orbitals which only depend on the Bohr radius and on polar coordinates. E.g. for methane, a tetrahedral shape is formed out of 2s, $2p_x$, $2p_y$ and $2p_z$-orbitals resulting in a sp^3-hybridization including an angle of 109.5°. The formed sp^3-orbitals permit a theoretical justification of the naturally tetrahedral form of a methane molecule. For trigonal pyramidal conformations a sp^2-hybrid orbital (120.0°) is used and for a linear shape a sp-hybridization (180.0°)[25] (Fig. 2.2).

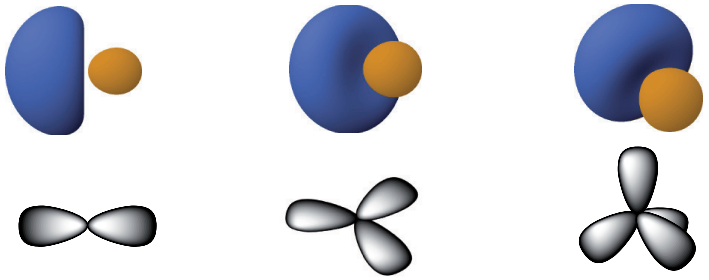

Figure 2.2.: Orbitals were generated by the Orbital Viewer Software[70]. Upper panel: sp, sp^2 and sp^3-hybrid orbital cartoon. Examples of molecules are in the lower panel: two sp-hybrid orbitals are adapted in a linear fashion with an angle of 180° as it can be found for acetylene, three sp^2-hybrid orbitals are arranged in a trigonal planar shape with an angle of 120° as in ethylene and four sp^3-hybrid orbitals are arranged as tetrahedral with an angle of 109.5° as reported for methane. Not hybridized orbitals are omitted.

An alternative theory, the *molecular orbital theory* (MO-theory)[71], describes the determination of molecular structures by using linear combinations of atomic orbitals (LCAO). Originally, the MO-theory was thought to replace the VB-theory before it was realized that they are closely related. In the VB-theory, electrons are mainly localized on their atomic centers which helps to model chemical bonds and delocalization coming from the resonance phenomena. In the MO-theory however, electrons are delocalized over the whole system, describing a chemical bond as a result of delocalized electrons in

multi-center orbitals[72]. However, to explain fundamental concepts such as the Bell-Evans-Polanyi principle[73] or the related Hammond's Postulate[74], the VB approach is the concept of choice. In general, the VB-theory is applied to study reactivities in terms of exploring the energetic barriers and entire reaction mechanisms[75]. For instance, the VB wave function of a H_2 molecule is a linear combination of three different configurations: one covalent and two ionic. Several traditional VB approaches are available, to express the wave function as explicitly covalent and ionic contributions such as the valence bond self-consistent field (VBSCF)[76] or the breathing orbitals valence bond (BOVB)[77]. Other simpler approaches (purely covalent) express the wave function as a single electronic configuration, applied in the generalized valence bond scheme (GVB)[78] or the spin-coupled valence bond scheme (SCVB)[79]. Essentially, VB-based QM-methods which deal with electronic wave functions can describe all kinds of Lewis structures. For a proper description of bonding pattern, the VB-theory is also applied for MM-approaches as discussed for the VALBOND TRANS force field in the following chapter.

3. Methods

3.1. *Ab initio* Methods

Over the past decade, density functional theory (DFT) has emerged as a convenient and versatile computational method. It has been successfully used to obtain a wide range of data such as thermochemistry, molecular structures, force field parameters, vibrational frequencies, nuclear magnetic resonance and electron spin resonance characteristics, UV spectra, dipole moments, transition-state structures, as well as activation barriers[80]. Its growing popularity has two reasons: first, the increasing variety, efficiency and availability of DFT methods and second, DFT methods are superior in accuracy to cost ratio relative to *ab initio* wave function based methodologies[81]. For example, Kohn-Sham density functional theory (KS-DFT) methods are in most cases better in line with experiment than results obtained from Hartree-Fock (HF) calculations at comparable computational effort[82]. DFT provides an approximated solution to the Schrödinger equation by describing a many-body system only in terms of electron densities. At present, it is one of the most popular methods for electronic structure calculation, started from simple atoms to complex molecules up to condensed phases. With DFT, a compromise was found between accuracy and cost, playing a crucial role in predicting bond energies, bond lengths, lattice structures, transition and excited states and other geometrical features[83]. The aim of a majority of QM-methods is the approximated solution of the time-independent non-relativistic Schrödinger equation which provides access to numerous properties. Here, the combined electron nuclei ground state wave function Ψ is an eigenfunction of the Hamiltonian $\hat{H}$ and the eigenvalue E_i gives the energy of the i-th state. Atomic units are used if not specified otherwise.

$$\hat{H}\Psi_i(\vec{r}_1, \vec{r}_2, ..., \vec{r}_N, \vec{R}_1, \vec{R}_2, ..., \vec{R}_M) = E_i\Psi_i(\vec{r}_1, \vec{r}_2, ..., \vec{r}_N, \vec{R}_1, \vec{R}_2, ..., \vec{R}_M). \tag{3.1}$$

In the time-independent Schrödinger equation, r are spatial coordinates (x, y and z) of N electrons and

R are the x, y, z components of M nuclei while the operator $\hat{H}$ acts on an eigenfunction Ψ represents the total energy[84].

$$\hat{H} = \sum_{a=1}^{M} -\frac{1}{2m_a}\nabla_{N_a}^2 + \sum_{i=1}^{N} -\frac{1}{2}\nabla_{r_i}^2 + \sum_{a=1}^{M}\sum_{b=1}^{a-1} \frac{Z_a Z_b}{|R_a - R_b|} + \sum_{i=1}^{N}\sum_{j=1}^{i-1} \frac{1}{|r_i - r_j|} - \sum_{i=1}^{N}\sum_{a=1}^{M} \frac{Z_b}{|r_i - R_b|} \tag{3.2}$$

i and j run over the N electrons in the system, while a and b describe the M nuclei. m_a is the mass of the nuclei, Z_a and Z_b the electrostatic interaction of the nuclei, and $\nabla_{r_i}^2$ is the Laplacian operator of the x, y and z spatial directions.

$$\nabla_{r_i}^2 = \frac{\partial^2}{\partial x_i^2} + \frac{\partial^2}{\partial y_i^2} + \frac{\partial^2}{\partial z_i^2} \tag{3.3}$$

The first term in eq. 3.2 characterizes the kinetic energy of the nuclei, while the rest describes the pure-electronic Schrödinger equation $\hat{H}_{el}$. Here, the second term corresponds to the kinetic energy ($\hat{T}$) of the electrons while the last three terms characterize the potential energy: repulsive nuclei-nuclei potential, as well as the repulsive electron-electron interactions ($\hat{V}_{ee}$) and the attractive electrostatic interactions between nuclei and electrons ($\hat{V}_{ne}$). A simplification of $\hat{H}$ is done in the Born Oppenheimer approximation[85], assuming that the mass of a nucleus is several times larger (~ 1800) than the electron mass[36]. Additionally, as nuclei velocities are much slower than electrons, a separation of the electronic problem is possible, at least approximately: it can be solved with a set of stationary nuclei[86]. The nuclei are therefore fixed in space, allowing to neglect their kinetic energies (first term of eq. 3.2) and leading to a simplification of the Hamiltonian $\hat{H}$ to a pure electronic contribution $\hat{H}_{el}$. The $\hat{H}_{el}$ therefore depends only on coordinates of the electrons[87]:

$$\hat{H}_{el} = \hat{T} + \hat{V}_{ee} + \hat{V}_{ne} \tag{3.4}$$

Most of the methods performing practical electronic structure calculations apply this approximation. *Ab initio* methods such as HF, multi-configuration self-consistent field (MCSCF), and configuration interaction (CI) (see Tab. 3.1) allow to treat the electronic Schrödinger equation as an eigenvalue

problem, using basis sets to find a discrete solution for the ground state Ψ_0 which provides the lowest energy E_0. This procedure is called the variational principle where the energy is computed as an expectation value E of the Hamiltonian $\hat{H}$ from any normalized wave function Ψ[88]:

$$E = \int d\vec{x}_1 ... \int d\vec{x}_N \Psi^*(x_1, ...x_N) + \hat{H}\Psi(x_1, ..., x_N) =< \Psi_0|\hat{H}|\Psi_0 > \tag{3.5}$$

Ψ^* is the complex conjugated of Ψ, and the last term "$\langle\ \rangle$" is Dirac's bra-ket notation giving an analog expression[89]. The variational principle may result in a convergence to an exact solution, however, the computational cost grows with the size of the system. Each electron is described by three spatial coordinates and one spin coordinate which results in a scaling of $4N$ variables regarding the HF method. The configuration interaction single double (CISD) method is feasible to get more accuracy, however, the scaling is already $6N$[90], implying that more complex systems are too demanding[91].

3.2. Density Functional Theory

The DFT approach avoids dealing with the whole wave function Ψ and rather characterizes the system with a reduced description, the electron density $\rho(r)$. The definition of electron density requires that $\rho(r)d^3r$ is the probability to find an electron in a volume of d^3r, which is just $|\phi(r)|^2$ for a single electron with a wave function $\phi(r)$. The fundament of DFT calculations is that the energy of a molecule can be determined exclusively from the electron density $\rho(r)$, whereby $\rho(r)$ needs less variables, as it is a function only depending on (x, y, z) coordinates. Another advantage is that the correlation, although approximated, is included more easily than in *ab initio* calculations[92]. For instance, MP (Møller-Plesset) perturbation theory, which is one of several post-Hartree Fock *ab initio* methods, adds electron correlation effects to the common Hartree Fock method[93]. This electron correlation comes from the perturbation theory of either second (MP2), third (MP3), or even fourth order (MP4)[94], which is very time consuming for molecules of more than a dozen heavy atoms. With DFT however, one can transform a many-electron problem into an easier manageable problem of non-interacting electrons moving in a self-consistent field[95]. Evaluating the energy of a system from its density is the basic idea behind DFT, which goes back to the early days of quantum mechanics[96–99]. The theory by Thomas[96] and Fermi[97] is called a true density functional theory, because the kinetic as well as the

electrostatic energy depend directly on the electron density [80]. However, the Thomas-Fermi functional is not well suited for the description of chemical bonds [100,101] and therefore did not find a use in the field of computational chemistry. Finally, in 1964, Hohenberg and Kohn provided a theorem proving that the ground-state energy of an electronic system is uniquely defined by its density [102,103]. Kohn and Sham (KS) developed a practical formulation of this theory and reported that the exact electron density as well as the exact total energy can be obtained from a set of one-electron equations [95]. In the KS-formulation the electron density is expressed as a linear combination of one-electron orbitals. A Slater-determinant is then formed from these orbitals to determine the so-called Kohn-Sham orbitals. The Kohn-Sham wave function is not an approximation to the exact wave function, it is rather a precisely defined attribute of any electronic system which is uniquely determined by the density [82] and identical in mathematical form to the HF wave function. The electron density from this determinant is then used to compute the potential energy [92]. Following Kohn and Sham, the total energy E is written as a functional of the charge density expressed by a single Slater determinant [95]:

$$E[\rho] = T_s[\rho] + V_{Ne}[\rho] + J[\rho] + E_{xc}[\rho] \tag{3.6}$$

ρ is the electron density, obtained as the sum of the squares of a set of orthonormal spin-orbtials:

$$\rho(r) = \sum_{i}^{N} |\phi_i(r)|^2 \tag{3.7}$$

$T_s[\rho]$ is the kinetic energy of the non-interacting reference system of a single determinant, which is not originated from the electron density, it is rather calculated like in the HF method. The only difference is that KS orbitals are used instead of HF orbitals, resulting in an energy expression of the one-electron orbitals of a non-interacting system.

$$T_s[\rho] = -\frac{1}{2} \sum_{i}^{N} \int {\phi_i}^{*KS} \nabla^2 \phi_i^{KS}(r) dr \tag{3.8}$$

N is the number of electrons, ϕ^{KS} are the Kohn-Sham orbitals, and ∇^2 is the Laplace operator [95]. $V_{Ne}[\rho]$ is the classical nucleus-electron potential (external potential) and

$$V_{Ne}[\rho] = -\int \rho(r) \sum_{a=1}^{M} \frac{Z_a}{|r - R_a|} dr \tag{3.9}$$

$J[\rho]$ is the classical Hartree or Coulomb energy:

$$J[\rho] = -\frac{1}{2} \int \int \frac{\rho(r)\rho(r')}{|r - r'|} dr dr' \tag{3.10}$$

$E_{xc}[\rho]$ describes the exchange (E_x) and correlation energy (E_c)[104]

$$E_{xc}[\rho] = (T[\rho] - T_s[\rho]) + (V_{ee}[\rho] - J(\rho)) \tag{3.11}$$

where the exact kinetic energy $T[\rho]$ (the real kinetic energy of the fully interacting system) is corrected by the independent-particle kinetic energy $T_s[\rho]$ (eq. 3.8), and the quantum mechanical electron-electron interaction $V_{ee}[\rho]$ is corrected by the classical Coulomb term.

However, the universal functional $E_{xc}(\rho)$ (should be valid for all kinds of systems) appearing in any functional derivative is not known. Therefore, the part of this functional which describes electronic exchange and correlation has to be approximated[105]. The Hartree Fock theory includes the exact exchange formula (eq. 3.12), but in general it has its deficiencies in describing chemical bonding and in the use of thermochemical applications[105].

$$E_{HFx} = -\frac{1}{2} \sum_{ij}^{N} \int \int \frac{\rho_{ij}(r)\rho_{ij}(r')}{|r - r'|} dr dr' \tag{3.12}$$

Nowadays, a large number of different approximate DFT functionals exist, based on first principle and/or empirical parameters.

3.2.1. DFT Functionals

A wide range of various DFT methods appeared over the last decades, however, in all the abundance of functionals, there are only few being used on a regular basis. A selection of the basic methods are given in Tab. 3.1.

Ab initio methods

Acronym	Name	Type
HF	Hartree-Fock	standard
MP2	Møller-Plesset (2^{nd} order perturb.)	electron correlation
MCSCF	Multi Configuration Self-Consistent Field	electron correlation
CI	Configuration Interaction	electron correlation
CC	Coupled Cluster	electron correlation

DFT methods

Acronym	Name	Type
X α	X alpha	exchange only
LDA	Local Density Approximation	exchange and correlation
SVWN	Slater, Vosko, Wilk and Nusair	exchange and correlation
GGA	Generalized Gradient Approximation	exchange and correlation
PBE	Perdew-Burke-Ernzerhof (GGA)	exchange and correlation
B3LYP	Becke-3-parameter-Lee-Yang-Parr	hybrid

Table 3.1.: *Ab initio* and DFT methods

The simplest useful DFT method is Slater's $X\alpha$ theory which was devised as a HF-like DFT method, approximating electron exchange (electrons of the same spin avoid each other) but not correlation (charges avoid each other)[106,107]. The fundament for common functionals is L(S)DA (= local (spin) density approximation) for spin (un-)compensated systems[95]. SVWN is the most often used LSDA[92] and uses the "standard" local exchange functional (often referred to as Slater or Dirac exchange)[98,107] and the local correlation functional VWN of Vosko *et al*[108]. LDA perfectly describes the homogeneous electron gas, implying that if the variation of the charge density is weak (as for solids), the description is supposed to be accurate. Unfortunately, for atoms and molecules the density varies too fast to give a correct exchange correlation and also bond dissociation energies are described poorly[109]. To overcome the problem of a rapidly varying charge density, the E_{xc} functional of the generalized gradient approximations (GGA)[110] depends on $\rho(r)$ and on its gradient. The most well-known GGAs are the PBE[111] and the BLYP[112,113] functionals.

Beyond these semi-local methods, where the electron density is considered not only in one point rather in the close proximity, hybrid functionals were developed which include a portion of exact HF exchange. For instance, the B3LYP-(Becke-3-parameter-Lee-Yang-Parr)-functional is a hybrid of "exact" (Hartree Fock) exchange with local and gradient-corrected exchange[112] and correlation terms, as it was first suggested by Becke[114].

$$E_{xc}^{B3LYP} = (1-a_0){E_x}^{LSDA} + a_0{E_x}^{HF} + a_x\Delta{E_x}^{B88} + a_c{E_c}^{LYP} + (1-a_c){E_c}^{VWN} \tag{3.13}$$

Where a_0, a_x and a_c are empirical coefficients determined by an appropriate fit to experimental data[114], ${E_x}^{LSDA}$ is the Slater exchange energy[107], ${E_x}^{HF}$ is the HF "exact" exchange energy, $\Delta{E_x}^{B88}$ is Becke's 1988 gradient correction for exchange[112], ${E_c}^{LYP}$ is the Lee-Yang-Parr gradient corrected correlation energy[113] and ${E_c}^{VWN}$ is the Vosko-Wilk-Nusair local correlation energy[108]. In this work, the hybrid density functional B3LYP method is used as the so-called hybrid functionals are generally significantly more accurate for geometries and thermochemistry than non-hybrid functionals and its results are partly comparable to MP2 (Møller-Plesset second-order perturbation theory) calculations[115]. B3LYP[113,114] is the most widely used functional in organic chemistry-related computations and has been very successful in the past and in present investigations[92], although more accurate methods exist[116,117] at similar cost. Thus, this "standard method" will be used to perform electronic structure optimizations to collect reference data and to characterize reaction pathways of several reactions.

3.2.2. Basis Sets

Parallel to the enhancements of new functionals, a large collection of basis sets arised. The majority of frequently used basis sets consist of atom centered Gaussian-type orbitals (GTOs). The function describing these orbitals eq. 3.14 can be decomposed into an angular part $Y_{l,m}(\Theta\phi)$ and a radial part $e^{(-\alpha(x^2+y^2+z^2))}$[118].

$$G(r) = Y_{l,m}(\Theta\phi)e^{(-\alpha(x^2+y^2+z^2))} \tag{3.14}$$

The number of exponents α for the radial part of eq. 3.14 specifies the complexity of the orbital, where

for each value of α one primitive Gaussian function can be constructed. A single primitive Gaussian function describes already a primitive Gaussian type orbital. Thus, the quality of the basis set depends on the amount of Gaussian functions with different exponents, centered on every atom. Only one exponent is taken for a minimal basis set meaning that e.g. for hydrogen only one basis function per atom is used, describing the 1s atomic orbital. Two exponents per atom are used for double zeta (DZ) basis sets while already three exponents are used for triple zeta (TZ) (e.g. STO-3G[119])[120]. Additional polarization functions are used to better describe distorted angle geometries, hybridizations and of cause polarizabilities, whereas diffuse functions, fairly delocalized Gaussians with small exponents, are useful for the description of negatively charged systems. Gaussians describe a wave function in an inappropriate way because the Gaussian function drops too fast according to the distance. This causes problems at the origin (where the atomic wave function has a cusp[121]) and also far away from the origin[122]. However, using a linear combination of several GTOs, so-called contracted Gaussian functions, helps to overcome this issue, therefore, a correct representation of the atomic wave function can be obtained[123]. One of the most common basis functions used nowadays are split-valence basis sets, also used in this work. E.g. for Pople's basis set 6-31G(d,p)[124], the core orbital is obtained by a contraction of 6 primitive GTOs, the inner part of the valence orbitals by a contraction of 3 primitive GTOs, and the outer part of a valence orbital is a single primitive GTO. The (d,p) corresponds to polarization functions of the p-orbitals for hydrogen and helium and d-orbitals for all other elements. The correlation consistent basis sets[125] where extrapolation techniques are used for convergence (e.g. cc-pVDZ[126]), should be mentioned to complement the presented collection of basis sets. Nevertheless, GTOs basis sets cannot be improved systematically, therefore they are limited in their accuracy, whereas plane waves and wavelets are systematic basis sets[84].

3.2.3. Determination of Reaction Barriers

DFT methods can provide accurate information about relative stabilities (thermodynamics), but they also allow the determination of conversion rates (kinetics) of chemical reactions. To investigate kinetics, it is necessary to analyze potential energy surfaces to find transition states (TS) which is a rather difficult task[127]. For such geometries, three regular translation degrees of freedom (DoFs) have to be considered, which is also the case for an ordinary molecule[128]. Therefore, all the internal DoF are at a minimum, except of one, the lowest frequency eigenvalue which is at a maximum[129]. This transitional

DoF recognized by its negative frequency is characteristic for a transition state. A TS has to have only one negative frequency, otherwise it is either a potential minimum if there are no negative frequencies, or a higher order saddle point. The vibration of that frequency corresponds to the motion along the reaction coordinate. According to the Eyring equation, the absolute rate constant $k(T)$ of the process is obtained from a transition state:

$$k(T) = \frac{k_B T}{hc^\circ} e^{(-\frac{\Delta G^\ddagger}{RT})} \tag{3.15}$$

R is the gas constant, T the absolute temperature, k_B the Boltzmann's constant, h the Planck's constant, c° the standard concentration and $\Delta G^\ddagger$ is the free activation energy [129].

For the process to find a TS, an algorithm needs to determine the Hessian matrix which is nothing else than second derivatives of the energy in relation to the nuclear motion. The algorithm has to fulfill two requirements: decreasing the energy of the nuclei for positive values of the Hessian and increasing the energy of the nuclei for negative values [123]. Global search algorithms such as e.g. the *linear synchronous transit* (LST) method [130] are implications of this procedure. The quadratic version of LST, the *quadratic synchronous transit methods* (QST) [131,132], assumes that the TS-geomerty lies along a parabolic connection of the initial and the final state which satisfies the quadratic shape of a saddle point [133]. Gaussian provides two variants of this QST approach [134]. QST2 requires the reactant and the product geometry as input geometries to interpolate between them in a non-linear way, finding a geometry close to the TS. Taking this evaluated structure, a local transition state optimization is started, to reach the final TS [135]. If the evaluation of a meaningful TS-geometry fails, which is the case for more complex reaction mechanisms, the QST3 method is used, where an approximated TS-geometry is also given by either guessing the reaction intermediate or by using geometries out of the *scan* approach (*grid search method*) [92]. The *scan* method uses a predefined reaction coordinate with geometry optimizations at each point. If a transition state of a bond formation is searched, it is straightforward to scan the coordinate along this bond, or more concrete, to scan one structural degree of freedom. Thus, a TS-like structure can be provided by this scan-approach [128].

If the TS-like structure, obtained either by guessing or by the scan approach, is close enough to the final

state, *Berny's* local search algorithm can be used, which determines the Hessian matrix analytically. However, this approach is very sensitive to the initial geometry, and it can bias the resulting transition state by the proposed mechanism[92]. An *intrinsic reaction coordinate* (IRC) approach iteratively provides the associated reactant and product for a given transition state to prove if a real transition state was obtained by any of these methods[136].

The obtained transition states can be used to determine the enantiomeric excess *ee*[137] of e.g. an asymmetric hydrogenation reaction which is one of the main steps in such experiments. Determining the *ee* for computational studies is according to:

$$ee = \frac{k_{favored} - k_{disfavored}}{k_{favored} + k_{disfavored}} \tag{3.16}$$

k is the rate constant of the formation of the corresponding enantiomer, which is expressed by the Eyring equation (see eq. 3.15). Using this relationship, the enantiomeric excess can be written as:

$$ee = \frac{(e^{-\frac{\delta\Delta G^{\ddagger}}{RT}}) - 1}{(e^{-\frac{\delta\Delta G^{\ddagger}}{RT}}) + 1} \tag{3.17}$$

whereby $\Delta\Delta G^{\ddagger}$ is the free activation energy[138] which can be determined by substracting the activation energy of the favored reaction path $\Delta G^{\ddagger}_{favored}$ from the disfavored one $\Delta G^{\ddagger}_{disfavored}$.

$$\Delta\Delta G^{\ddagger} = \Delta G^{\ddagger}_{favored} - \Delta G^{\ddagger}_{disfavored} \tag{3.18}$$

3.2.4. ADMP - Atom-Centered Density Matrix Propagation

A QM-MD approach can provide useful information to explore the potential energy surface around the reactant state, product state and other intermediate states including the TS of a certain reaction. In the present work, the atom-centered density matrix propagation (ADMP)[139–142] is used to study the dynamics on a QM level. A confirmation of the ADMP method reliability was presented e.g. in a detailed study of Staudinger's PH_3 + NH_3 reaction, where a dynamic and mechanistic understanding was feasible[143]. Moreover, ADMP supported the description of other reactions[144]. Therefore, it

may also help to identify critical interaction of a substrate with a catalyst where normal single point calculations are limited to determine reaction barriers. The ADMP approach is used in this work to sample reference data either with a NVE or optionally a NVT ensemble. This approach can be directly applied without expensive parametrization, however the required CPU time is an order of magnitude higher than for MM approaches. An alternative method to the IRC algorithm can be used, based on a QM/MD approach, to model the minimum-energy reaction pathway. Therefore, an ADMP simulation (NVT) using the damping velocity Verlet algorithm (DVV)[145] was performed, which starts from the TS going downward to the corresponding reactant resp. product. Resulting MD structures basically oscillated around the equilibrium structures which were obtained from the Gaussian IRC path calculation.

3.2.5. DFT Drawbacks

Common DFT methods suffer from several shortcomings which mainly arise from the approximated exchange-correlation functional. The compensation of these drawbacks is an active field of research and remain challenging in the future[146]. One of the shortcomings lies within the Kohn-Sham theorem which is based on an uncertain assumption, the *ν-representability* condition[147]. It assumes that an existing potential is the same for the density of interacting electrons as for the density of non-interacting electrons. Using this assumption, Hohenberg and Kohn proved that a valid functional $F[\rho]$ exists to obtain the kinetic and electrostatic energy of each electron density. This procedure is limited due to an undefined $F[\rho]$, if ρ is not ν-representable[148].

Concerning this condition (that ρ is not ν-representable), another problem can arise from one-determinant DFT methods, which cannot adequately describe different spin states, leading to the *spin multiplicity failure*[149]. This occurs particularly in strongly correlated systems where more than one occupation number is close to one (meaning that more relevant determinants exist), in this case multi-reference methods may help[146]. The multi-configuration character of the wave function can also cause problems in predicting transition state energies[150–152]. The kinetic energy term $T_S[\rho]$ in eq. 3.8 only provides an approximated energy of the interacting electrons, leading to missing contributions from virtual orbitals. Unfortunately, this *transition state drawback* is relevant in the present work and may be responsible for deviations from experimental results. Functionals using a smaller fraction of exchange may perform better[153–156]. The underestimation of transition states is also a consequence of a *deficiency*

in dispersion interactions at the DFT level[157,158]. Especially local or semi-local density functionals (e.g. LDA or GGA) but also non-local hybrid functionals are not sufficient enough to describe the long-range van der Waals interactions, and will therefore fail the attractive $1/R^6$ behavior[146]. The CCSD(T) method[159] is one of the major achievements beyond DFT to overcome the lack of dispersion. It additionally uses wave function correlations for long interelectronic distances. Finding long-range corrected correlation functionals for DFT functionals is still an active field of research[160–163].

The *self-interaction error* is another problem[164]. In Hartree-Fock and post Hartree-Fock methods, an orbital is not interacting with itself, however, this non-physical behavior is found for most DFT methods[165,166]. Actually, the exchange correlation term is thought to cancel the self-interaction as DFT only approximates the exchange-correlation term, an electron has at least partially an electrostatic interaction with itself[167,168]. These incorrect self-interactions can cause a *delocalization error*[169] where non-integer charges may be assigned to electrons. These non-integer charges can arise if e.g. two atoms are pulled apart[170]. In this case, one of the atoms will not have zero, one or two electrons but rather delocalized electrons, resulting in fractional occupation numbers. These delocalizations are associated with an incorrect drop in energy for approximated functionals to such an extent that the stronger the character of delocalized electrons the lower the energy of the system[146]. One of the most prominent DFT shortcomings, the *band gap problem* which is related to the condition of incorrect fractional charges; It is defined as the difference between the electron affinity and the ionization energy. This quantity can be expressed as the difference of $\epsilon_{LUMO} - \epsilon_{HOMO}$, where ϵ_{LUMO} is the KS eigenvalue of the lowest unoccupied molecular orbital and ϵ_{HOMO} the eigenvalue of the highest occupied molecular orbital, respectively. The band gap problem often appears in transition metal complexes[171,172] and elongated covalent bonds[149,173–175]. It is also a weak point in describing the density distribution which, for example, may result in a poor representation of electron transfer or other electromagnetic features[176].

Wave function based methods (HF and post HF-methods), like CCSD, can be improved systematically by adding triple excitation for example[177]. However, there is *no systematic improvement* for DFT methods. It is easier to find correction terms for every failure to increase its accuracy[94].

Apart from all these shortcomings, it must be pointed out that DFT is one of the most widely used approaches for electronic structure calculations, because in many studies the DFT-achieved accuracy is

satisfying.

3.2.6. Computational Details

All electronic structure calculations in this work, if not stated differently, were carried out with Gaussian03[134] in the gas phase using the B3LYP functional[113,114]. Ligands were computed with the 6-31G(d,p)[124] basis set including polarization functions, while the metal center was treated with LANL2DZ[178] including an effective core potential. Transition states were computed at 0 K with the scan approach, Berny's optimization algorithm, or the QST2/QST3 method. If more than one negative Hessian eigenvalue appeared during the transition state optimization, we turned off the eigenvalue check with *noeigen* to avoid failures. IRC calculations were carried out (Gaussian09) to validate obtained transition states. An additional validation of transition states obtained from the B3LYP method was done by applying the GGA functional PBE[111] on the same system.

3.3. Force Fields

In recent years, the use of molecular mechanic (MM) approaches became a very popular and fast developing scientific field, introduced by the early studies of transition metal coordination[179], the prediction of relative stabilities and the stereochemistry of inorganic complexes[180]. The pure theoretic studies were followed by a computer-based investigation of minimizing bond and angle strain energies for five-membered rings[181] which established the usage of CPU power. A huge variety of applied MM models are known to date, starting with Allinger's MM1[182], MM2[49], MM3[183] and MM4[184] force fields, CHARMM[40], Amber[185], Gromos[186], UFF[187], OPLS[188] and many other MM methods.

Standard force fields use an empirical approach to compute energies, to model molecular shapes and to quantify dynamical properties of various organic and inorganic species. This approach allows treatment of very large systems, for instance, biological relevant protein folding[189] or mechanistic insight in the regulation of ion channels[190] while QM methods are limited to few hundred atoms. Although heavily distorted geometries are hard to capture, the accuracy is under control by the decision of how many parameters are used to describe the system. The applied parameters can be either directly extracted

from experimental data or they are fitted to experimental findings. Using high-level QM calculations as a reference is also common but with the limitation that the force fields cannot be more accurate than the defective QM data. Beside the high speed of MM methods however, a parametrization is costly and varies for different force fields according to different applied mathematical equations to describe molecular interactions. To ensure the transferability of derived parameters, different "atom types" are introduced which account for closely related systems. The more atom types are used to describe an atomistic model the more accurate is the prediction of energies and structures, and it allows fine-tuning of other physical properties.

Most of the common force fields are additive, meaning that they approximate the total potential as sum of simple energy contributions:

$$V_{\text{tot}} = V_{\text{bond}} + V_{\text{angle}} + V_{\text{dihe}} + V_{\text{elstat}} + V_{\text{vdW}} \tag{3.19}$$

The potential energy term V_{bond} describes bond stretching, while V_{angle} is relevant to model quantitatively angular distortions and dihedrals (torsions) V_{dihedral} account for the angles between two planes. The three mentioned potential energy terms describe interaction between covalently bound atoms and are therefore grouped in the so-called "bonded terms". The non-bonded interactions are described by long-range interactions, such as the electrostatic V_{elstat}, where atomic charges or multipoles model essential interactions and the vdW forces V_{vdW} which account for the interaction of neutral (not covalent-bound) atoms. In MM calculations, the non-bonded terms are computationally more expensive due to the large number of atom-atom interactions in space. This requires, at least to some extent, the usage of cutoffs which limits the influence of long-ranging interactions. For some force fields additional terms such as Urey-Bradley and improper dihedral angles are also implemented. The exact potential terms of (non-)bonded interactions varies with the corresponding force field, thus the CHARMM force field is described in more detail as it is used within this work.

3.4. Generalized Force Fields

Generalized force fields such as UFF[187], MM2[49] or CHARMM[40] are frequently used to study transition metal complexes as well as organic compounds or biological systems. A wide range of parameters

are provided for proteins[191], lipids[192,193], nucleic acids[53,194] and partially for carbohydrates[195–197]. The advantage of those force fields is strikingly presented by using for instance the UFF force field to determine the geometries of several transition metal compounds[198], although UFF was set up to model organic compounds. The use of a modified MM2 force field which was applied on octahedral complexes is another example but with modest results[199]. Therefore, if generalized force fields are also dealing with complexes, they should incorporate several transition metals and all their corresponding spin and oxidation states. As a consequence, a large amount of parameters are needed which increases the work of parametrization and lowers the simplicity of the underlying force field. In many cases however, the obtained accuracy, by using generalized force fields, is satisfying for the intended purpose.

3.4.1. CHARMM Force Field

Generalized molecular mechanics force fields such as CHARMM are routinely used for atomistic simulations of biomolecules in condensed phases. For such simulations, an ideally transferable set of force field parameters is required to compute meaningful observables. To model the interaction of atoms in the selected system, CHARMM uses approximations for the additive terms which were schematically mentioned in eq. 3.19.

$$\begin{aligned} V_{\text{bond}} &= \sum K_b(r - r_e)^2 \\ V_{\text{angle}} &= \sum K_\theta(\theta - \theta_e)^2 \\ V_{\text{dihe}} &= \sum K_\phi(1 + \cos(n\phi - \delta)) \\ V_{\text{impr}} &= \sum K_\gamma(\phi - \phi_e)^2 \\ V_{\text{elstat}} &= \frac{1}{4\pi\epsilon_0}\sum \frac{q_i q_j}{r_{ij}} \\ V_{\text{LJ}} &= \sum \epsilon_{ij}\left[\left(\frac{\sigma_{ij}}{r_{ij}}\right)^{12} - \left(\frac{\sigma_{ij}}{r_{ij}}\right)^{6}\right] \end{aligned} \tag{3.20}$$

Here, V_{bond} models the bond stretch term which is approximated by a harmonic oscillator, where K_b is a stretching force constant, r the instantaneous bond length and r_e the equilibrium or reference bond distance. The force constant K_b and the equilibrium bond length r_e differ according to the considered

pair of atoms (Fig. 3.1). The potential V_{angle} and V_{impr} are modelled with the same ansatz, whereby the applied improper torsions can be attributed to enforce planarity in an aromatic system or to arrange out-of-plane geometries. As an option, Urey-Bradley terms can be specified in addition to angle potentials to fine-tune the angle bending by 1,3 non-bonded interactions. The dihedral potential V_{dihe} uses a Fourier expansion based on cosine functions which are periodic and they are able to describe n-fold symmetries. This can model multiple potential energy minima. Therefore, the function has to be periodic and to keep the symmetry. The cosine function defines this symmetry by having stationary points at 0° and 180°. This way it accounts for low barriers between adapted geometries where K_ϕ is a half of the barrier height, n is the periodicity of the dihedral (number of minima), and the phase δ determines the location of the maximum.

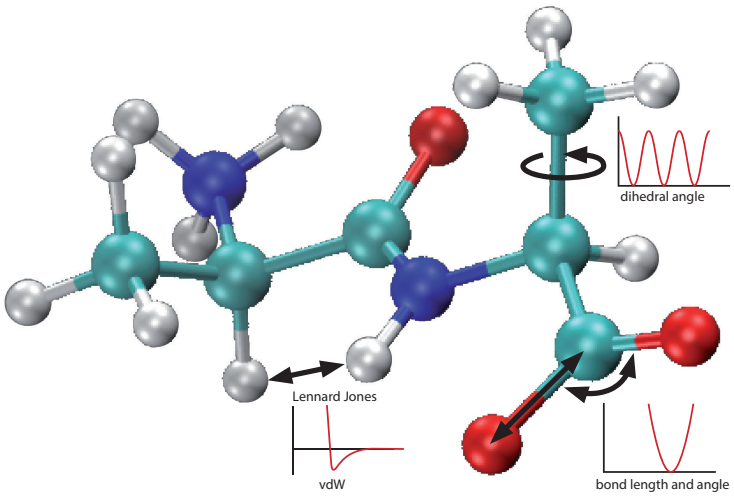

Figure 3.1.: Typical normal modes of a force field.

Considering the non-bonded terms, the electrostatic potential V_{elstat} is approximating the charge density of atoms as point charges and their interaction with Coloumb's law, where q_i are used, while r_{ij} defines the distance between particular atoms. The electrostatics are only taken into account for atom pairs which do not belong to the same molecule or are at least three bonds away [191]. Atomic charges are no observables but can be derived by different methods. Derived point charges are supposed to model all relevant properties, which is essential especially for the electrostatics of metal force fields. The ϵ_0 is a dielectric constant which is usually $\epsilon = 1$ for calculations in vacuum but can be raised to mimic the solvent environment explicitly.

The vdW interactions are described by a "Lennard-Jones-(12,6)-potential" which includes an attractive long-range term, showing a r^{-6} dependence on the vdW forces and a r^{-12} component which describes the Pauli-repulsion (due to overlapping orbitals) for short internuclear distances r_{ij}. ϵ_{ij} is the potential well depth and σ_{ij} is the sum of LJ-radii which are essential for the attractive and the repulsive energy contribution, respectively. σ_{ij} is described as the sum of two radii depending on the composition of the atom pair. CHARMM uses the Lorentz-Berthelot[200,201] rules to avoid that ϵ_{ij} and σ_{ij} has to be determined for every pair of atoms, it rather assigns parameters to every element or more specific to every atom type. However, other and partially more elaborate combination rules exist[57,202–205].

3.4.2. Molecular Mechanics - Drawbacks

Applying the described standard force fields on inorganic compounds can rise several problems[46,206–209]. Already the choice of reference data is quite critical for the parametrization of FFs. If applicable, experimental data such as crystallographic structures or infrared spectra are taken, but it can be problematic to extract force constants from experimental IR spectra due to strong electronic effects and low frequencies of the metal-ligand interaction[210]. However, experimental data are insufficiently homogeneous and to some extent even not available. High-level QM calculations are used instead to overcome this problem, but the quality of the obtained data strongly depends on the chosen QM-method. At best, reliable reference data are predicted by post-Hartree Fock methods (like CC or CI), but to carry out sampling with such expensive methods is often not feasible. A much faster alternative is DFT or MP2 which allows calculations for a large set of model compounds used as a reference collection. Especially DFT provides a compromise between speed and accuracy and accounts for relativistic effects by including effective core potentials (ECPs)[6] but at the same time its accuracy is highly dependent on the functional (see DFT section). The limited flexibility of the functional form of the FF however can be problematic in capturing the large variation of conformations for floppy molecules.

The nature of the ligand, coordinated to the metal ion, can highly affect the equilibrium geometry of the system and the molecular dynamics. Monodentate ligands are grateful, but dealing with bidentate ligands can introduce already a lot of strain. To mimic π-type ligands is even more challenging due to the possibility that the central atom can coordinate with several parts of the ligand, allowing a high rotational flexibility[211,212]. A straightforward procedure to deal with metal coordination is realized via

pure non-bonded forces. Applied vdW and electrostatics even enable an exchange of ligands during a MD simulation. However, the orientational dependence of the ligand facing the metal center is not sufficiently described, it rather works for specific complexes[213]. An advanced approach was introduced by Kepert *et al.*, where only the ligand-ligand interactions are used to model the coordination[214]. It includes therefore all M-L bonds, but it neglects all L-M-L angles. However, additional terms are needed to model planar systems e.g. quadratic planar complexes.

An alternative approach, which is used within this work, is to handle these η^2, η^3, ..., complexes by introducing dummy atoms. This procedure was already applied in several studies, e.g. Norrby *et al.* modelled a η^3-allyl coordinating group by using the dummy as a link[215]. However, the usage of dummy atoms generates additional unrealistic interactions which either have to be removed afterwards or have to be kept small by not assigning a charge, a mass and vdW parameters to them. In another study, Doman *et al.* presented metallocene compounds, where the cyclopentadienyl (Cp) ring is attached to a dummy atom, centered in the middle of the ring[212]. The localization of the dummy atom enables an equal distribution of the forces within the Cp, facilitating vibrational analysis of the selected compound. Following studies established this procedure[216,217] however, it is not an optimal solution to treat η-binding ligands.

The vdW forces, mostly described by the Lennard-Jones-(12,6)-potential, can describe the energy landscape as long as the internuclear distance r_{ij} is large enough. At short distances of two atoms, the LJ formula overestimates repulsion[183,218,219], therefore varying the exponents of r^{-6} and r^{-12} can result in a much better agreement of FF derived energies and *ab initio* data[220].
In the CHARMM force field, point charges are usually atom centered and the electrostatics describes the polarization only in an averaged way. However, MD simulations in a highly dielectric medium (e.g. water or even in gas phase) may affect intermolecular energetics which are not sufficiently captured by pairwise additive force fields[213]. Polarizable force fields have an enhanced treatment of the varying charge distribution in response to the dielectric medium or other external factors[221]. It basically adds the contribution of the polarization energy to the conventional non-bonded potential[222]. In some simple systems where covalent bonding predominates, it is an attempt to completely remove electrostatic interactions which also works for small complexes[223] and even for the large molecule of carbonic anhydrase[224]. In contrast, a study (using Amber) about the refinement of parameters for metallo-proteins gives more weight to the electrostatic potential[225]. However, the most atomistic systems reveal a

varying charge distribution whereas additive force fields such as CHARMM are very limited with its point charge description. Using additional multipoles can significantly improve the accuracy of the FF[226–228]. Other advantageous implementations were provided by adding a potential term to specify hydrogen bonding to predict vibrational analysis for nucleic acids with a MM approach[229] and adding cross terms to enhance the quality of protein FFs in relation to high-level QM and crystallographic data[230].

The harmonic approximation gives a poor description for long bond distances due to the parabolic shape of the potential and it even prohibits bond breaking. A better choice for modelling extreme distortions is provided by using a Morse potential (see MS-ARMD section) which captures anharmonicity, although more parameters are necessary. It describes the elongation behaviour of a covalent bond between two atoms until their final dissociation. Applying the Morse potential on metal complexes can be essential to model the strongly varying length of the soft bond between the metal and the coordinating ligands[231].

The harmonic angular potential V_{angle} (eq. 3.20) is an essential additive term for treating metal complexes. As long as the bending deformation is small, the harmonic approximation is sufficient. However, treating transition metal complexes where angle potentials are even softer than bonds can result in large distortions. Sterically demanding ligands and especially the bidentate nature of ligands can additionally cause extreme distortions. For these circumstances, specific force field terms were applied to capture significant geometrical changes. A first attempt to handle extreme distortions in metal complexes is the inclusion of Urey-Bradley angular forces (non-bonded interactions) but additional modifications have to be made (see VBT section).

A torsion angle is defined by two central atoms and two terminal atoms which give rise to a large number of possible dihedral types. To assign parameters to every type is very costly and therefore a lack of such dihedral parameters exists. The user is either forced to fit all possibilities or what is usually done, to take related values based on the center atoms or even to set the dihedral potentials to zero (if they can be neglected)[46].

The large variety of metals and their various spin states imply that clearly more complex geometries can be adapted. This can result in a higher coordination number compared to usual organic molecules

exhibiting a typical tetra-coordinated species, arranged in a tetrahedral or square planar shape. There are other common arrangements such as trigonal- and square-pyramidal geometries, their bipyramidal analogs or octahedral shapes. Depending on the sterical hindrance of the ligands, these structural shapes can form various other pseudo geometries. Treating such highly complex systems with a generalized force field is very limited[232–234].

A specific problem can arise by treating octahedral complexes. However, in octahedral complexes, angles are described with atom types defining only one value to a certain L-M-L angle. Here, the L-M-L pattern can adapt a geometry where the ligands are in an axial position (180°) or where one of the ligands is coordinated equatorially (90°). Using one of the values for the L-M-L pattern will result in a wrong description for the other arrangement. In addition to this problem, it is also relevant to define which ligands are affected by the trans influence or if the metal d-orbitals are distorted by the Jahn-Teller effect[235,236]. A way out of this definition problem is to introduce more atom types and therefore even more parameters resulting in an exhaustive fitting procedure. However, a reduction of parameters to describe metal-organic compounds, without the loss of accuracy, became realistic for more specific force fields.

A general problem for force field parametrization is the source of reference data. The current lack of experimental data causes a lack of available data or the deficient transferability of parameters. To face the difficulties of applied general force fields, essential problems are summarized in the following. First, the lack of generalized force fields to model transition metal complexes, especially if heavy distortions occur. Second, the required set of parameters for all p- and d-block elements can reach an enormous dimension. Third, potential energy curves are not adequate for large distortions and fourth, the treatment of transition metal complexes is not straightforward, because it does not follow a certain pattern. Accordingly, there is an emphasis putted on developing specialized force fields which will lead to more reliable results.

3.5. Metal Specialized Force Fields

Specialized metal force fields have addressed some of the mentioned problems with remarkable success, although this specialization is limited to organometallic species. Several groups are using the approach

that equilibrium angle parameters depend on the electron configuration of the metal complex[237] and consider angular overlaps[238] but other approaches exist. Common specialized force fields can reduce the number of parameters by different approaches which are described in the following.

3.5.1. SIBFA - Sum of Interactions Between Fragments Ab Initio

The development of rapid methods to compute accurate energies for metal-containing systems has been a subject of interest for the past 20 years. SIBFA (sum of interactions between fragments *ab initio*)[20,226,239–241] is a fragment-based energy decomposition method which can treat organometallic complexes and metalloproteins[242–245]. SIBFA is based on high-level *ab initio* data and basically disassembles a molecule into rigid blocks which are connected by bonds. To derive the interactions between fragments, the force field explicitly accounts for anisotropic fragment polarization, repulsion and charge transfer, as well as incorporating distributed multipole moments centered at both nuclear positions and bond barycenters. Therefore, the intermolecular interfragment interaction energy (ΔE_{int}) is expressed as

$$\Delta E_{\text{int}} = E_{\text{MTP}} + E_{\text{rep}} + E_{\text{pol}} + E_{\text{ct}} + E_{\text{disp}} \tag{3.21}$$

The total interaction energy consists partially of the contributions which were already mentioned in eq. 3.19. (1) The multipolar electrostatics (E_{MTP}) is a sum of interactions between multipoles which were derived from the molecular wave function according to the approach of Vigne-Maeder and Claverie[246]. (2) The short-range exchange repulsion (E_{rep})[247] involves bond-bond, bond-lone pair and lone-pair lone-pair interactions in order to model anisotropic effects. (3) The contribution of induced dipoles (E_{pol}) is computed with a self-consistent iterative procedure[248] which considers the distributed polarizabilities on individual fragments. (4) The charge-transfer energy (E_{ct}) incorporates a function[249] for the overlap between lone pair hybrid orbitals as well as for the interplay of ionization potential of the electron donor and the electron affinity of the acceptor. (5) The dispersion energy (E_{disp}) includes an exchange-dispersion part and can include directionality effects by an explicit addition of fictive atoms[250]. Beside several improvements of the SIBFA FF[20], one extension permits to consider the ligand field splitting of d-electrons (Fig. 3.2).

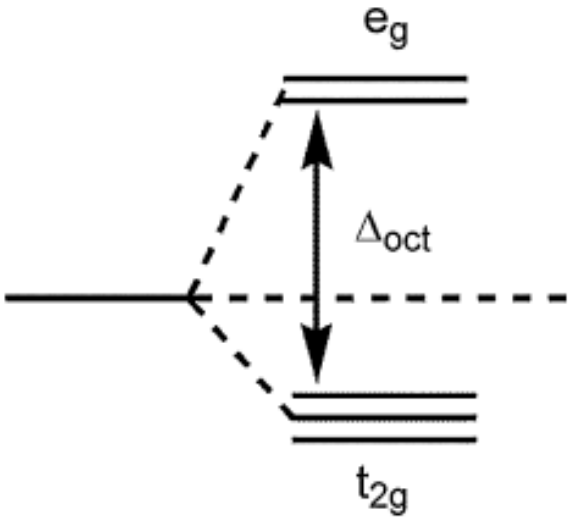

Figure 3.2.: Octahedral d-orbital splitting diagram[21].

This FF is referred as the SIBFA-LF[239] FF that uses an additional energy term (E_{LFSE}) which is based on an angular overlap model (AOM) and allows to account for Jahn-Teller[251] distortions. Such a ligand field effect causes a splitting of the energy levels of the d-orbitals and therefore assigns different relative energies to each orbital. The AOM relates this change in the relative energies with the overlap between the metal d-orbitals and ligand orbitals[239]. The additional detail afforded by these energetic terms makes SIBFA computationally more expensive than less detailed force fields such as CHARMM[48] and AMBER[185], but as a consequence SIBFA can yield molecular structures and energies that are in close agreement with *ab initio* data while maintaining a lower computational overhead than would be required for a full *ab initio* computation.

3.5.2. LFMM - Ligand Field Molecular Mechanics

An alternative to SIBFA is LFMM (ligand field molecular mechanics)[21,252–254] which combines a conventional force field with added terms explicitly capturing electronic effects. LFMM has been applied to Cu(II) complexes by using amine[255] compounds and crystallographic structure data as a reference. It was also applied to copper enzymes[256] where DFT calculations served as a reference. LFMM parameters for zinc, manganese and nickel complexes are also available which represents a wide range for such a force field[8,252,257].

LFMM is based on the ligand field theory (LFT)[258] which describes the energy of d-orbitals while, using additional terms. The ligand field stabilization energy (LFSE)[259] can also be taken into account. If d-d interelectronic effects are considered, the LFSE has a significant contribution to the total energy of metal containing systems which is e.g. reported for Werner-type complexes[260–262]. It is basically a function that covers the d^n-configuration and also the extent of the ligand field splitting. The d-orbital splitting (Jahn-Teller effect) remarkably influences the metal-ligand distances of equatorial and axial located atoms which is essential to describe low- and high-spin complexes[231]. LFMM includes an extension of the LFT according to Hitchman[263,264], which accurately predicts these changes in the M-L bond lengths. Within this extension, equatorial and axial changes in bond lengths are coupled and constrained by using Lagrangian multipliers[265]. The total potential energy is a sum of individual contributions from bonded terms E_{bond}, E_{angle}, E_{dihe}, non-bonded terms $E_{\mathrm{non-bonded}}$, including LJ and electrostatics and the conceptually relevant E_{LFSE} energy term:

$$\Delta E_{\mathrm{tot}} = E_{\mathrm{bond}} + E_{\mathrm{angle}} + E_{\mathrm{dihe}} + E_{\mathrm{non-bonded}} + E_{\mathrm{LFSE}} \tag{3.22}$$

As reported in eq. 3.22, the E_{LFSE} energy term is directly included in the total potential energy. This assigns a kind of QM/MM character to the LFMM method, as it combines the MM treatment of the ligand periphery with the use of a bond-centered angular overlap model (AOM) to treat the LFSE of the TM center. For this reason, the complex is separated into two parts, the coordination region which contains the metal and its directly coordinated atoms and the ligand region which accounts for all atoms except for the metal center (Fig. 3.3).

The QM implementation is however limited to the treatment of the metal atom while other atoms are treated with a MM approach. Although the first derivatives of the LFSE are solved analytically[266], the LFMM approach is more time-consuming than a purely MM based approach. Additionally, LFMM assumes that the d-orbitals of a metal center are weakly influenced by the surrounding environment. Therefore, LFMM typically deals successfully with first-row TM-complexes[267]. To capture d-electron effects of third-row TM-complexes, an implementation using hybrid orbital strength functions (based on valence bond theory) might be more reliable.

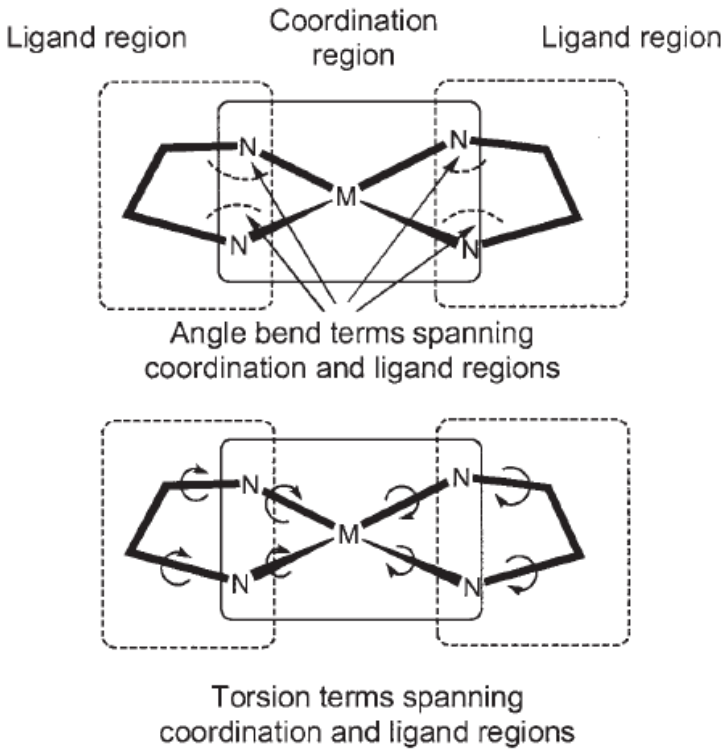

Figure 3.3.: Schematic representation of division into coordination and ligand region and force field terms which span the two[254].

3.5.3. VALBOND Force Field

VALBOND[22,23,59–61] is a valence bond theory-inspired extension (for valence bond theory[25] see Chapter 2) of the conventional CHARMM force field, to treat metal-containing complexes. For the VALBOND FF as well as for the majority of molecular mechanic methods, the specification of a topology is one of the first steps. Among others, a decision has to be made which atoms are connected by localized bonds and which atom pairs are treated with non-bonded interactions. PerlMol[268] supports the set up of the topology and input files for organometallic complexes by using data from Gaussian files. For MM approaches, localized bonds (formed by an overlap of hybrid orbitals) are better described by VB-theory than by MO-theory where linear combinations of atomic orbitals form delocalized bonds. According to valence bond theory, the power or the strength of bond formation has a strong angular dependence and ask for precise definition of angle bending terms. Such an angle bending term is implemented in the metal specialized VALBOND force field[22,23,59–61].

VALBOND uses hybrid orbital strength functions to realistically describe valence-angle distortions

L_1-M-L_2 involving two ligands (L_1 and L_2) and a shared metal atom (M). Following the seminal work by Pauling[62,63] who examined chemical bonding from the perspective of valence bond theory, VALBOND aimed at correctly capturing the bending potentials over a wide range of angular distortions. VALBOND can describe both non-hypervalent and hypervalent (complexes with more than 12 electrons) molecules[60] and transition metal complexes[22,61] because the functional form for valence-angle distortions L_1-M-L_2 in the FF is suitable to also describe considerable angular distortions in the geometry. Basically, VALBOND provides a more specific angular term and therefore it has to rely on a conventional force field such as CHARMM[40], Amber[185] or GROMOS[186] to include all essential interactions. For our use, VALBOND is combined with the CHARMM force field.

The derivation of the strength of a bond formation depends on the overlap Δ between two hybrid orbitals of L_1-M and M-L_2. This overlap is expressed as a function of m and n hybridizations of the corresponding hybrid orbital.

$$\Delta = \frac{1}{1+m+n}(1 + m\cos\alpha + \frac{n}{2}(3\cos^2\alpha - 1)) \tag{3.23}$$

Each of the non-hypervalent bonds (L_1-M and M-L_2) has overlapping sp^md^n-hybrid orbitals including an angle α between them. According to Pauling, a non-orthogonal positioning of the hybrid orbitals decreases their strength from the maximum value. Therefore, the strength can be expressed in terms of the maximum strength S^{max} which is reached when $\alpha = 180°$:

$$S(\alpha) = S^{max}\sqrt{1 - \frac{1-\sqrt{1-\Delta^2}}{2}} \tag{3.24}$$

At a certain angle α, this quantity regulates the decrease in strength of two sp^md^n hybrids in dependence on their non-orthogonality at that position. That means, in terms of a sp^3 configuration, if the two orbitals are not maintaining a tetrahedral angle of 109.47°, a defect in the orthogonality will cause a reduction of the maximum strength S^{max}. Whereas the maximum strength S^{max} between two orbitals is a function purely based on the m and n hybridization exponents:

$$S^{max} = \sqrt{\frac{1}{1+m+n}}(1+\sqrt{3m}+\sqrt{5n}) \tag{3.25}$$

Considering these strength functions, Landis an co-workers implemented a general procedure to determine the angular dependency of all types of hybrid orbitals. It essentially describes the angular part of a wave function and provides a pendant to the local electron density. Therefore, the strength is comparable with the power of a bond formation. However, one drawback for the hybridization procedure has to be mentioned. The hybrid orbitals are solely based on an angular contribution but ignores the radial component of the orbitals. This results in a slightly different hybridization than it is determined by VB-computations including both, the angular and the radial contributions[269]. Nevertheless, the geometry based on hybrid orbital strength functions (eq. 3.24) have proven to describe sufficiently the angular contributions in the VALBOND force fields[59].

For a molecule, several strength functions exist which have to be combined to determine the total energy contribution of the angular term. Pauling's pair defect approximation[270] method is applied to describe the potential energy surface for the bending of two or more ligands which are not identical. This approximation takes the defects into account which are caused by non-equilibrium geometries. The defect-energy $S(\alpha)$ (depending on the angle α) is subtracted from the maximum strength of each hybrid orbital S^{max} in eq. 3.26. A scaling factor k is adjusting the energy contributions of the hybrid orbitals in order to obtain correct vibrational frequencies for the bending modes according to Hartree-Fock computations[271]. The defects $S(\alpha)$ are solely depending on the hybridization of one ligand orbital and its position and not on the hybridization of other ligands. The energy contribution of such a bond orbital is given by:

$$E_{nonhyp} = k(S^{max} - S(\alpha)) \tag{3.26}$$

Adding the energy contribution of a second bond orbital results in the angular energy of one angle, summing over all these angles determines the total angular potential. This general expression is implemented in the VALBOND force field and is taken into account for non-hypervalent bond-angles. The representation of the angular energy functions for different hybridizations can indicate the positioning of corresponding minima illustrated in Fig. 3.4 by Schmid *et. al*[217].

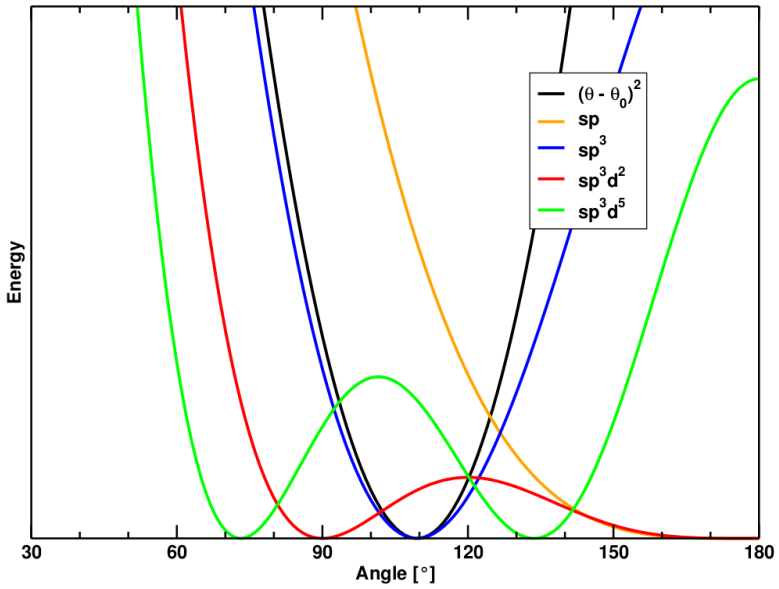

Figure 3.4.: VALBOND energies as a function of the angle for different hybridizations. The energy function of a harmonic angle with $\theta_0 = 109.5°$ is marked in black for comparison[217].

VALBOND defines complexes, which are counting more than 12 electrons in their valence orbitals, as *hypervalent*[272]. The concept of hypervalency introduces a three-center-four-electron bonding model which is used instead of p-orbitals[60]. The energy contribution of such a hypervalent three-center-four-electron bond is

$$E_{hyp} = k(1 - \Delta(\alpha + \pi)^2) \tag{3.27}$$

where k is again a scaling factor, Δ the overlap function (eq. 3.23) depending on the bond angle α. The energy for one angle is then determined by summing all hypervalent and non-hypervalent hybrid orbital energies multiplied by a bond order factor (BOF):

$$E_{angle} = \sum \mathrm{BOF_i} \times E_{hyp} + \sum \mathrm{BOF_j} \times E_{nonhyp} \tag{3.28}$$

The bond order factor of hybrid orbitals can range from 0 to 1 and is normally 0.25 for hypervalent bonds and 1 for non-hypervalent bonds and is not influenced by the bond character (single bond, double bond, ...). Depending on the assignment of the three-center-four-electron bonds, for hypervalent

molecules, it has to be accounted for the existence of several resonance structures. Each resonance structure is weighted by a factor c_i which is depending on the geometry[60].

$$c_i = \frac{\prod_{i=1}^{hype} \Delta_i^2}{\sum_{j=1}^{res} \prod_{i=1}^{hype} \Delta_i^2} \tag{3.29}$$

Here, the products run over all hypervalent angles i and *res* stands for the number of resonance configurations, which is further explained in the literature[60]. The total energy of the angular term is then the sum of energies E_i of all resonance structures weighted by c_i.

$$E_{\text{tot}} = \sum_{i}^{n} c_i E_i \tag{3.30}$$

With VALBOND, a general scheme was established to accurately predict equilibrium geometries. The use of general hybridization parameters and scaling factors to derive the angular term significantly reduces the set of parameters compared to the conventional set of equilibrium bond angles and the corresponding force constants. However, assignments of hybridizations are not trivial and can be unprofitable for some complexes. Nevertheless, with few exceptions, the combination of VALBOND and the CHARMM force field provides a powerful tool to deal with simple organic and inorganic molecules, radicals and metal complexes.

3.5.4. VBT - VALBOND TRANS Force Field

Originally developed for structural investigations, VALBOND has been extended to capture electronic effects such as the trans influence. This VALBOND TRANS (VBT) force field has been shown to provide a robust means to investigate structures of model-complexes. Very recently, it has also been applied to study the dynamics, vibrational and NMR spectroscopy of a Pt-based catalyst used in hydroformylation[273] and for solvent dynamics of transition metal complexes[29,274].

In this extension, VALBOND was modified to capture the structural and the thermodynamic trans influence which is defined as "the tendency of a ligand to selectively weaken the bond trans to itself" [235]. The *energetic trans influence* for L_1-M-L_2 angles can be regulated by the following expression

$$E_{\text{trans}} = \sum_{hype} p_{\text{AB}} \Delta(\alpha + \pi)^2 \tag{3.31}$$

The adjustable parameter p_{AB} depends on the types of ligands L_1 and L_2 involved in a L_1-M-L_2 bonding motif. p_{AB} is determined by fitting to model compound energies[223].

For the *structural trans influence*, bond lengths are modified according to a trans influence intensity i:

$$r_{\text{A(B)}} = r^0_{\text{A}}(1 + s_{\text{A}} \cdot i_{\text{B}}/100) \tag{3.32}$$

$r_{\text{A(B)}}$ is the equilibrium bond length A–M when atom B is *trans* to A, r^0_A is the unperturbed equilibrium bond length A–M, i_B is the bond lengthening intensity induced by atom type B and s_A is the bond lengthening sensitivity of atom type A. The trans influence and therefore the relative change of the bond length $r_{\text{A(B)}}$ is captured in VBT as[223]

$$r_{\text{A(B)}} = r^0_{\text{A}}(1 + s_{_{\text{A}}} \cdot \Delta(\alpha + \pi)^2 \cdot i_{\text{B}}/100) \tag{3.33}$$

Fortunately, a large set of trans influence parameters is available, however depending on the ligands, a refinement of the specific parameters can be beneficial to capture structural changes and energetics. VALBOND and VALBOND TRANS do not include expensive energy terms as they are implemented in LFMM and SIBFA. This allows to carry out MD simulations for large systems over a long period of time with a comparable accuracy to LFMM and SIBFA. For our needs, the VBT FF is the most suitable method.

3.5.5. Other Metal Force Fields

Several other TM specialized force fields exist, however, they are not used frequently. The precursor of the VALBOND FF is the SHAPES[238] force field which is also using angular overlap functions. It employs angular potential energies by describing them with periodic Fourier terms. The MOMEC[231]

force field is an approach were only ligand-ligand repulsion is considered. The YETI FF [224,275,276] is mainly used to model metal-ligand interactions to determine the toxicity of small molecules where used directionality terms for hydrogen bonds and salt linkages are beneficial. Other, even less frequently used FF such as Shelnutt's force field [277] or the DREIRING FF [278] also exist. All metal specialized force fields can be applied for structure optimization but currently only VALBOND TRANS allows MD simulations in explicit solvent within a reasonable time span. Elucidation of a chemical process with one or more transition states however asks for a combined tool which enables the formation of new compounds.

3.6. Adiabatic Reactive Molecular Dynamics

During a chemical reaction, the oxidation state or the connectivity of atoms changes. Conventional force fields cannot describe these changes as they assume fixed connectivity and atomic charges, and they were made for low amplitude vibrations and conformational motions. Various MD methods based on FFs were developed to follow chemical reactions [279,280]. Their common feature is the use of a switching function to change smoothly between the FFs of reactant and product states. Peyman and Beckhaus used a Morse function as a switching function to alter the potential energy terms of the FF during the dimerization of di-*tert*-butylmethyl radicals [281]. They mentioned that the description of the changing hybridization during the reaction is a challenging step. A subsequent study by Hase and co-workers [282] also used switching functions to shift between different equilibrium parameters to develop a potential energy surface for the recombination reaction of H + CH_3 → CH_4. Other reactive molecular mechanic approaches, developed during the last decade, are reviewed elsewhere [279].

Recently, the adiabatic reactive molecular dynamic [284–286] (ARMD) method was developed in our group which is a general surface-crossing algorithm that allows one to follow bond-breaking and bond-forming processes in classical molecular dynamic simulations. In ARMD the dynamics of the system is propagated on the $V_0(x)$=min[$V_1(x)$, $V_2(x)$] surface where V_1 and V_2 are the force fields for reactants and products, respectively (see Fig. 3.5). During dynamics, when the energy of the two surfaces become equal, the system is re-simulated from a while earlier by gradually switching in time from V_1 to V_2 to cross between surfaces.

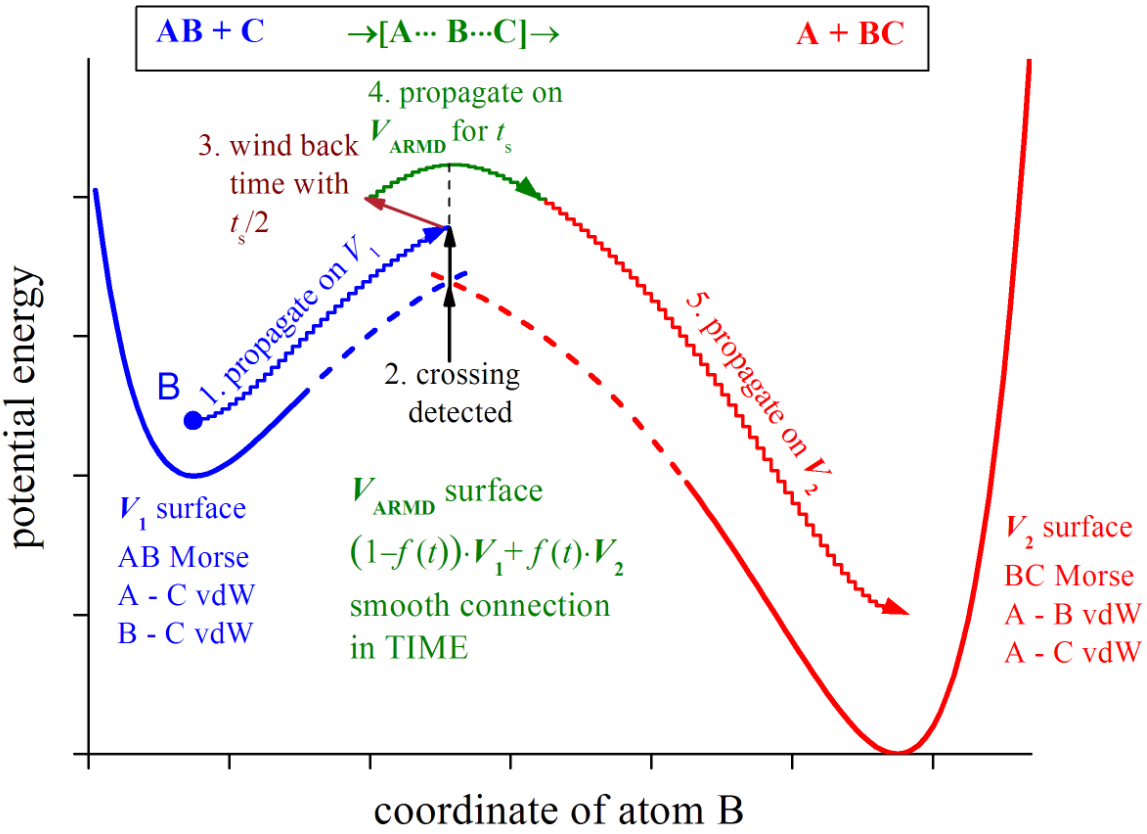

Figure 3.5.: Scheme of the adiabatic reactive molecular dynamics (ARMD) method. A transfer reaction of atom B is depicted where the coordinates of the donor (A) and the acceptor (C) are fixed. At the crossing region of V_1 and V_2, the two surfaces are switched in time. The Morse bond is replaced by vdW interactions or *vice versa* to account for the correct interaction[283].

The latest multi-state variant of the ARMD method is based on coordinate-dependent switching function and thereby conserves energy during the crossing between the two force fields. This new method was implemented in CHARMM and is referred as the multi-state adiabatic reactive molecular dynamics (MS-ARMD)[24,283] as it enables a smooth connection of several states. It permits the investigation of the energetics and dynamics at an atomistic level in chemical reactions and also the determination of reaction rates. The MS-ARMD switching method is demonstrated in Fig. 3.6 for two surfaces. A gradual switch from the reactant (V_1) to the product surface (V_2) is achieved by mixing the potentials in the region where they are close in energy.

For the general case where several surfaces are included, the effective global surface $V_{\mathrm{MS-ARMD}}$ corresponds to the lowest-energy surface V_{min}, except for the geometries where more surfaces have similar low energy (Fig. 3.6). The global surface is determined as a linear combination of all PESs weighted

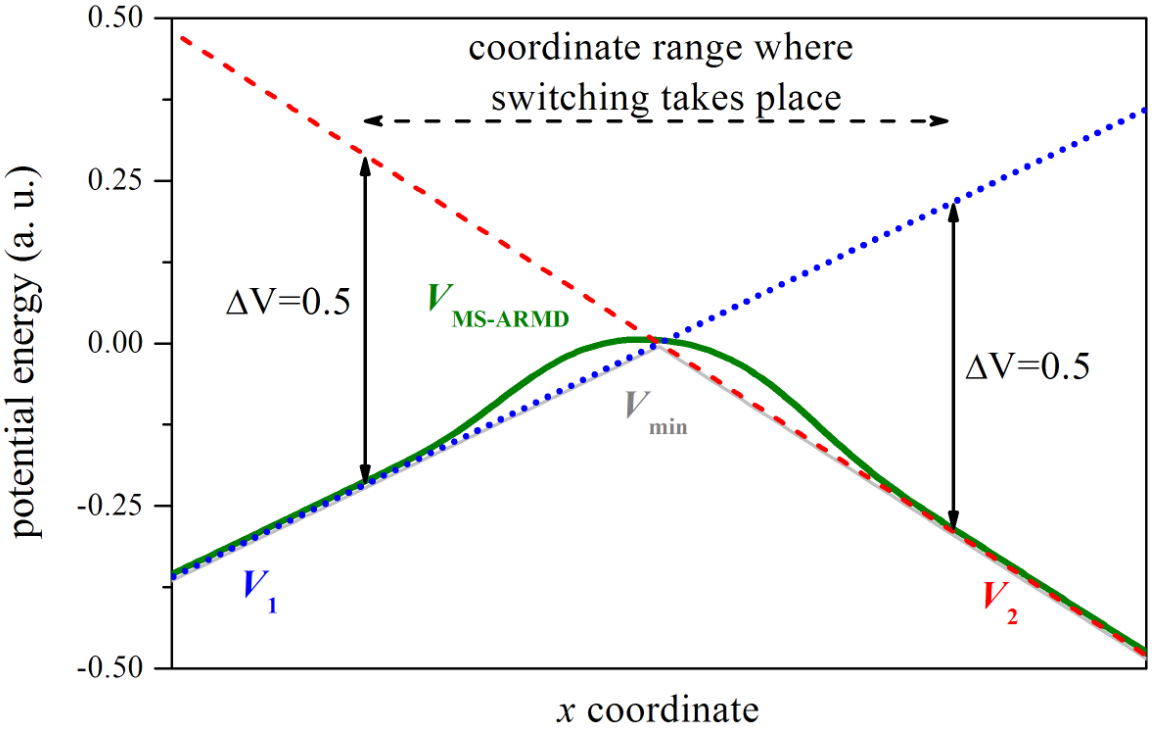

Figure 3.6.: Multi-state adiabatic reactive molecular dynamic switching (MS-ARMD) method is illustrated for two surfaces V_1 and V_2. The effective surface $V_{\mathrm{MS-ARMD}}$ corresponds to the lowest-energy surface V_{min}, except for the region where V_1 and V_2 get close in energy (within $\Delta V = 0.5$ arbitrary units) where the energy of the surfaces start mixing[283].

by mixing coefficients w_i.

$$V_{\text{MS-ARMD}}(\mathbf{x}) = \sum_{i=1}^{n} w_i(\mathbf{x}) V_i(\mathbf{x}) \tag{3.34}$$

The energy-based mixing starts when the PES-energy lies within the range of $[V_{\mathrm{min}}, V_{\mathrm{min}} + \Delta V]$. The value of parameter ΔV is the equivalent quantity of the switching time in ARMD (see t_{s} in Fig. 3.5), which is optimized to match *ab initio* data on the reaction path. A higher weight is given to those PESs which are closer in energy to the lowest-energy surface V_{min}. The crossing region of the global surface can be further adjusted by products of Gaussian and polynomial functions (GAPO). Those can be used to avoid an unrealistic high-energy crossing point (transition state) of the involved PESs, they rather support the control of properties in the crossing region. The construction of the global surface usually proceeds as the following steps: first, each of the surfaces are parameterized separately, second the crossing regions are optimized by adjusting the leveling parameter of each FF, the parameter ΔV

and optionally the parameters of GAPO functions. Parametrization means the optimization of all FF parameters of the global surface in order to match *ab initio* data by using a suitable fitting algorithm.

3.7. Fitting Algorithms for Force Field Parametrization

The optimal value of the force field parameters are determined by using a fitting algorithm which usually minimizes the deviation from a reference (e.g. *ab initio* energies). The quality or the progress of such an algorithm can be tested by a penalty function which is usually the determination of the root mean square deviation (RMSD). The structural difference between the force field and the *ab initio* optimized structures of model compounds is measured by the RMSD of the geometries expressed in Å units. This strategy is applied in the optimization of the VALBOND TRANS force field. The energy RMSD ($RMSD_E$, in kcal/mol) can also be calculated for several structures. For the comparison of reference data with different units, a more elaborate penalty function is needed which assigns weights to different parameter groups. Finally, the penalty function should be minimized at the best possible rate with respect to all parameters. Different fitting algorithms can be applied depending on the investigated quantities, on the linear dependency or higher correlated dependency of the parameters and on their number.

The most simple approach to refine parameters is the systematic *grid scan* where all possible parameter combinations are evaluated within a grid. However, this approach is only feasible for a small number of parameters. A *Monte Carlo* algorithm facilitates a random variation of parameters but again convergence is rather slow[287]. A more robust concept also used in this work is the *simplex* algorithm where the penalty function is minimized in certain step sizes. Considering an one-dimensional problem, the algorithm evaluates the error of a derived point and steps further by mirroring the previous step size until the downhill movement is over. If the next evaluated point is worse, the step size is contracted as long as convergence is achieved. For a set of initial parameters it may be critical to find a global minimum. This procedure is also applied for higher-dimensional problems but its efficiency is also limited by the number of parameters[287]. Genetic algorithms[287,288] and artificial neural network techniques[289] can also be used, for more detail the reader is referred to the literature.

More elaborate algorithms use derivatives of the penalty function. The gradient (the vector of the

first partial derivatives) of the selected function with respect to the chosen parameters gives the information about an optimal direction of change[287]. Including second derivatives can remarkably accelerate the convergence as the Hessian provides information of the local curvature, although the determination of the Hessian itself is time consuming. Independent of the usage of higher order derivatives, all derivative-based algorithms need to determine the Jacobian which is nothing else than a matrix where all first derivatives of selected data points are determined[290]. The determination of the Jacobian is therefore also implemented in the *steepest descent* (SD) algorithm. Here, the evolution of the parameters is along a line in the direction of the negative gradient whereby the step size is not optimized. The method works fine for large gradients but gets slow close to the minimum[287]. Using a *conjugate gradient* (CONJ) method helps out of the problem that the direction of every new determined gradient is taken, it rather constructs new vectors to maintain a related direction of the old gradient. The *Gauss-Newton* approach includes a quadratic approximation to enhance the convergence around the minimum, but it is rather slow far away from the optimum[290]. The one-dimensional form of this algorithm is the *Newton-Raphson* method which is often applied as its poor global convergence properties are not relevant close to the optimum[287]. The advantageous properties of the steepest decent and the Gauss-Newton methods are combined in the *Levenberg-Marquardt*[291,292] algorithm which has a robust performance even far from the minimum. This switching is controlled by a factor λ which is adapted as the fit proceeds.

The Levenberg-Marquardt algorithm is implemented in the non-linear least square fitting programm I-NoLLS[293] which can be adapted efficiently to our purposes. It enables the fitting of PES and provides, besides Levenberg-Marquardt, several other fitting algorithms. I-NoLLS can be adapted efficiently to the related problem by deciding about step sizes, inclusion or exclusion of parameters, the fitting algorithm and the use of weighted constraints as the fit proceeds. I-NoLLS was interfaced in the program CH-NoLLS with the VBT FF[27], but it can also be interfaced with other programs. The CH-NoLLS program allows to derive optimized geometries and relative energies for a given FF parametrization and thus, enables a flexible parameter refinement.

Part II.

Applications

4. Towards Force Fields for Atomistic Simulations of Iridium-Containing Complexes

4.1. Abstract

The structural and energetic characterization of metal complexes is important in catalysis and photochemical applications. Unravelling their modes-of-action can be greatly assisted by computation, which typically is restricted to computationally demanding methods including electronic structure calculations with density functional theory. Here, we present an empirical force field based on valence bond theory applicable to a range of octahedral Ir(III) complexes with different coordinating ligands, including iridium complexes with a chiral N,P-ligand. Using an approach applicable to metal-containing complexes in general, it is shown that with one common parametrization 85 % of the 116 diastereomers - all within 21 kcal/mol of the lowest energy conformation of each series - can be correctly ranked. For neutral complexes, all diastereomers are ranked correctly. This helps to identify the most relevant diastereomers which, if necessary, can be further investigated by more demanding computational methods. Furthermore, if one specific complex is considered, the root mean square deviation between reference data from electronic structure calculations and the force field is $\approx$ 1 kcal/mol. Together with the possibility to carry out explicit simulations in solution, this paves the way for an atomistic understanding of iridium-containing complexes in catalysis.

4.2. Introduction

It is of great interest in organometallic chemistry and homogeneous catalysis to characterize chemical structures of metal complexes and relate them to their reactivity. This can be done quite successfully by using computational methods. Quantum chemical methods such as density functional theory (DFT)

are a milestone in computational chemistry and are therefore often used as a reference for estimating relative energies of potentially relevant structures involved in catalytic processes. However, given the size of the systems, which usually contain several hundred electrons, the routine use of DFT to screen entire libraries of organometallic complexes is computationally prohibitive. Furthermore, the systems of interest can exhibit complicated electronic structures which also poses practical problems such as slow convergence of the Hartree-Fock cycles. It would, therefore, be advantageous to have computationally less demanding, albeit quantitatively still reliable and robust methods. Atomistic force fields are an attractive alternative as they allow rapid computation of energies, and the structures of the systems can be modelled conveniently by fitting appropriate point charges and Lennard-Jones (LJ) parameters. However, parametrizing such force fields for transition-metal-containing complexes is not yet routine. Motivated by our interest in Ir-based complexes[294–296], we set out to explore the possibility to parametrize a robust force field for iridium-containing complexes.

The development of rapid methods to compute energies for metal-containing systems was already the focus in several studies using molecular mechanic methods[10]. SIBFA (sum of interactions between fragments *ab initio*) FF[20,226,239–241] treated successfully organometallic complexes and metalloproteins[242–245]. The LFMM (ligand field molecular mechanics) FF was also effective in the determination of the energetics of copper complexes[255] and enzymes[256]. For a detailed insight see Chapter 3. The excellent performance of those two methods even provide details about the ligand field spitting (Jahn-Teller effect) and deliver results close to *ab initio* data. However, the expensive energetic terms of those approaches prohibit long lasting molecular dynamic simulations. The usage of the VALBOND TRANS (VBT) force field which is based on the valence bond theory[25] (see Chapter 2) can carry out such simulations while d-electron effects of third-row TM-complexes are captured[29,273,274,297].

In this work, we present a parametrization for Ir-containing complexes which is suitable to describe the structures and energetics of a range of chemically relevant systems. Some of the complexes (see Fig. 4.1) were already used in synthetic or reactivity studies. For instance, complex **2a** was characterized as a product from diastereoselective addition of H_2[298]. Complex **3a** was used in mechanistic studies of oxidative addition and reductive elimination reactions[299] while complex **4a** served as a precursor for the synthesis of heterobimetallic compounds[300].

The work focusses on two points: a) the accuracy with which different diastereomers of a given bonding pattern can be captured with an optimized empirical force field based on VBT, and b) the transferability of such a parametrization to a range of chemically related complexes. We explore the parametrization of a robust force field for a range of chemically distinct Ir(III) complexes using a generally applicable approach. VBT allows to rapidly screen libraries of compounds and to investigate their properties. A reliable and robust force field is presented which can successfully identify the diastereomers which are lowest in energy, building a basis for subsequent MD simulations. Particular emphasis is put on the question of how transferable such a parametrization can be.

4.3. Methods

4.3.1. Intermolecular Interactions

The VALBOND TRANS (VBT)[22,23,59–61,223] in combination with the CHARMM[40] force field is used to perform all minimizations on several classes of Ir(III) complexes. The combined force fields explicitly account for electronic effects, here the trans influence, by modelling the interactions between the metal (M) and the ligand (L). The Ir(III) complexes depicted in Fig. 4.1 have more than 12 electrons and are therefore classified as hypervalent. Hypervalency requires the weighting of all resonance structures as it is closer described in Chapter 3.

The non-bonded terms V_{elstat}, V_{LJ} (ref eq. 3.20), the partial atomic charges q_i and the Lennard-Jones (LJ) parameters ϵ_i and σ_i are considered for refinement to develop a reliable FF for Ir(III) species. For atom pairs, the LJ-parameters are combined through the Wigner-Kirkwood combination rules $\sigma_{\text{AB}} = (\sigma_{\text{A}} + \sigma_{\text{B}})/2$ and $\epsilon_{\text{AB}} = \sqrt{\epsilon_{\text{A}}\epsilon_{\text{B}}}$, where A and B are atom types of the atoms involved in the interaction. Although more elaborate combination rules exist[57,202], the conventional Wigner-Kirkwood rules are used in the following to be compatible with the most widely used force field parametrizations. For electrostatics, 1-4 interactions were taken into account. The bonded terms and the recent extension of VBT parameters[223] other than CO remain unchanged.

Non-bonded parameters were refined with the least-square fitting program CH-NoLLS[26,27] using the Levenberg-Marquart algorithm[292,301] (see Chapter 3). Determined energies using the refined parameter

set were compared to the energies of minimized DFT calculations. Electronic structure calculations for all complexes were performed using Gaussian03[134] with the B3LYP[113,114] functional and the 6-31G(d,p)[124] basis set on ligands and LanL2DZ[178] on the iridium atom including core potentials and partially f-functions. A variety of DFT hybrid functionals including B3LYP have been shown to perform well for iridium-containing complexes[28,117,217]. Additional calculations were performed using the B3PW91[112,302,303] functional to confirm the results obtained by B3LYP.

4.3.2. Complexes Investigated

The present work is concerned with octahedral Ir(III) complexes with sd^2-hybridization. Here, the covered chemical space is summarized in Fig. 4.1. Due to the availability of their X-ray structures and the importance of complexes of this type as catalysts for asymmetric hydrogenation reactions[296,304–306], complexes **2a**, **3a** and **4a** were considered. To enlarge the test set, analogs were designed with minor changes in their substituents. The variation of these substituents are limited to changes in the second coordination sphere of the phosphorus-ligand and include PPh_3, $P(CH_3)_3$ or PH_3. Overall, five different types of complex families as shown in Fig. 4.1 were considered.

4.3.3. Fitting Procedure and Reference Data

The adjustment of the non-bonded parameters was carried out by a recently developed fitting strategy which combines the interactive non-linear least squares fitting program (I-NoLLS) with an engine that uses VBT to compute optimized geometries and total energies for a given force field parametrization[27]. The specific fitting strategy was to maintain the parameters of one type of non-bonded interaction constant while varying the other one until a $RMSD_E$ convergence within 0.1 kcal/mol was obtained. Subsequently, the procedure was reversed and iterated until overall stabilization of the fit. The force field terms to be optimized were non-bonded parameters, namely partial atomic charges and the LJ-parameters.

The reference data for all force field parameters are taken from electronic structure calculations. Although experimental data from X-ray structures are available for some of the complexes (**2a**, **3a** and **4a** in Fig. 4.1), this data was not considered sufficiently homogeneous to justify inclusion in the fit.

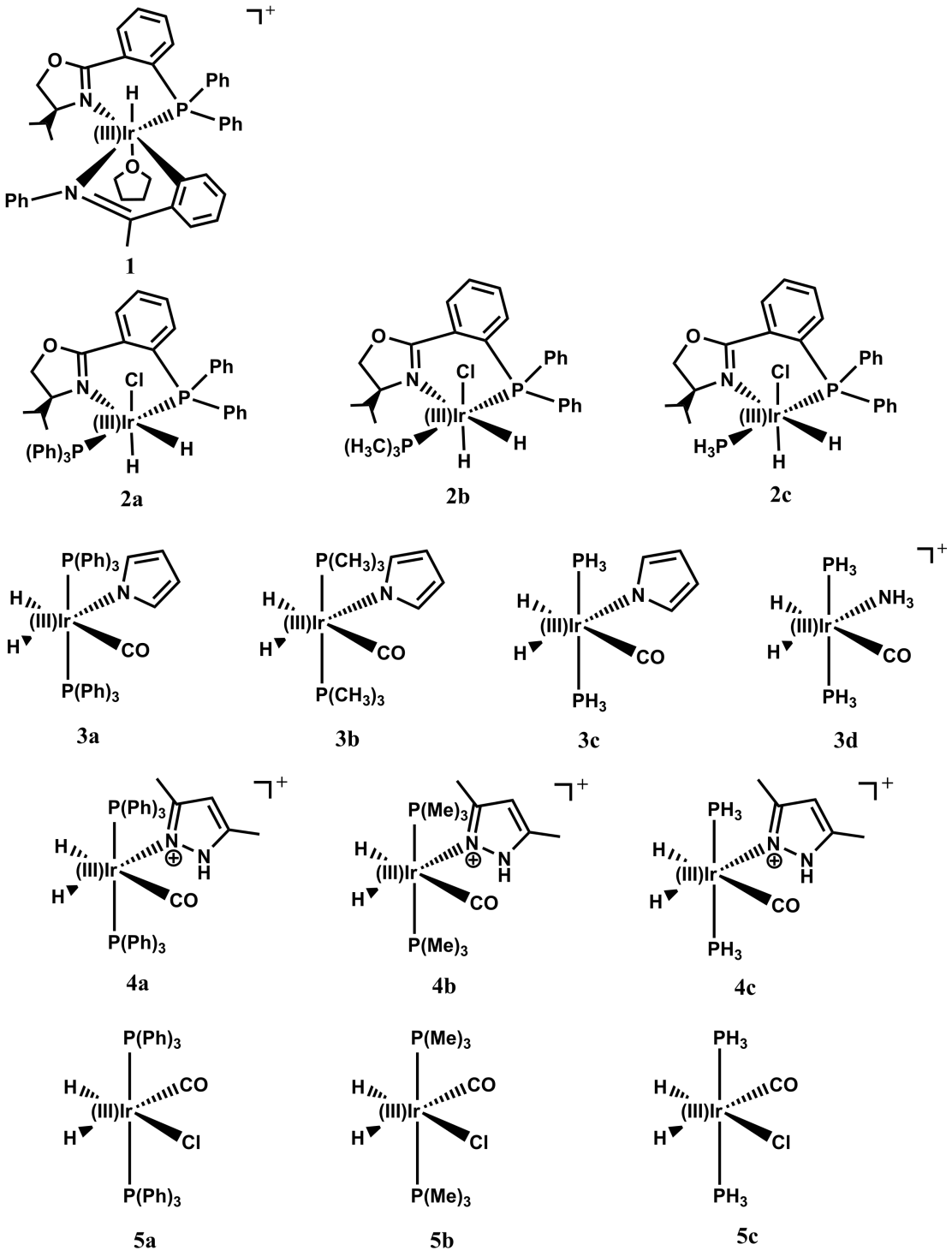

Figure 4.1.: Model Ir(III) complexes considered in the present work. The structures were obtained from the Cambridge Crystallographic Data Base[298–300].

Rather, structural data was used to compare with optimized structures after the force field parameters were optimized.

All optimized reference structures were obtained from DFT calculations for all 116 complexes of the test and training set. Further calculations were performed using an additional $f-$function on the iridium center to explore the effect of polarization functions on the metal. However, their effect on the reference energies is minor as is shown in Fig. 4.2. Finally, reference data for all diastereomers of complexes **2a**, **2b** and **2c** were carried out with the B3PW91 functional and yielded a correlation coefficient of $r = 0.99$ compared to B3LYP energies.

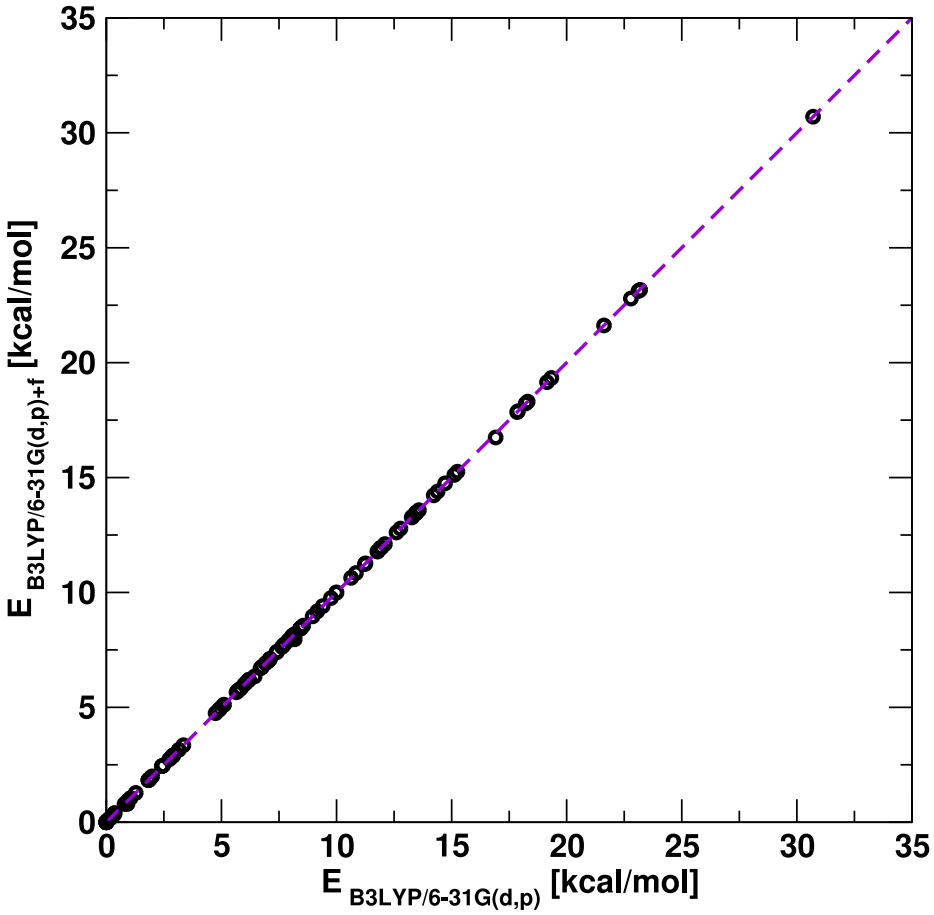

Figure 4.2.: The effect on the energetics induced by an added polarization function on the metal center ($f-$function on iridium). The DFT energies for all 116 complexes using polarization functions on the metal center are plotted against those without the additional function in the basis set. The RMSD_E between the two sets of data is 0.009 kcal/mol.

At the beginning of a fit, initial parameters are required. As the systems under consideration include Ir(III), no charge assignments by equivalence with existing functional groups in CHARMM22[48] were made. Rather, atomic charges were determined from the electron density directly using different

schemes: Mulliken[307] charges, NBO[308] charges and charges from CHELPG[309]. During the fitting, the total charge of the system remains constant which was achieved by using suitable constraints. Soft constraints were also used to maintain individual atom charges and LJ-parameters in a realistic range.

Refinements were carried out by starting from all three different charge types to assess the sensitivity of the results. This was motivated by the fact that different charge definitions distribute partial charges (PCs) differently throughout a molecule. Mulliken[307] and Coulson[91] charges are calculated directly from the wave functions, whereas NBO charges derived from assigning charges from localized orbitals[308,310] and CHELPG[309] charges are fitted to reproduce the *ab initio* electrostatic potential (ESP) around the molecule. For larger basis sets, Mulliken charges are known to be plagued with convergence problems[311–313]. This is less pronounced for CHELPG[314]. However, CHELPG charges can differ substantially for atoms in similar chemical environments, due to a conformational dependence[315]. Larger systems may also cause problems, as buried atoms are too far away from the grid points which are relevant to derive the ESP. Due to this problem, it is also common that different conformers show a broad distribution of charges, therefore, the averaged charges of all possible conformers[315] should be considered. NBOs best reflect the Lewis structure, because orbital details such as polarization, atomic hybrid compositions and others are included but two center bonds and lone pairs are clearly separated[316]. The analysis of the natural orbitals in relation to their "residence" and their characteristics allows a classification into bonding electrons, core-electrons, lone pairs and anti-bonding orbitals[310].

4.4. Results

First, the effect of refining non-bonded parameters is illustrated for a single Ir(III) complex. In a next step, the transferability of parameters across one family of related complexes (**2a, 2b, 2c**) is considered in more detail. Then, a training set of complexes which differ substantially in their structure (complexes **2a**, **3a**, **4a**, **5a**) is considered to determine the degree of transferability of the parametrization across different molecular architectures. Finally, it is discussed to what extent the parameters can be applied to further iridium complexes, i.e. the transferability across chemical space.

Marked differences were observed between the three charge schemes tested, which has implications

for fitting where parameters are loosely constrained to their initial values. Fig. 4.3A to C compare Mulliken, NBO and CHELPG charges of all 12 optimized diastereomers for complex **2a**. For Mulliken charges it is found that within one family no significant charge redistribution takes place whereas NBO and CHELPG reveal changes in the charge distribution of aromatic carbon atoms (CA). For NBO and CHELPG charges, 2 out of 36 CA atoms differ by 0.12 e and 0.24 e, respectively. This suggests that atomic charges are less transferable between chemically similar environments using these schemes than using Mulliken charges.

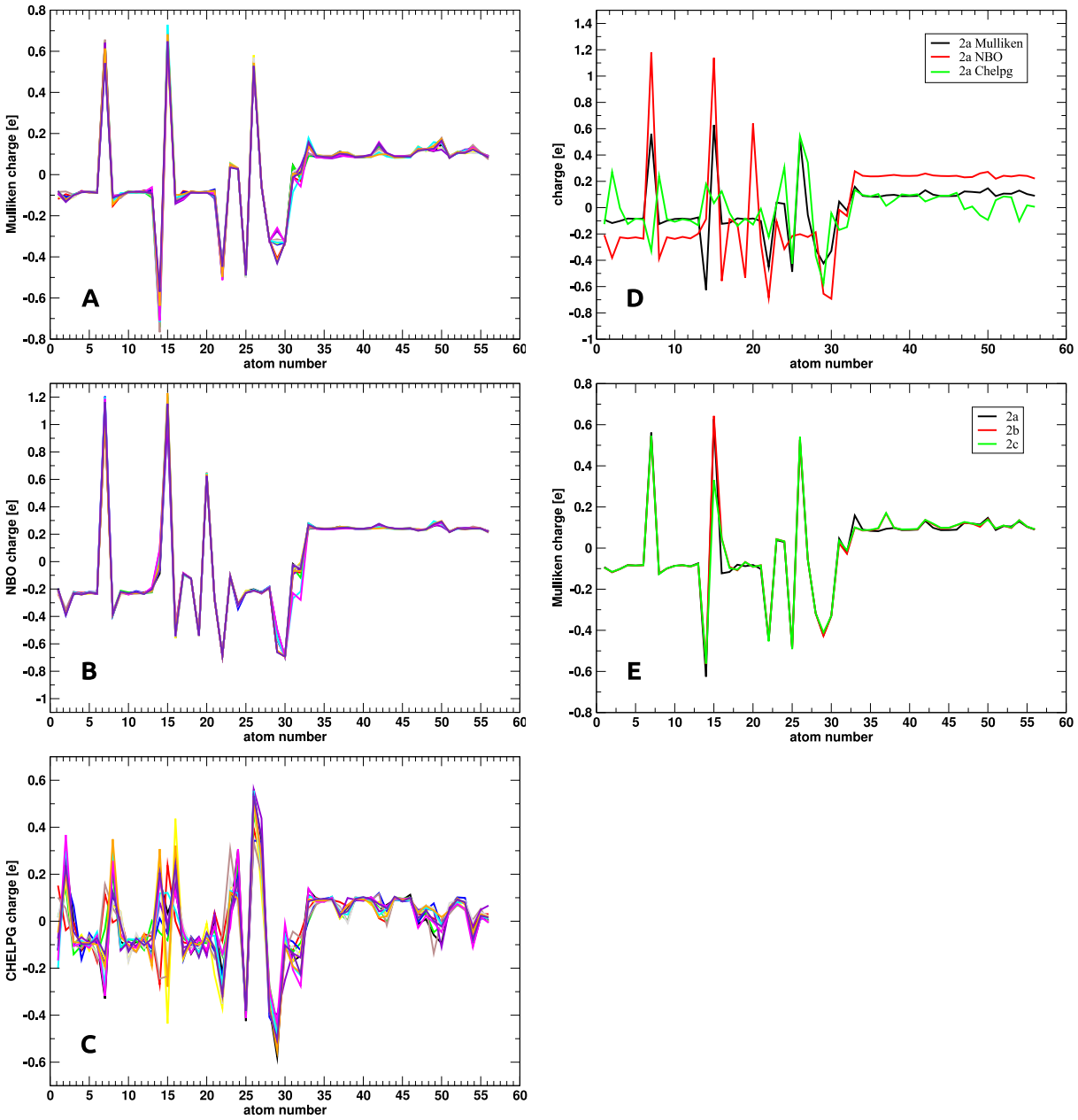

Figure 4.3.: Panels A-C: Mulliken, NBO and CHELPG charges of the 12 diastereomers of complex 2a according to their atom number. For CHELPG charges, an Ir radius of 2.13 Å was taken for the DFT calculations. Panel D: Comparison of Mulliken, CHELPG and NBO charges of complex 2a. Here, the P atoms have positions 7 and 15, the Ir atom position 14 (to keep a clear overview, only 57 atoms out of 90 are shown). Panel E: Mulliken charges of one corresponding diastereomer of complex 2a, 2b and 2c (only relevant atoms are shown). The alternate P-ligand is at position 15.

Fig. 4.3D represents how the charge assignments from Mulliken, NBO and CHELPG differ, e.g. for the phosphorus (P) and the iridium (Ir) atom. The P atoms (numbers 7 and 15) have a partial charge of $q_{\mathrm{P}} = 0.6\ e$ when a Mulliken analysis is used, whereas for Ir (number 14) $q_{\mathrm{Ir}} = -0.6\ e$. This compared with $q_{\mathrm{P}} = 1.2\ e$ and $q_{\mathrm{Ir}} = -0.1\ e$ from an NBO analysis and $q_{\mathrm{P}} = -0.3\ e$ and $q_{\mathrm{Ir}} = 0.2\ e$ from CHELPG charges where the signs of the two charges are reversed.

It is also of interest to consider the effect of substitutions on the periphery of the complex and how they influence the PCs on the entire complex. For this, a complex family (**2a**, **2b** and **2c**) is used which only differs by the substituents PPh_3, $P(CH_3)_3$ and PH_3. The Mulliken charges, Fig. 4.3E, all remain quite similar. The only exception is the phosphorus atom where the charge changes by around 0.3 e. Structurally, bond lengths between the metal center and ligands differ little but a trend from PPh_3 over $P(CH_3)_3$ to PH_3 is detectable, where the bond lengths decrease with decreasing steric hindrance. Thereby the iridium-phosphorus bond shortens from PPh_3 to $P(CH_3)_3$ by 0.027 Å and to PH_3 by 0.020 Å while elongation of other M-L bonds are smaller. L-M-L angles almost remain unchanged, except for the Cl-Ir-P angle, which is 93° for PPh_3 and for $P(CH_3)_3$ and PH_3 the angle is 85°.

4.4.1. Parametrization of a Single Ir-Complex

First, the optimization of non-bonded parameters for the octahedral Iridium(III)-PHOX catalyst **1** with a diphenylphosphino-coordinated group (see Fig. 4.4) is described in detail.

The DFT-optimized structures of all possible diastereomers span a range of 21 kcal/mol. For fitting, the energy of the lowest energy diastereomer was given an increased weight. The fitting procedure can be separated into iterations and microiterations. For one iteration, parameters of one particular interaction type (electrostatic or van der Waals) are fitted while parameters of the other type are frozen and *vice versa*. Fitting of the electrostatic or van der Waals parameters for the current iteration occurs over several microiterations where the atomic charges or Lennard-Jones parameters are progressively refined. A sequence of microiterations is terminated when no further reduction in the RMSD_E is possible. As the parameters are highly correlated, not all of them are allowed to fully relax which also avoids too large (or even nonphysical) changes in parameter space. Such decisions need to be taken as the fit progresses for which I-NoLLS is ideally suited.

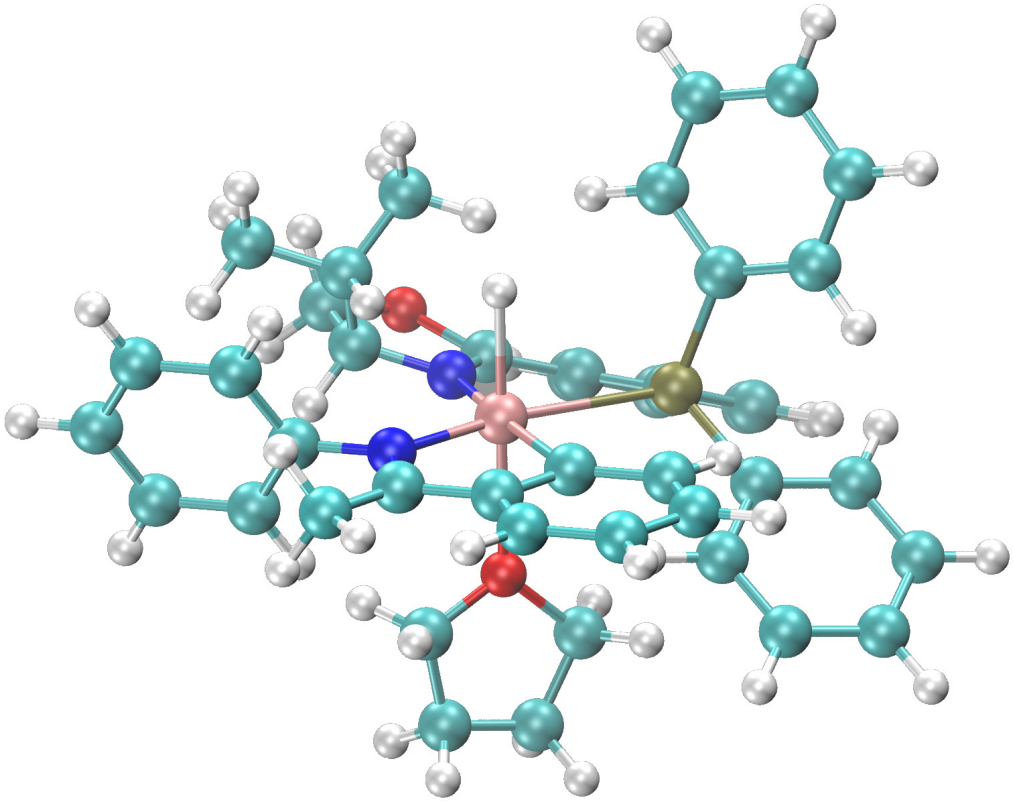

Figure 4.4.: Pseudo octahedral Ir(III) complex with a bidentate PHOX-ligand (**1**). Color code: Ir (pink), N (dark blue), P (green), O (red), C (light blue) and H (white).

For complex **1** (Fig. 4.1), three fitting iterations were necessary. In the first iteration, five microiterations of σ_i were followed by five microiterations of ϵ_i (Fig. 4.5).

The well-depth ϵ_i of the phosphorous atom changed most, decreasing from -0.585 to -1.378 kcal/mol and increasing the total van der Waals energy of the complex. The Ir radius also increased significantly from 1.91 Å to 2.48 Å. Other σ_i values changed little during fitting, although they were not constrained. The total energy RMSD_E decreased from 6.84 to 4.26 kcal/mol, an improvement of almost 40 %. A linear regression between target (DFT) and computed (VBT) energies before and after the first round of LJ-fitting gave correlation coefficients of $r = 0.81$ and $r = 0.91$ respectively.

For the partial charges, starting values were taken from the three different charge schemes averaged over all diastereomers. Soft constraints were applied to prevent unphysical values. Using Mulliken charges for the initial guess yields the best results, requiring 12 microiterations with LJ-parameters

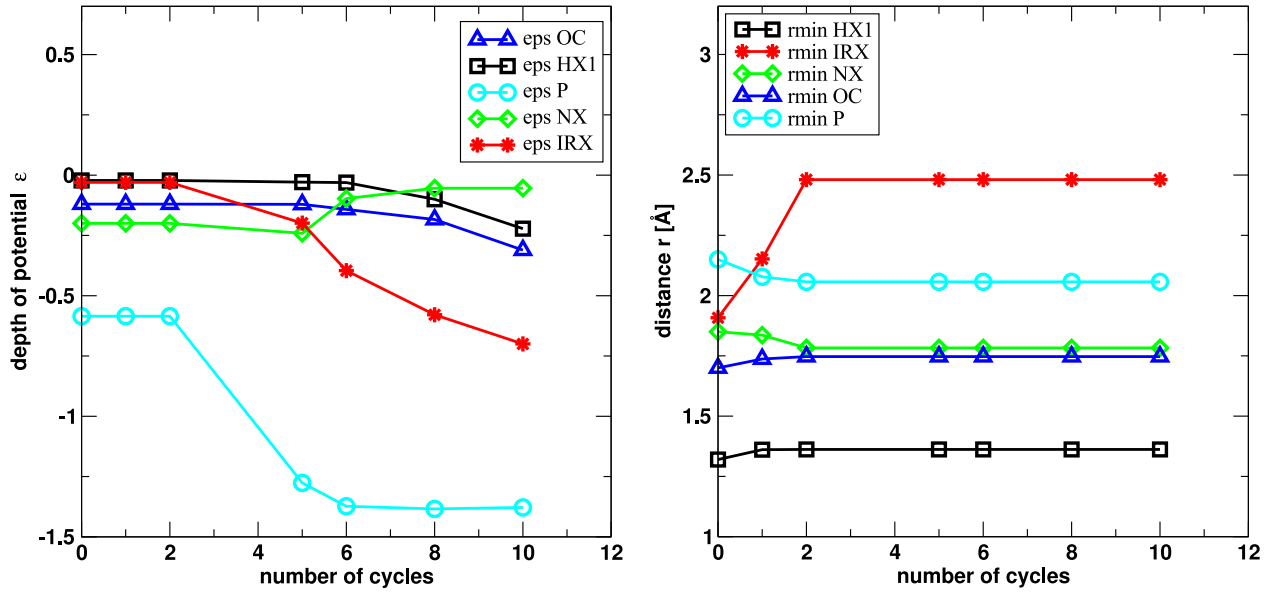

Figure 4.5.: Fitting of the Lennard-Jones Parameter ϵ (left) and $r_{\min}$ (right). Blue triangle: O atom, black square: H atom, cyan circle: P atom, green diamond: N atom and red star: Ir atom.

fixed. The largest changes were observed in q_{Ir} which reached 1.41 e, and q_{P} which reached 0.15 e. In combination with the improved LJ-parameters, the total RMSD$_E$ was now 2.49 kcal/mol. Starting from NBO and CHELPG charges yielded RMSD$_E$ values of 3.25 and 3.31 kcal/mol respectively.

After a second iteration, the RMSD$_E$ was reduced further to 2.29 kcal/mol (fit started from Mulliken charges), 3.16 kcal/mol (NBO charges) and 2.85 (CHELPG charges). After a third iteration the final RMSD$_E$s were 2.24 kcal/mol ($r = 0.95$, Fig. 4.6), 2.66 kcal/mol, and 2.32 kcal/mol when starting from Mulliken, NBO, and CHELPG charges, respectively. The fit using Mulliken charges was also best able to reproduce the overall energetic ranking of the 20 diastereomers and correctly identified the diastereomer with lowest energy. NBO charges failed to correctly identify the lowest-energy diastereomer, despite the increased statistical weight given to this complex during the fitting. CHELPG charges also identified the lowest-energy diastereomer but with a slightly inferior overall RMSD$_E$.

For the present case, starting the fit from Mulliken charges turned out to give the lowest RMSD$_E$. Different charge sets mean a different balance (relative magnitude) of the charges in the complex. As correlation between parameters makes constraints necessary during fitting, it is important that starting values are reasonable or final values would be constrained within a suboptimal range. To

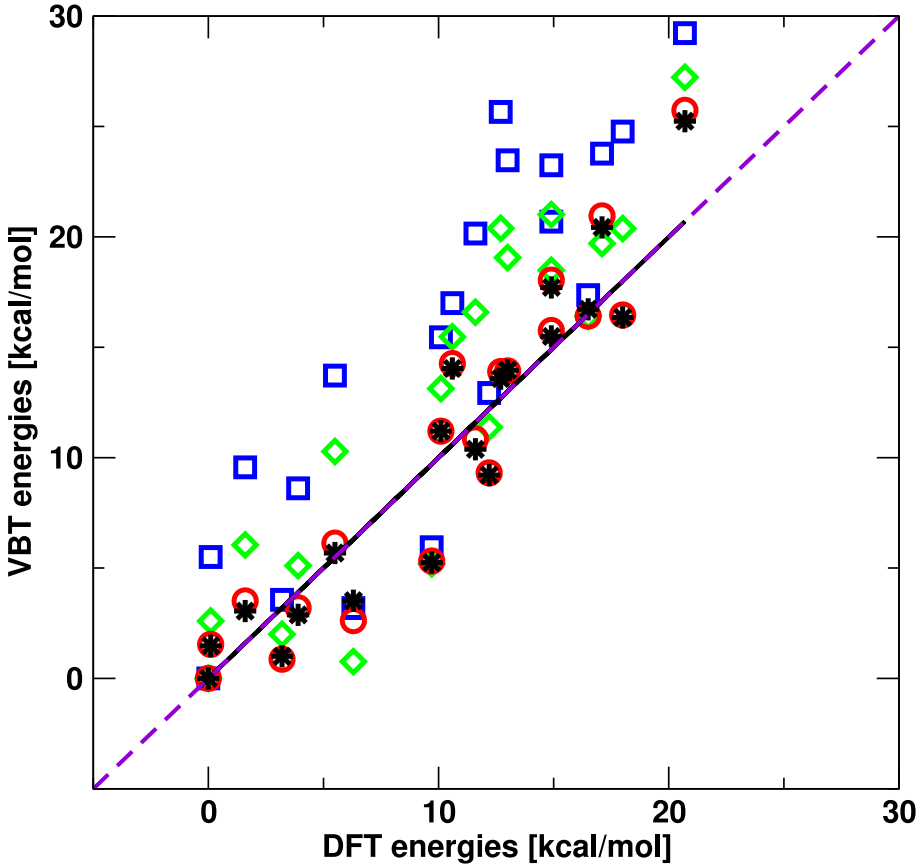

Figure 4.6.: Comparison of unfitted relative energies for complex **1** with a $RMSD_E$ of 6.84 kcal/mol (blue squares), LJ-fitted relative energies with a $RMSD_E$ of 3.33 kcal/mol (green diamonds) and LJ and Mulliken fitted relative energies with a $RMSD_E$ of 2.33 kcal/mol (red circles). For the final refinement, LJ and Mulliken were refitted and a $RMSD_E$ of 2.29 kcal/mol (black stars) is obtained with a correlation coefficient of $r = 0.95$ (black solid line). The dashed purple line is the 1:1 correlation

verify if the parameters obtained are also valid for other Ir(III) complexes, further pseudo-octahedral complexes have to be considered to assess their transferability. Atomic charges and Lennard-Jones parameters could be further refined if solution-phase data is available. For organometallic complexes such data is not always easy to obtain. A first attempt has been recently undertaken where NMR properties were compared with experiments for a Pt-complex[274] and in a parametrization of d^6 piano stool complexes[217]. A possible strategy in the present case would rather be to first determine balanced non-bonded parameters for fragments (ligands) and then follow the procedures outlined in the present work by keeping, e.g., the relative charges of the ligands constant.

Trans-Parameters for CO-ligands

As complexes in families **2** to **5** contain CO as a ligand, trans-parameters for a carbon atom bound to an oxygen atom needed to be determined. For the trans-parameters, two model complexes, **3d** and **5c**, were chosen arbitrarily to refit the energetic and structural trans-parameters for carbon. First, complexes **3d** and **5c** were fitted separately, then they were fitted together to obtain more robust parameters. The fits were carried out with I-NoLLS. For the energetic trans effect, DFT energies of complexes **3d** and **5c** were taken and DFT bond lengths were taken for the structural trans effect to fit bond lengthening sensitivity s_A and intensity i_B parameters in eq. 3.32. With the refitted trans-parameters (with Mulliken charges from DFT calculations and original LJ-parameters[223]) it was possible to compute more accurate VBT energies ($\sim$ 1.5 kcal/mol) for all complexes in Fig. 4.1 containing a CO-ligand (Table 4.1).

Energetic trans effect	3d	5c	3d,5c
p_{C-H}	11.08	12.03	11.55
p_{C-N}	−2.94		−2.94
p_{C-P}	6.65	5.70	6.17
Structural trans effect	3d	5c	3d,5c
s_C	1.00	1.11	0.28
i_C	1.19	0.06	−1.68

Table 4.1.: Fitted energetic trans-parameters p_{CX} for complex **3d**, **5c** and (**3d,5c**) and fitted structural trans-parameters "sensitivity" s_C and "intensity" i_C. The parameters in the last column are used for all further calculations.

4.4.2. Transferability of Parameters for Complex 1

Using the trans-parameters for CO-ligands we first set out to assess the performance of the non-bonded parameters obtained from the fit of complex **1** (see above) for complexes **2** and **3** and their substituted analogs (Fig. 4.1). To determine the transferability of these optimized LJ-parameters and atomic charges, those based on Mulliken charges were tested for families **2** and **3**. Complex **1** and **2** have in common a bidentate PHOX-ligand whereas complex **3** has only monodentate ligands. For complexes **2a-c**, the RMSD$_E$s are 6.34, 5.23 and 4.20 kcal/mol and for complexes **3a-c**, RMSD$_E$s of 13.68, 8.21 and 7.26 kcal/mol were obtained. Repeating this calculation for complex families **2** and **3** with unfitted Mulliken charges yielded an averaged RMSD$_E$ of 10.98 kcal/mol which is indeed 3.5 kcal/mol higher in energy than the averaged RMSD$_E$ of the fitted energies mentioned above. However, the performance of

the parameters is considerably inferior to the results obtained for complex **1**. This demonstrates that although for complex **1** the fit is satisfactory, the parameters are not transferable. The fitted parameters of the reference complex **1** are not suitable for complexes in families **2** and **3**. There are several possible reasons for this. First, complex **1** is chelated and has therefore considerable strain whereas complexes in family **3** have chemically simpler ligands. Furthermore, most of the complexes in families **2** and **3** are overall neutral which may affect the transferability of the parameters. In other words, the chemistry of complex **1** may not be suitable to derive force field parameters that can be more widely used.

Isolated fitting of complex **2a** starting from Mulliken charges results in a $\mathrm{RMSD}_E \approx 1$ kcal/mol, after a single iteration. Using the fitted parameters from **2a** for complexes of the same family (**2b** and **2c**) exhibited a good transferability. However, using it for any other complex in Fig. 4.1 led to considerably larger deviations. Thus, fitting a set of non-bonded parameters for a single complex allows to reach an excellent RMSD_E compared to reference *ab initio* data, but the parameters are not necessarily transferable to other systems.

4.4.3. A More Robust Set - Complexes with Substitutions at Phosphorus

To generate a more robust parametrization, three different complexes were included in the fitting set instead of a single reference complex. Therefore, complexes **2a-c** were taken for a new fit of the non-bonded parameters. This minor change should enable to get more reasonable RMSD_Es for every single complex.

Each of the complexes **2a-c** include 12 diastereomers which were all included in the fit. Initial charge assignments were the averaged Mulliken charges. In a first round, the charges were fitted with 14 microiterations and the LJ-parameters for 9 microiterations, whereby the potential depth and the distance were fitted alternately. Next, another round of charge-fitting was carried out until convergence was achieved after additional 10 microiterations. LJ well depths were constrained to ensure physically meaningful values $\epsilon < 0$. Changes of all vdW-radii are minor during the fitting except for atom type HX1 which increased by more than 0.1 Å. Initially, the RMSD_E is 10.4 kcal/mol (unfitted parameters) between the DFT-reference and the VBT energies. The combined fit for all complexes **2a-c** reduced the final averaged RMSD_E to 3.2 kcal/mol (**2a**: 3.35 kcal/mol, **2b**: 2.92 kcal/mol and **2c**: 3.28 kcal/mol) which is a considerable improvement.

The benefit of refined non-bonded parameters is illustrated in Fig. 4.7. Energies of complexes **2a-c** were calculated with different charge assignments: (black) unfitted Mulliken charges with standard LJ, (red) averaged unfitted Mulliken charges with standard LJ, and (green) I-NoLLS-refined charge and LJ-parameters. The comparison in Fig. 4.7 confirms that the fitted parameters are clearly superior to standard assignments. In all three cases, the fitted parameters lead to a correlation between VBT- and DFT-calculated energies close to $r = 1$ (0.93 to 0.97) whereas the unfitted parameters yield clearly inferior results. More important, the fitted parametrizations allow to correctly identify the low-energy diastereomers whereas this is not the case for the unfitted parametrizations. Transferring the fitted charges and LJ-parameters of complexes **2a-c** to other model complexes which were not included in the fit (complexes **3a** to **5c**) yields an averaged RMSD_E of 4.22 kcal/mol. Compared to the RMSD_E for the complexes **3a-5c** with unfitted parameters (11.76 kcal/mol), the new parameters are clearly superior and indicate some degree of transferability.

4.4.4. Extension to Different Complex Classes

Until now, the robustness and transferability of a) optimized parameters for complex **1** applied to families **2** and **3** and b) optimized parameters for family **2** transferred to families **3** to **5** have been considered. In a next step, chemical space was broadened by using complexes **2a**, **3a**, **4a** and **5a** as the training set. This should further improve the transferability of the parametrizations. All refinements were carried out with initial charges from Mulliken, NBO and CHELPG. Following the same fitting protocol as above, the final averaged RMSD_E for complexes **2a**, **3a**, **4a** and **5a** starting from Mulliken and NBO charges were 3.76 kcal/mol and 4.45 kcal/mol, respectively. With CHELPG charges the RMSD_E is 3.58 kcal/mol. In all cases, charges and LJ-parameters are in physically reasonable ranges (Tab. 4.2).

To test the transferability of the fitted parameters, the complexes from the training set and the complexes excluded from the fit (**2b**, **2c**, **3b-d**, **4b**, **4c**, **5b** and **5c**) served as the test set (116 individual complexes in total). Averaged RMSD_E values between VBT and DFT reference energies (see Tab. 4.3) from refined Mulliken charges are 3.28 kcal/mol whereby NBO (3.67 kcal/mol) lead to 3.49 kcal/mol and CHELPG charges with 3.49 kcal/mol also yield good fits.

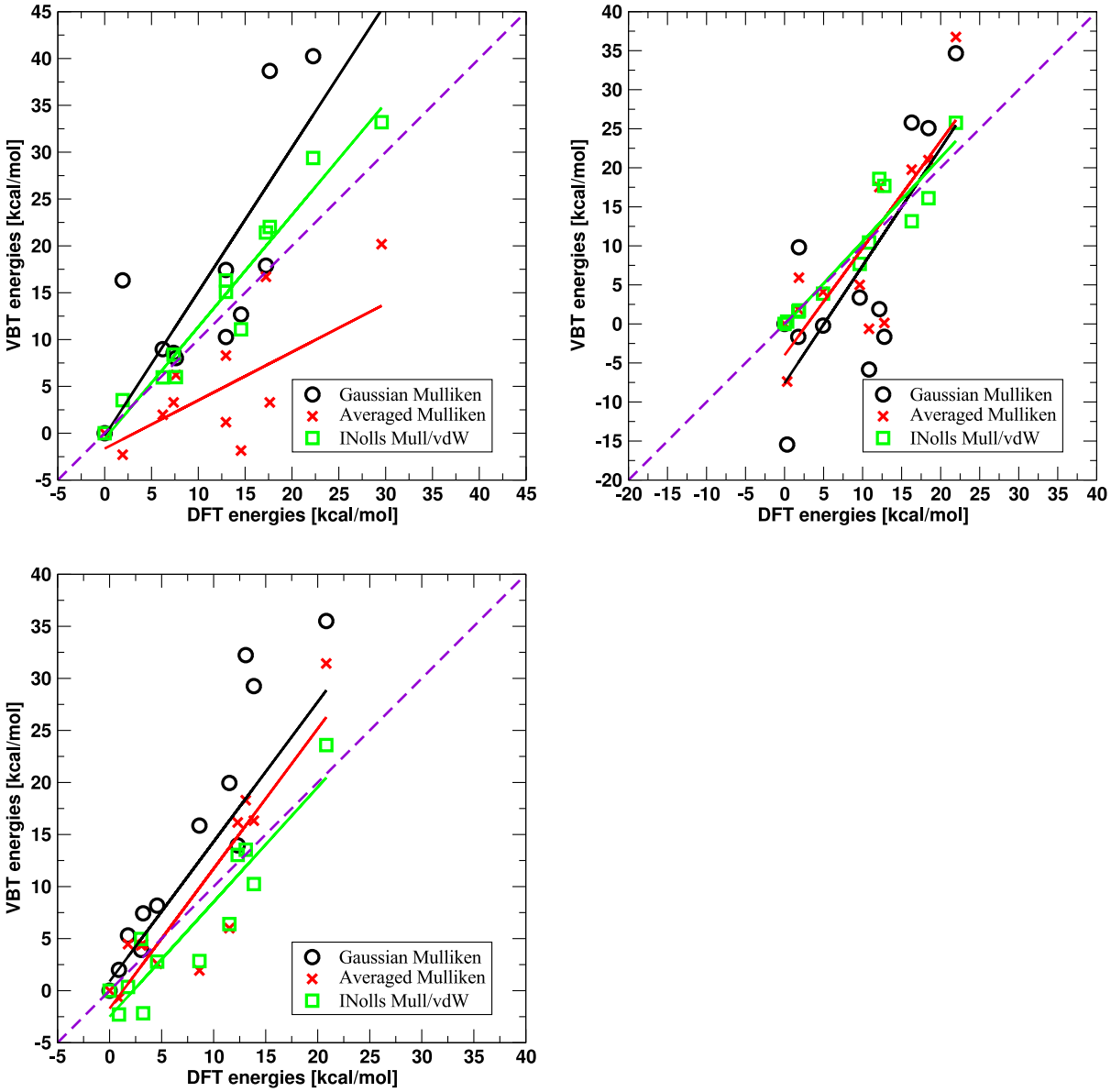

Figure 4.7.: Energies of all diastereomers of PHOX-complex **2a**, **2b** and **2c** calculated with different parameter sets: black circle: Gaussian Mulliken charges, red cross: averaged Mulliken charges, green square: I-NoLLS (re)fitted Mulliken charges and fitted LJ-parameters. Correl. coeff **2a**: 0.86, 0.62, 0.97; **2b**: 0.80, 0.82, 0.95; **2c**: 0.99, 0.91, 0.93. $RMSD_E$ **2a**: 10.72, 13.94, 3.35; **2b**: 10.32, 7.39, 2.92; **2c**: 9.09, 4.59, 3.28. The dashed purple line is the 1:1 correlation.

With fitted Mulliken charges, using the four complexes **2a-5a** as the training set, the lowest-energy diastereomers of all complexes except for **4b** and **4c** are identified correctly. For neutral complexes, we always find the correct assignment. For complex **4b**, two diastereomers from VBT are lower in energy

	2a-2c			**2a-5a**								
	charges	Lennard-Jones		charges			Lennard-Jones					
atom type	Mulliken [e]	ϵ [kcal/mol]	σ [Å]	Mulliken [e]	NBO [e]	CHELPG [e]	ϵ [kcal/mol]			σ [Å]		
H	0.0185			0.0043	0.0343	0.0121						
HA	0.2357			0.0791	0.1473	0.0757						
HP	0.1427			0.0196	0.0824	0.0355						
HX1	0.2869	−0.0304	1.4315	0.0111	−0.0690	−0.2705	−0.0285	−0.0245	−0.0205	1.3462	1.2749	1.3530
CA	−0.0975			0.0011	−0.0561	−0.0241						
CE1				0.4263	0.3140	0.3877						
CPH2	0.6855			−0.1516	0.0409	0.4005						
CT1	−0.1727			−0.2401	−0.2480	−0.1967						
CT2	−0.7576			0.3047	0.0560	0.0347						
CT3	−0.7035			−0.0223	−0.2761	−0.0615						
IRX	−0.2943	−0.0143	1.9086	−0.5088	−0.3596	−0.1631	−0.5902	−0.1606	−0.1755	2.0030	1.9116	2.1674
NR2	−0.2230			−0.1572	−0.2055	−0.0887						
NX				−0.2499	−0.2613	−0.0492	−0.2000	−0.2000	−0.2000	1.8500	1.8500	1.8500
OC	−0.1615	−0.0023	1.6038	−0.0334	−0.1178	−0.0434						
OX				−0.2405	−0.1498	0.0953	−0.0038	−0.1913	−0.0863	1.4248	1.7970	1.4760
P	0.2340	−0.5697	2.1317	−0.0133	0.2295	0.1236	−0.7516	−1.2257	−0.9931	2.0404	1.9839	1.9268
CLA	−0.0449			−0.2083	−0.2868	−0.1585						

Table 4.2.: Fitted charges starting from a Mulliken analysis for the family **2** (complexes **2a** to **2c**) with the corresponding fitted LJ-parameters ϵ and σ. Fitted charges starting from Mulliken, CHELPG and NBO, for the set of complexes: **2a**, **3a**, **4a** and **5a** with their corresponding fitted LJ-parameters (dielectric constant $\epsilon_0 = 1$). The NX atom type remained fixed, due to a faster convergence of the entire fit. Fitting NX does not improve the results.

	2a	2b	2c	**3a**	3b	3c	3d	**4a**	4b	4c	**5a**	5b	5c	Ø
Mulliken	**3.26**	4.08	2.67	**4.17**	4.07	3.13	1.78	**4.03**	4.40	2.59	**3.56**	3.28	1.66	3.28
NBO	**3.84**	4.23	2.90	**5.40**	4.40	3.52	1.20	**4.16**	6.79	2.73	**4.40**	3.32	0.86	3.67
CHELPG	**2.52**	3.40	2.28	**4.62**	5.74	5.15	1.14	**3.45**	4.27	2.61	**3.71**	5.40	1.03	3.49

Table 4.3.: $RMSD_E$ values [kcal/mol] for all complex classes **2a-5c**. The training set consists of complexes **2a**, **3a**, **4a** and **5a**. For each of the classes, charge refinements were started from Mulliken, NBO and CHELPG charges, respectively. $RMSD_E$ values for the complexes not included in the training set provide a measure of the transferability of the parametrization. The last column gives the averaged $RMSD_E$ for all 116 diastereomers.

than the diastereomer lowest in energy from DFT calculations and for complex **4c** one diastereomer is misassigned. Starting from NBO and CHELPG charges, the lowest-energy diastereomer was not correctly assigned for 6 (complexes **2b, 2c, 4b, 4c, 5a** and **5b**) and for CHELPG 7 complexes were misassigned (**2b, 2c, 3b, 3c, 4b, 4c**, and **5b**). However, for every complex there was only one misassignment. Hence, starting the refinement from Mulliken charges best captures the most relevant lowest-energy diastereomers. The three lowest-energy diastereomers of all 13 complexes (39 diastereomers) considered have an averaged RMSD_E of 1.66 kcal/mol compared to 3.28 kcal/mol when all 116 diastereomers are considered.

The best performing complexes are **2c, 3d, 4c** and **5c**. Considering the three lowest-energy diastereomers of these complexes yields an averaged RMSD_E of 0.97 kcal/mol. The best results are obtained for complexes **5c** and **3d** which have a RMSD_E of 1.7 kcal/mol and 1.8 kcal/mol, respectively, for all diastereomers. This is considerably better than the average RMSD_E of 3.28 kcal/mol (see above), given that the two complexes were not part of the training set. This comparison provides an impression of the degree of transferability of the parameters but also reflects the simple nature of the ligands. The ligands are small and lead to insignificant steric interactions. It is worth noting that the fitted RMSD_E for complex **3d** is excellent for all three charge concepts.

As an independent test of the parametrization, geometrical properties are further considered. The parametrization based on refined Mulliken charges leads to an overall RMSD of 0.26 Å (see Fig. 4.8).

For the bond lengths to the metal center an averaged deviation of 0.04 Å is found whereas the Ir-NH_3 bond length has the largest difference with 0.11 Å. This could be further improved by specifically fitting the bonded terms. For the angles the averaged deviation is 7.8°. The angle which differs most is the in-plane P-Ir-P angle with 101.5° instead of 84.4°. This can be easily accounted for by either refitting the VBT force constant or by assigning a different hybridization to the IRX-HX1 atom pair. The diastereomer with the highest energy of complex **3d** has an averaged difference in bond length of 0.08 Å (angles: 5.7°). Overall, the structures and corresponding energies are reproduced quite well. The availability of the crystal structure and the complexity of complex **2a**, a comparison of this crystal structure with the DFT-optimized and the VBT-optimized structure (Fig. 4.9) exhibits also a good agreement with a RMSD of 0.43 and 0.51 Å respectively.

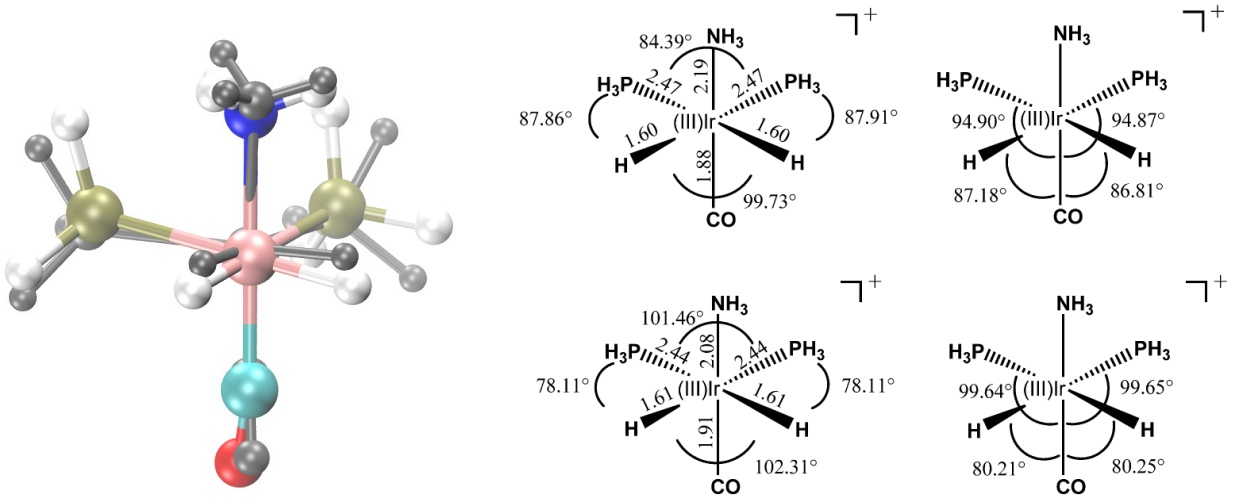

Figure 4.8.: Left: energetically lowest diastereomer of complex **3d**. The DFT reference structure (grey) and the VBT structure (coloured) with a RMSD_E of 0.26 Å (every atom is aligned except for hydrogen). Right: bond lengths and angles in-plane on the left, angles out of plane on the right. Upper complexes describe DFT structure and the lower complexes the VBT structure.

Fig. 4.10 compares all M-L bond lengths of the 116 complexes from DFT and VBT calculations. The short bond lengths around 1.5 Å correspond to the M-HX1 bonds and the longest are the M-CLA bonds. The differences reported in Fig. 4.10 exhibit a related pattern which is already found in complex **2a** (Fig. 4.9) and **3d** (Fig. 4.8). All VBT M-L bond lengths, compared to those from DFT, are within 0.05 Å and result in a correlation coefficient of $r = 0.98$.

To further test the robustness of the parametrizations, for complex **3d** the minimum energy structure was randomly distorted and the energies of the structures were computed with both DFT and VBT. Again, for VBT the fitted LJ and Mulliken charge parameters were used which were obtained from the **2a-5a** training set. Bonds and angles were randomly changed in increments of 0.025 Å and 4.0° up to a maximum distortion of 0.25 Å and 40.0° and the correlation between DFT and VBT energies is reported in Fig. 4.11.

The averaged RMSD_E is 0.74 kcal/mol with a correlation coefficient of $r = 0.99$ which suggests that

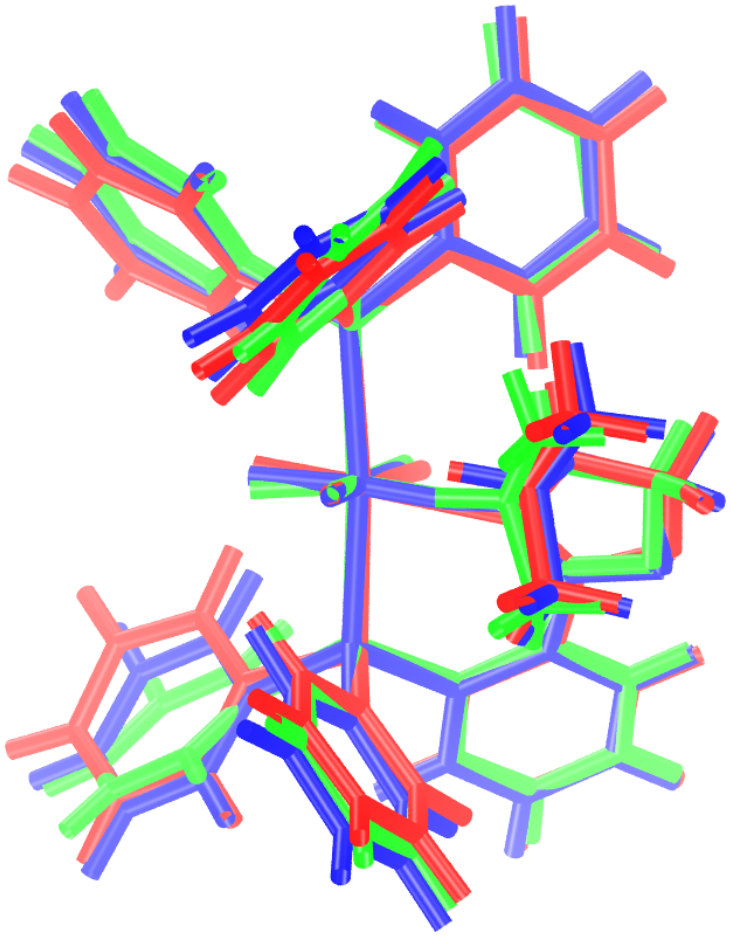

Figure 4.9.: Comparison of the crystal structure (green), the DFT-optimized (blue) and the VBT-optimized (red) structures of complex **2a**. The RMSD of DFT-optimized structure is 0.43 Å and RMSD of VBT-optimized structure is 0.51Å.

the energies for structures away from the minimum can also be quite well described by the present parametrization. The ability of the fitted parameters to describe perturbed geometries, away from the global minima, was further evaluated using a QM/MD simulation of complex **5b**. The VALBOND energies of 1000 snapshots taken from the MD trajectory were compared to the results of B3LYP single-point calculations, yielding a $RMSD_E$ of 2.47 kcal/mol (see Fig. 4.12) and the RMSD of the structures sampled along the trajectory differ by up to 0.8 Å. The non-bonded parameters were those from Table 4.2 and the bonded terms (bonds, angles, dihedrals) were fitted to reference data from QM/MD as we are not aware of suitable experimental reference data. However, in previous work, we reported a comparison of vibrational frequencies for solvent dynamics with transition metal complexes[29,273].

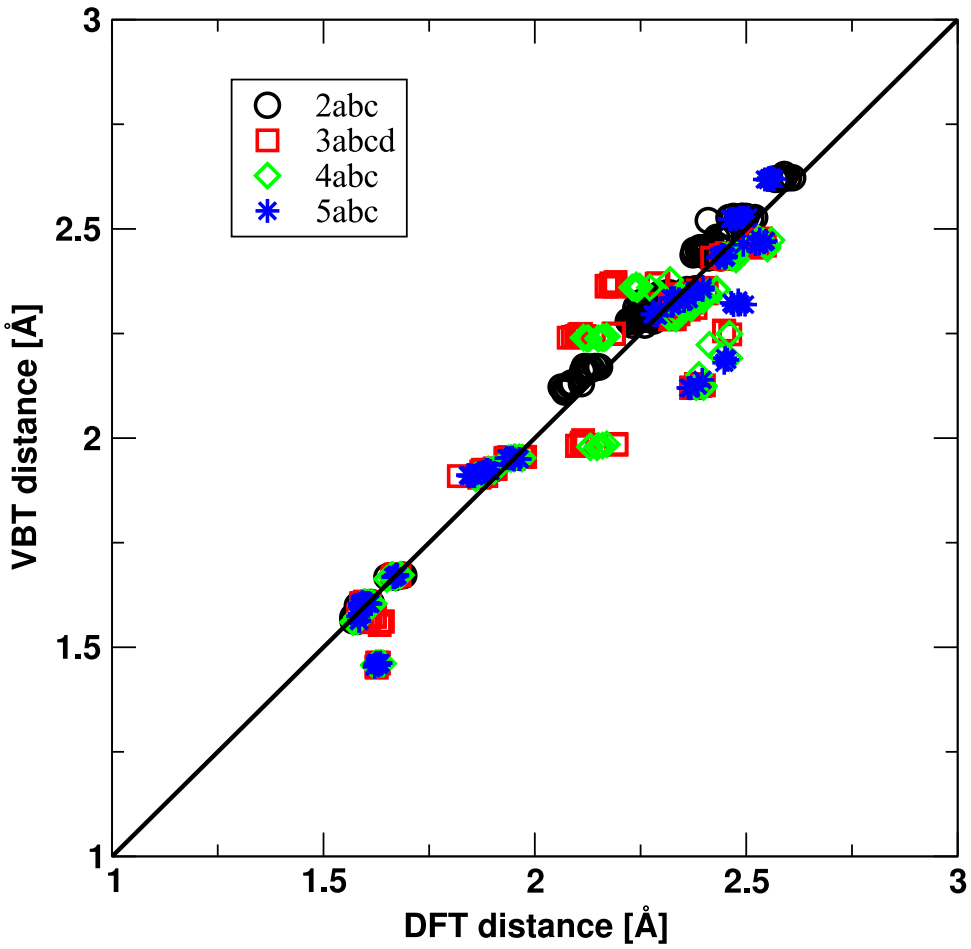

Figure 4.10.: Comparison of the VBT and DFT M-L bond lengths of all optimized complexes. The structural RMSD is 0.05 Å, with a correlation coefficient of $r = 0.98$.

Consequently, the fit for complex **2a-5a** generates a robust set of charge and LJ-parameters (Tab. 4.2), which can be applied successfully for the complexes in the fit, as well as for the complexes which were not part of the training set. RMSD_Es for a single complex can of course be further reduced by specifically fitting to all its diastereomers, as shown for complex **1**. However, the parametrization based on complexes **2a-5a** provides a balanced and robust parametrization for Ir(III) complexes with ligands containing H, C, N, O, P and Cl and allows to cover considerable chemical space.

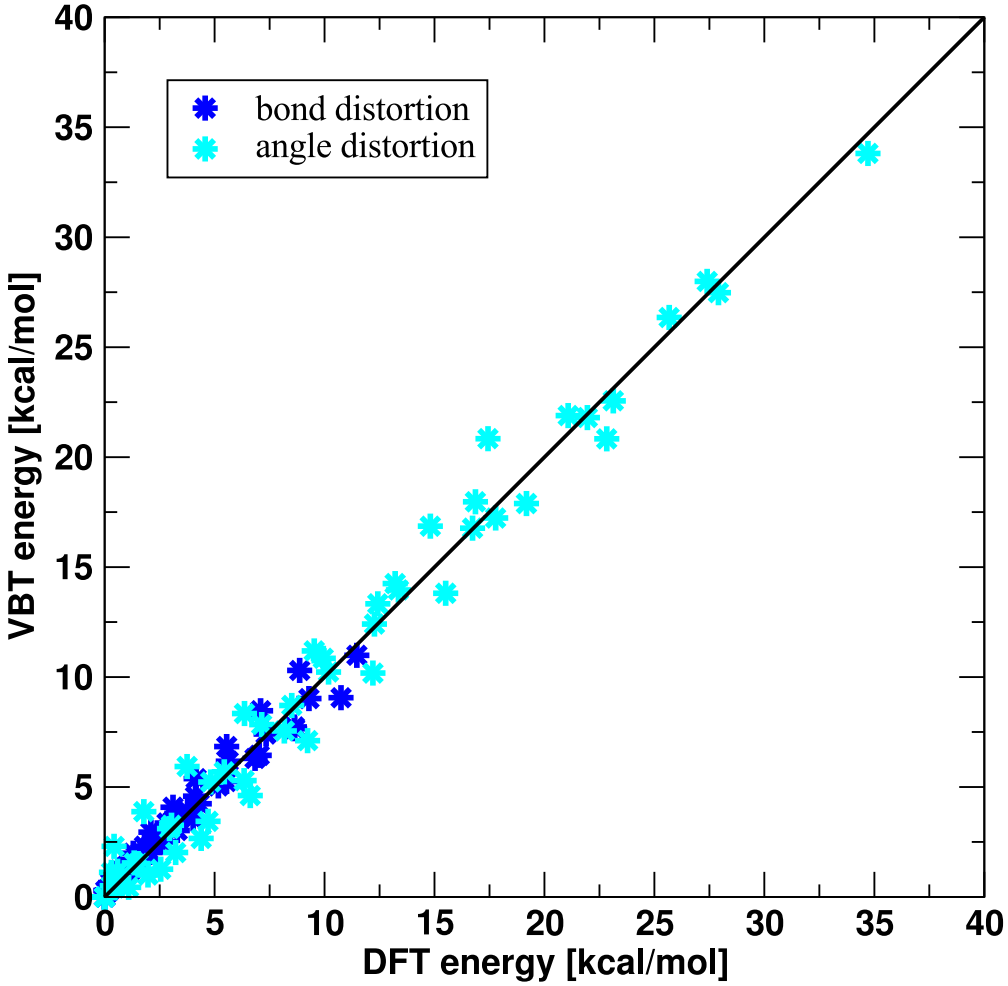

Figure 4.11.: Comparison of the VBT and DFT energies, with and without random distortions of bond lengths (step size 0.1 Å) and angles (step size 4°). The averaged energetic RMSD_E is 0.74 kcal/mol, with a correlation coefficient of $r = 0.99$.

4.5. Conclusions

The present work establishes that meaningful force field parametrizations with VBT for octahedral Ir(III)-containing complexes are possible. The procedure used is generally applicable to metal-containing complexes and not limited to Ir(III) systems. For a single complex, the energies of all diastereomers - with energies spanning up to 21 kcal/mol in DFT reference calculations - can be reliably ($\approx$ 1 kcal/mol, i.e. "chemical accuracy") determined and provide a correct energetic ordering of the diastereomers. This is of particular relevance for practical applications in which the low-energy structures are important to follow specific reaction mechanisms[32,33,294,317]. The parameters of one single complex are, however, not directly transferable to other Ir-based complexes. In the present case, this is not so surprising because complex **1** exhibits some strong steric effects. Using one entire family of test compounds

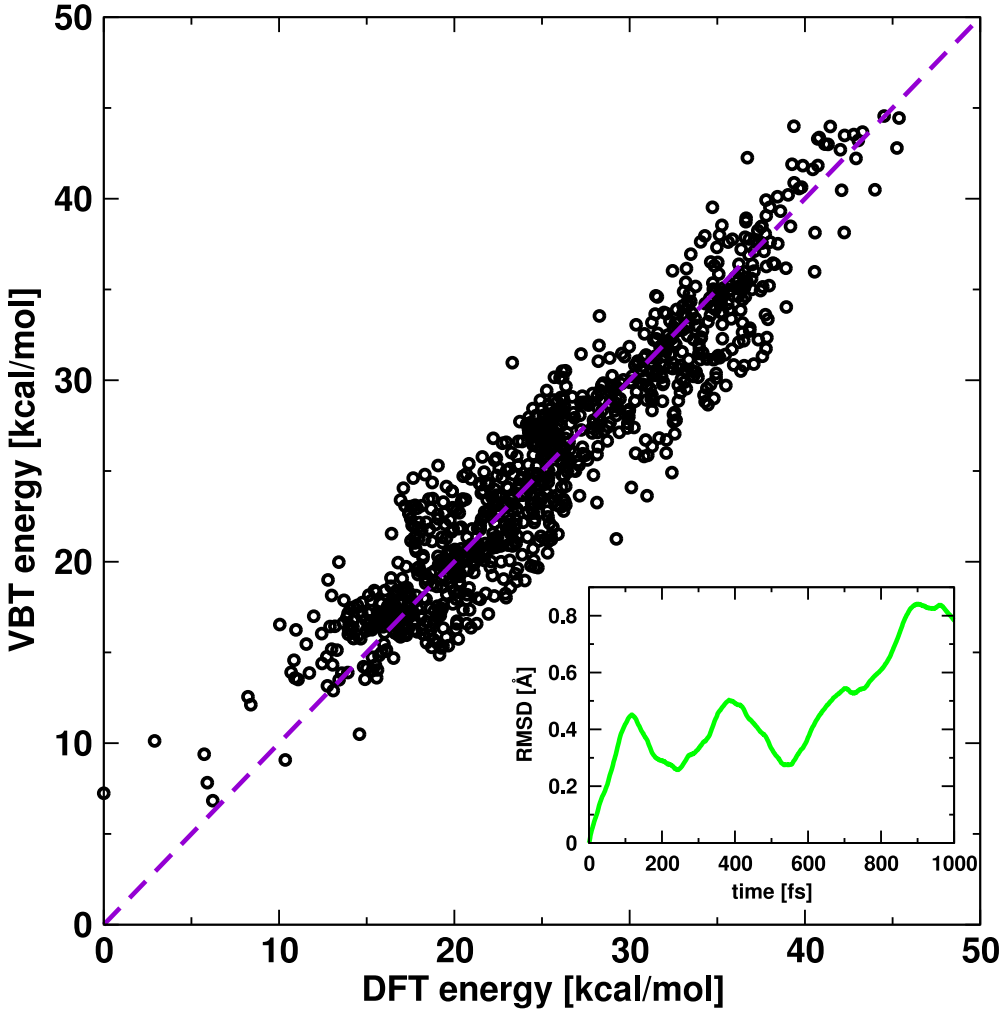

Figure 4.12.: Fitting of bonded parameters (bonds, angles, dihedrals) of complex **5b** to reference data obtained by ADMP[139–141] (atom-centered density matrix propagation). Non-bonded parameters were those from Table 2. The $RMSD_E$ for 1000 snapshots is 2.47 kcal/mol. The simulation was carried out in the NVT ensemble at 300 K for 1.0 ps with a time step of 1.0 fs. The inset shows the structural change (RMSD) along the trajectory.

(here family **2**), for which the fit of the individual complexes yields robust parametrizations, allows correct ranking of most low-energy diastereomers of families **3** to **5** which were not included in the fit. Transferability is further improved if the fit is carried out across a number of complex families. In that case, the averaged $RMSD_E$ including all 116 diastereomers of families **2** through **5** is 3.28 kcal/mol (using fitted Mulliken charges) which further improves to $\approx$ 1.7 kcal/mol if only the three lowest diastereomers of each complex are considered. In 11 out of 13 cases, the lowest-energy diastereomer was correctly predicted, and if only neutral complexes are considered, even all assignments were correct. In concrete applications VBT will allow to reduce the computing time of DFT-optimizations by close

to an order of magnitude and considerably speed up screening of ligand libraries. Overall, refinements based on Mulliken charges appear to be superior to those starting from NBO and CHELPG, although the differences are not substantial.

For the present case, VBT-based refined force fields for transition metals perform well in capturing structures and energetics around the minimum energy structure. This opens the possibility to investigate questions of practical relevance, including the solvent structure around transition metal complexes[273], following reaction paths between reactant and product[47], or investigating transition state structures in protein-catalyzed reactions. The parametrization of the non-bonded interactions can be further improved by fitting them to solvation-free energies of the ligands surrounding the Ir. Subsequently, such parameters can be used and further refined following the approach outlined in the present work. However, fitting directly to solvation-free energies of the complexes depends much on the availability of suitable experimental reference data. For all these applications, rapid and reliable means to evaluate the energetics of the complexes is required. Force fields, such as those discussed in the present work, provide a useful starting point for future applications. For example, reaction paths can be studied by combining the force fields discussed here with suitable computational strategies such as reactive molecular dynamics[284,318]. The real advantage of a force field-based approach is that energies can be rapidly evaluated. However, for more quantitative studies, such explorations will need to be combined with suitable experimental data (NMR, solvation energies) and additional electronic structure calculations to refine the parametrization. The present work is a first step towards such applications. However, the ease with which suitable force field parameters can be determined will be a crucial aspect[21].

5. MS-ARMD for Homogeneous Water-Oxidation Catalysis

5.1. Abstract

The oxidation of water to dioxygen is one of the most fundamental processes in nature. *In vitro* homogenous catalysis based on metal-catalysis can be used to mimic this natural process. Half-sandwich iridium complexes, used as catalyst precursors, in combination with the primary oxidant cerium(IV) ammonium nitrate, have been proven to be efficient catalysts for such a long-lasting and rapid oxygen evolution[28]. To study the role of various Ir(III)-catalysts, a powerful tool is provided, which couples the CHARMM[19] force field with the surface crossing algorithm, multi-state adiabatic reactive molecular dynamics (MS-ARMD)[24,283,286,318,319]. MS-ARMD includes an advanced FF parametrization tool, which allows to derive refined parameters (Morse parameters, general vdW) especially suited for reactions. Efficient energy calculations and molecular mechanics (MM) simulations of tetrahedral metal complexes are carried out using CHARMM, while MS-ARMD enables bond breaking and bond formation to model reaction pathways. The characterization of the transition state (TS) requires accurate fitting of the several energy surfaces which corresponds to the reactant, the product and intermediate states. To screen various Ir-catalysts in terms of their reactivity, bonded and non-bonded parameters had to be determined. These parameters were obtained by a simplex fitting algorithm, using ADMP-MD derived structures as a reference. The parameters, obtained for one model iridium-complex, should then be transferred to related reactions. Additional MD simulations in explicit solvent should also clarify, if there are just two waters involved in the proposed transition state[28] or even more.

5.2. Introduction

One of the most abundant natural processes on earth is the oxidation of water to form dioxygen[320], which is essential for most of the living organisms. It is not remarkable that this oxidation process gained much interest in the field of chemistry[321–323]. Over the last decades, many different catalysts were developed to carry out artificial photosynthesis, but initially with low turnover numbers (TON)[324]. To increase the catalyst efficiency, ruthenium[325–328], manganese[329,330], iron[331] and cobalt-phosphate[332–334] compounds were investigated and have proven to be promising O_2-evolving catalysts. More recently, the first iridium-based water oxidation catalysts[335] came up, followed by other iridium-based catalysts[28,336] and half-sandwich iridium complexes[337]. A wide range of these cyclopentadienyl containing iridium catalysts were developed, containing: carbonyl-bridged phenyl-pyridine ligands[336], alkoxide coordinating groups[338,339], carbene complexes[340] and chelate derivates[341], binuclear (COD)Ir systems[342] and finally complementary complexes with small functional groups[343]. These water oxidation catalysts (WOCs) are highly active, robust, water-soluble, and easily tunable for example by using stronger donating ligands to improve the catalytic activity[344]. Especially the half-sandwich Ir complexes exhibited remarkable TONs[28] and concerned our interest in analyzing the variety of catalysts and revealing the mechanisms of such water oxidation in more detail.

Based on DFT studies, Crabtree and co-workers suggested three different mechanisms of WO catalyzed by half-sandwich iridium complexes of the type Cp*Ir(N-C)X, [Cp*Ir(N-N)X]X and [CpIr(N-N)X]X[28] (Fig. 5.1). They proposed that the pentamethyl-cyclopentadienyl ligand (Cp*) causes an electron-rich environment which can stabilize the high-valent Ir-intermediates. The netto reaction of the water oxidation process is

$$2H_2O \rightarrow O_2 + 4H^+ + 4e^-$$

and if iridium oxide species are involved here, the capacity of losing electrons and protons can easily lead to high oxidation states $Ir^V{=}O$. Therefore, an intermolecular addition of water to such a high-valent metal-oxo center and the resulting formation of a O-O bond is plausible[345]. The rate limiting O-O bond formation is based on a coupling of two oxygens, which have an opposite reactivity: the water oxygen has to act as a nucleophile, while the oxygen bound to iridium acts as an electrophile[28] (Fig. 5.1).

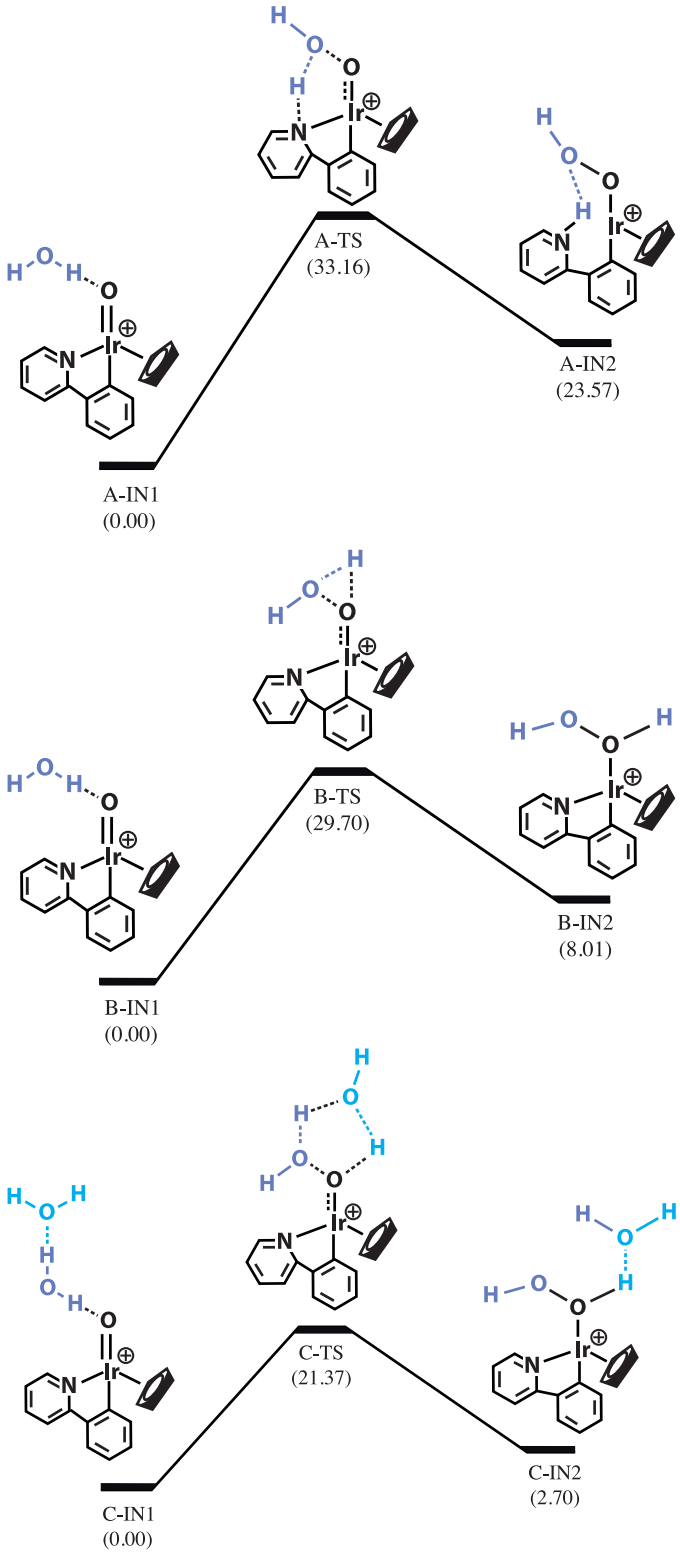

Figure 5.1.: Three different water oxidation pathways: A (top), B (middle) and C (bottom)[28].

Reaction pathway A is an endothermic process (23.6 kcal/mol) in which a single water molecule is involved in the reaction (Fig. 5.1, top). This water forms a hydrogen bond to the oxo-ligand containing the catalyst-substrate complex A-IN1. While the nitrogen in the A-IN1 intermediate is protonated, a O-O bond formation can take place to yield the A-IN2 complex. The reaction pathway B is more likely in terms of energy, where the oxo-ligand containing intermediate has now two functions: forming the new O-O bond and accepting the proton which is released from water (Fig. 5.1, middle). However, the energetically most favorable mechanism is pathway C, where a relatively low-energy transition state is postulated (21.4 kcal/mol). Here, two water molecules and the catalyst form a cyclic transition state followed by a concerted formation and cleavage of three bonds (Fig. 5.1, bottom). These suggested mechanisms were based on electrochemical data and ^{18}O-labelling experiments which confirmed that water molecules are the source for the O_2 production[28].

Computational methods can be very efficient and powerful to mimic reaction pathways and their intrinsic intermediates. The density functional theory (DFT) provides a versatile tool to investigate molecular structures and activation barriers. For this purpose, DFT is often used to estimate reference data as initial parameters for force fields. Nevertheless, the DFT approach is computationally expensive and large screenings and longer molecular dynamics (MD) in explicit solvent are infeasible. Force fields like CHARMM[40] and AMBER[185] provide an approach, which is much faster while they can describe structural features and MD simulations in DFT-quality[297]. CHARMM is originally developed for protein MD, but with certain extensions organometallic compounds can be also treated whereby realistic and transferable parameters are essential to develop robust force fields.

To investigate reaction pathways, the CHARMM force field is combined with the MS-ARMD tool which enables bond breaking and forming. This surface crossing algorithm requires expensive parametrization to mimic a complex mechanistic study of water oxidation. Using this approach should clarify which catalysts are promising for water oxidations and if the participation of water as a solvent has more effects on the stabilization of the intermediate states as already known[28].

5.3. Methods

5.3.1. Intermolecular Interactions

The molecular aspects of iridium containing WOCs have already been studied by density functional theory (DFT) calculations[28]. As faster approaches are needed to screen entire libraries of catalysts, DFT is a suitable method in order to accumulate reference data for the parametrization of the CHARMM FF. For this purpose, reference data were derived from the atom-centered density matrix propagation (ADMP)[139–142,346–348], the intrinsic reaction coordinate (IRC) approach, and from 2D-scans. All electronic structure calculations were performed with Gaussian09, more details to the used methods and the exact DFT set up are specified in Chapter 3.

A description of the entire potential energy surface was realized with the MS-ARMD[24,283] which is newly implemented in CHARMM. MS-ARDM is a general surface-crossing algorithm which allows to follow bond-breaking and bond-forming processes in classical molecular dynamic simulations. To monitor those processes, the harmonic representation of the bonding potential is replaced by an anharmonic Morse potential[349] with an asymptotic level of the form:

$$V_{\mathrm{Morse}} = \mathrm{D_{e,i}}(1 - \exp(-\beta_i(r_i - r_{0,i})))^2 \tag{5.1}$$

where $D_{e,i}$ is the dissociation energy, β_i is the anharmonicity parameter, r_i is the distance between the two atoms and $r_{0,i}$ is the equilibrium bond length. The Morse potential and other parameters were fitted with a simplex algorithm, while initial values for the charges were taken from Mulliken[307,311,350,351] population analysis. Geometrical parameters were obtained from SwissParam and from DFT calculations. The separate fit of individual states along the reaction path enables a smooth connection by combining them to a global surface which is further explained in Chapter 3. The application of this global surface faciliates MD simulations for water oxidation processes in the gas phase and in explicit solvent.

5.3.2. Procedure

The chemical investigation covered in the present work is summarized in (Fig. 5.1) and describes three different reaction mechanisms for the oxidation of water, catalyzed by half-sandwich iridium complexes. To consider an entire reaction pathway and the intrinsic transition states, it was necessary to fit the reactant, product and intermediate surfaces of reaction pathway A, B and C. Therefore, an appropriate set of initial parameters for partial atomic charges q_i (Mulliken charges) and vdW parameters (ϵ_i and σ_i) was generated for the non-bonded interactions. For the bonded interactions, the Morse parameters with the dissociation energy $D_{e,i}$, the anharmonicity parameter β_i and the equilibrium bond length $r_{0,i}$ as well as equilibrium values and force constants for bonds, angles, dihedral angles and improper angles were set up. An adjustment of these parameters was carried out with a simplex algorithm fitting program, using DFT energies of snapshots obtained from an ADMP simulation as a reference. The reactant force field (r-FF) and the product force field (p-FF) were then fitted separately, and afterwards r-FF and p-FF have to be combined to fit the minimum energy path. Depending on the complexity of the reaction pathway, additional intermediate structures have to be fitted. MD simulations are then carried out with the CHARMM FF to determine the transition state in vacuum and later on in explicit solvent.

5.3.3. Fitting Procedure

Initial Mulliken charges and Lennard-Jones (LJ) parameter were taken from a recent fit, where both quantities were adapted to octahedral Ir(III) complexes. It is also required that the "total charge" of the atoms selected in the fit, remains constant which is achieved by a suitable constraint: one atom is excluded during the fitting process to adjust the total charge at the end of each cycle. To obtain a valuable set of Morse parameters, partial-scans of the relevant bond breakages and bond formations were performed.

An adjustment of all the parameters was carried out with a simplex procedure, which is a semi-local optimization procedure especially efficient for non-linear optimization problems. This procedure enables to compute total energies for a given CHARMM parametrization. The specific fitting strategy allows a temporary exclusion of requested parameters, so that charges or vdW or Morse parameters or parts of

the system can be fitted separately and it allows weighting and also complete exclusion of reference points which are outside a user-defined range. Thus, one type of interaction can be kept constant while the other parameter groups can be varied until convergence is obtained. Additional constraints were also set for individual parameters to keep the fit in a realistic environment. It would be possible to fit the two surfaces at the same time, but not efficient except for small and simple systems. Here, the fit was carried out for the reference geometries of the reactant side first and then for the product side.

To obtain around 1000 reference geometries and energies for one surface, either random distorted structures or a DFT-MD approach can be used. The ADMP molecular dynamics model is such a DFT-MD approach. To collect reference data from a NVT ensemble, *ab initio* MD such as ADMP can be immediately used, whereas for FFs, an initial parametrization is required. It further allows a realistic sampling of structures during a MD simulation, although the method is time consuming.

5.3.4. MD Simulations

All MD simulations were carried out in vacuum with the CHARMM FF combined with the MS-ARMD tool. For the five-coordinated *eta*-cyclopentadien complex, the CHARMM lone-pair module was used. The *eta*-bonds are modelled by a dummy-atom, which is located in the center of mass, referring to the atomic positions of the five cyclopentadienyl carbon atoms. The dummy atom overtakes the interaction to the metal center while the metal-carbon interaction of the Cp-ring are switched off completely. An integrator step size of 1.0 fs was used for MD simulations. The heating process for 10 000 steps to 300 K, is followed by an equilibration (NVT) of 1 000 000 steps at this temperature. Verlet dynamics (NVE) for 1 000 000 steps were carried out while the MS-ARMD module can take a snapshot of the TS, if a transition from r-FF to p-FF occurs.

5.4. Results

5.4.1. Sampling Reference Data with DFT

In order to obtain adequate reference structures different approaches were applied. First, 2D-DFT scans were carried out e.g. for the entire reaction of pathway A along the O-O and the N-H coordinates.

However, the resulting PES obeyed a high complexity and provided several geometries with extremely high energies. As the transition state is geometrically related to the product, a 2D-DFT scan from the TS to the product surface of path A yielded a more useful PES, as illustrated in Fig. 5.2.

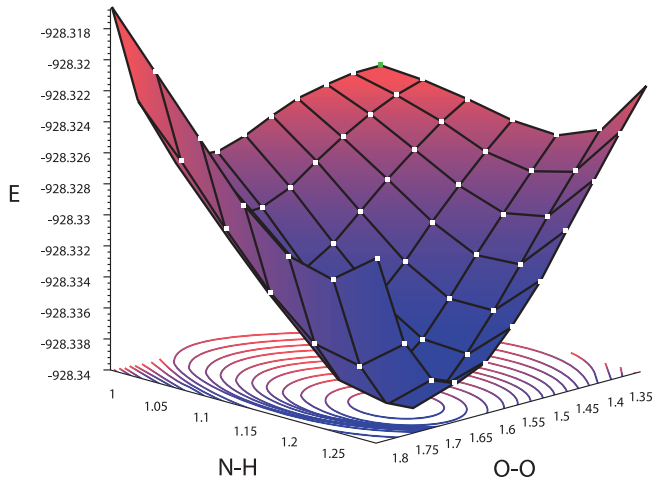

Figure 5.2.: 2D DFT scan of the O-O and N-H bond of the TS over to the product for reaction pathway A.

Such a 2D-grid search provided information about the energy surface away from the pathway. However, the PES (at least to the reactant) is too sophisticated for a sufficient sampling of relevant reference structures. To obtain more reliable parameters for the entire reaction, reference structures were sampled along the IRC (intrinsic reaction coordinate) instead of the 2D-scan. Here, only relevant reference structures were collected which may capture the specific reaction conditions in a better way. The potential energy as a function of intrinsic reaction coordinate is shown in Fig. 5.3 for all three transition pathways. According to the energy differences which were already mentioned in Fig. 5.1, it is obvious that pathway C is the most favorable one (in gas-phase) as it has the lowest energy barrier.

Although Fig. 5.3, reports only one step reactions, it also points out that at least for path A and C, neither the PES from reactant to TS, nor the PES from TS to the final product can be described by a single FF. Several FF were necessary to capture the immense geometrical changes during the reaction, which became evident by monitoring the bond length motions (Fig. 5.4).

Fig. 5.4 illustrates that for the most unfavorable pathway A, the NA-H bond changes from 2.72 Å to 1.05 Å so the hydrogen atom has to move 1.67 Å to reach the product state. The key step,

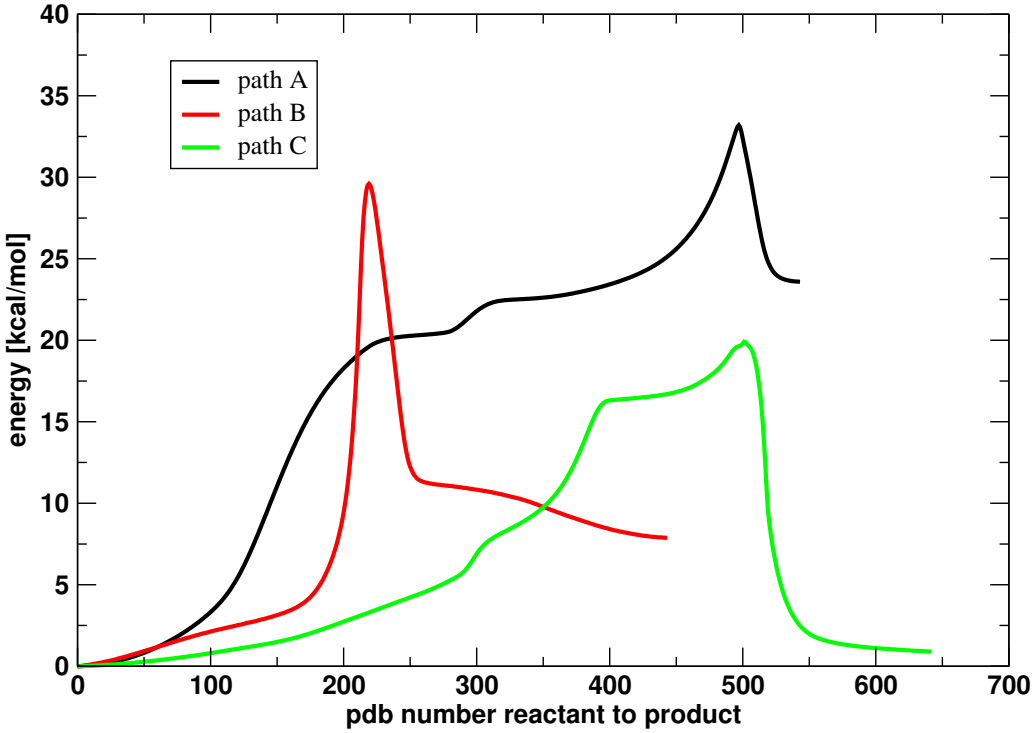

Figure 5.3.: IRC path for reaction pathway A, B and C.

the O-O bond formation, needs to overcome a distance of 1.37 Å to reach the final geometry, which implies an energetically expensive transition. Fig. 5.4 path A also faces the different attitude for bond formation and breakage. For instance, the IRX-NA bond starts to break right after the reactant state, while the OH1-H breakage happens at the very end of the reaction. The minimum energy path of A, along the intrinsic reaction coordinate (steepest descent path) is derived by DFT calculations and illustrated in Fig. 5.5 (black path). The minimum energy path indicates a small slope between the snapshots 275 and 350 (snapshots are illustrated in Fig. 5.5 at that position) which belongs to a flip of the water molecule. After the water is reorientated a long energy plateau follows before the rate limiting step, the O-O bond formation, takes place. Additionally, a dynamical reaction path is depicted in Fig. 5.5 red curve, which is close to the intrinsic reaction coordinate obtained by using ADMP with a damped velocity Verlet (DVV) integrator[145]. The dynamics were carried out with a time step of 1.0 fs, but only every sixth snapshot was taken to derive a comparable plot to the DFT-IRC (black curve). The shape of the energy path along the IRC is closely related to the DVV-MD path. As the DVV-MD generates distorted structures along the IRC, energies are higher than for the steepest decent path (DFT-IRC). Unfortunately, the time for the DVV MD is not linearly related to the number of snapshots along the IRC, therefore a precise match can not be expected.

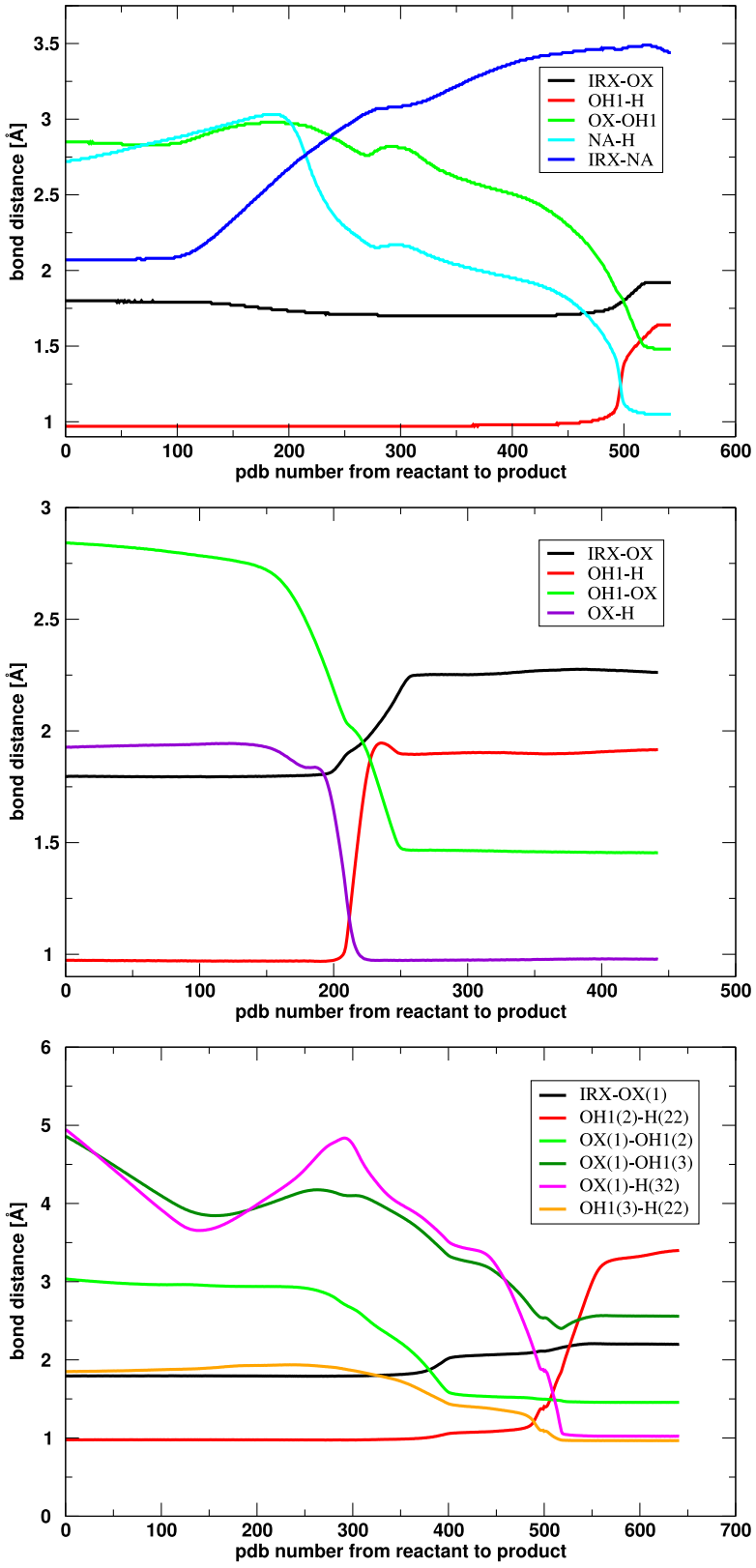

Figure 5.4.: The relevant atom motions during the reaction process of pathway: A (top), B (middle) and C (bottom).

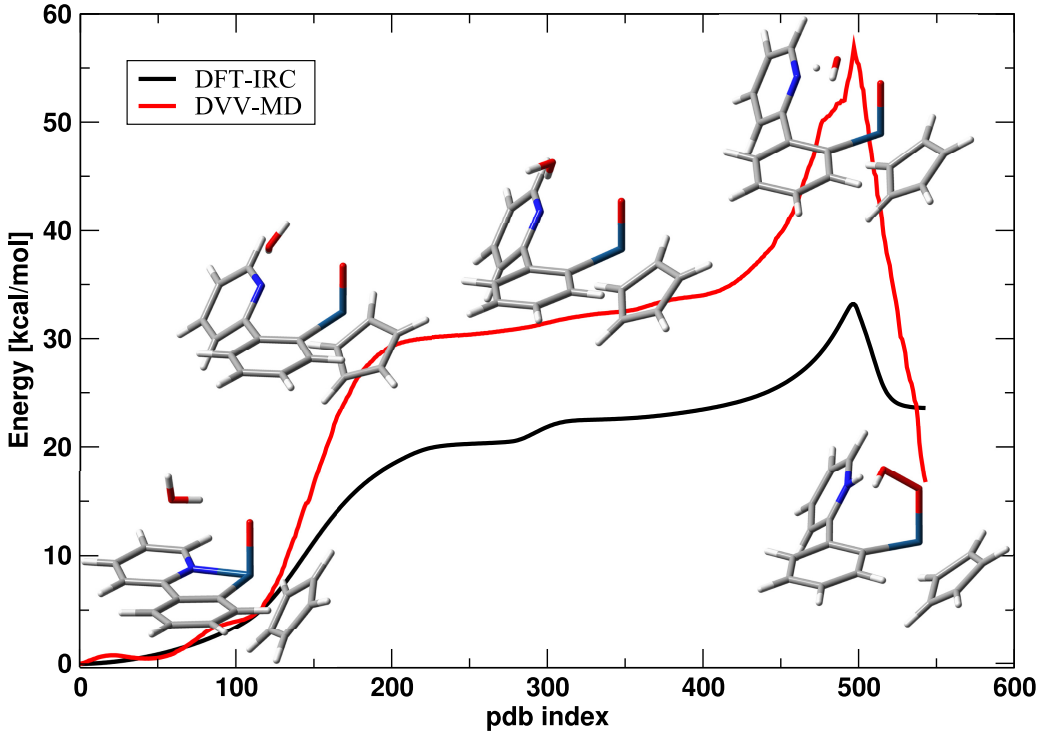

Figure 5.5.: Illustration of pathway A. Black: Minimum energy pathway along the intrinsic reaction coordinate (IRC) with snapshots depending on the local geometry of the energy curve. Red: ADMP simulation with a DVV algorithm along the intrinsic reaction coordinate. For comparison to the DFT-IRC, only every sixth energy was taken for the plot.

The late formation of bonds (around pdb index 500 for pathway A) reflects that we deal with a late transition state (Fig. 5.4, A). This is confirmed by the shape of the IRC curve in Fig. 5.5 where the TS state is much closer to the product state than to the initial geometry. In Fig. 5.3 for reaction pathway B (red), bond forming/breaking occurs almost at the same time which gives a more symmetric shape of the IRC. This allows to describe the reaction pathway B with less FFs compared to pathway A and C. Although the atoms of the O-O bond have to move almost as far as in path A (1.37 Å), other geometrical changes are smaller, resulting in a lower-lying energy barrier for the TS (compared to path A). Fig. 5.4 C reports large migration distances for the water hydrogens e.g. for the H(32) to the OX(1) (3.92 Å) or the H(22) to the OH1(2) (2.38 Å), but the cyclic transition state sufficiently stabilizes the transition state intermediate. As in path A, several FFs are needed to describe the reaction pathway C which obeys large geometrical changes.

Generally, DFT-derived energy curves along the IRC (steepest descent path and dynamical path)

bond	D_e	β	r_e
Ir-N	21.46	1.78	2.20
O-H	83.14	2.85	0.94
N-H	99.26	2.56	0.98
O-O	91.41	2.75	1.24

Table 5.1.: Morse parameters fitted to DFT data on the B3LYP level.

provide reference data along the reaction coordinate. To fit separate surfaces however, more structures were needed around the equilibrium geometry. Therefore, an ADMP simulation was carried out to obtain around 1000 reference geometries and energies for one surface.

5.4.2. Surface Fitting

Reaction Pathway A

Single-bond scans were performed with DFT, and their subsequent fit was carried out in order to gain a Morse-potential parametrization for pathway A. Part scans of the bond breaking and forming events were performed with a non-linear curve fitting to determine a reasonable set for the corresponding surface. For the reactant surface (r-FF), two bond breaking events were considered: the dissociation between the pyridine nitrogen and the iridium, and the breaking of the O-H bond of the water molecule (Fig. 5.1). For the product surface (p-FF), two bond formations were considered: the important O-O bond formation and the acceptance of the proton by the nitrogen, which was originally released from water. Only the relevant parts of the molecules were considered to assure a fast scan of these breakages and formations and to avoid sterical effects. According to literature, the dissociation energy of water is 117.57 kcal/mol[352], and according to the *cccbdb.nist.gov* database, the equilibrium bond length r_e of the O-H bond of water is 0.96 Å. The r_e of N-H is 0.99 Å (originated from pyrrole), and the r_e of the O-O bond (originated from hydroxy peroxy radical) is 1.33 Å. Other initial Morse parameters, where no experimental values are available, were taken from the fitted parameters listed in Tab. 5.1.

Reaction pathway A which has the highest energy barrier for the O-O bond forming step (33.16 kcal/mol) was investigated. The r-FF was fitted first, whereby 1000 ADMP-MD snapshots around the equilibrium geometry were used as a reference. Only relevant, structure-decisive parameters were taken into account to limit the amount of parameters for fitting, while others remained at their initial

values. Bond lengths and force constants were fitted first followed by the Morse potentials including the dissociation energy, the distance of the atom pair, and the anharmonicity parameter. Morse potentials were only introduced if a harmonic approximation failed as their equilibrium bond length changes heavily during the reaction. The fitting was continued by adjusting the angles, dihedrals and improper angles, alternately. The non-bonded parameters were optimized after the energies converged for the fit of the bonded terms. LJ and special LJ-parameters (for 1-4 interactions) parameters were adjusted as well as relevant charges around the iridium and the iridium itself. The fitting cycles were repeated until overall convergence was achieved. A comparison of the DFT-derived reference energies with the CHARMM/MS-ARMD-derived energies using the fitted parameters is illustrated in Fig. 5.6. A $RMSD_{\mathrm{E}}$ of 1.86 kcal/mol was obtained for 1000 geometries of the r-FF of path A.

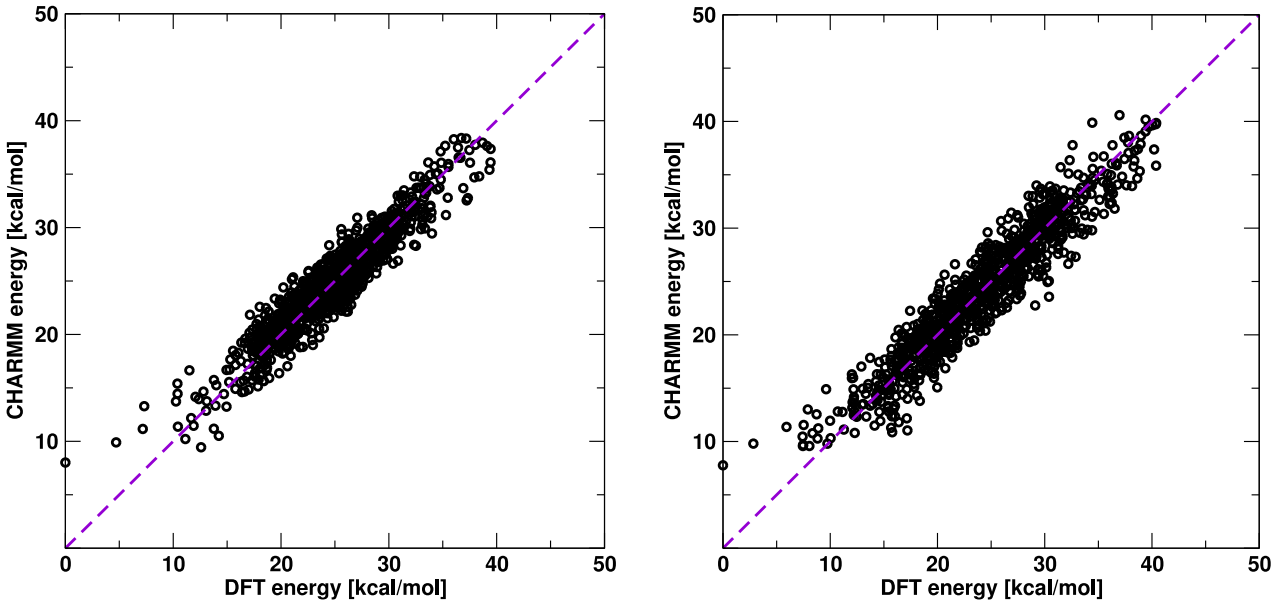

Figure 5.6.: CHARMM/MS-ARMD energies, derived from fitted parameters for the reactant A-IN1 (left) and product A-IN2 (right) of pathway A, are compared to DFT reference energies. The purple dashed line is the 1:1 correlation.

Subsequently, the p-FF of path A was fitted using the same procedure. The critical point was to adjust the dihedral angle to capture the twist of the 2-phenylpyridine ring which is only monoligated and bound to the iridium over one carbon atom. In the product state, the nitrogen is not coordinated to the metal center any longer. For the fit of the p-FF, a $RMSD_{\mathrm{E}}$ of 2.17 kcal/mol was obtained. However, more FFs were necessary to capture the complex shape of the IRC of path A. Therefore, the same fitting procedure was carried out for an intermediate state int275-FF and

for the transition state TS-FF. A RMSD of 4.25 kcal/mol was obtained for the int275-FF and 2.73 kcal/mol for the TS-FF. The combined force fields, r-FF, int275-FF, TS-FF and p-FF were then used to calculate the energies along the IRC with CHARMM/MS-ARMD. The energies obtained with CHARMM/MS-ARMD are given in Fig. 5.7 (red curve) whereby the Gaussian derived energies were taken as reference values for the IRC (Fig. 5.7 black curve). The r-FF and the int275-FF can reproduce the energy profile, but the TS-FF and p-FF do not properly describe the PES. However, applied corrections using Gaussian polynomials resulted in a good RMSD_E of 0.65 kcal/mol (Fig. 5.7, green curve).

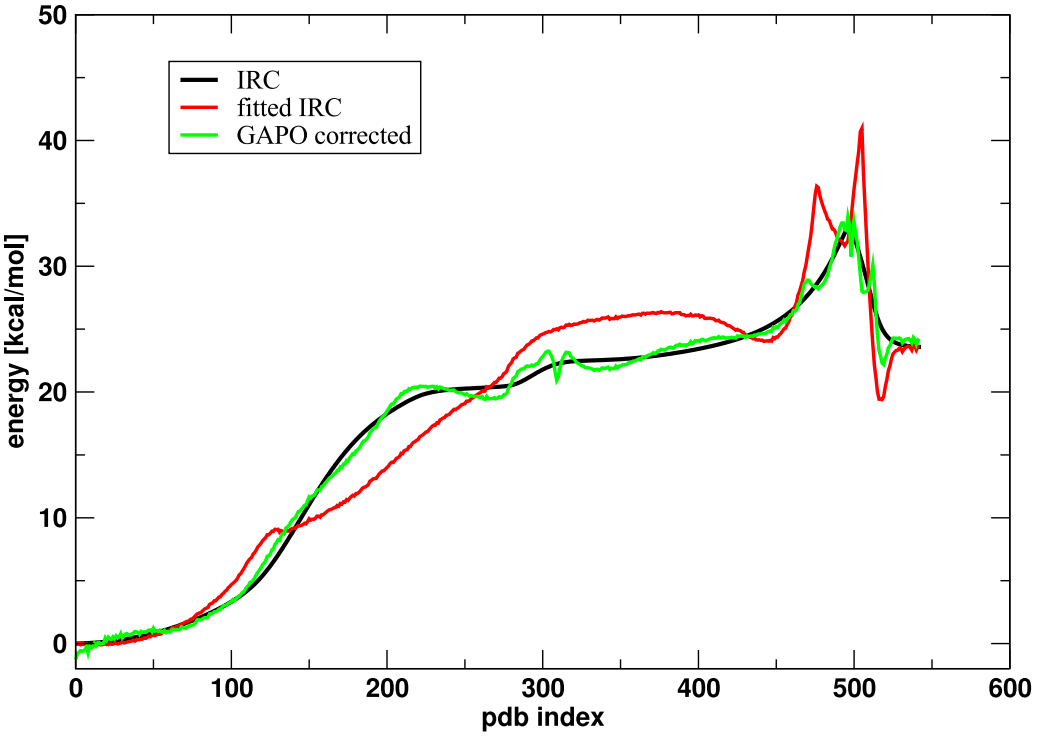

Figure 5.7.: IRC and IRC descriptions of pathway A. Black curve: DFT-derived IRC, red curve: CHARMM/MS-ARMD fitted IRC and green curve: GAPO corrected IRC.

The CHARMM/MS-ARMD fitted IRC (Fig. 5.7, red curve) depicted a description problem around the transition state. A lack of reference data which can describe the curve shape in this region might cause the inaccurate approximation as only ADMP references were used in the fit. Therefore, the GAPO corrected IRC fit (Fig. 5.7, green curve) showed some fluctuations around the TS which caused problems in the energy conservation. A refit would be needed, which includes additional references from the IRC, to capture the IRC in a more accurate way.

Reaction Pathway B

Reaction path B revealed a lower TS barrier (29.6 kcal/mol) than path A and additionally showed a more symmetric IRC curve. As travel distances of atoms, which form or break bonds during the reaction, are reasonable (Fig. 5.4, middle panel), a description of the PES with only two FFs was feasible. Both FFs were fitted close to the defined PES by including additional IRC structures as a reference. Assigning a higher weight to them faciliated a better description of the shape around the TS. The adjustment of bonded and non-bonded parameters for the r-FF and p-FF of pathway B resulted in a $RMSD_{\mathrm{E}}$ of 1.54 and 1.94 kcal/mol, respectively (Fig. 5.8).

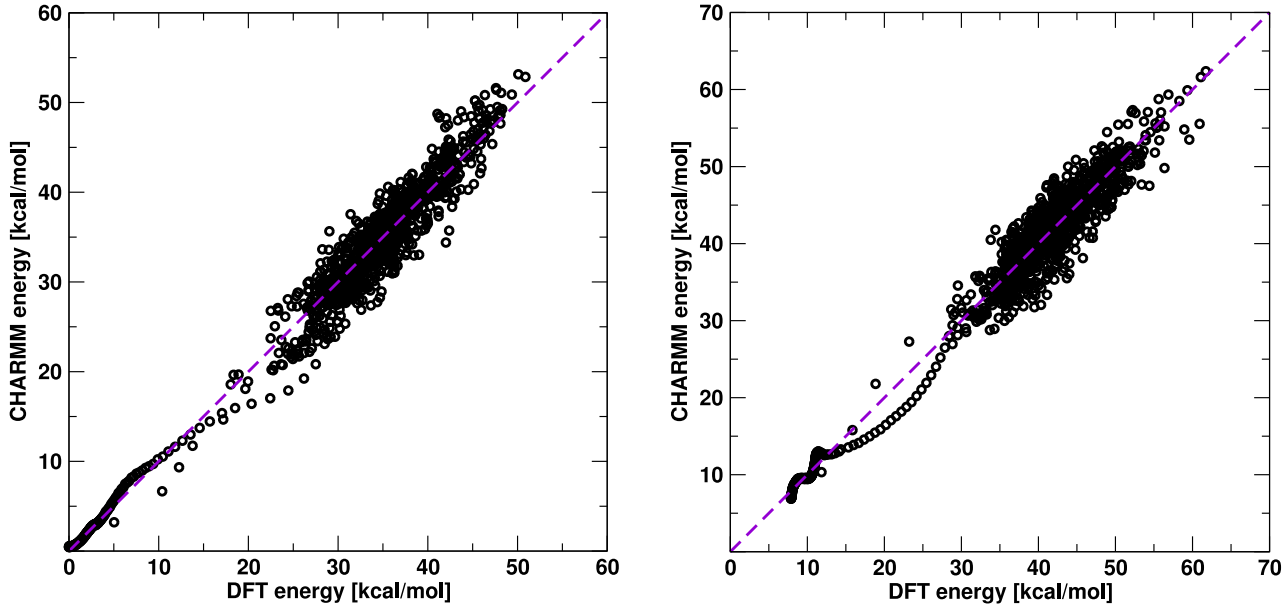

Figure 5.8.: CHARMM/MS-ARMD energies, derived from fitted parameters for the reactant B-IN1 (left) and product B-IN2 (right) of pathway B, are compared to DFT reference energies. The purple dashed line is the 1:1 correlation.

The combined r-FF and p-FF of CHARMM/MS-ARMD (Fig. 5.9, red curve) can describe the QM-derived IRC (Fig. 5.9, black line) with a RMSD_E of 1.08 kcal/mol. The accuracy was improved by correcting the global surface with a single GAPO. The RMSD_E was reduced to 0.47 kcal/mol as depicted in Fig. 5.9, green curve. The inclusion of IRC structures in the fit provided a more realistic description of the IRC in Fig. 5.9, red curve, even without the correction by GAPOs. Therefore, a successful fitting of a global surface becomes feasible by using a combination of ADMP and IRC reference data and by fitting a large set of bonded and non-bonded parameters (around 200 parameters).

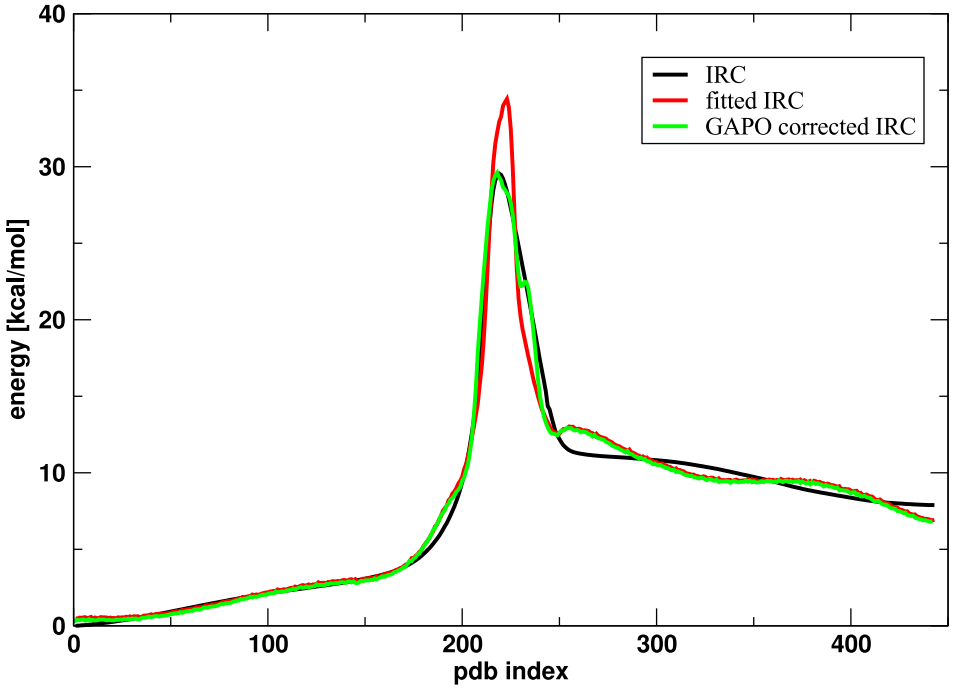

Figure 5.9.: IRC and IRC descriptions of pathway B. Black curve: DFT-derived IRC, red curve: CHARMM/MS-ARMD fitted IRC and green curve: GAPO corrected IRC.

In atomistic simulations with the global surface of path B, a transition was induced by heating the system up to 1000 K. Constraining the O-O bond distance to 3.5 Å enabled to sample around the reactant structure which avoids that the water moves too far from the complex as it happens in gas phase calculations. After several simulations, a transition was obtained which was compared to the DFT-derived transition state in Fig. 5.10. Starting the CHARMM/MS-ARMD simulation from the DFT-derived TS also provided a TS during MD simulations which is almost identical to the DFT-derived TS (RMSD 0.1 Å).

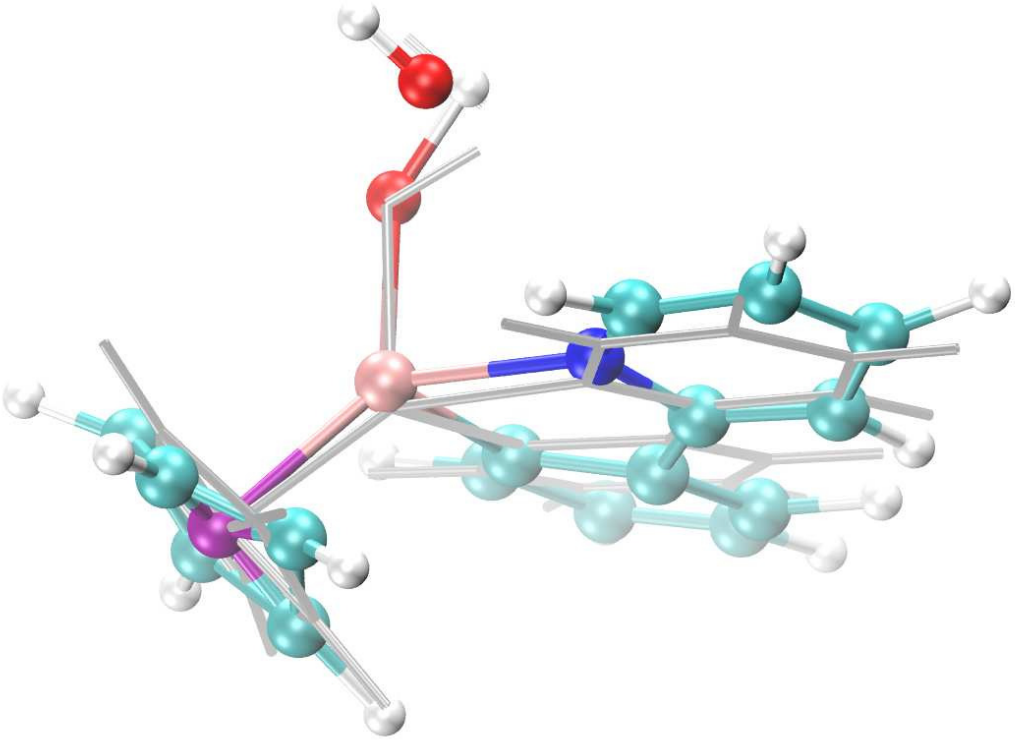

Figure 5.10.: Transition states of pathway B. Grey complex: DFT-derived TS, colored complex: CHARMM/MS-ARMD-derived TS during MD simulation with a RMSD of 0.96 Å. Color code: iridium (pink), carbon (light blue), hydrogen (white), nitrogen (blue), oxygen (red), dummy atom (purple).

Reaction Pathway C

Reaction path C is the most favored pathway of the reactions depicted in Fig. 5.1, bottom with a barrier of 21.37 kcal/mol. Path C is not fitted yet, but a similar fitting procedure may result in a comparable accuracy.

5.5. Further Procedure

The combined CHARMM/MS-ARMSD tool proved that, with an adequate parametrization, it can describe MM results in close agreement to QM data. The description of path A already showed that the reaction curve can be captured, however, a refit including IRC reference structures could further improve the approximation in the TS region. The fitted CHARMM/MS-ARMD energy profile of path B, where IRC structures were included in the fit, can describe the reaction curve nearly perfect with a

$RMSD_E$ below 0.5 kcal/mol. Subsequent atomistic simulations provided a transition state which is comparable to the DFT-derived TS.

Once the global surfaces of all three transition paths are fitted, atomistic simulations of all paths can be carried out in the gas phase and in explicit solvent. Further, a transition path sampling (TPS) can be carried out to determine the corresponding reaction rate[127]. For a TPS, the TS-like structure derived from Gaussian calculations needs to be constrained in the way that the O-O bond cannot vary more than +/- 0.1 Å. This keeps the iridium complex in a TS-like structure along the MD simulation. Taking e.g. 100 snapshots from this trajectory provides 100 new initial structures to start independent trajectories. The unconstrained dynamics will either form the reacant or the product, which allows a determination of the reaction rate. Umbrella sampling[353] (combined with the weighted histogram analysis method (WHAM)[354,355]) along the O-O reaction coordinate can provide further information about free energy barriers and therefore about the reliability of the FF. After the evaluation of the global surfaces of the three pathway A, B and C, a screening of different catalysts becomes feasible.

6. Structure and Dynamics of Solvent Shell around Photoexcited Metal Complexes

6.1. Abstract

Understanding the geometry, energetics and dynamics of solvated transition metal (TM) compounds is decisive in characterizing and optimizing their function. Here, we demonstrate that it is possible to quantify the structural dynamics of solvated $[Ru^{II}(bpy)_3]$, an important TM-complex for solar-energy harvesting research, by using state-of-the-art force fields together with molecular simulations. Electronic excitation to $[Ru^{III}(bpy)_3]$ leads to a non-equilibrium system in which excess energy is redistributed to the surrounding solvent following a cascade of dynamical effects that can be characterized by the simulations. The study reveals that the structure of the surrounding solvent relaxes towards equilibrium from a sub-picosecond to few-picosecond time scale. Analysis of solvent residence and rotational reorientation times during relaxation demonstrate increased dynamics in the inner solvation sphere on the picosecond time scale. Energy transfer to the solvent occurs on different time scales for the different degrees of freedom and range from a few hundred femtoseconds to several picoseconds.

6.2. Introduction

The dynamics of solvated transition metal containing species is of fundamental importance in catalysis and charge transfer[356,357]. One of these - light-induced charge transfer - is of particular importance due to possible applications in solar energy conversion[358,359]. The comprehensive understanding of mechanisms governing solar energy conversion and its transfer to the environment can serve as a basis for development of more efficient light-harvesting materials. Progress in ultrafast spectroscopic techniques provided new insights about structural changes on the sub-picosecond scale. Time-resolved

infrared (TRIR) and Raman (TRR) spectroscopy provide information about molecular structure evolution during very rapid chemical processes[360]. Examination of the vibrational modes gives direct insight into the structural dynamics of many important processes including excited state intramolecular hydrogen or proton transfer[361,362], hydrogen bonding during solvation dynamics[363], bond cleavage in organometallic compounds or proteins[364], or *cis-trans* isomerization in retinal proteins[365,366]. Also, transitions between excited electronic states can be followed by inspection of the fingerprint IR- or Raman-active vibrations. Complementary to that, structural and kinetic information on the reaction dynamics in liquids, including temporal rearrangements of solvent around solute, can be obtained from time-resolved X-ray liquidography (TRXL)[367,368]. Experimental characterization alone is, however, usually not sufficient to explain and interpret the complex and heterogeneous dynamics at molecular and atomistic scales while simulations provide necessary, complementary and much needed information[369–371].

Ruthenium-tris-(2,2'-bipyridine), $[Ru^{II}(bpy)_3]^{2+}$, is a particularly well characterized TM-compound which was the subject of previous theoretical[372–374] and experimental[1,2,375–378] studies during the past two decades. This polypyridine complex absorbs light in the visible range, which leads to a singlet metal-to-ligand charge-transfer state (^{1}MLCT) that undergoes ultrafast intersystem crossing to a ^{3}MLCT triplet state[1,375] which cools vibrationally to an unusually long-lived triplet state with a life time of 600 ns[359,378,379] (Fig. 6.1). Although the available studies do not fully agree on all quantitative aspects, they all contain the following three elements[1,2,375]: ultrafast internal conversion from the Franck-Condon excited singlet in tenths of femtoseconds; sub-picosecond to picosecond cooling of the vibrationally excited triplet; and radiative decay of the long-lived triplet on the sub-microsecond scale.

The radiative decay shown in blue in Fig. 6.1 is efficiently (95%)[380] quenched to the triplet metal-centered state (^{3}MC) from which the system decays non-radiatively to the ground state. Thus, deactivation of only a small fraction (5%) of the excited state population can be investigated directly by experimental studies. Previous computational work focused on exploring the properties of the first solvation shell[372] and electron localization[373] during the initial stages of ^{3}MLCT relaxation. Contrary to that, the present work focuses on the investigation of the solvent role in the photocycle of the ruthenium complex. In particular, the ability of water to absorb excess energy in the initial stage of the deactivation may contribute importantly to the unusual stability of the radiative excited

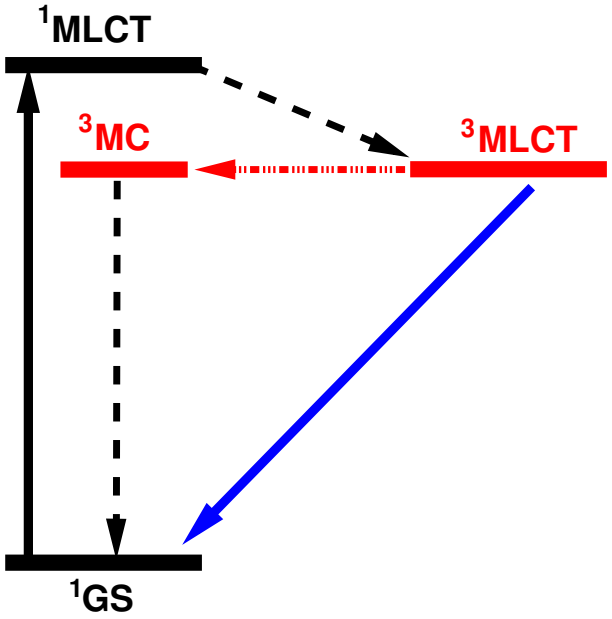

Figure 6.1.: Photocycle of the ruthenium complex. The blue line corresponds to radiative decay with a fluorescence lifetime of ≈ 600 ns. Ultrafast non-radiative processes shown as dashed lines. Vibrational relaxation studied here is shown in red.

state of the compound. The time scales for energy transfer and signal decay are estimated from non-equilibrium MD simulations. Our approach is motivated by the fact that the time required for internal conversion from the ^{1}MLCT to the ^{3}MLCT state is very rapid (≈ 15 fs)[375]. The explicit computational characterization of this process is now possible due to recent technical progress[381]. The measured quantities involve time-dependent radial distribution functions, the kinetic energy of the solvent, and computed IR spectrum. We are particularly interested in the time scale and pathway for energy transfer to the surrounding solvent or whether the excess energy after photo-excitation is rather redistributed to the low frequency modes through intramolecular vibrational-energy redistribution (IVR) as suggested by Chergui and co-workers[375]. The results of the present work should serve as a basis for future and more atomistically resolved work including TRXL[368].

6.3. Methods

6.3.1. Computational Details

All MD simulations were carried out with CHARMM[40] and provisions for VALBOND-TRANS (VBT)[223]. VALBOND itself is an extension of conventional force fields based on valence bond theory and capable of more realistically describe angle bending energies in metal complexes[22,60,382]. The approach is based

on the concept that the L_1-M-L_2 bending energy is a function of the overlap of the hybrid orbitals on the central metal atom, where L_1 and L_2 are ligands and M is the metal atom. Unlike the simple harmonic approximation, VALBOND bending functions capture the energetics at very large angular distortions. It also supports hypervalent compounds by means of 3-center-4-electron bonds[60]. As a result, VBT can describe geometries found in organometallic compounds, such as octahedral, trigonal biplanar, and square planar. In order to have a complete force field, VALBOND has to be combined with another force field (in the present work it is CHARMM22[48]) to account for the bond stretching, torsional, and nonbonded energy terms. A more recent generalization of VALBOND implements the description of the ligand trans influence which is an electronic effect. The corresponding force field is VALBOND-TRANS (VBT) where trans parameters for Ru(II) and Ru(III) had been previously determined[223] (see more in Chapter 3). The remaining parameters for the bipyridine rings were those from the CHARMM22[48] and CHARMM General Force Field (CGenFF[383]).

Optimized structures for $[Ru^{II}(bpy)_3]^{2+}$ and $[Ru^{III}(bpy)_3]^{3+}$ were determined from density functional theory (DFT) calculations with the B3LYP[114] functional and the 6-31G(d,p)[124] basis set on nitrogen, carbon and hydrogen and LanL2DZ[178] on the ruthenium atom including ECP. For the force field simulations, partial charges for both oxidation states of the complex were determined from a Mulliken analysis and from analyzing the natural bond orbitals (NBO)[384] (see Tab. 6.1). For most simulations Mulliken charges were used. A comparison between Mulliken and NBO charges for the Ru-water radial distribution functions around the Ru(II) and Ru(III) complex is provided in Fig. 6.2. The DFT calculations were performed using the Gaussian03 suite of codes[134].

The computational setup for the present study consists of a ruthenium complex solvated in a pre-equilibrated cubic box of edge length 37.25 Å containing 1694 water molecules, with 5143 atoms in total (see Fig. 6.3). Periodic boundary conditions (PBC) were applied; the nonbonded interactions (electrostatic and Lennard-Jones) were truncated at a distance of 14 Å and switched between 10 and 12 Å. First, the systems were heated and equilibrated for 1 ns at 300 K. Newton's equations of motion were propagated in the *NVE* ensemble with a Verlet integrator. Two water models were used in the present work. In simulations with the standard TIP3P model[385] all H-bonds were constrained by applying SHAKE[386,387] and the time step in the simulations was 1 fs. Alternatively, a flexible KKY water model[388] with revised force constants[389] was employed to study energy transfer from the

		Ruthenium		Nitrogen		1.1'-Carbon		2.2'.3-Carbon		Hydrogen	
Basis on Ru(II)	Basis set	Mulliken	NBO	Mulliken	NBO	Mulliken	NBO	Mulliken	NBO	Mulliken	NBO
LanL2DZ	6-31G(d,p)	0.72	0.59	−0.52	−0.43	0.19	0.12	−0.08	−0.21	0.15	0.26
LanL2DZ	6-311(d,p)	1.00	0.61	−0.56	−0.44	0.18	0.14	−0.07	−0.17	0.15	0.23
SDD	cc-PVTZ	0.53	0.53	−0.19	−0.39	0.02	0.11	−0.08	−0.17	0.16	0.23
Basis on Ru(III)	basis set	Mulliken	NBO	Mulliken	NBO	Mulliken	NBO	Mulliken	NBO	Mulliken	NBO
LanL2DZ	6-31G(d,p)	1.01	1.01	−0.56	−0.46	0.20	0.12	−0.07	−0.19	0.18	0.28
LanL2DZ	6-311(d,p)	1.20	1.02	−0.60	−0.47	0.20	0.14	−0.06	−0.15	0.17	0.24
SDD	cc-PVTZ	0.81	0.99	−0.21	−0.43	0.03	0.12	−0.07	−0.15	0.18	0.24

Table 6.1.: Partial atomic charges for the Ru(II) and Ru(III) complex from Mulliken and NBO analyses for different basis sets. Charges on the nitrogen, 1,1'-carbon (carbons directly bound to N), 2,2',3-carbon (carbons bond to N over 2 to 3 bonds) and hydrogen atoms are averaged.

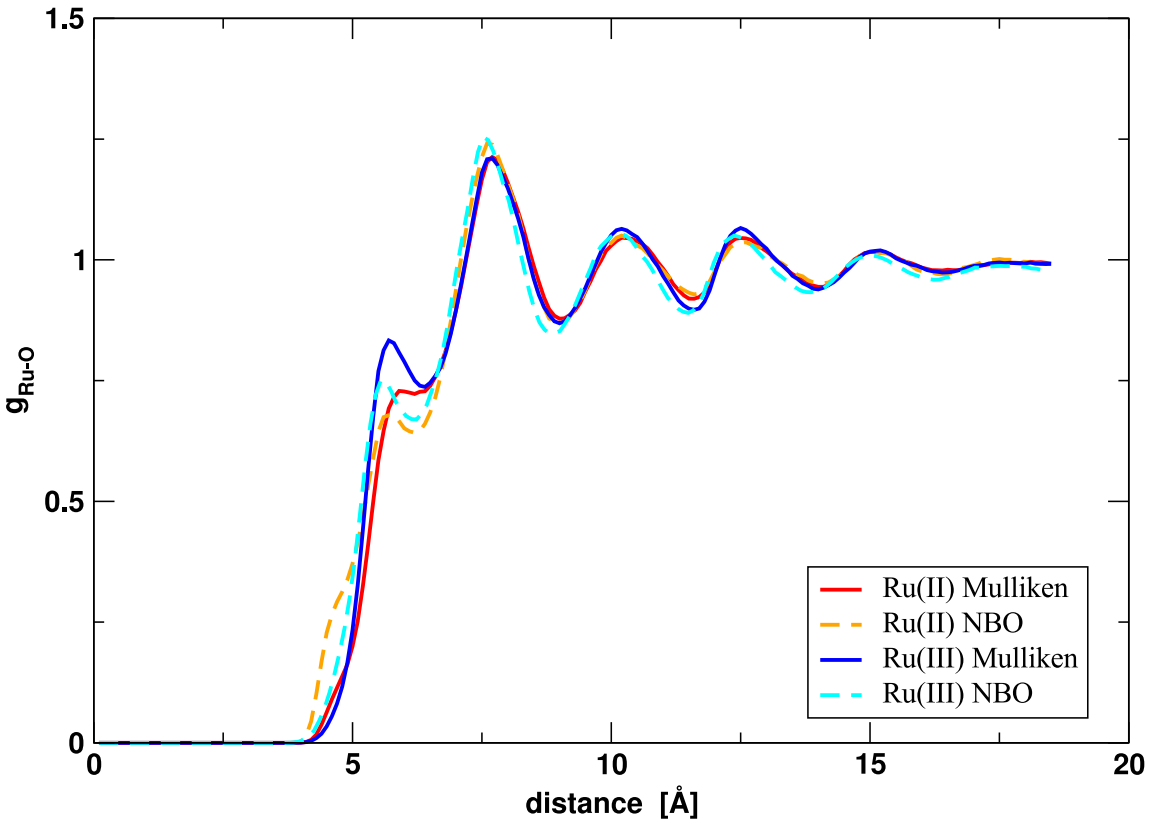

Figure 6.2.: Radial distribution function (RDF) for Ru-O_{Wat} determined for Ru(II) and Ru(III) with Mulliken and NBO charges. With Mulliken charges (red, solid) the first water shell around the Ru(II)-complex is at 5.9 Å which shifts to 5.7 Å for NBO charges (orange, dashed). The difference of 0.2 Å is related to the decreased charge of Ru(II) (0.59 e) from an NBO analysis compared to a Mulliken charge of 0.72 e (see Tab. 6.1. For the Ru(III) complex the first shell is at 5.7 Å (Mulliken charge 1.01 e for Ru(III); blue, solid) compared to 5.6 Å for NBO charges (Ru(III) charge of 1.01 e; cyan, dashed). For the second, third and subsequent solvation shells, no appreciable effects are observed for the two different charge concepts.

metal-complex to the surrounding solvent. The nonbonded parameters (charges and van der Waals) for water were taken from the TIP3P model and because the bonds to the H-atoms are flexible, the time step was reduced to 0.4 fs. From the latest one hundred trajectories of 50 ps length (for the TIP3P and KKY model) initial geometries and velocities were stored. For the Ru(II) complex this data was used as initial conditions for the non-equilibrium simulations. Electronic excitation from Ru(II) to Ru(III) was induced by changing the force field parameters between the two oxidation states. This perturbation leads to a non-equilibrium situation (denoted as $Ru(III)^{exc}$) from which the system relaxes towards the equilibrium state $Ru(III)^{eq}$. One hundred independent non-equilibrium simulations were performed for each water model for 40 ps each.

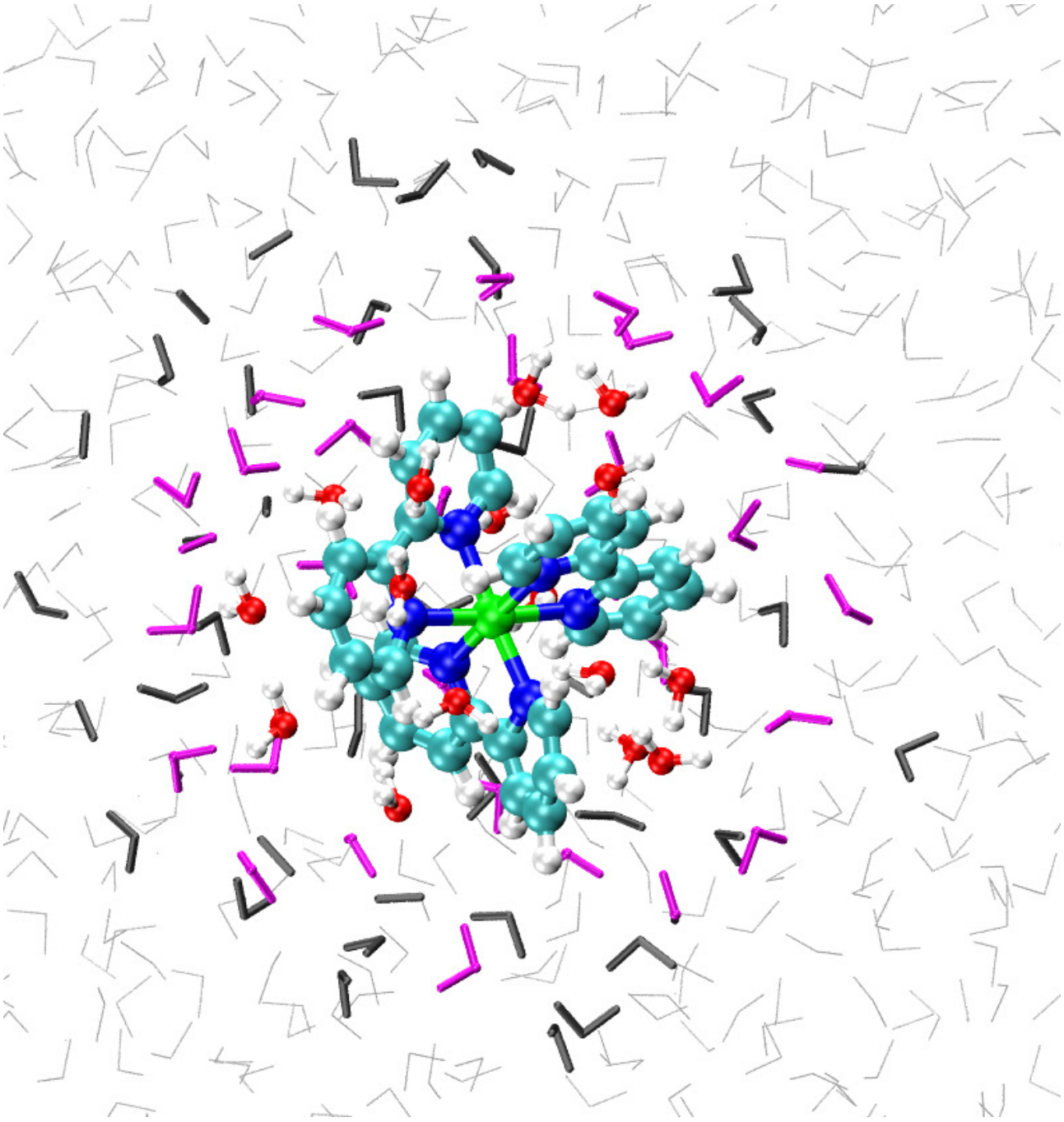

Figure 6.3.: $[Ru^{II}(bpy)_3]^{2+}$ complex solvated in water, snapshot from MD simulation. Water molecules within first, second, and third shell are marked in red (ball and sticks), magenta, and thick grey, respectively. Bulk water is represented by grey lines.

6.3.2. Analysis of Trajectories

From the coordinate and velocity trajectory the observables relevant to this study are computed.

Radial distribution functions: Radial distribution functions $g(r)$ were calculated from the time series and averaged over all trajectories for a given system ($Ru(II)^{eq}$, $Ru(III)^{eq}$, and $Ru(III)^{exc}$). For the present work they were calculated for the Ru-O_W ($g_O(r)$) and Ru-H_W ($g_H(r)$) distances, where O_W and H_W refers to water-oxygen and water-hydrogen atoms, respectively. The corresponding running coordination number $N(r)$ is defined as

$$N(r) = 4\pi \int_0^{r_s} r^2 g(r) \rho dr \tag{6.1}$$

where ρ is the water density. Additional structural information on the water organization within shells can be obtained from $N_H(r)/N_O(r)$. For bulk water $N_H(r)/N_O(r) = 2$, whereas values different from 2 suggest structuring of the water, however, without providing more detailed information about the precise nature of the structure.

Water rotational reorientation times: The rotational reorientation time τ_r is calculated by fitting the corresponding rotational time correlation function $R_r(t) =< \vec{u}(0)\vec{u}(t) >$ of the unit vector along the molecular dipole moment $\vec{u}(t)$ to an exponential function of the form $R_r(t) = A\exp(-t/\tau_r)$. This analysis was carried out within CHARMM[40].

Water residence times: Water exchange dynamics was followed by determining residence times of water molecules in different shells around the complex. The residence time was calculated from the time correlation function $R(\tau)$ following Koneshan *et al*[390].:

$$R(\tau) = \frac{1}{N n_W} \sum_{i=1}^{N} \sum_{j=1}^{n_W} \Theta_j(t)\Theta_j(t+\tau) \tag{6.2}$$

Here, N is the number of trajectories, $\Theta_j(t)$ is the step function with $\Theta_j(t) = 1$ if water molecule j lies within the inspected coordination shell and zero otherwise. The criterion for the water belonging to a shell is fulfilled if the distance between the Ru-atom and the O_{WAT} is smaller than the shell radius

r_s, determined from $g_O(r)$. Time scales for exchange dynamics were obtained by fitting $R(\tau)$ to a three-exponential decay:

$$R_3(\tau) = A_1 \exp\left(-\frac{t}{T_1}\right) + A_2 \exp\left(-\frac{t}{T_2}\right) + (1 - A_1 - A_2) \exp\left(-\frac{t}{T_3}\right) \tag{6.3}$$

Using only two time scales lead to a considerably worse fit of $R(\tau)$. The parameters A_1 and A_2 describe the relative importance of the processes associated with each of the time scales. Residence times were determined for the first, second, and the third shell (shells I, II and III) around the complex for all simulations performed.

Energy transfer to the solvent: Energy transfer to the solvent was followed by monitoring the kinetic energy ($E_{\mathrm{kin}}^{(\mathrm{W})}(t)$) of the water molecules within a radius r_s around the Ru-atom. The specific value $r_s = 11.6$ Å includes the first three solvation layers at the time of excitation and was chosen from inspection of $g_O(r)$ (see Fig. 6.4). Water molecules exchanging from distances further away at a later time were not included in the analysis. Typically, about 200 water molecules are included in the analysis. For each water molecule the kinetic energy was decomposed into translational ($E_{\mathrm{T}}^{(\mathrm{W})}$), rotational ($E_{\mathrm{R}}^{(\mathrm{W})}$), and vibrational ($E_{\mathrm{V}}^{(\mathrm{W})}$) contributions. Furthermore, the contributions to the symmetric stretching (v_1), bending (v_2), and asymmetric stretching (v_3) modes were determined. The decomposition was based on the transformation of the space-fixed Cartesian coordinate system into the molecule-fixed normal coordinate system[389,391].

IR spectra: For the IR spectra, the real-time dipole-dipole autocorrelation function $C(t)$ is calculated. The vibrational spectrum $C(\omega)$ is computed from the Fourier transform of $C(t)$[392]. IR spectra were only determined from trajectories based on the KKY model. For computing $C(t)$, the dipole moments of all waters up to the third shell around the Ru-atom are used. The correlation function was accumulated for 2^{14} time steps and then Fourier transformed with a Blackman filter to yield $C(\omega)$[393]. The IR spectrum is calculated from:

$$A(\omega) \propto \omega(1 - \exp(-\hbar\omega/(k_B T)))C(\omega) \tag{6.4}$$

where k_B is the Boltzmann constant, $\hbar$ is the Planck constant, and T is the temperature. The spectra

reported are averages over 100 independent trajectories.

6.4. Results and Discussion

6.4.1. Equilibrium Simulations

First, the equilibrium dynamics of the Ru(II) and Ru(III) complex are analyzed. The radial distribution functions (RDFs) of water oxygen $g_{\mathrm{O}}(r)$ and hydrogen $g_{\mathrm{H}}(r)$ atoms with corresponding running coordination numbers $N_{\mathrm{O}}(r)$ and $N_{\mathrm{H}}(r)$ have been computed for Ru(II)$^{\mathrm{eq}}$ and Ru(III)$^{\mathrm{eq}}$. The profiles of $g_{\mathrm{O}}(r)$ and $N_{\mathrm{O}}(r)$ along with the one determined for the non-equilibrium simulations are presented in the left panel of Fig. 6.4. For Ru(II)$^{\mathrm{eq}}$ and Ru(III)$^{\mathrm{eq}}$ they primarily differ for shell-I ($\leq$ 6.4 Å) around the Ru atom. The corresponding running coordination numbers show that for Ru(III)$^{\mathrm{eq}}$ the complex can accommodate one water molecule more (corresponding to $\approx$ 10 %) in the first solvation shell than Ru(II)$^{\mathrm{eq}}$ (right panel of Fig. 6.4). Beyond the first shell differences between RDFs decrease. Nevertheless, the difference in the amount of water molecules is preserved up to shell III.

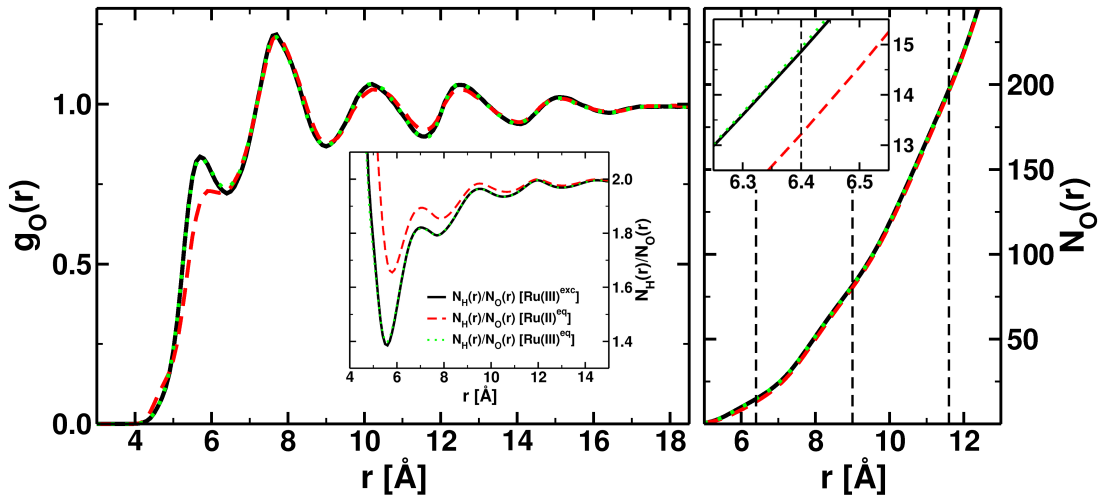

Figure 6.4.: Left panel: Radial distribution functions for Ru-$\mathrm{O_{WAT}}$ determined for excited (non-equilibrium) Ru(III)$^{\mathrm{exc}}$ (solid black), and equilibrium Ru(II)$^{\mathrm{eq}}$ (dashed red), and Ru(III)$^{\mathrm{eq}}$ (dotted green) simulations. Curve in the inset reports the $N_{\mathrm{H}}(r)/N_{\mathrm{O}}(r)$ ratio as a function of the distance from the Ru-atom. For detailed explanation see text. Right panel: Running coordination number for oxygen $N_{\mathrm{O}}(r)$ as a function of the distance from the Ru-atom. Vertical dotted lines correspond to the r_s values for shells II and III, respectively. Inset shows the magnitude of $N_{\mathrm{O}}(r)$ profile around r_s=6.4 Å.

More information regarding the organization of the water molecules can be obtained from analyzing

the ratio $N_H(r)/N_O(r)$ (see Fig. 6.4 inset). In bulk water, $N_H(r)/N_O(r) = 2$ whereas near a solute molecule the ratio can deviate considerably from this value due to orientational effects of the solvent molecules. Because $g_H(r)$ and $g_O(r)$ (and therefore $N_H(r)$ and $N_O(r)$) are very small close to the Ru-atom, $N_H(r)/N_O(r)$ can assume unphysical values (larger than 2) which, however, should not be interpreted because $0 \leq N_O(r) < 1$ in this region. Around the first maximum of $g_O(r)$, $N_H(r)/N_O(r)$ drops below 2 (1.40 and 1.65 for $Ru(II)^{eq}$ and $Ru(III)^{eq}$, respectively), reflecting the fact that the water-oxygens are oriented towards the positive charge of the ruthenium complex (i.e. depletion of H-atoms), and then approaches the bulk-value of $N_H(r)/N_O(r) = 2$ asymptotically. The difference between $N_H(r)/N_O(r)$ for $Ru(II)^{eq}$ and $Ru(III)^{eq}$ remains always above 0.1 for distances within shell-I which suggests that water ordering is more pronounced for $Ru(III)^{eq}$ compared to $Ru(II)^{eq}$. This reflects the stronger electrostatic attraction of water to Ru(III) compared to Ru(II). For r corresponding to the second shell the difference drops to approximately 0.05 and for $r = 12$ Å $N_H(r)/N_O(r) \approx 2$.

In Table 6.2 water rotational reorientation times (τ_r) determined for both water models and for all three shells and bulk water are reported. Reorientation times from simulations with the KKY model are systematically longer than those from using TIP3P water. All values for $Ru(III)^{eq}$ presented in Table 6.2 are shorter than those obtained for $Ru(II)^{eq}$. For both equilibrium simulations, τ_r for the first shell are more than four times larger than the bulk value and more than three times larger than values determined for shell-II suggesting that rotational dynamics close to the solute is considerably slowed down. Rotational reorientation times from the TIP3P model show the same gradual decrease of τ_r in going from the first shell towards the bulk, although they are a factor of 2 to 3 smaller compared to simulations with KKY. Earlier work on reorientation times established that different water models lead to τ_r ranging from 0.7 (TIP3P) to 1.7 ps (SPC/E)[394]. Experimentally observed[395] water reorientation times (τ_r=1.95 ps) are significantly better reproduced by simulations using the KKY (τ_r=1.4 ps) than the TIP3P (τ_r=0.7 ps) water model. Based on this, the following analysis will be based on simulations with the KKY model, unless stated otherwise.

Water residence times determined from the procedure outlined in the Methods section 6.3.2 for the first three shells (see Fig. 6.3) are reported in Tab. 6.3. Based on tracking individual water molecules, three types of processes involving the solvent water molecules could be distinguished and characterized by time constants T_1, T_2, and T_3 in eq. 6.3.

Table 6.2.: Water rotational reorientation times $(\tau)_r$. Results obtained with KKY and TIP3P water model.

	Ru(II)^{eq}			Ru(III)^{eq}			Ru(III)^{exc}		
shell	I	II	III	I	II	III	I	II	III
τ_r (TIP3P)[1] [ps]	3.7	0.9	0.8	2.1	0.9	0.8	2.6	0.7	0.7
τ_r (KKY)[2] [ps]	8.4	2.4	2.0	6.3	2.0	1.7	8.2	2.4	2.0

Table 6.3.: Time constants for residence correlation functions $R(\tau)$.

	Ru(II)^{eq}			Ru(III)^{eq}			Ru(III)^{exc}		
r [Å]	6.4	9.0	11.6	6.4	9.0	11.6	6.4	9.0	11.6
T_1 (KKY)[3] [ps]	0.22	0.26	0.33	0.22	0.28	0.30	0.17	0.26	0.31
T_2 (KKY)[4] [ps]	5.8	6.7	8.0	6.2	6.5	6.5	3.6	6.5	7.1
T_3 (KKY)[5] [ps]	32	57	92	34	53	82	29	57	89

The first process, attributed to T_1, is related to the librational motion (rotational reorientation) of solvent molecules which is usually a very rapid stochastic process. The second term (T_2) characterizes exchange of one water molecule between neighboring shells, while the third term (T_3) describes the time required for a replacement of all solvent molecules in a particular shell (see Fig. 6.5) or, in other words, characterizes the persistence time of a shell. The physical interpretation presented here is in line with earlier work[396] based on a bi-exponential fit in which, however, the latter two processes were characterized by only one time constant.

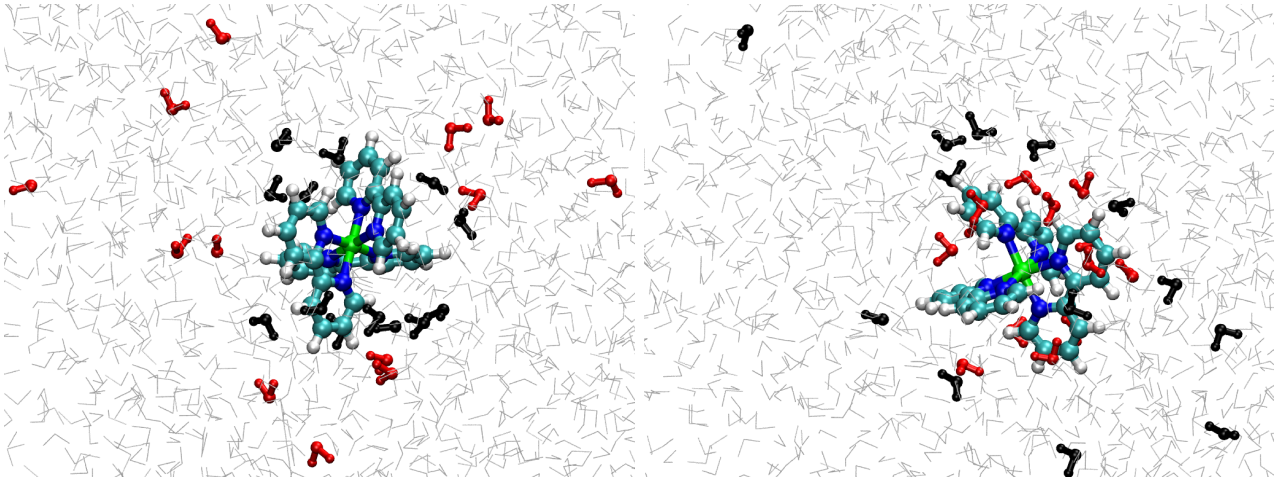

Figure 6.5.: Water exchange dynamics. Water molecules involved in the first solvation shell at $t = 0$ are fully replaced by outer-shell water molecules (black) by $t = 34$ ps. In other words - complete exchange of the first solvation shell occurs within ≈ 30 ps.

The shortest time T_1 is on the sub-picosecond time scale (≈ 0.2 ps) which is similar for both equilibrium simulations and corresponds to time scales found in previous simulations[397]. For the first solvation shell the T_2 time for Ru(III)^{eq} (6.2 ps) is slightly longer (by 0.4 ps) than for Ru(II)^{eq}. This change, although small, indicates that a particular water structuring for shell-I persists for longer times around Ru(III). This is consistent with the slowed-down rotational dynamics around Ru(III) compared to Ru(II). For the second and third shell ($r = 9.0$ and 11.6 Å, respectively), T_2 for Ru(III)^{eq} is 0.2 and 1.5 ps shorter than the corresponding values for Ru(II)^{eq} (see Table 6.3). As the third component, on the several 10 ps time scale, is related to a partial or complete replacement of entire water shells (see below), the corresponding time constant T_3 should depend sensitively on the number of solvent molecules in the shell. Indeed, for both equilibrium simulations T_3 gradually increases with shell size and therefore the number of water molecules in the shell. Similar to T_2, the value of T_3 for shell-I is slightly smaller (3 ps) for Ru(II)^{eq}, while for shells II and III the values are close to those for Ru(III)^{eq}. Fig. 6.5 illustrates the complete exchange of the first solvation shell during an MD simulation. At $t = 0$ the water molecules within shell-I are represented in red whereas at $t = 34$ ps the shell-I waters are black. Correspondingly, the shell-I water molecules from the $t = 0$ snapshot have exchanged and migrated into shells beyond the first shell. This supports the interpretation of T_3 as the time scale on which entire water shells exchange.

The present results for the Ru(II)^{eq} complex (radial distribution function, running coordination numbers, water residence times) compare favorably with previous QM/MM and classical simulations despite the very different theoretical approaches employed[372]. Direct comparison of water residence times for the first solvation shell around the Ru(II) complex with previous work is limited as different analysis procedures were employed. However, it is worthwhile to mention that if a bi-exponential fit is assumed instead of equation 6.3 for the exchange dynamics, a relaxation time of $T_2 = 12.2$ ps is found which compares favorably with 12.4 ps found previously[372]. An advantage of the procedure employed in the present work is that it is parameter-free and does not require the calibration of a parameter t^* that accounts for water molecules which temporarily leave the water shell and re-enter rapidly[372].

6.4.2. Non-equilibrium Simulations

As mentioned in the Methods section 6.3, photo-excitation was induced by instantaneously changing the force field parameters from Ru(II) to Ru(III). Such an approach is not aiming at reproducing the full life cycle of the ruthenium complex[375,378,398] (see Fig. 6.1) but rather focuses on the relaxation of

the dominant ^{3}MLCT state.

Structural Reorganization of the Solvent after Photoexcitation: To describe structural changes in the solvent after photoexcitation of $[Ru(bpy)_3]^{2+}$, the radial distribution function $g_O(r)$ for the water around the Ru-atom was analyzed. The overall shape and features of $g_O(r)$ reflect the results from the Ru(III)^{eq} simulations. Similarly to Ru(III)^{eq}, for non-equilibrium Ru(III)^{exc} simulations the first, second and the third solvent shells contain an approximate number of 15, 81 and 197 water molecules, respectively. These values correspond to $N_O(r)$ determined for the three local minima of $g_O(r)$ at r_s = 6.4, 9.0 and 11.6 Å away from the Ru-atom (see Fig. 6.4). As one can see there, overall changes in the shape of $g_O(r)$ are rather small and they do not involve shifts in the position of the main peaks. The most pronounced differences in the radial distribution functions for Ru(III)^{exc} and Ru(II)^{eq} are found within the first shell around the Ru atom (see left panel of Fig. 6.4). Since the differences between RDF profiles for Ru(III)^{exc} and Ru(III)^{eq} are very small - because they are dominated by the equilibrium part of the Ru(III)^{exc} simulation - it is expected that water reorganization is rapid after non-equilibrium preparation of the system. For additional insight into the time scale for geometrical relaxation we computed radial distribution functions for short windows (160 ps) centered at 80, 240, 880, and 1520 fs after excitation (see Fig. 6.6). For the inner-shell maximum at $\approx$ 6 Å relaxation proceeds on the sub-picosecond time scale. After 80 and 240 fs the $g_O(r)$ still deviates from the equilibrium Ru(III)^{eq} distribution whereas by 880 fs the solvent shell has mostly relaxed. The outer-shell dynamics proceeds further on the picosecond time scale but deviations from the thermodynamic equilibrium at distances $r \geq 8$ Å are dominated by the limited amount of averaging.

The geometrical relaxation of the water shell after photoexcitation has been also considered recently by theory[399] and experiment[399,400]. QM/MM simulations on $I^-/I^0(H_2O)_n$ complexes report reorganization times of 3 to 4 ps[399], while XAS experiments[399,400] reported changes in the shell structure after 50 ps. The time resolution of the experiment was, however, not able to give precise answer on the time scale of the reorganization process. Overall, the time scale of the process obtained of the much more computationally demanding QM/MM simulations on solvated halides compare favorably with the ones reported in the present work.

Water rotational reorientation and residence times: Water rotational reorientation times determined

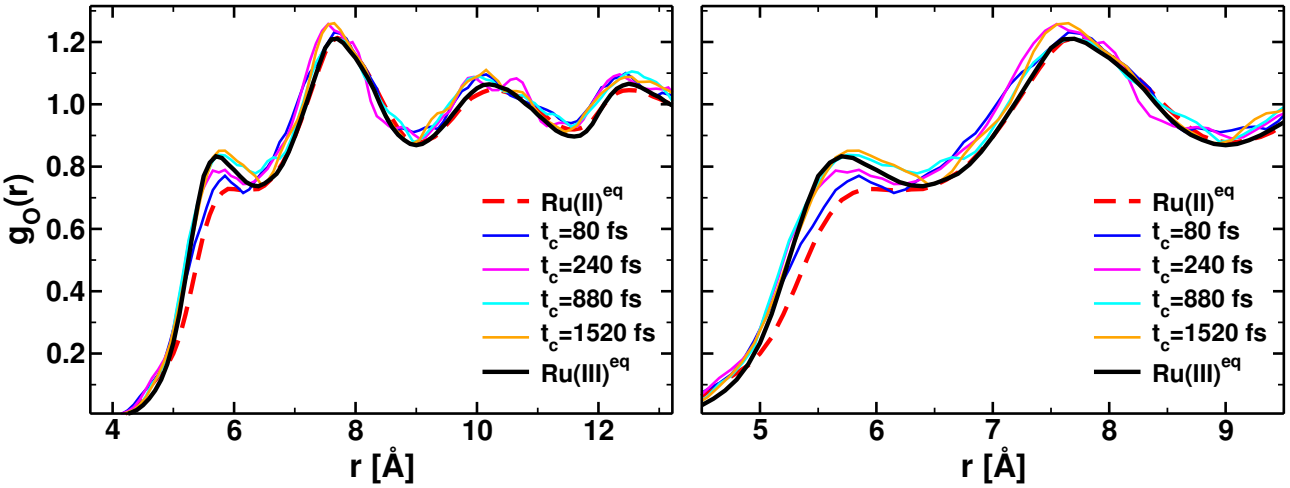

Figure 6.6.: Radial distribution functions for Ru-O_{WAT} determined for equilibrium $Ru(II)^{eq}$ (dashed red), and excited (non-equilibrium) $Ru(III)^{exc}$ (solid black) simulations. Additional lines represent profiles calculated for 160 fs window of time centered at 80 (blue), 240 (magenta), 880 (cyan), and 1520 fs (orange) after excitation. See text for further explanation.

from non-equilibrium simulations are reported in Table 6.2. For the first shell $\tau_r = 8.2$ ps from the non-equilibrium simulations, which is close to the originating state ($Ru(II)^{eq}$), but differs from 6.2 ps for $Ru(III)^{eq}$. This suggests that dynamically the system is still predominantly in a $Ru(II)^{eq}$-state, probably through the coupling within the solvent modes. For all three shells, τ_r for $Ru(III)^{exc}$ is closer to $Ru(II)^{eq}$ than to $Ru(III)^{eq}$ simulations which indicates that geometrical characteristics decay on different time scales than the intramolecular dynamics when preparing a non-equilibrium state of the system.

Solvent residence times for water within the first, second and third shell are collected in Table 6.3. For the first shell all three components are noticeably shorter for the non-equilibrium simulations (0.17, 3.6 and 29 ps) than those determined from both equilibrium simulations. This suggests that the excitation from Ru(II) to Ru(III) introduces energy into the system which is rapidly transferred to the solute and leads to increased exchange dynamics close to the metal atom. The most pronounced change is found for the T_2 component, which can be attributed to the "hot" first-shell waters serving as a source of kinetic energy released after non-equilibrium preparation of the Ru-complex. Differences in the residence times between equilibrium and non-equilibrium simulations reduce, however, very rapidly with the size of the shell, and lead to similar values for shells II and III. This finding agrees with results obtained for water rotational reorientation times and with the radial distribution functions and it demonstrates that

the solvent molecules in shell-I contribute most to the dissipation of the energy resulting from excitation.

Energy Transfer to the Solvent: Following non-equilibrium preparation of the system, the energy related to the perturbation at $t = 0$ is deposited entirely into potential energy of the system. Information concerning energy flow during the non-equilibrium $Ru(III)^{exc}$ simulations can be obtained by monitoring the kinetic energy of the water molecules. This provides insight into energy transfer between the solute and the solvent and also energy migration within the solvent.

First, the total kinetic energy per water molecule is considered (Fig. 6.7, panel A). This quantity is defined as the difference between the kinetic energy of all water molecules in the non-equilibrium state ($Ru(III)^{exc}$) and the continued equilibrium $Ru(II)^{eq}$ trajectory averaged over all trajectories.

$$\Delta E_{kin}^{(W)}(t) = \langle E_{kin}^{(W)}(t)(Ru(III)^{exc}) - E_{kin}^{(W)}(t)((Ru(II)^{eq})\rangle \tag{6.5}$$

After excitation the average kinetic energy increases significantly by ≈ 6 kcal/mol for all water molecules within 11.6 Å (shells I through III) away from the Ru atom (0.03 kcal/mol per water). For about 200 fs this value is approximately constant, increasing occasionally to 8 kcal/mol (0.04 kcal/mol per water) and then decaying on a time scale of several ps to a value insignificantly higher than that for $Ru(II)^{eq}$.

Decomposition of the kinetic energy into vibrational (E_V), rotational (E_R), and translational (E_T) contributions (Fig. 6.7, panels B, C, and D, respectively) shows that changes in the respective degrees of freedom occur on different time scales.

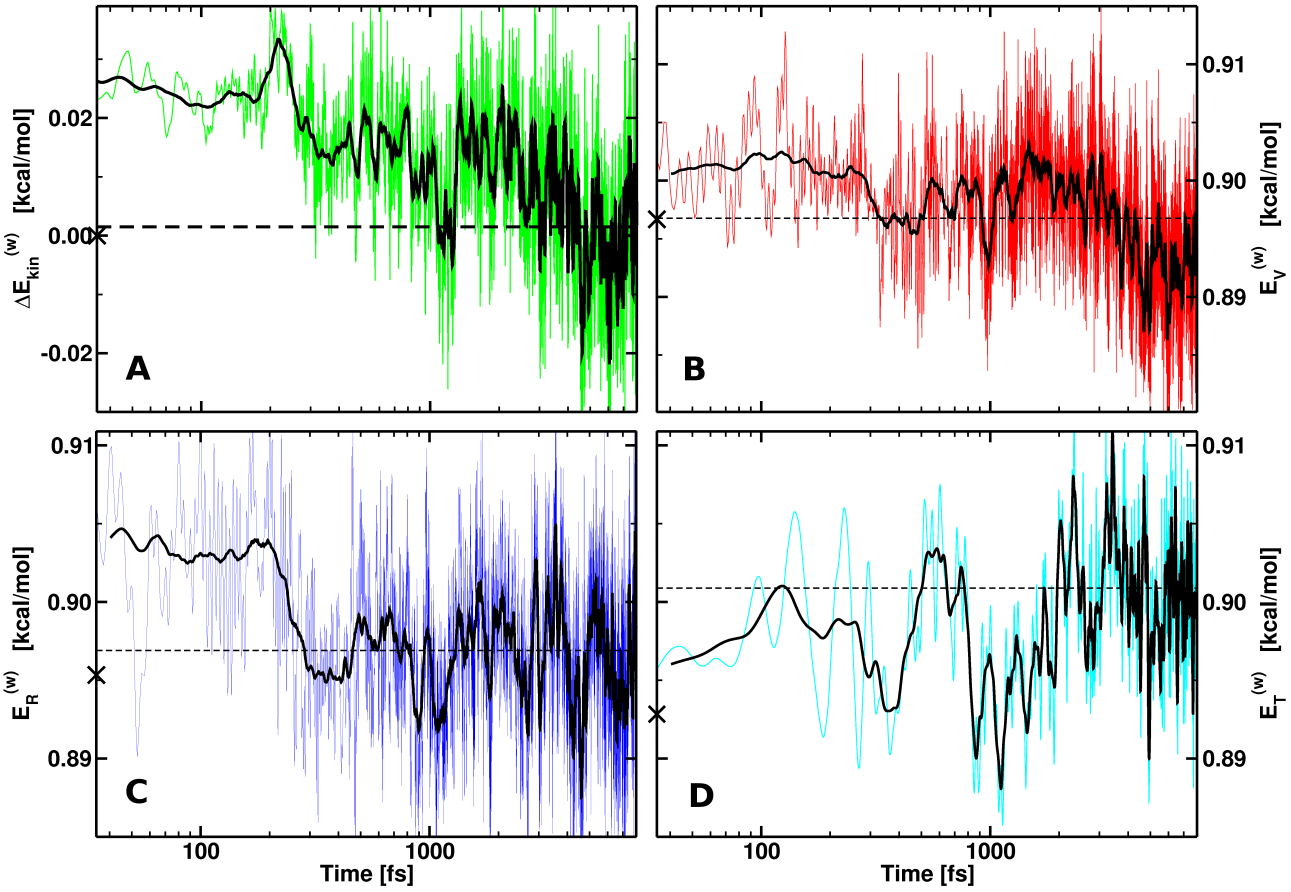

Figure 6.7.: Panel A: Relative kinetic energy per single water molecule ($E_{\mathrm{kin}}^{(\mathrm{W})}$, green) computed as a difference between the kinetic energies of excited (non-equilibrium) Ru(III)$^{\mathrm{exc}}$ and continued equilibrated Ru(II)$^{\mathrm{eq}}$ simulations, averaged over 100 trajectories. Values of kinetic energy for Ru(III)$^{\mathrm{exc}}$ decomposed into vibrational (Panel B, red), rotational (Panel C, blue), and translational (Panel D, magenta) components. Time $t = 0$ fs corresponds to the moment of excitation. Solid black lines show running averages computed over 80 fs; dashed lines correspond to mean values of the respective component, while the initial value is marked by a cross on the vertical axis. All values averaged over all water molecules within 11.6 Å around the Ru-atom.

The energy originating from the perturbation is initially transferred into rotational degrees of freedom on a sub-ps time scale. The change of the rotational component reaches a maximum of ≈ 5 kcal/mol in about 10 fs, after which it decays within 300 fs to the average of the entire simulation (see Fig. 6.8). The magnitude of energy transferred into the vibrational component reaches a value of ≈ 2.3 kcal/mol around 100 fs after excitation. For the next 3 ps the energy of vibrational component oscillates around 1-2 kcal/mol and than starts to drop towards a minimum at around 6 ps after which it climbs back to the average similar to the level before the excitation. The translational component raises by ≈ 2 kcal/mol within 100 fs, but then drops back and oscillates around the initial value for the next 2 ps, after which its raises for the next 3 ps to its average value. The maximum in $\Delta E_{\mathrm{kin}}^{(\mathrm{W})}(t)$ at ≈ 200 fs after excitation originates from the translational component. It is worthwhile to mention that all individual components are thermalized on average after the energy has been redistributed throughout the system.

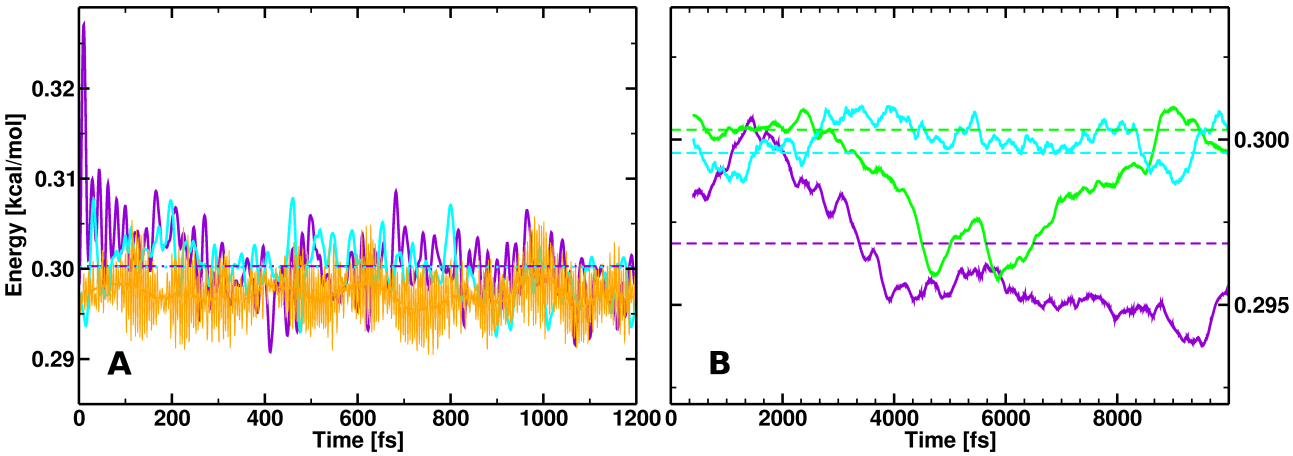

Figure 6.8.: Decomposition of the rotational (Panel A) and vibrational (Panel B) energies for the water molecules around the Ru-atom. The three energy components of E_{R} correspond to rotations around the molecule-fixed $x-$ ($\mathrm{L_x}$, violet), $y-$ ($\mathrm{L_y}$, cyan), and $z-$ ($\mathrm{L_z}$, orange) axes for a water molecule in the $xy-$plane with its C_{2v} axis parallel to the $y-$axis. The running averages for three vibrational components of E_{V} correspond to the symmetric stretching (green), bending (violet), and asymmetric stretching (cyan) modes. Time $t = 0$ fs corresponds to the moment of excitation; dashed lines correspond to mean values of the respective component. All values averaged over all water molecules within 11.6 Å around the Ru-atom.

Further insight can be gained by considering the water-librational modes L_x, L_y and L_z[389] and the internal vibrations separately, as shown in Fig. 6.8, panel A. Initially, energy is transferred into the libration mode L_x, while L_y and L_z remain largely unperturbed. The L_x mode corresponds to rotation around the $x-$axis, defined for a water molecule in the $xy-$plane with its $C_{2\mathrm{v}}$ axis parallel to the

$y-$axis. The energy absorbed in L_x decays to its average on a time scale of 300 fs which corresponds to the rotational component in the previous paragraph. Decomposition of the vibrational term (Fig. 6.8, panel B) shows that during the initial phase (up to 2 ps) the most pronounced increase in magnitude is observed for the water-bending mode while the two stretching modes are largely unaffected. After 2 ps the energy in the symmetric stretching begins to drop along with the bending term up to around 5-6 ps. The major vibrational dynamics appears to be finished by ≈ 2 ps after which the vibrations are largely thermalized again. This agrees with the observation that most of the energy flows into rotational and translational degrees of freedom. Transfer of energy to specific vibrational and rotational modes of the solvent (i.e. water) has been previously observed for the vibrational cooling of CN^- for which energy was absorbed mostly by the water bending mode (v_2) - as found in the present case - and rotation around the z-axis (L_z)[389]. The vibrational frequency of the cyanide anion closely matches the sum of v_2 and L_z which leads to a resonance condition, whereas in the present case the energy is in the electronic degrees of freedom. This explains why no specific vibrational relaxation mechanism appears to be operative and most of the energy transfers into translational and rotational degrees of freedom.

The analysis of the kinetic energy of the Ru-complex shows that after its instantaneous raise following the non-equilibrium perturbation, potential energy is rapidly converted into kinetic energy (through collisions) and efficiently transferred into solvent rotational modes, particularly L_x, after which it is redistributed to the vibrational modes (mostly bending mode). The first process takes place on the sub-picosecond scale and it is followed by energy redistribution over the stretching and translational modes. After about 6 ps kinetic energy of the water remains constant, while energy is redistributed among vibrational and translational degrees of freedom on longer time scales.

Vibrational Spectra: For the process studied here - relaxation of an optically excited state through coupling to the solvent - it is of interest to consider the possibility to use spectroscopic signatures in the IR to interpret the relaxation mechanism. For this purpose the vibrational spectrum of water has been computed. The complete IR-spectrum with stretching (symmetric v_1 and asymmetric v_3) and bending (v_2) peaks together with the librational modes is shown in Fig. 6.9. We note that compared to the condensed-phase spectrum, the KKY model provides quite a realistic framework for the liquid water spectrum. A comparison with recent centroid-path method simulations on an *ab initio* potential energy surface (green line) shows that the current simulations are in good agreement with experiment for the

low-frequency modes whereas for the bending and stretching modes the frequency maxima are well captured. Only the width of the stretching bands is considerably underestimated[401,402]. The computed band maxima at 1619 and 3384 cm^{-1} are lower by 20 to 25 cm^{-1} compared to the experimental values for liquid water[403].

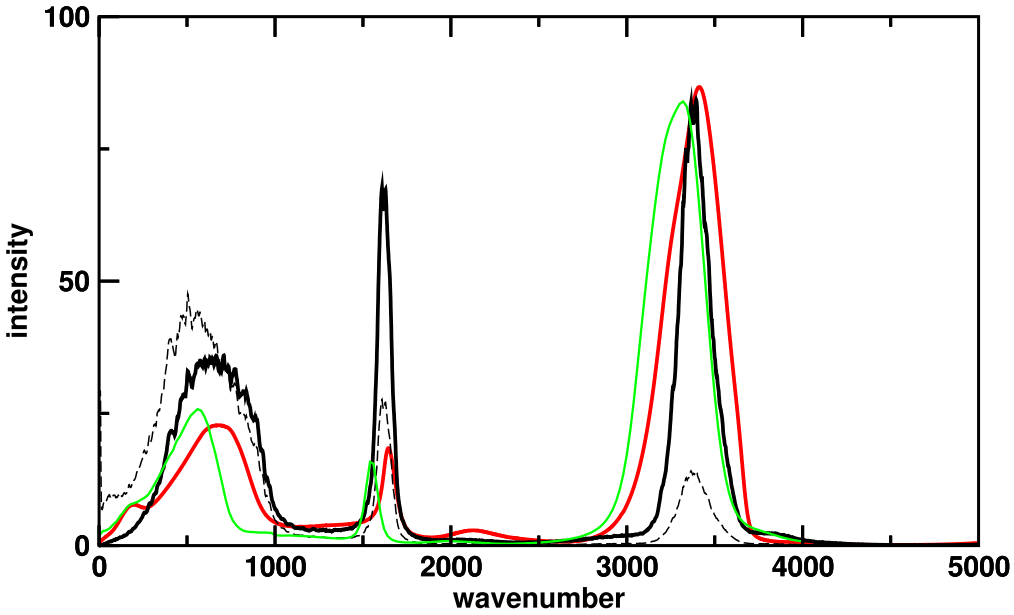

Figure 6.9.: Computed vibrational spectrum (black lines) compared to water spectroscopy in the bulk (red)[402] and from previous computational work (green)[401]. For direct comparison, the maximum of the intensity for the OH-vibration is scaled to approximately the same value. The dashed black line is the Fourier transform of the dipole-dipole autocorrelation function whereas the solid black line is further Boltzmann-weighted and multiplied by the refractive index $n(\omega)$.

From the simulations it is possible to determine vibrational spectra corresponding to the equilibrium part of a non-equilibrium simulation. For this, dipole moment autocorrelation functions were determined over a 30 ps window (out of total 40 ps time) by moving the initial time t_0 in increments of 1 ps. In other words, the interval $[0, 30]$ ps contains most of the non-equilibrium part whereas the interval $[10, 40]$ contains least of it. The obtained spectra were again averaged over 100 independent trajectories. It is found that the v_2 peak (bending vibration) shifts by 2 cm^{-1} over a time delay of 10 ps which may be detectable experimentally. The stretching band is broad and unstructured and will therefore be a less sensitive probe. Nevertheless, we would like to mention that using the information that this peak consists of two bands (corresponding to v_1 and v_3), both fitted band maxima evolve as a function of time after electronic excitation. Such effects may be experimentally amenable by

using more sophisticated band-shape analysis. The times over which vibrational features change after perturbation of the system found in other species[404–407] vary from few (in iron-porphyrin proteins[406]) to few tenths of ps (metalloporphyrines[404,405,407]). Thus, the presented time scales for the temporal evolution of spectroscopic features are well within the range of typical time scales for internal energy transfer into the solvent from experiments.

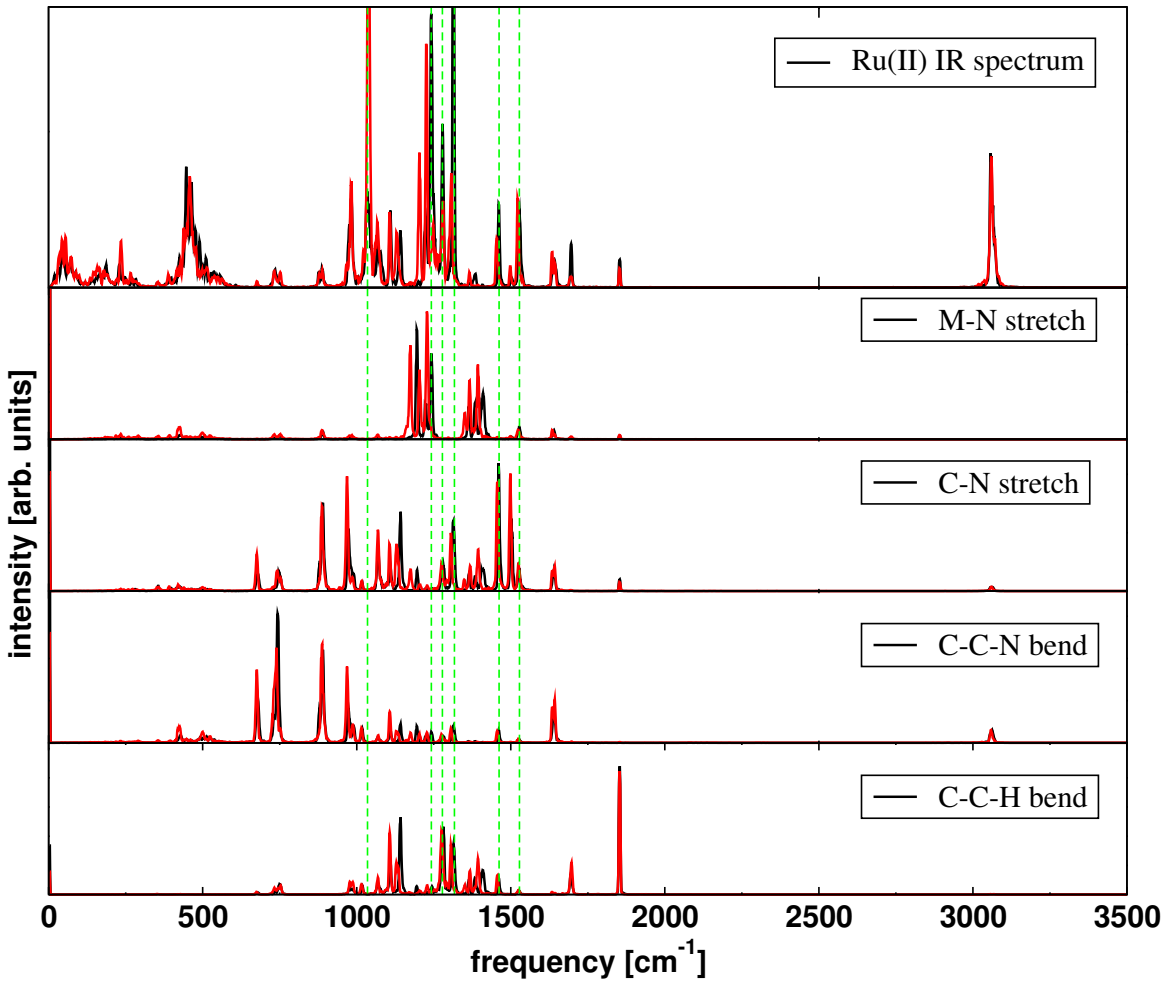

Figure 6.10.: Top panel: Computed vibrational spectrum of $[Ru^{II}(bpy)_3]$. The black curve corresponds to the Ru(II) spectrum with ^{14}N and the red curve is the Ru(II) spectrum for the ^{15}N isotope. Lower panels: Power spectra of the metal-nitrogen, carbon-nitrogen stretch and the CCN and CCH bending vibrations. The color code is identical to that in the upper panel. The power spectra confirm the experimental finding[408] that the modes are highly mixed and assignments to local mode vibrations are difficult. Dashed vertical lines allow to associate signatures in the vibrational spectrum with corresponding peaks in the power spectra.

A vibrational spectrum of the $[Ru^{II}(bpy)_3]$ complex is computed and superimposed with its ^{15}N isotope

spectrum (6.10, upper panel). The $^{14}N/^{15}N$ isotope shift (20 cm^{-1}) permits the identification of the C-N stretching mode at 1365 cm^{-1} for ^{15}N (red curve) and 1385 cm^{-1} for ^{14}N (black curve). The lower panels in Fig. 6.10 represent the power spectrum of the isotope ratio for the C-N, M-N stretching modes and the CCN and CCH bending modes. The observed peak shift of the C-N power spectrum confirms the correct assignment of the C-N stretch.

The characteristic IR-bands of the $[Ru^{II}(bpy)_3]$ complex in water are compared to the experimental spectrum[408] (Fig. 6.11). The computed spectrum is in close agreement with the experimental results and validates the set up of our force field used in the underlying work.

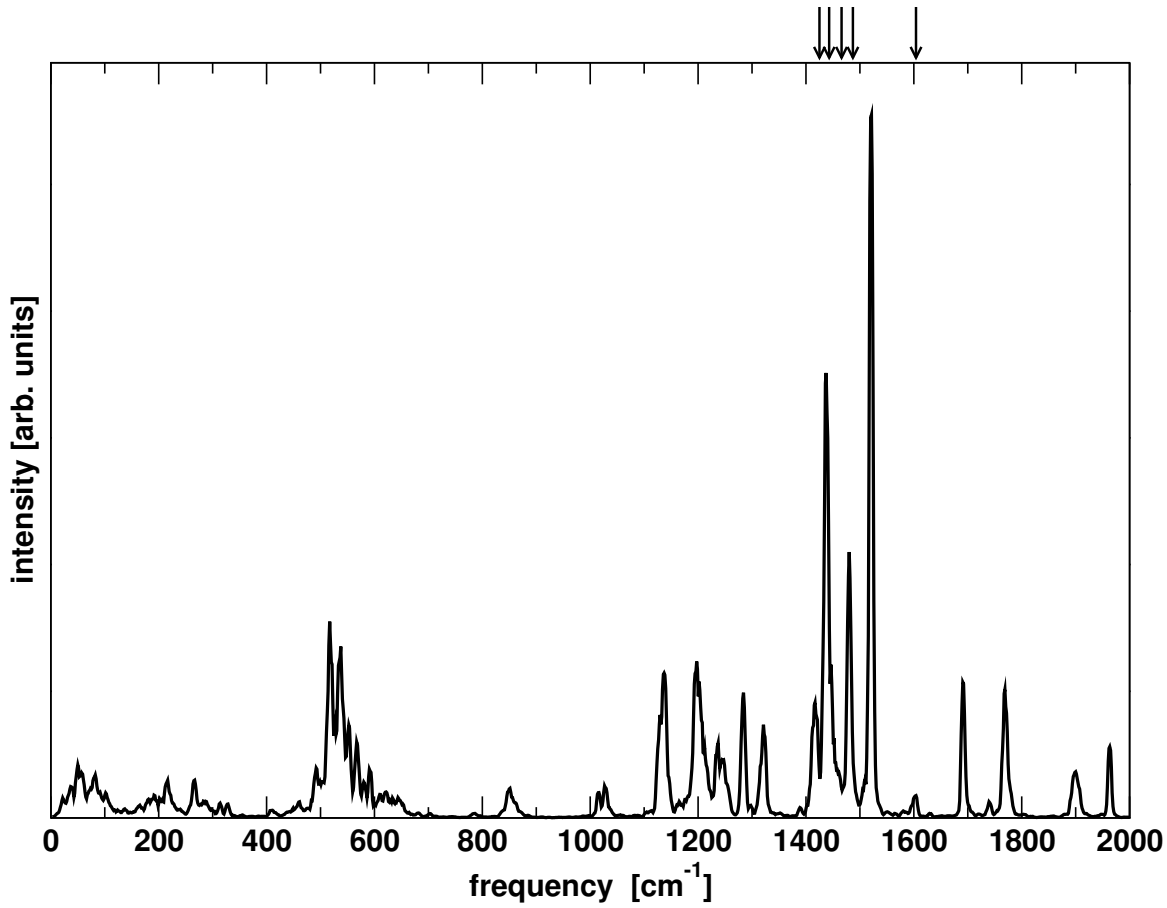

Figure 6.11.: Infrared spectrum of $[Ru^{II}(bpy)_3]$ in water, together with the experimental line positions in the fingerprint region (black arrows), measured in acetonitrile[408]. The computed spectrum was shifted by ≈ 190 cm^{-1} to align the CN-stretching band[408].

6.5. Conclusions

The present work reveals important features of the solvent dynamics on the picosecond time scale following electronic excitation of $[Ru(bpy)_3]^{2+}$. As with previous dynamics studies[274] the VBT force field has been shown to provide robust results compared with computationally more demanding QM/MM simulations[373] while allowing to realistically sample configurational space and averaging over hundreds of independent trajectories. Structural and dynamical characteristics provide a detailed picture of the energy migration pathways in $[Ru(bpy)_3]^{2+}$. The vibrational signatures of the surrounding water suggest that it should be possible to follow electronic relaxation of the TM complex by monitoring the time-dependent solvent response. One promising band to use for this purpose is the ν_2 band of water. Its peak evolves on a picosecond time scale over a few cm^{-1} as a function of probing the system after photoexcitation. The simulations suggest that energy transfer to the solvent is a competing process to IVR as a relaxation mechanism following electronic excitation of $[Ru(bpy)_3]^{2+}$ in solution. The time scales over which the electronic excitation on the complex is converted into solvent modes correspond to experimentally observed time scale of the initial phase of photo-decay[1,2]. Force fields such as VBT in conjunction with atomistic simulations are expected to contribute to our ability in characterizing the dynamics in solvated species from experiments such as time resolved liquidography (TRXL)[367] for which simulation-data is required to analyze the experimental data.

Part III.

Conclusion

7. General Conclusion and Outlook

The high potential of QM and MM methods was used by applying them for transition metal complexes, where the investigation and the understanding of computed data can pave the way for new experimental approaches. In the present thesis, we reported the extensive use of empirical force fields and DFT methods towards the exploration of metal-catalyzed reactions. The value of DFT-derived data is well-known as they can compute very accurate quantities compared to experimental findings. However, the investigation on an atomistic level remained largely unexplored and is therefore focused in this work. Four relevant and up-to-date studies were reported:

A computational study of TM-catalyzed reactions required to characterize complex geometries and to relate them to their reactivity. Together with the possibility to carry out simulations in explicit solvent, this needed to be captured by an adequate force field. As no suitable method existed for this purpose, we developed a new empricial force field to fulfill both requirments[11]. Therefore, a parametrization of the VALBOND TRANS force field was carried out to refine non-bonded parameters for different test sets of octahedral Ir(III) compounds. The successful refinement provided a set of parameters that can correctly identify the energy-lowest diasteromer in 85 % of the evaluated 116 complexes. For neutral complexes (92 complexes), all diastereomers were ranked correctly. At the same time, a high accuracy (1.7 kcal/mol) was obtained by comparing the three energy-lowest diastereomers of all complexes to QM data, while the transferability of the corresponding parameters to a range of chemically related compounds, was exhibited. By fitting all diastereomers of a single complex even higher accuracies (1 kcal/mol) were obtained. A further refinement of bonded parameters with a subsequent comparison to QM/MD data confirmed that we have a reliable and robust force field which can perform realistic MD simulations. The applied fitting procedures are not limited to Ir-complexes, they rather provide a general approach to develop suitable FFs for other metal-containing compounds. The availability of such force fields (specialized for several metals) is a first step towards the screening

of compound-libraries to investigate their properties.

A second study was addressed to the reaction mechanism of the artificial oxidation of water to dioxygen mediated by half-sandwich iridium complexes. The combination of the CHARMM force field with the multi-state adiabatic reactive molecular dynamic (MS-ARMD) approach developed in our group provided a useful tool to monitor chemical reactions. This combined approach opened a new area for previously investigated reaction mechanisms. The characterization of their transition states required an accurate fitting of several potential energy surfaces by adjusting bonded and non-bonded parameters with a simplex algorithm. A subsequent merging of the single fitted FFs resulted in a global surface that captured the QM-minimum energy curve along the intrinsic reaction coordinate. MS-ARMD single-point calculations along the QM-IRC path elucidated the essential oxygen-oxygen bond formation at an atomistic level. This established the basis to run MD simulations to determie realistic barrier heights and rate constants for the used catalyst. In a further step, a screening of related iridium complexes can be carried out to evaluate the potency of new catalysts. A higher accuracy may be achieved by combining the VALBOND TRANS FF with the MS-ARMD code to consider important trans effects.

The third investigation focused on a ruthenium-tris-(2,2'-bipyridine) complex which was recently found to be highly effective for solar-energy harvesting. The structural dynamics of solvated $[Ru^{II}(bpy)_3]^{2+}$ was investigated after photo-excitation [29] to explore the redistribution of excess energy to the surrounding solvent. The VALBOND TRANS force field was used to mimic the electronic excitation by switching between two force fields with a different charge parametrization. The time-dependent solvent response showed a relaxation towards the equilibrium state on a sub-picosecond time scale. An investigation of the different degrees of freedom (DoF) also provided a time range in which the energy transfer to the solvent appeared. It was revealed that the changes in DoFs occured on different time scales and most of the energy flows in rotational and translational DoFs. The analysis of the kinetic energy of the Ru-complex showed that after its instantaneous raise following the non-equilibrium perturbation, potential energy is rapidly converted into kinetic energy (through collisions) and efficiently transferred into solvent modes. The relaxation process was also analyzed by spectroscopic IR-signatures where a peak shift for the bending vibration of the water was found which may be detectable experimentally. The obtained results, using the VALBOND TRANS force field, are comparable with more expensive

QM/MM methods but enable to average over hundreds of independent trajectories. Our procedure provides the possibility to follow electronic excitation by monitoring the time-dependent solvent response and allows to study various other transition metal containing compounds. A subsequent investigation of the related $[Fe^{II}(bpy)_3]^{2+}$ is in preparation.

The thesis revealed important aspects of TM-based applications and successfully established new specialized force fields and the use of underlying methods. A validation of those methods and their results provide general approaches to extend the work in present and related areas. It established the use of empirical force fields in different fields: the characterization of complex geometries including their reactivity potential, entire reaction pathways for TM-catalyzed reactions as well as the process of photo-excited metal complexes. However, further work is desirable to broaden the field of applications and to improve the methods to provide a user-friendly implementation.

References

Bibliography

[1] A. C. Bhasikuttan, M. Suzuki, S. Nakashima and T. Okada, *J. Am. Chem. Soc.*, 2002, **124**, 8398.

[2] N. H. Damrauer, G. Cerullo, A. Yeh, T. R. Boussie, C. V. Shank and J. K. McCusker, *Science*, 1997, **275**, 54.

[3] A. Warshel and S. T. Russell, *Quart. Rev. Biophys.*, 1984, **17**, 283.

[4] S. T. Russell and A. Warshel, *J. Mol. Bio.*, 1985, **185**, 389.

[5] A. Brauman and C. A. Coulson, *Supplementary Tables of Molecular Orbital Calculations*, Pergamon Press, Oxford, 1956.

[6] K. B. Lipkowitz and D. B. Boyd, *Reviwes in Computational Chemistry*, VCH, New York, 1996.

[7] K. Rasmussen, *Potential Energy Functions in Conformational Analysis*, Springer, Berlin, 1985.

[8] R. J. Deeth, *Inorg. Chem.*, 2008, **47**, 6711.

[9] P. Comba and T. Gyr, *Eur. J. of Inorg. Chem.*, 1999, **10**, 1787.

[10] P. Comba, T. W. Hambley and B. Martin, *Molecular Modeling of Inorganic Compounds*, Wiley-VCH, Weinheim, 2009.

[11] F. D. Hofmann, M. Devereux, A. Pfaltz and M. Meuwly, *J. Comp. Chem.*, 2014, **35**, 18.

[12] E. Negishi, *J. Organomet. Chem.*, 2002, **653**, 34.

[13] G. J. Sunley and D. Watson, *Catalysis Today*, 2000, **58**, 293.

[14] R. Noyori, *Angew. Chem. Int. Ed.*, 2002, **41**, 2008.

[15] R. F. Heck and J. P. Nolley, *J. Org. Chem.*, 1972, **37**, 2320.

[16] R. H. Grubbs, *Handbook of Metathesis*, Wiley VCH, Germany, 2003.

[17] D. Rageot and A. Pfaltz, *Helv. Chim. Acta*, 2012, **95**, 2176.

[18] F. Menges and A. Pfaltz, *Adv. Synth. Catal.*, 2002, **344**, 40.

[19] A. D. MacKerell, Jr., D. Bashford, M. Bellott, J. R. L. Dunbrack, J. D. Evanseck, M. J. Field, S. Fischer, J. Gao, H. Guo, S. Ha, D. Joseph-McCarthy, L. Kuchnir, K. Kuczera, F. T. K. Lau, C. Mattos, S. Michnick, T. Ngo, D. T. Nguyen, B. Prodhom, I. W. E. Reiher, B. Roux, M. Schlenkrich, J. C. Smith, R. Stote, J. Straub, M. Watanabe, J. Wiorkiewicz-Kuczera, D. Yin and M. Karplus, *J. Phys. Chem. B*, 1998, **102**, 3586.

[20] N. Gresh, G. A. Cisneros, T. a. Darden and J.-P. Piquemal, *J. Chem. Theo. Comp.*, 2007, **3**, 1960.

[21] R. J. Deeth, A. Anastasi, C. Diedrich and K. Randell, *Coord. Chem. Rev.*, 2009, **253**, 795.

[22] C. R. Landis, T. Cleveland and T. K. Firman, *J. Am. Chem. Soc.*, 1998, **120**, 2641.

[23] C. R. Landis, T. K. Firman, D. M. Root and T. Cleveland, *J. Am. Chem. Soc.*, 1998, **120**, 1842.

[24] X. Tong, T. Nagy, J. Y. Reyes, M. Germann, M. Meuwly and S. Willitsch, *Chem. Phys. Lett.*, 2012, **547**, 1.

[25] L. Pauling, *The nature of the chemical bond*, Cornell University Press, Ithaca, New York, 1960.

[26] M. Law and J. Hutson, *Comput. Phys. Commun.*, 1997, **102**, 252.

[27] M. Meuwly and M. Devereux, *J. Chem. Inf. Model.*, 2010, **50**, 349.

[28] J. D. Blakemore, N. D. Schley, D. Ballcells, J. F. Hull, G. W. Olack, C. D. Incarvito, O. Eisenstein, G. W. Brudvig and R. H. Crabtree, *J. Am. Chem. Soc.*, 2010, **132**, 16017.

[29] J. J. Szymczak, F. D. Hofmann and M. Meuwly, *Phys. Chem. Chem. Phys.*, 2013, **15**, 6268.

[30] C. F. Weise, M. Pischl, A. Pfaltz and C. Schneider, *Chem. Commun.*, 2011, **47**, 3248.

[31] R. Dietiker and P. Chen, *Angew. Chem. Int. Ed.*, 2004, **43**, 5513.

[32] P. Brandt, C. Hedberg and P. G. Andersson, *Chem. Eur. J.*, 2003, **9**, 339.

[33] Y. Fan, X. Cui, K. Burgess and M. B. Hall, *J. Am. Chem. Soc.*, 2004, **126**, 16688.

[34] K. H. Hopmann and A. Bayer, *Organometallics*, 2011, **30**, 2483.

[35] S. J. Roseblade and A. Pfaltz, *C. R. Chimie*, 2007, **10**, 178.

[36] F. Jensen, *Introduction to Computational Chemistry*, Wiley, United Kingdom, 2006.

[37] J. Goodman, *Chemical Applications of Molecular Modelling*, Royal Society of Chemistry, Cambridge, 1998.

[38] K. Gundertofte, T. Liljefors, P.-O. Norrby and I. Pettersson, *J. Comp. Chem.*, 1996, **17**, 429.

[39] T. A. Halgren, *J. Comp. Chem.*, 1996, **17**, 490.

[40] B. R. Brooks, R. E. Bruccoleri, B. D. Olafson, D. J. States, S. Swaminathan and M. Karplus, *J. Comp. Chem.*, 1983, **4**, 187.

[41] W. D. Cornell, P. Cieplak, C. I. Bayly, I. R. Gould, K. M. Merz Jr., D. M. Ferguson, D. C. Spellmeyer, T. Fox, J. W. Caldwell and P. A. Kollman, *J. Am. Chem. Soc.*, 1995, **117**, 5179.

[42] J. R. Maple, M. J. Hwang, T. P. Stockfisch, U. Dinur, M. Waldman, C. S. Ewig and A. T. Hagler, *J. Comp. Chem.*, 1994, **15**, 162.

[43] F. Mohamadi, N. G. J. Richards, W. C. Guida, R. Liskamp, M. Lipton, C. Caulfield, G. Chang, T. Hendrickson and W. C. Still, *J. Comp. Chem.*, 1990, **11**, 440.

[44] A. K. Rappe and W. A. Goddard, *J. Chem. Phys.*, 1991, **95**, 3358.

[45] E. Sigfridsson and U. Ryde, *J. Comp. Chem.*, 1998, **19**, 377.

[46] P.-O. Norrby and P. Brandt, *Coord. Chem. Rev.*, 2001, **212**, 79.

[47] P.-O. Norrby, *Organometallics*, 1999, **18**, 4574.

[48] A. D. MacKerell, Jr., D. Bashford, M. Bellott, R. L. Dunbrack, Jr., J. D. Evanseck, M. J. Field, S. Fischer, J. Gao, H. Guo, S. Ha, D. J. McCarthy, L. Kuchnir, K. Kuczera, F. T. K. Lau, C. Mattos, S. Michnick, T. Ngo, D. T. Nguyen, B. Prodhom, W. E. Reiher, III, B. Roux, M. Schlenkrich, J. C. Smith, R. Stote, J. E. Straub, M. Watanabe, J. Wiorkiewicz-Kuczera, D. Yin and M. Karplus, *J. Phys. Chem. B*, 1998, **102**, 3586.

[49] N. L. Allinger, *J. Am. Chem. Soc.*, 1977, **99**, 8127.

[50] M. J. Hwang, T. P. Stockfisch and A. T. Hagler, *J. Am. Chem. Soc.*, 1994, **116**, 2515.

[51] P.-O. Norrby, T. Rasmussen, J. Haller, T. Strassner and K. N. Houk, *J. Am. Chem. Soc.*, 1999, **121**, 10186.

[52] S. B. E. J. Fabricius and K. Rasmussen, *Acta Chem. Scand.*, 1994, **48**, 548.

[53] A. D. MacKerell Jr, J. Wiorkiewicz-Kuczera and M. Karplus, *J. Am. Chem. Soc.*, 1995, **117**, 11946.

[54] P. Brandt, B. Norrby, B. Akermark and P.-O. Norrby, *Inorg. Chem.*, 1998, **37**, 4120.

[55] M. J. Dudek and J. W. Ponder, *J. Comp. Chem.*, 1995, **16**, 791.

[56] D. Yin and A. D. MacKerell, Jr., *J. Comp. Chem.*, 1998, **19**, 334.

[57] T. A. Halgren, *J. Am. Chem. Soc.*, 1992, **114**, 7827.

[58] A. Bondi, *J. Chem. Phys.*, 1964, **68**, 441.

[59] D. M. Root, C. R. Landis and T. Cleveland, *J. Chem. Phys.*, 1993, **66**, 27.

[60] T. Cleveland and C. R. Landis, *J. Am. Chem. Soc.*, 1996, **118**, 6020.

[61] T. K. Firman and C. R. Landis, *J. Chem. Phys.*, 2001, **123**, 11728.

[62] L. Pauling, *Proc. Natl. Acad. Sci.*, 1928, **14**, 359.

[63] L. Pauling, *J. Am. Chem. Soc.*, 1931, **53**, 1367.

[64] E. Frankland, *Phil. Trans. Roy. Soc. London*, 1852, **142**, 417.

[65] F. A. Kekule, *Ann. Chem.*, 1857, **104**, 129.

[66] J. H. van't Hoff, *Arch. Neerland. Sci. Exact. Nat.*, 1974, **9**, 445.

[67] A. Werner, *Z. Anorg. Chem.*, 1893, **3**, 267.

[68] G. N. Lewis, *J. Am. Chem. Soc.*, 1916, **38**, 762.

[69] W. Heitler and F. London, *Z. Phys.*, 1927, **44**, 455.

[70] D. Manthey, *Orbital Viewer*, 2004.

[71] R. S. Mulliken, *J. Phys. Chem.*, 1940, **44**, 827.

[72] D. J. Klein and N. Trinajistic, *Valence Bond Theory and Chemical Structure*, Elsevier, Amsterdam, 1990.

[73] M. P. M. G. Evans, *Trans. Faraday Soc.*, 1938, **34**, 11.

[74] G. S. Hammond, *J. Am. Chem. Soc.*, 1955, **77**, 334.

[75] A. Shurki, *Theor. Chem. Acc.*, 2006, **116**, 253.

[76] J. H. van Lenthe and G. G. Barlint-Kurti, *J. Chem. Phys.*, 1987, **78**, 5699.

[77] P. C. Hiberty and S. Shaik, *Theor. Chem. Acc.*, 2002, **108**, 255.

[78] W. J. Hunt, P. J. Hay and W. A. Goddard, *J. Chem. Phys.*, 1972, **57**, 738.

[79] J. Gerratt, D. L. Cooper, P. B. Karadakov and M. Raimondi, *Chem. Soc. Rev.*, 1997, **26**, 87.

[80] T. Ziegler, *Chem. Rev.*, 1991, **91**, 651.

[81] P. J. Stephens, F. J. Devlin and C. S. Ashvar, *Faraday Discuss.*, 1994, **99**, 103.

[82] K. Burke, *The ABC of DFT*, Burke reasearch group, California, 2000.

[83] K. Burke and L. Wagner, *Int. J. Quant. Chem.*, 2013, **113**, 96.

[84] W. Koch and M. C. Holthausen, *A Chemist's Guide to Density Functional Theory*, Wiley-VCH Verlag GmbH, Weinheim, 2001.

[85] M. Born and R. Oppenheimer, *Ann. d. Phys.*, 1927, **84**, 457.

[86] V. Magnasco, *Methods of Molecular Quantum Mechanics*, Wiley, United Kingdom, 2009.

[87] R. G. Parr and W. Yang, *Density functional theory of Atoms and Molecules*, Oxford University Press, Oxford, 1989.

[88] K. I. Ramachandran, G. Deepa and K-Namboori, *Computational Chemistry and Molecular Modeling*, Springer, Berlin, 2008.

[89] P. A. M. Dirac, *Cambridge Philos. Soc.*, 1939, **35**, 416.

[90] T. S. Cheww and E. A. Carter, *J. Chem. Phys.*, 2010, **132**, 074104.

[91] A. Szabo and N. S. Ostlund, *Modern Quantum Chemistry*, Dover, Mineola, New York, 1996.

[92] D. C. Young, *Computational Chemistry: A Practical Guide for Applying Techniques to Real-World Problems*, John Wiley and Sons, New York, 2001.

[93] C. Moller and M. S. Plesset, *Phys. Rev.*, 1934, **46**, 618.

[94] C. J. Cramer, *Essentials of Computational Chemistry*, John Wiley and Sons, Hoboken, 2004.

[95] W. Kohn and L. J. Sham, *Phys. Rev.*, 1965, **140**, A1133.

[96] L. H. Thomas, *Proc. Cambridge Philos. Soc.*, 1927, **23**, 542.

[97] E. Z. Fermi, *Z. Phys.*, 1928, **48**, 73.

[98] P. A. M. Dirac, *Cambridge Philos. Soc.*, 1930, **23**, 542.

[99] E. P. Wigner, *Phys. Rev.*, 1934, **46**, 1002.

[100] E. Teller, *Rev. Mod. Phys.*, 1962, **34**, 627.

[101] J. W. Sheldon, *Phys. Rev.*, 1955, **99**, 1291.

[102] P. Hohenberg and W. Kohn, *Phys. Rev.*, 1964, **136**, B864.

[103] P. E. M. Siegbahn, *Quart. Rev. Biophys.*, 2003, **36**, 91.

[104] M. Levy, *Proc. Natl. Acad. Sci. USA*, 1979, **76**, 6062.

[105] A. D. Becke, *J. Chem. Phys.*, 1993, **98**, 1372.

[106] J. C. Slater, *The Self-Consistent Field for Molecules and Solids*, McGraw- Hill, New York, 1974.

[107] J. C. Slater, *Phys. Rev.*, 1951, **81**, 385.

[108] S. H. Vosko, L. Wilk and M. Nusair, *Can. J. Phys.*, 1980, **58**, 1200.

[109] A. D. Becke, *J. Chem. Phys.*, 1992, **96**, 2155.

[110] J. P. Perdew and Y. Wang, *Phys. Rev. B*, 1986, **33**, 8800.

[111] J. P. Perdew, K. Burke and M. Ernzerhof, *Phys. Rev. Lett.*, 1996, **77**, 3865.

[112] A. D. Becke, *Phys. Rev.*, 1988, **A 38**, 3098.

[113] C. Lee, W. Yang and R. G. Parr, *Phys. Rev.*, 1988, **B 37**, 785.

[114] A. D. Becke, *J. Chem. Phys.*, 1993, **98**, 5648.

[115] K. Kim and K. D. Jordan, *J. Phys. Chem.*, 1994, **98**, 10089.

[116] H. Kruse, L. Goerigh and S. Grimme, *J. Org. Chem.*, 2012, **77**, 10824.

[117] A. Kazaryan and E. J. Baerends, *J. Comp. Chem.*, 2013, **34**, 870.

[118] J. M. Seminario, *Recent Developments and Applications of Modern Denisty Functional Theory*, Elsevier, Amsterdam, 1996.

[119] W. J. Hehre, R. F. Stewart and J. A. Pople, *J. Chem. Phys.*, 1969, **51**, 2657.

[120] A. Hinchliffe, *Molecular Modelling for Beginners*, Wiley and Sons, United Kingdom, 2008.

[121] T. Kato, *Commun. on Pure and Applied Math.*, 1957, **10**, 151.

[122] C. Haettig, W. Klopper and D. P. Tew, *Chem. Rev.*, 2012, **112**, 4.

[123] A. R. Leach, *Molecular Modelling - Principles and Applications*, Prentice Hall, Edinburgh, 2001.

[124] W. J. Hehre, R. Ditchfie and J. A. Pople, *J. Chem. Phys.*, 1972, **56**, 2257.

[125] J. T. H. Dunning and P. J. Hay, *Mod. Theo. Chem.*, 1976, **3**, 1.

[126] J. T. H. Dunning, *J. Chem. Phys.*, 1989, **90**, 1007.

[127] A. Fernandez-Ramos, J. A. Miller, S. J. Klippenstein and D. G. Truhlar, *Chem. Rev.*, 2006, **106**, 4518.

[128] C. Dykstra, *Theory and Applications of Computational Chemistry: The First Forty Years*, Elsevier, Amsterdam, 2005.

[129] H. Eyring, *Chem. Rev.*, 1935, **17**, 65.

[130] K. Jankowski and K. Kowalski, *J. Chem. Phys.*, 1999, **110**, 9345.

[131] S. Hirata, M. Nooijen and R. J. Bartlett, *Chem. Phys. Lett.*, 2000, **326**, 292.

[132] S. A. Kucharski, M. Wloch, M. Musial and R. J. Bartlett, *J. Chem. Phys.*, 2001, **115**, 8263.

[133] C. Peng, P. Y. Ayala, H. B. Schlegel and M. J. Frisch, *J. Comp. Chem.*, 1996, **17**, 49.

[134] M. J. Frisch, G. W. Trucks, H. B. Schlegel, G. E. Scuseria, M. A. Robb, J. R. Cheeseman, J. A. Montgomery, Jr., T. Vreven, K. N. Kudin, J. C. Burant, J. M. Millam, S. E. S. Iyengar, J. Tomasi, V. Barone, B. Mennucci, M. Cossi, G. Scalmani, N. Rega, G. A. Petersson, H. Nakatsuji, M. Hada, M. Ehara, K. Toyota, R. Fukuda, J. Hasegawa, M. Ishida, T. Nakajima, Y. Honda, O. Kitao, H. Nakai, M. Klene, X. Li, J. E. Knox, H. P. Hratchian, J. B. Cross, C. Adamo, J. Jaramillo, R. Gomperts, R. E. Stratmann, O. Yazyev, A. J. Austin, R. Cammi, C. Pomelli, J. W. Ochterski, P. Y. Ayala, K. Morokuma, G. A. Voth, P. Salvador, J. J. Dannenberg, V. G. Zakrzewski, S. Dapprich, A. D. Daniels, M. C. Strain, O. Farkas, D. K. Malick, A. D. Rabuck, K. Raghavachari, J. B. F. resman, J. V. Ortiz, Q. Cui, A. G. Baboul, S. Clifford, J. Cioslowski, B. B. Stefanov, G. Liu, A. Liashenko, P. Piskorz, I. Komaromi, R. L. Martin, D. J. Fox, T. Keith, M. A. A. Laham, C. Y. Peng, A. Nanayakkara, M. Challacombe, P. M. W. Gill, B. Johnson, W. Chen, M. W. Wong, C. Gonzalez and J. A. Pople, *Gaussian 03, Revision C.01*, Gaussian, Inc., Wallingford CT, U.S.A., 2004.

[135] D. M. York and T. S. Lee, *Multi-scale Quantum Models for Biocatalysis*, Springer, New York, 2009.

[136] K. Fukui, *Acc. Chem. Res.*, 1981, **14**, 363.

[137] R. Brückner, *Reaktionsmechanismen*, Spektrum Akademischer Verlag, Heidelberg, 2004.

[138] S. T. Schneebeli, M. L. Hall, R. Breslow and R. Friesner, *J. Am. Chem. Soc.*, 2009, **131**, 3965.

[139] D. L. Bunker, *Meth. Comp. Phys.*, 1971, **10**, 287.

[140] H. B. Schlegel, J. M. Millam, S. S. Lyengar, G. A. Voth and A. D. Daniels, *J. Chem. Phys.*, 2001, **114**, 9758.

[141] H. B. Schlegel, S. S. Lyengar, X. Li, J. M. Millam and G. A. Voth, *J. Chem. Phys.*, 2002, **117**, 8694.

[142] S. S. Lyengar, H. B. Schlegel and G. A. Voth, *J. Phys. Chem. A*, 2003, **107**, 7269.

[143] W. Q. Tian and A. Wang, *J. Chem. Theo. Comp.*, 2005, **1**, 353.

[144] L. Joubert and C. Adamo, *J. Chem. Phys.*, 2005, **123**, 211103.

[145] H. P. Hratchian and H. B. Schlegel, *J. Phys. Chem. A*, 2002, **106**, 165.

[146] A. J. Cohen, P. Mori-Sanchez and W. Yang, *Chem. Rev.*, 2012, **112**, 289.

[147] W. Kohn, *Phys. Rev. Letters*, 1983, **51**, 1596.

[148] M. Levy, *Proc. Natl. Acad. Sci. USA*, 1979, **76**, 6061.

[149] A. J. Cohen, P. Mori-Sanchez and W. Yang, *J. Chem. Phys.*, 2008, **129**, 121104.

[150] B. J. Lynch, P. L. Fast, M. Harris and D. G. Truhlar, *J. Phys. Chem. A*, 2000, **104**, 4811.

[151] Y. Zhao, B. J. Lynch and D. G. Truhlar, *J. Phys. Chem. A*, 2004, **108**, 2715.

[152] Y. Zhao, N. Gonzalez-Garcia and D. G. Truhlar, *J. Phys. Chem. A*, 2005, **109**, 2012.

[153] N. E. Schultz, Y. Zhao and D. G. Truhlar, *J. Phys. Chem. A*, 2005, **109**, 4388.

[154] N. E. Schultz, Y. Zhao and D. G. Truhlar, *J. Phys. Chem. A*, 2005, **109**, 11127.

[155] J. P. Perdew and F. Furche, *J. Chem. Phys.*, 2006, **124**, 044103.

[156] N. E. Schultz, Y. Zhao and D. G. Truhlar, *J. Comp. Chem.*, 2008, **29**, 185.

[157] S. Kristyan and P. Pulay, *Chem. Phys. Lett.*, 1994, **229**, 175.

[158] A. Milet, T. Korona, R. Moszynski and E. Kochanski, *J. Chem. Phys.*, 1999, **111**, 7727.

[159] E. Goll, H. J. Wener and H. Stoll, *Phys. Chem. Chem. Phys.*, 2005, **7**, 3917.

[160] S. N. Steinmann and C. Corminboeuf, *J. Chem. Theo. Comp.*, 2010, **6**, 1990.

[161] S. N. Steinmann and C. Corminboeuf, *J. Chem. Theo. Comp.*, 2011, **7**, 3567.

[162] Y. Zhao and D. Truhlar, *Theor. Chem. Acc.*, 2008, **120**, 215.

[163] O. A. von Lilienfeld, I. Tavernelli, U. Rothlisberger and D. Sebastiani, *Phys. Rev. Lett.*, 2004, **93**, 153004.

[164] Y. K. Zhang and W. T. Yang, *J. Chem. Phys.*, 1998, **109**, 2604.

[165] J. P. Perdew and M. Levy, *Phys. Rev. B*, 1997, **56**, 16021.

[166] R. Merkle, A. Savin and H. Preuss, *J. Chem. Phys.*, 1992, **97**, 9216.

[167] J. P. Perdew and A. Zunger, *Phys. Rev. B*, 1981, **23**, 5048.

[168] P. Mori-Sanchez, A. J. Cohen and W. Yang, *J. Chem. Phys.*, 2006, **125**, 201102.

[169] P. Mori-Sanchez, A. J. Kohen and W. Yang, *Phys. Rev. Lett.*, 2008, **100**, 146401.

[170] J. P. Perdew, R. G. Parr, M. Levy, J. Balduz and L. Jose, *Phys. Rev. Lett.*, 1982, **49**, 1691.

[171] H. Paulsen and A. X. Trautwein, *J. Phys. Chem. Solids*, 2004, **65**, 793.

[172] M. Swart, *J. Chem. Theo. Comp.*, 2008, **4**, 2057.

[173] E. J. Baerends, *Phys. Rev. Lett.*, 2001, **87**, 133004.

[174] P. Mori-Sanchez, A. J. Cohen and W. Yang, *Phys. Rev. Lett.*, 2009, **102**, 066403.

[175] H. Braunschweig, R. D. Dewhurst, K. Hammond, J. Mies, K. Radacki and A. Vargas, *Science*, 2012, **336**, 1420.

[176] G. Onida, L. Reining and A. Rubio, *Rev. Mod. Phys.*, 2002, **74**, 601.

[177] R. J. Bartlett, I. Grabowski, S. Hirata and S. Ivanov, *J. Chem. Phys.*, 2005, **122**, 034104.

[178] P. J. Hay and W. R. Wadt, *J. Chem. Phys.*, 1985, **82**, 270.

[179] J. P. Mathieu, *Ann. Phys*, 1944, **19**, 335.

[180] E. J. Corey and J. R. Bailar, *J. Am. Chem. Soc.*, 1959, **81**, 2620.

[181] D. A. Usher, E. A. Dennis and F. H. Westheimer, *J. Am. Chem. Soc.*, 1965, **87**, 2320.

[182] N. L. Allinger, *Adv. Phys. Org. Chem.*, 1976, **13**, 1.

[183] N. L. Allinger, Y. H. Yuh and J. H. Lii, *J. Am. Chem. Soc.*, 1989, **111**, 8551.

[184] N. L. Allinger, K. Chen and J. H. Lii, *J. Comp. Chem.*, 1996, **17**, 642.

[185] S. J. Weiner, P. A. Kollman, D. A. Case, U. C. Singh, C. Ghio, G. Alagona, S. Profeta Jr and P. Weiner, *J. Am. Chem. Soc.*, 1984, **106**, 765.

[186] W. F. van Gunsteren and H. J. C. Berendsen, *Groningen Molecular Simulation (GROMOS) Library Manual*, BIOMOS b.v., Groningen, 1987.

[187] A. K. Rappe, C. J. Casewit, K. S. Colwell, W. A. Goddard and W. M. Skiff, *J. Am. Chem. Soc.*, 1992, **114**, 10024.

[188] W. L. Joergensen, D. S. Maxwell and J. Tirado-Rives, *J. Am. Chem. Soc.*, 1996, **118**, 11225.

[189] K. Lindorff-Larsen, S. Piana, R. O. Dror and D. E. Shaw, *Science*, 2011, **334**, 517.

[190] M. O. Jensen, V. Jogini, D. W. Brohani, A. E. Leffler, R. O. Dror and D. E. Shaw, *Science*, 2012, **336**, 229.

[191] A. D. MacKerell, Jr., D. Bashford, M. Bellott, J. R. L. Dunbrack, J. D. Evanseck, M. J. Field, S. Fischer, J. Gao, H. Guo, S. Ha, D. Joseph-McCarthy, L. Kuchnir, K. Kuczera, F. T. K. Lau, C. Mattos, S. Michnick, T. Ngo, D. T. Nguyen, B. Prodhom, I. W. E. Reiher, B. Roux, M. Schlenkrich, J. C. Smith, R. Stote, J. Straub, M. Watanabe, J. Wiorkiewicz-Kuczera, D. Yin and M. Karplus, *J. Phys. Chem. B*, 1998, **102**, 3586.

[192] S. E. Feller and A. D. MacKerell Jr, *J. Phys. Chem. B*, 2000, **104**, 7510.

[193] S. E. Feller, K. Gawrisch and A. D. MacKerell Jr, *J. Am. Chem. Soc.*, 2002, **124**, 318.

[194] A. D. MacKerell Jr and N. K. Banavali, *J. Comp. Chem.*, 2000, **21**, 105.

[195] M. Kurtel, J. W. Brady and K. J. Neidoo, *J. Comp. Chem.*, 2002, **23**, 1236.

[196] O. Guvench, S. N. Greene, G. Kamath, R. W. Pastor, J. Brady and A. D. MacKerell Jr, *J. Comp. Chem.*, 2008, **29**, 2543.

[197] E. R. Hatcher, O. Guvench and A. D. MacKerell Jr, *J. Comp. Chem.*, 2009, **5**, 1315.

[198] A. K. Rappe, K. S. Colwell and C. J. Casewit, *J. Inorg. Chem.*, 1993, **32**, 3438.

[199] P. C. Yates and A. K. Marsden, *J. Comp. Chem.*, 1994, **18**, 89.

[200] H. A. Lorentz, *Ann. Phys.*, 1881, **248**, 127.

[201] D. Berthelot, *C. R. Hebd. Acad. Sci.*, 1898, **126**, 1703.

[202] C. M. Baker, P. E. M. Lopez, X. Zhu, B. Roux and A. D. MacKerell Jr, *J. Chem. Theo. Comp.*, 2010, **6**, 1181.

[203] E. P. Wigner, *Phys. Rev.*, 1932, **40**, 749.

[204] J. G. Kirkwood, *Phys. Rev.*, 1933, **44**, 31.

[205] J. G. Kirkwood, *Phys. Rev.*, 1934, **45**, 116.

[206] P. Comba, *Coord. Chem. Rev.*, 1999, **182**, 343.

[207] P. Comba, *Coord. Chem. Rev.*, 1999, **186**, 81.

[208] P. Comba, N. Okon and R. Remenyi, *J. Comp. Chem.*, 1999, **781**, 20.

[209] D. Hancock, *Analyst*, 1997, **122**, R51.

[210] K. Nakamoto, *Infrared and Raman Spectra of Inorganic and Coordination Compounds*, Wiley, New York, 1978.

[211] F. Haeffner, T. Brinck, M. Haeberlein and C. Moberg, *Nature Structural Biology*, 1997, **397**, 39.

[212] T. N. Doman, C. R. Landis and B. Bosnich, *J. Am. Chem. Soc.*, 1992, **114**, 7264.

[213] J. W. Caldwell and P. A. Kollman, *J. Am. Chem. Soc.*, 1995, **117**, 4177.

[214] D. L. Kepert, *Inorganic Stereochemistry*, Springer, Berlin, 1982.

[215] P.-O. Norrby, *J. Am. Chem. Soc.*, 1993, **115**, 4859.

[216] T. N. Doman, T. K. Hollis and B. Bosnich, *J. Am. Chem. Soc.*, 1995, **117**, 1352.

[217] M. H. Schmid, T. R. Ward and M. Meuwly, *J. Chem. Theo. Comp.*, 2013, **9**, 2313.

[218] N. L. Allinger and J. H. Lii, *J. Am. Chem. Soc.*, 1989, **111**, 8576.

[219] N. Karasawa, S. Dasgupta and W. A. Goddard, *J. Chem. Phys.*, 1991, **95**, 2260.

[220] C. Kramer, P. Gedeck and M. Meuwly, *J. Chem. Theo. Comp.*, 1957, **9**, 1499.

[221] T. A. Halgren and W. Damm, *Current Opinion in Structural Biology*, 2001, **11**, 236.

[222] H. Yu and F. van Gunsteren, *Comput. Phys. Commun.*, 2005, **172**, 69.

[223] I. Tubert-Broman, M. Schmid and M. Meuwly, *J. Chem. Theo. Comp.*, 2009, **5**, 530.

[224] A. Vedani and D. Dunitz, *J. Am. Chem. Soc.*, 1985, **107**, 7653.

[225] S. C. Hoops, K. W. Anderson and K. M. Merz, *J. Am. Chem. Soc.*, 1991, **113**, 8260.

[226] N. Gresh, P. Claverie and A. Pullman, *Theor. Chim. Acta*, 1984, **66**, 1.

[227] N. Plattner and M. Meuwly, *Biophys. J.*, 2008, **94**, 2505.

[228] T. Bereau, C. Kramer, F. W. Monnard, E. S. Nogueira, T. R. Ward and M. Meuwly, *J. Phys. Chem. B*, 2013, **117**, 5460.

[229] S. J. Weiner, P. A. Kollman, D. T. Nguyen and A. Case, *J. Comp. Chem.*, 1986, **7**, 230.

[230] A. D. MacKerell, Jr., M. Feig and C. L. Brooks, *J. Comp. Chem.*, 2004, **25**, 1400.

[231] P. Comba and T. W. Hambley, *Molecular Modeling of Inorganic Compounds*, VCH, New York, 1995.

[232] P. V. Bernhardt and P. Comba, *Inorg. Chem.*, 1992, **31**, 2638.

[233] P. Comba, *Coord. Chem. Rev.*, 2003, **238**, 9.

[234] M. Zimmer, *Coord. Chem. Rev.*, 2009, **253**, 817.

[235] B. J. Coe and S. J. Glenwright, *Coord. Chem. Rev.*, 2000, **203**, 5.

[236] M. a. Halcrow, *Chem. Soc. Rev.*, 2013, **42**, 1784.

[237] C. A. Tolman, *Chem. Rev.*, 1977, **77**, 313.

[238] V. S. Allured, C. Kelly and C. R. Landis, *J. Am. Chem. Soc.*, 1991, **113**, 1.

[239] J.-P. Piquemal, B. Williams-Hubbard, N. Fey, R. J. Deeth, N. Gresh and C., *J. Comp. Chem.*, 2003, **24**, 1963.

[240] N. Gresh, *J. Comp. Chem.*, 1995, **16**, 856.

[241] J.-P. Piquemal, N. Gresh and C. Giessner-Prettre, *J. Phys. Chem. A*, 2003, **107**, 10353.

[242] N. Gresh, C. Policar and C. Giessner-Prettre, *J. Phys. Chem. A*, 2002, **106**, 5660.

[243] N. Gresh, J.-P. Piquemal and M. Krauss, *J. Comp. Chem.*, 2005, **26**, 1113.

[244] B. de Courcy, J.-P. Piquemal and N. Gresh, *J. Chem. Theo. Comp.*, 2008, **4**, 1659.

[245] B. de Courcy, J.-P. Piquemal and N. Gresh, *J. Am. Chem. Soc.*, 2010, **132**, 3312.

[246] F. Vigne-Maeder and P. Claverie, *J. Chem. Phys.*, 1988, **88**, 4934.

[247] J. N. Murrell and J. J. C. Teixeira-Dias, *Mol. Phys.*, 1970, **19**, 521.

[248] D. R. Garmer and W. Stevens, *J. Phys. Chem. A*, 1989, **93**, 8263.

[249] J. N. Murrell, M. Randic and D. R. Williams, *Proc. R. Soc. A*, 1966, **284**, 566.

[250] S. Creuzet, J. Langlet and N. Gresh, *J. Chim.-Phys. Phys. Chim. Biol.*, 1991, **88**, 2399.

[251] H. Jahn and E. Teller, *Proc. R. Soc. A*, 1937, **161**, 220.

[252] V. J. Burton, R. J. Deeth, C. M. Kemp and P. J. Gilbert, *J. Am. Chem. Soc.*, 1995, **117**, 8407.

[253] R. J. Deeth, *Coord. Chem. Rev.*, 2001, **212**, 11.

[254] R. J. Deeth, N. Fey and B. Williams-Hubbard, *J. Comp. Chem.*, 2005, **26**, 123.

[255] R. J. Deeth and L. J. A. Hearnshaw, *Dalton Trans.*, 2005, **22**, 3638.

[256] R. J. Deeth, *Inorg. Chem.*, 2007, **46**, 4492.

[257] R. J. Deeth and K. Randell, *Inorg. Chem.*, 2008, **47**, 7377.

[258] C. J. Ballhausen, *Introduction to Ligand Field Theory*, McGraw-Hill, New York, 1962.

[259] D. A. Johnson and P. G. Nelson, *Inorg. Chem.*, 1995, **34**, 5666.

[260] M. Gerloch and R. G. Woolley, *J. Chem. Soc. Dalton Trans*, 1981, 1714.

[261] M. Gerloch and R. G. Woolley, *Proc. Inorg. Chem.*, 1983, **31**, 371.

[262] A. J. Bridgeman and M. Gerloch, *Proc. Inorg. Chem.*, 1997, **45**, 179.

[263] M. A. Hitchman, *Inorg. Chem.*, 1982, **21**, 821.

[264] R. J. Deeth and M. A. Hitchman, *Inorg. Chem.*, 1986, **25**, 1225.

[265] P. Comba and M. Zimmer, *Inorg. Chem.*, 1994, **33**, 5368.

[266] R. J. Deeth and D. L. Foulis, *Phys. Chem. Chem. Phys.*, 2002, **4**, 4292.

[267] R. J. Deeth and N. Fey, *Organometallics*, 2004, **23**, 1042.

[268] I. Tubert-Brohman, *The Perl Journal*, 2004, **8**, 3.

[269] W. A. Goddard and L. B. Harding, *Annu. Rev. Phys. Chem.*, 1978, **29**, 363.

[270] L. Pauling, *Proc. Natl. Acad. Sci.*, 1975, **72**, 4200.

[271] M. J. Frisch, G. W. Trucks, M. Head-Gordon, P. M. Gill, M. W. Wong, J. B. Forseman, B. G. Johnson, H. B. Schlegel, M. A. Robb, E. S. Replogle, R. Gomperts, J. L. Andres, K. Raghavachari, J. S. Binkley, C. Gonalez, R. L. Martin, D. J. Fox, D. J. Defrees, J. Baker, J. J. P. Stewart and J. A. Pople, *Gaussian 92*, Gaussian, Inc., Pittsburgh PA, U.S.A., 1992.

[272] J. Musher, *Angew. Chem. Int. Ed.*, 1969, **8**, 54.

[273] J. Huang and M. Meuwly, *J. Phys. Chem. B*, 2012, **396**, 116.

[274] J. Huang, D. Haussinger, U. Gellrich, W. Seiche, B. Breit and M. Meuwly, *J. Phys. Chem. B*, 2012, **116**, 14406.

[275] A. Vedani, *J. Comp. Chem.*, 1988, **9**, 269.

[276] A. Vedani and D. W. Huhta, *J. Am. Chem. Soc.*, 1990, **112**, 4759.

[277] J. A. Shelnutt, C. J. Medforth, M. D. Berber, K. M. Barkigia and K. M. Smith, *J. Am. Chem. Soc.*, 1991, **113**, 4077.

[278] Mayo, *J. Phys. Chem.*, 1990, **94**, 8897.

[279] K. Farak, F. Muller-Plathe and M. C. Bohm, *Chem. Phys. Chem.*, 2012, **13**, 1127.

[280] E. Iype, M. Huetter, A. P. J. Jansen, S. Nedea and C. C. M. Rindt, *J. Comp. Chem.*, 2013, **34**, 1143.

[281] A. Peyman and H.-D. Beckhaus, *J. Comp. Chem.*, 1992, **13**, 541.

[282] W. L. Hase, S. L. Mondro, R. J. Duchovic and D. M. Hirst, *J. Am. Chem. Soc.*, 1987, **109**, 2916.

[283] T. Nagy, J. Y. Reyes and M. Meuwly, *J. Chem. Theo. Comp.*, 2013, submitted.

[284] J. Danielsson and M. Meuwly, *J. Chem. Theo. Comp.*, 2008, **4**, 1083.

[285] S. Mishra and M. Meuwly, *J. Am. Chem. Soc.*, 2010, **132**, 2968.

[286] S. Lutz and M. Meuwly, *Chem. Phys. Chem.*, 2012, **13**, 305.

[287] W. H. Press, S. A. Teukolsky, W. T. Vetterling and B. P. Flannery, *Numerical Recipes - The Art of Scientific Computing*, Cambridge University Press, New York, 2007.

[288] J. Hunger and G. Huttner, *J. Comp. Chem.*, 1999, **20**, 455.

[289] T. H. Fischer, W. P. Petersen and H. P. Luethi, *J. Comp. Chem.*, 1995, **16**, 923.

[290] P. R. Bevington, *Data Reduction and Error Analysis for the Physical Sciences*, McGraw-Hill, London, 1969.

[291] K. Levenberg, *Quart. Appl. Math.*, 1944, **2**, 164.

[292] D. Marquardt, *SIAM J. Appl. Math.*, 1963, **11**, 431.

[293] M. Law and J. Hutson, *J. Comp. Chem.*, 1997, **102**, 252.

[294] C. Mazet, S. P. Smidt, M. Meuwly and A. Pfaltz, *J. Am. Chem. Soc.*, 2004, **43**, 14176.

[295] S. Bell, B. Wuestenberg, S. Kaiser, F. Menges, T. Netscher and A. Pfaltz, *Science*, 2006, **311**, 642.

[296] D. H. Woodmansee and A. Pfaltz, *Chem. Commun.*, 2011, **47**, 7912.

[297] O. Wiest and W. Yundong, *Computational Organometallic Chemistry*, Springer, Berlin, 2012.

[298] D. Carmona, J. Ferrer, M. Lorenzo, M. Santander, S. Ponz, F. J. Lahoz, J. A. Lopez and A. O. Luis, *Chem. Commun.*, 2002, **8**, 870.

[299] M. S. Driver and J. F. Hartwig, *Organometallics*, 1998, **17**, 1134.

[300] A. L. Bandini and M. Manassero, *Inorg. Chem.*, 1987, **26**, 1351.

[301] K. Levenberg, *Quart. Appl. Math.*, 1944, **2**, 164.

[302] J. P. Perdew, J. A. Chevary, S. H. Vosko, K. A. Jackson, M. R. Pederson, D. J. Singh and C. Fiolhais, *Phys. Rev. B*, 1992, **46**, 6671.

[303] J. P. Perdew, K. Burke and Y. Wang, *Phys. Rev. B*, 1996, **54**, 16533.

[304] S. J. Roseblade and A. Pfaltz, *Acc. Chem. Res.*, 2007, **40**, 1402.

[305] X. H. Cui and K. Burgess, *Chem. Rev.*, 2005, **105**, 3272.

[306] K. Kaellstroem, I. Munslow and P. G. Andersson, *Chem. Eur. J.*, 2006, **12**, 3194.

[307] R. S. Mulliken, *J. Chem. Phys.*, 1955, **23**, 1833.

[308] J. P. Foster and F. Weinhold, *J. Am. Chem. Soc.*, 1980, **102**, 7211.

[309] C. M. Breneman and K. B. Wiberg, *J. Comp. Chem.*, 1990, **11**, 361.

[310] A. E. Reed, L. A. Curtiss and F. Weinhold, *Chem. Rev.*, 1988, **88**, 899.

[311] R. S. Mulliken, *J. Chem. Phys.*, 1955, **23**, 1841.

[312] P. Politzer and R. S. Mulliken, *J. Chem. Phys.*, 1971, **55**, 5135.

[313] J. Baker, *Theor. Chim. Acta*, 1985, **68**, 221.

[314] F. Maartin and H. Zipse, *J. Comp. Chem.*, 2005, **26**, 97.

[315] K. B. Wiberg and P. R. Rablen, *J. Comp. Chem.*, 1993, **14**, 1504.

[316] F. Weinhold and C. R. Landis, *Chem. Ed.*, 2001, **2**, 91.

[317] C. Markert, M. Neuburger, K. Kulicke, M. Meuwly and A. Pfaltz, *Angew. Chem. Int. Ed.*, 2007, **46**, 5892.

[318] D. R. Nutt and M. Meuwly, *Biophys. J.*, 2006, **90**, 1191.

[319] S. Mishra and M. Meuwly, *Biophys. J.*, 2009, **96**, 2105.

[320] G. C. Dismukes, V. V. Klimov, S. V. Baranov, Y. N. Kozlov, J. DasGupta and A. Tyryshkin, *Proc. Natl. Acad. Sci.*, 2001, **98**, 2170.

[321] J. P. McEvoy and G. W. Brudvig, *Chem. Rev.*, 2006, **106**, 4455.

[322] T. J. Meyer, *Acc. Chem. Res.*, 1989, **22**, 163.

[323] J. H. Alstrum-Acevedo, M. K. Brennaman and T. J. Meyer, *Inorg. Chem.*, 2005, **44**, 6802.

[324] L. L. Tinker, N. McDaniel and S. Bernhard, *J. Mater. Chem.*, 2009, **19**, 3328.

[325] M. Yagi, S. Tokita, K. Nagoshi, I. Ogino and M. Kaneko, *J. Chem. Soc. Faraday Trans.*, 1996, **92**, 2457.

[326] M. Yagi, N. Sukegawa and M. Kaneko, *J. Phys. Chem. B*, 2000, **104**, 4111.

[327] J. K. Hurst, J. L. Cape, E. Clark, S. Das and C. Qin, *Inorg. Chem.*, 2008, **47**, 1753.

[328] T. Wada, K. Tsuge and K. Tanaka, *Angew. Chem. Int. Ed.*, 2000, **39**, 1479.

[329] J. Limburg, J. S. Vrettos, L. M. Liabel-Sands, R. Rheingold, H. Crabtree and G. W. Brudvig, *Science*, 1999, **283**, 1524.

[330] J. Limburg, J. S. Vrettos, H. Y. Chen, J. C. dePaula, H. Crabtree and G. W. Brudvig, *J. Am. Chem. Soc.*, 2001, **123**, 423.

[331] W. C. Ellis, N. D. McDaniel, S. Bernhard and T. J. Collins, *J. Am. Chem. Soc.*, 2010, **132**, 10990.

[332] W. M. Kanan and D. G. Nocera, *Science*, 2008, **321**, 1072.

[333] Y. Surendranath, M. Dinca and D. G. Nocera, *J. Am. Chem. Soc.*, 2009, **131**, 2615.

[334] M. Risch, V. Khare, I. Zaharieva, L. Gerenscer, P. Cherney and H. Dau, *J. Am. Chem. Soc.*, 2009, **131**, 6936.

[335] N. D. McDaniel, F. J. Coughlin, L. L. Tinker and S. Bernhard, *J. Am. Chem. Soc.*, 2008, **130**, 210.

[336] A. Savini, G. Bellachioma, G. Ciancaleoni, G. Zuccaccia, D. Zuccaccia and A. Macchioni, *Chem. Commun.*, 2010, **46**, 9218.

[337] J. F. Hull, D. Ballcells, J. D. Blakemore, C. D. Incarvito, O. Eisenstein, G. W. Brudvig and R. H. Crabtree, *J. Am. Chem. Soc.*, 2009, **131**, 8730.

[338] T. P. Brewster, J. D. Blakemore, N. D. Schley, C. D. Incarvito, N. Hazari, G. W. Brudvig and R. Crabtree, *Organometallics*, 2011, **30**, 965.

[339] N. D. Schley, J. D. Blakemore, J. D. Subbaiyan, C. D. Incarvito, F. D'Souza, R. Crabtree and G. W. Brudvig, *J. Am. Chem. Soc.*, 2011, **133**, 10473.

[340] D. G. H. Hetterscheid and J. N. H. Reek, *Chem. Commun.*, 2011, **47**, 2712.

[341] R. Lalrempuia, N. D. McDaniel, H. Mueller-Bunz, S. Bernhard and M. Albrecht, *Angew. Chem. Int. Ed.*, 2010, **49**, 9765.

[342] W. L. Dzik, S. E. Calvo, J. N. H. Reek, M. Lutz, M. A. . Ciriano, C. Tejel, G. H. Hetterscheid and B. de Bruin, *Organometallics*, 2011, **30**, 372.

[343] D. B. Grotjahn, D. B. Brown, J. K. Martin, D. C. Marelius, M.-C. Abadjian, H. N. Tran, G. Kalyuzhny, K. S. Vecchio, Z. G. Specht, S. A. Cortes-Lkamas, V. Miranda-Soto, C. van Niekerk, C. E. Moore and A. L. Rheingold, *J. Am. Chem. Soc.*, 2011, **133**, 19024.

[344] X. Liu and F. Wang, *Coord. Chem. Rev.*, 2012, **256**, 1115.

[345] S. Romain, L. Vigara and A. Llobet, *Acc. Chem. Res.*, 2009, **42**, 1944.

[346] L. M. Raff and D. L. Thompson, *Theory of Chemical Reaction Dynamics*, Ed. M. Baer, Boca Raton, FL, 1985.

[347] W. L. Hase, *Advances in Classical Trajectory Methods*, JAI, Stanford, CT, Standford, 1991.

[348] D. L. Thompson, *Encyclopedia of Computational Chemistry*, Wiley, Chichester, 1998.

[349] P. M. Morse, *Phys. Rev.*, 1929, **34**, 57.

[350] R. S. Mulliken, *J. Chem. Phys.*, 1955, **23**, 2338.

[351] R. S. Mulliken, *J. Chem. Phys.*, 1955, **23**, 2343.

[352] B. Ruscic, D. Feller, D. A. Dixon, K. A. Peterson, L. B. Harding, R. L. Asher and A. F. Wagner, *J. Phys. Chem. A*, 2001, **105**, 1.

[353] G. M. Torrie and J. P. Valleau, *J. Comp. Chem.*, 1977, **23**, 187.

[354] S. Kumar, J. M. Rosenberg, D. Bouzida, R. H. Swendsen and P. A. Kollman, *J. Comp. Chem.*, 1992, **13**, 1011.

[355] B. Roux, *Comput. Phys. Commun.*, 1995, **91**, 275.

[356] V. Balzani, A. Juris, M. Venturi, S. Campagna and S. Serroni, *Chem. Rev.*, 1996, **96**, 759.

[357] A. Savini, G. Bellachioma, G. Ciancaleoni, C. Zuccaccia, D. Zuccaccia and A. Macchioni, *Chem. Commun.*, 2010, **46**, 9218.

[358] L. Kalyanasundaram and M. Gratzel, *Coord. Chem. Rev.*, 1998, **177**, 347.

[359] S. H. Wadman, J. M. Kroon, K. Bakker, R. W. A. Havenith, G. P. M. van Klink and G. van Koten, *Organometallics*, 2010, **29**, 1569.

[360] E. T. Nibbering, H. Fidder and E. Pines, *Annu. Rev. Phys. Chem.*, 2005, **56**, 337.

[361] M. Rini, J. Dreyer, E. T. J. Nibbering and T. Elsaesser, *Chem. Phys. Lett.*, 2003, **374**, 13.

[362] M. Rini, A. Kummrow, J. Dreyer, E. T. J. Nibbering and T. Elsaesser, *Faraday Discuss.*, 2003, **122**, 27.

[363] D. K. Palit, T. Q. Zhang, S. Kumazaki and K. Yoshihara, *J. Phys. Chem. A*, 2003, **107**, 10798.

[364] P. T. Snee, C. K. Payne, K. T. Kotz, H. Yang and C. B. Harris, *J. Am. Chem. Soc.*, 2001, **123**, 2255.

[365] A. Popp, L. Ujj and G. H. Atkinson, *Proc. Natl. Acad. Sci.*, 1996, **93**, 372.

[366] J. Herbst, K. Heyne and R. Diller, *Science*, 2002, **297**, 822.

[367] T. K. Kim, J. H. Lee, M. Wulff, Q. Kong and H. Ihee, *Chem. Phys. Chem.*, 2009, **10**, 1958.

[368] H. Ihee, M. Wulff, J. Kim and S. Adachi, *Int. Rev. Phys. Chem.*, 2010, **29**, 453.

[369] S. Lutz, K. Nienhaus, G. U. Nienhaus and M. Meuwly, *J. Phys. Chem. B*, 2009, **113**, 15334.

[370] K. Nienhaus, S. Lutz, M. Meuwly and G. U. Nienhaus, *Chem. Phys. Chem.*, 2010, **11**, 119.

[371] K. Nienhaus, S. Lutz, M. Meuwly and G. U. Nienhaus, *Chem. Eur. J.*, 2013, **19**, 3558.

[372] M.-E. Moret, I. Tavernelli and U. Rothlisberger, *J. Phys. Chem. B*, 2009, **113**, 7737.

[373] M.-E. Moret, I. Tavernelli, M. Chergui and U. Rothlishberger, *Chem. Eur. J.*, 2010, **16**, 5889.

[374] K. C. Zheng, J. P. Wang, W. L. Peng, X. W. Liu and F. C. Yun, *J. Mol. Struct.*, 2002, **582**, 1.

[375] A. Cannizzo, F. van Mourik, W. Gawelda, G. Zgrablic and M. Chergui, *Angew. Chem. Int. Ed.*, 2006, **45**, 3174.

[376] A. T. Yeh, C. V. Shank and J. K. McCusker, *Science*, 2000, **289**, 935.

[377] M. M. Benfatto, S. D. Longa, K. Hatada, K. Hayakawa, W. Gawelda, C. Bressler and M. Chergui, *J. Phys. Chem. B*, 2006, **110**, 14035.

[378] A. N. Tarnovsky, W. Gawelda, M. Johnson, C. Bressler and M. Chergui, *J. Phys. Chem. B*, 2006, **110**, 26497.

[379] K. D. Demadis, C. M. Hartshorn and T. J. Meyer, *Chem. Rev.*, 2001, **101**, 2655.

[380] A. Juris, V. Balzani, F. Barigelletti, S. Campagna, P. Belser and A. von Zelewsky, *Coord. Chem. Rev.*, 1988, **84**, 85.

[381] I. Tavernelli, B. F. E. Curchod and U. Rothlisberger, *Chem. Phys.*, 2011, **391**, 101.

[382] D. M. Root, C. R. Landis and T. Cleveland, *J. Am. Chem. Soc.*, 1993, **115**, 4201.

[383] K. Vanommeslaeghe, E. Hatcher, S. Achary, S. Kundu, J. Zhong, E. Shim, O. Darian, P. Lopes, I. Vorobyov and J. A. D. MacKerell, *J. Comp. Chem.*, 2010, **31**, 671.

[384] A. E. Reed, R. B. Weinstock and F. Weinhold, *J. Chem. Phys.*, 1985, **83**, 735.

[385] W. L. Jorgensen, J. D. Chandrasekhar, J. D. Madura, R. W. Impey and M. L. Klein, *J. Chem. Phys.*, 1983, **79**, 926.

[386] J.-P. Ryckaert, G. Ciccotti and H. J. C. Berendsen, *J. Chem. Phys.*, 1977, **23**, 327.

[387] M. Yoneya, H. J. C. Berendsen and K. Hirasawa, *Mol. Simul.*, 1994, **13**, 395.

[388] N. Kumagai, K. Kawamura and T. Yokokawa, *Mol. Simul.*, 1994, **12**, 177.

[389] M. W. Lee and M. Meuwly, *J. Phys. Chem. A*, 2011, **115**, 5053.

[390] S. Koneshan, J. C. Rasaiah, R. M. Lynden-Bell and S. H. Lee, *J. Phys. Chem. B*, 1998, **102**, 4193.

[391] E. B. Wilson, J. C. Decius and P. C. Cross, *Molecular Vibrations - The Theory of Infrared and Raman Vibrational Spectra*, McGraw-Hill, New York, 1955.

[392] D. A. McQuarrie, *Statistical Mechanics*, Harper's Chemistry Series, New York, 1976.

[393] M. P. Allen and D. J. Tildesley, *Computer Simulation of Liquids*, Clarendon Press, Oxford, 1987.

[394] D. V. der Spoel, P. J. van Maaren and H. J. C. Berendsen, *J. Chem. Phys.*, 1998, **108**, 10220.

[395] R. Ludwig, *Chem. Phys.*, 1995, **195**, 329.

[396] E. Hawlicka and D. Swiatla-Wojcik, *Phys. Chem. Chem. Phys.*, 2000, **2**, 3175.

[397] D. Laage, G. Stirnemann, F. Sterpone, R. Rey and J. T. Hynes, *Annu. Rev. Phys. Chem.*, 2011, **62**, 395.

[398] W. Gawelda, M. Johnson, F. M. F. de Groot, R. Abela, C. Bressler and M. Chergui, *J. Am. Chem. Soc.*, 2006, **128**, 5001.

[399] V. T. Pham, T. J. Penfold, R. M. van der Veen, F. Lima, A. E. Nahhas, S. L. Johnson, P. Beaud, R. A. C., Bressler, I. Tavernelli, C. J. Milne and M. Chergui, *J. Am. Chem. Soc.*, 2011, **133**, 12740.

[400] C. Bressler and M. Chergui, *Annu. Rev. Phys. Chem.*, 2010, **61**, 263.

[401] F. Paesani, S. S. Xantheas and G. A. Voth, *J. Phys. Chem. B*, 2009, **113**, 13118.

[402] J. E. Bertie and Z. Lan, *Appl. Spectrosc.*, 1996, **50**, 1047.

[403] S. Y. Venyaminov and F. G. Pendergast, *Anal. Biochem.*, 1997, **248**, 234.

[404] Y. Mizutani, Y. Usugi and T. Kitagawa, *J. Chem. Phys.*, 1999, **111**, 8950.

[405] P. O. J. Scherer, A. Seilmeier and W. Kaiser, *J. Chem. Phys.*, 1985, **83**, 3948.

[406] Y. Mizutani and T. Kitagawa, *Science*, 1997, **278**, 443.

[407] U. Sukowski, A. Seilmeier, T. Elsaesser and S. F. Fischer, *J. Chem. Phys.*, 1990, **983**, 4094.

[408] K. M. Omberg, J. R. Schoonover, J. A. Treadway, R. M. Leasure, R. B. Dreyer and T. J. Meyer, *J. Am. Chem. Soc.*, 1997, **119**, 7013.

Part IV.

Appendix

Inversion of the Selectivity for Iridium-Catalyzed Hydrogenation Reactions

1. Abstract

Iridium-phosphinooxazoline have proven to be powerful catalysts for asymmetric hydrogenation reactions. In the literature, a long debate about mechanistic insights is present, and there are still divergent opinions about intermediate states concerning an Ir(I)/(III) or an Ir(III)/(V) mechanism [1–7]. A remarkable experimental work [8] involving a second stereogenic center in the hydrogenation process reported an inversion of the diastereoselectivity caused by a small change on the periphery of the PHOX-aryl substituent. The substrate, an ester functionalized alkene, enabled coordination of the ester oxygen to the metal center leading to different transition states compared to substrates lacking a coordinating group. On a theoretical level, DFT calculations shall explain the observed inversion of the selectivity and provide a general overview about mechanistic details involving metal-coordinating substrates. It is qualitatively demonstrated that a reaction involving Ir(I)/(III) intermediates leads to an inversion of the selectivity and that specific interactions may be responsible for this change. An Ir(III)/(V) mechanism did not confirm such an inversion. In addition, it is presented that in case of coordinating ester groups, the proposed Ir(III)/(V) transition states are comparable in energy to those in the Ir(I)/(III) mechanism but can be more favored by using an inverted order of hydrogen transfer.

2. Introduction

The concept of catalysis is one of the most important milestones in organic chemistry. Moreover, in asymmetric catalysis a chiral catalyst can convert an achiral substrate in an enantiomerically enriched product [9]. The value of chiral (especially enantiomerically pure) compounds became evident

by the large production volume in the pharmaceutical industry, material research companies and others. Especially the asymmetric hydrogenation of olefinic species was a breaktrough[10,11] which was awarded with the Nobel prize in 2001 to W. S. Knowles, R. Noyori and K. B. Sharpless. Asymmetric hydrogenation is one of the most powerful methods to prepare optically active compounds to date[12,13]. High enantioselectivites with low catalyst loadings and mild reaction conditions are attractive features while an access to a wide range of target substances can be provided. A new class of phosphinooxazoline (PHOX)-ligands applied in metal catalyzed hydrogenations have proven to be excellent for a variety of reactions such as enantioselective copolymerization of styrene and carbon monoxide[14], copper-catalyzed Diels-Alder reactions[15], or asymmetric hydrosilylation of imine and carbonyl compounds[16]. A remarkable contribution of PHOX-ligands is reported in several highly-efficient iridium-catalyzed asymmetric hydrogenation reactions with a variety of (un-)functionalized olefins[17–23]. High turnover numbers (TONs) and high enantiomeric excess (*ee*)[24–27] confirmed the success of reactions catalyzed by iridium complexes, which provides an adequate quantity of chiral building blocks. PHOX-ligands allow tailor-made modifications by varying the oxazoline ring, the backbone, or the periphery around the phosphine[20]. However, only little is known about the actual underlying mechanism, and several divergent opinions exist concerning mechanistic details.

The earliest mechanistic study of Ir catalysts goes back to 1977 when Crabtree *et al.*[28] isolated hydride-complexes in non-coordinating solvent dichloromethane (DCM) and stated a positive impact of the solvent on the reaction rate compared to studies with a coordinating solvent such as tetrahydrofuran (THF)[29]. They emphasized that a catalytic system can only be specified by giving a precise description of the reactions parameters (e.g. substrates, pressure, temperature, precursors of the reaction, etc.) and underlined their statement with a study of high reactivities for cationic Ir-mediated catalysts for the hydrogenation of tetraalkyl-substituted C=C bonds[30]. In the following years, the focus lay on hydrogenation reactions in which phosphinooxazoline-ligands guided enantioselective Ir-catalysis with promising results[20]. Inspired by this fundamental study, a cascade of other N,P-ligand investigations followed[24,31–37] highlighted by the discovery of N,P-based asymmetric hydrogenation catalysts which do not require the presence of functional groups next to the C=C bond[38]. In this respect Ir catalysts have a much broaden application range than rhodium and ruthenium catalysts, which require a coordinating group at the olefin[16,39,40].

As catalyst deactivation caused by the formation of inactive hydride-bridged trinuclear complexes was still a prohibitive problem in the beginning, a debate about the ideal reaction conditions was triggered for iridium-PHOX mediated hydrogenations[30]. NMR studies and X-ray analysis confirmed the presence of these inactive species[41]. However, recent results reported that the most success in avoiding the deactivation was achieved by using anhydrous dichloromethane as a solvent and tetrakis[3,5-bis(trifluoromethyl)phenyl]borate (BAr_F) as a counterion[17,18,42]. BAr_F is air stable and quite robust against moisture while its weak coordination to the metal center does not affect the olefin coordination which is the case for other counterions such as $PF_6{}^-$. Based on these facts, it was concluded that the faster the olefin insertion takes place the more the hydrogenation is superior over the deactivation pathway[39]. The counterion can also have an effect on the reactivity of the hydrogenation catalyst[43], e.g. BAr_F showed high turnover numbers (TONs) >5000 h^{-1}[42]. Pressure dependencies and different temperatures seemed to play only a minor role[13] with some exceptions where changes of the reaction environment can reverse the selectivity[44,45]. In our electronic structure calculations, handling the BAr_F counterion was too time consuming and therefore neglected. For the same reason, calculations were only carried out in the gas phase. Obviously, it is known by now how to realize magnificent experimental results in this field of asymmetric hydrogenations but we still lack the fundamental knowledge of mechanistic insights.

2.1. Reactivity and Relative Stabilities

The control of the product stereochemistry by iridium catalysts based on substrate control has been known for some time[46–48]. The reactivity of chiral metal catalysts is dependent on thermodynamic factors which are responsible for the stability of the catalyst-olefin complex[49]. The thermodynamic stability of substrate-dihydride-complexes is influenced by the electronic properties of the metal ion. The more electronegative the metal ion the more stable the complex due to back donation effects. However, the electronegativity of the metal ion can be manipulated by the addititon of electron-donating or withdrawing ligands. In general, the thermodynamic stability (formation enthalpy) has a negative influence on the catalytic activity which may explain why more labile complexes are better catalysts than more stable species[50].

Kinetic factors play a key role in the insertion and dissociation (reductive elimination) step of the

Ir-alkyl intermediate[51]. According to the Curtin-Hammet principle, kinetic factors are predominant, as they influence the product ratio depending on relative Gibbs free energies of the transition states. Halpern reported in an example that in an equilibrium of two reactant states, the thermodynamically unfavored reactant can be converted to the predominant product precursor as it reacts faster due to a lower energy barrier[52]. Our study will focus on the kinetics of the hydrogenation reaction, and therefore on the analysis of the rate limiting step, which is defined by the transition with the highest Gibbs free energy barrier. Concerning hydrogenations with rhodium catalysts, the selective step is reported to be the oxidative addition of the hydrogen[52]. For iridium catalyzed reactions it remains uncertain where the first irreversible step takes place.

The first proof of an olefin dihydride intermediate which occurs during a hydrogenation reaction was provided by NMR spectroscopy[53]. Another experimental and theoretical study of a $[(\text{PHOX})\text{Ir}(\text{H})_2(\text{COD})]^+$ (COD = 1,5-cyclooctadiene) catalyst treated with dihydrogen reported two diastereomeric $[(\text{PHOX})\text{Ir}(\text{H})_2(\text{solvent})_2]^+$ complexes (out of four possible diastereomeric *cis*-dihydride addition products, Fig. 1) where the conformation was investigated by NMR[54].

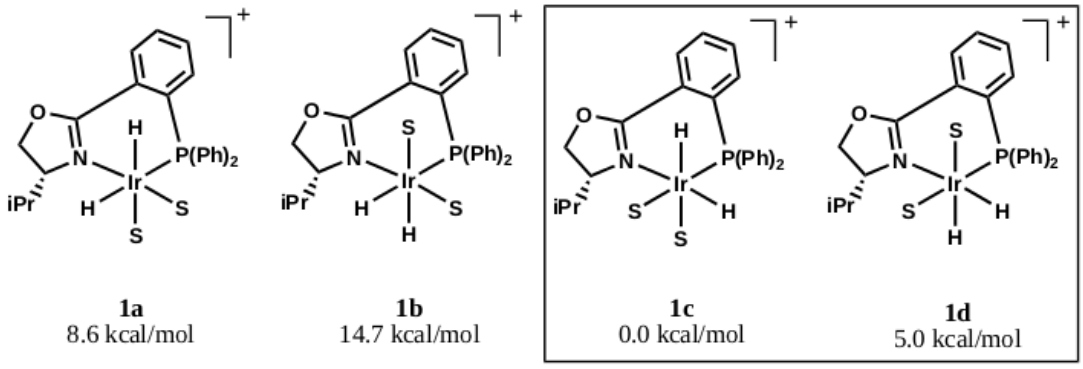

Figure 1.: Four possible isomers $[(\text{PHOX})\text{Ir}(\text{H}_2)\text{S}_2]\text{BAr}_F$ arising from *cis*-addition of molecular hydrogen. The frame indicates the species observed by NMR, the counterions are omitted for clarity. For relative energies, methyl chloride was used to simulate presence of a solvent[54].

Subsequent analysis of relative energies of the possible stereoisomers was done by DFT calculations where strong influencing ligands caused an energy difference up to 14.7 kcal/mol. In the computational study, methyl chloride molecules occupy the vacant positions of the dissociated COD-ligand, showing that the addition of a hydride *trans* to the Ir-N bond and *cis* to the Ir-P bond is clearly the favored complex[54] (Fig. 1). Dominating over the isomers **1a** and **1b** which are not detectable by NMR, **1c** is the preferred isomer which is in line with Crabtree's investigations: These already showed that a

coordinating hydrogen to the metal center is electronically favored if it is *trans* to the N-ligand[55,56]. It can be summarized that electronic effects of the coordinating N and P atoms are essential, as they direct the addition of dihydrogen *trans* to the nitrogen. Steric effects also play a significant role as they decisively influence the stereoselectivity[54].

The understanding of relative stabilities of diastereomers and structural aspects can pave the way to identify relevant mechanistic details, not only concerning the reaction pathway but as well to explore geometrical properties of the initial catalyst-substrate complex. It was demonstrated for allylic substitutions that with PHOX-ligands, an attack of the allylic carbon by a nucleophile preferentially happens *trans* to the phosphorus atom[57,58]. Additional NMR and crystal structure studies[59,60] as well as the DFT-based work of Ploechl *et al.*[61] supported these findings. It was also reported that the soft P atom can be replaced by sulfur without significant reduction of enantioselectivity, suggesting that the stereochemistry is controlled by the oxazoline moiety while the soft ligand is responsible for the reactivity[62]. The analysis of crystal structures give rise to this and to several other important features of the PHOX-ligand. For instance, the inner chelate cycle MNCCCP is non-planar, leading to a non-equivalent conformation of the substituents on the phosphorus, two are oriented equatorial and one axial. Considering the crystal structures, Helmchen suggested that the effect of the equatorially arranged aryl substituents is the dominating interaction for preferences of the *exo* over *endo* conformations in allylic substitutions[63]. He emphasized that a bulky substituent on the oxazoline moiety leads to a stronger bending of MNCCCP chelate ring, pushing the equatorial located P-phenyl group closer to the substrate and causing a destabilization of the *endo* isomer in allylic substitutions[20]. This indicates that analogous structural factors affect asymmetric hydrogenation reactions in a similar way and may explain the inversed stereoselectivity if an *o*-tolyl residue is exchanged by a mesityl substituent[8].

2.2. Coordination Sphere of Ir-PHOX

New substrate classes were investigated with conventional catalysts, leading to moderate results[39,43,64]. Despite, excellent results were recently found for N,P-ligands in terms of enantiomeric excess and conversion[24,65], asymmetric hydrogenation reactions are still a field of active research in which we try to explore the limits of reactivity by the help of computational methods.

The modular structure of PHOX-ligands, where the N and P atoms are coordinated on the metal center, enables a large variety of substituents to fine tune the steric and electronic properties of the catalyst. This facilitates the access to plenty ligand-substrate interactions playing a crucial role in the enantiocontrol. Such an effective control was demonstrated for metal-catalyzed allylic alkylations where two different coordinating heteroatoms induce an electronical non-equivalence which causes different reactivities leading to different ratios of enantiomers[20]. An introduced stereocenter in the oxazoline-ring (next to the N atom) allows to remarkably influence the selectivity by varying the *R*- and *S*-configuration and by using small or bulky substituents[66]. A strategy for hydrogenation of substrates with a stereogenic center is also reported where iridium-PHOX catalysts (Fig. 2) control the outcome with excellent diastereoselectivities[8].

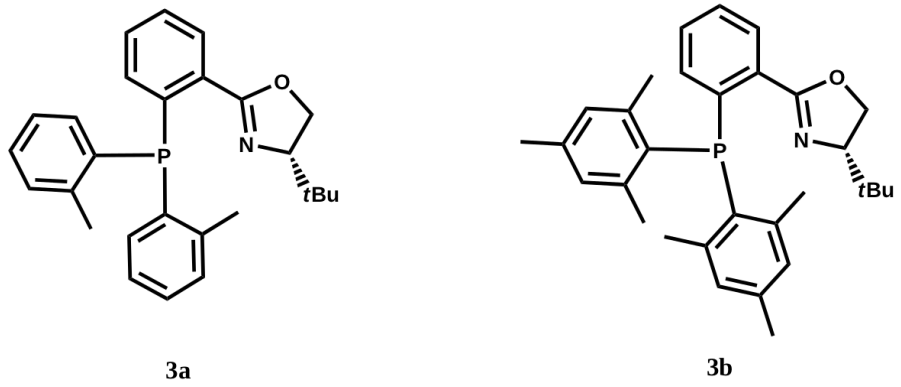

Figure 2.: Iridium-phosphinooxazoline catalyst **3a** with a *o*-tolyl residue and catalyst **3b** with a mesityl residue. Both catalysts have a *S*-configuration on the oxazoline moiety.

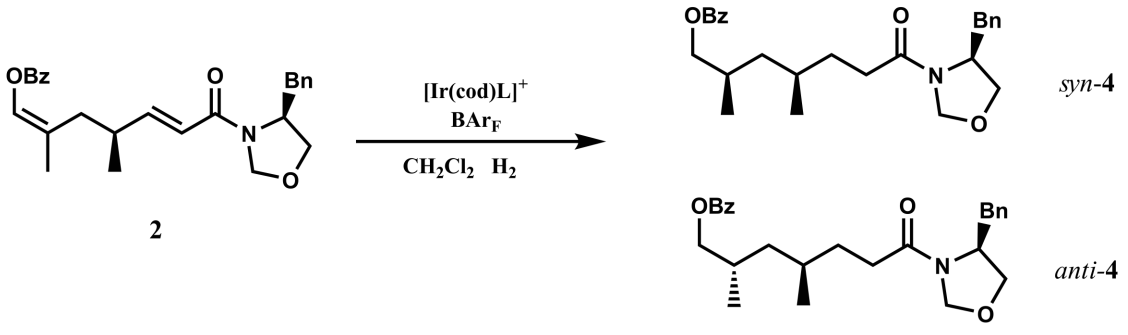

Figure 3.: Reaction conditions: **2** (0.10 mmol), **3** [(PHOX)Ir(cod)L]BAr_F (0.002 mmol), 85 bar H_2, 0.5 ml CH_2Cl_2, 18 h, rt. Determined by chiral HPLC. For assignment of absolute configuration by ESI[8].

As modifications in the PHOX periphery strongly influence the selectivity[32,67], an adequate ligand-

Entry	Ligand	syn/anti	Conversion
1	**3a**	72:28	>99
2	**3b**	4:96	>99
3	*ent*-**3b**	97:3	>99

Table 1.: Reaction conditions: Ligand **3** (0.10 mmol), [Ir(cod)L]BAr_F (0.002 mmol), 85 bar H_2, 0.5 ml CH_2Cl_2, 18 h, rt[8].

substrate combination was found with the chiral PHOX-ligand **3a** bearing a bis(*o*-tolyl)phosphanyl (*o*-tolyl) group[17,27,39], its mesityl-analog **3b**, and an α,β-unsaturated ester compound **2** as a substrate[8].

The hydrogenation of **2** ensured an excellent diastereoselectivity with 96:4 for the benzoate *anti*-**4** (Entry 2 Tab. 1). A favorisation of *syn*-**4** diastereomer was obtained (Entry 3 Tab. 1) with an inverse stereocenter at the oxazoline-ring (*R*-configuration) for the *ent*-**3b** ligand. This was already reported by several other studies[39] and thus expected. Intriguingly, the selectivity was almost completely inverted, 72:28, if **3a** is used instead of **3b** (Entry 1, Tab. 1). As this is of particular interest, mechanistic and structural properties were investigated to identify the underlying reasons that may be responsible for this reversal of enantioselection. Two aryl substituents on the olefin tend to give higher selectivities[13,26,43,45,68], but it is not straightforward to explain why an addition of two methyl groups to each of the two phenyl-rings on the phosphine group of the catalyst causes a reversed selectivity, as the added methyl groups are not directly involved in the reaction. Motivated by this surprising result, electronic structure calculations were set up to study reactivities and reaction barriers of this specific reaction.

2.3. Proposed Hydrogenation Mechanisms

Filling the gap of mechanistic ambiguity brought a diversity of experimental and theoretical studies[1–3,5,6]. The most accepted sequence of a hydrogenation reaction starts with an oxidative addition of the H_2 followed by a coordination of the olefin species. The transfer of a metal coordinated hydride to the olefin is the next - rate limiting - step followed by the reductive elimination to yield the final product[50].

In a computational and kinetic study, Brandt, Hedberg and Andersson reported several reaction

mechanisms of iridium-PHOX catalyzed hydrogenation where the most favored reaction path involved Ir(III)/(V) species[1,7]. Here, the vacant sites resulting from dissociation of the COD-ligand are occupied by two solvent molecules and two hydrogens, which is consistent with an experimental mechanistic study investigating the oxidative addition of dihydrogen to a Ir(I) species[2]. This oxidative addition of a H_2 to the Ir-COD is rapid at low temperature and known in more detail[2,69,70]. Migratory insertion of the olefin and the coordination of a second H_2 facilitate the Ir(V) species in which the reaction is first-order regarding the H_2 pressure. A first-order rate dependence was also found for the catalyst concentration while a zero-order dependence was found for the alkene concentration. The first hydrogen transfer is suggested to involve the axial hydride followed by a hydrogen transfer from the side-on coordinated H_2[1]. However, due to small substituents on the C=C bond (ethylene) used in this study, it remains uncertain if the chosen model system is representative for trisubstituted olefins. Less demanding substituents only have minor steric effects, however, the addition of H_2 is supposed to be a highly selective step where steric and electronic effects play an essential role[54]. The phosphanooxazoline was replaced by a less demanding dimethylvinylphosphine and an imine functionality[1] which can be problematic using the approach to determine the steric influence on the paths lowest in energy. In addition, a constraint was used which prohibits the redistribution of coordinated groups[43]. A complementary study using the same mechanistic approach illustrated an explicit selectivity model describing the relation between steric and electronic effects. It was reported that with a series of phosphine thiazole complexes the alteration of the ligand ring size has a high impact and that a change from oxygen to sulphur in the oxazoline residue can be favorable[68].

Burgess and Hall introduced a second independent theoretical study[3] which basically supports the Ir(III)/(V) approach by DFT calculations on the complete ligand and the full substrate (aryl-substituted alkenes). Here, the coordinated olefin of an iridium-dihydride complex is *trans* to carbene forming an alkyl-compound by hydrogenation. The main difference to Brandt's suggested mechanism is that the order of the hydrogen transfer is *vice versa*. Burgess *et al.* suggested that a first H atom of axial side-on located H_2 occurs followed by the axial hydride on the opposite side. Reductive elimination then allows the reduced alkene to dissociate from the metal center[3]. Determined enantioselectivities correspond to experimental data[44,71]. This approach abandons the coordination of solvent molecules, it introduces instead a fast equilibrium of monoligated and η^2-bound hydrogen to the iridium center which also enables a redistribution of coordinated ligands[43]. Calculations based on the Ir(I)/(III) are not included

in their study. A subsequent kinetic study supports the mechanism over the Ir(III)/(V) species but also mentions the existence of the Ir(I)/(III) which should be less rapid and selective[72]. Indeed solvated Ir(I)/(III) species are higher in energy, but the obtained selectivities are also in line with experimental findings[73,74]. It is even supposed that due to the much higher concentration of solvent compared to H_2 pressure the energetics of transition states become very similar for the two mechanistic approaches.

In 2007, Burgess reported on the reversal of face selectivity for esters and allylic alcohol substrates. Moreover, he could reproduce the results by DFT calculations on the basis of Ir(III)/(V) mechanism[4]. However, for this specific reaction an alternative was proposed, where the alkene is *trans* to the nitrogen of the oxazoline-ligand and a hydride is *trans* located to the carbene. Although those *trans* effects are destabilizing, they simultaneusly lower the reaction barrier for the migratory insertion step and facilitate access to one enantiomer. To yield the opposite enantiomer, a different route was suggested which is in line with the originally proposed mechanism where the olefin is *trans* to the carbene[1,3]. However, in both routes, one of the η^2-H_2 hydrogens was transferred first followed by the axially coordinated hydride[4].

Inconsistent results were obtained if computational data were compared to experiments done by para-hydrogen induced polarization (PHIP) ^{1}H NMR[6] and mass spectroscopy[5]. The PHIP study investigated a hydrogenation of [D_8] styrene where a H_2 molecule can only react pair-wise with the corresponding olefin suggesting an Ir(I)/(III) mechanism. However, it cannot be ruled out that a parallel Ir(III)/(V) mechanism occurs at the same time[6]. On top of this study, Chen and Dietiker reported an experimental investigation including the hydrogenation of styrene with [(PHOX)Ir$(H)_2$(COD)]BAr_F analyzed by electrospray ionization tandem mass spectroscopy in the gas phase. It was possible to identify all masses of the species involved in the Ir(I)/(III) reaction pathway[5] and to interpret other observations ruling out an Ir(III)/(V) mechanism. The key observation was that an incorporation of one and two deuteriums but not of three was detected which is required for a mechanism over an Ir(V) species[43]. However, experiments were only carried out in the gas phase which does not rule out a Ir(III)/(V) mechanism in a real solvated system.

It becomes obvious that the dependence on substrates, temperature and hydrogen pressure requires different pathways which determine the corresponding stereochemical outcome. Although computa-

tional data favor an Ir(III)/(V) mechanism whereas experimental investigations report the observation of species pointing to the Ir(I)/(III) pathway, a final conclusion cannot be drawn yet, thus, further investigations have to follow.

2.4. Comparison of the Ir(I)/(III) and the Ir(III)/(V) Mechanisms

Two commonly accepted mechanisms are shown in Fig. 4 and Fig. 5. The Ir(I)/(III) catalytic cycle suggested by Dietiker and Chen[5] is analogous to the hydrogenation mechanism with rhodium[16,52,75] and starts from the precatalyst [Ir(I)(PHOX)(COD)]BAr_F **pre-I**. Oxidative addition of hydrogen and an olefin addition lead to the olefin-dihydride intermediate **I** with a coordinated solvent. Compound **I** undergoes migratory insertion by a transfer of the axial hydrogen to the olefin leading to a coordinated alkyl-hydride **II**. A subsequent transfer of the equatorial hydrogen (reductive elimination) gives Ir(I)-intermediate **III** which releases the final hydrogenated product. A following oxidative addition of H_2 and another alkene addition complete the catalytic cycle. (Fig. 4)[73]. In this reaction process, the resting state is supposed to be **I** and the rate limiting step is proposed as the transfer of the axial hydrogen. However, it remains also possible that the transfer of the equatorial H may be the first hydrogen transfer.

An alternative cycle (Fig. 5), especially supported by computational studies[1,3,4,76], involves Ir(III)/(V) species. Instead of a coordinating solvent molecule, the olefin-dihydride intermediate **I** has here a dihydrogen molecule coordinated to the iridium in a η^2-fashion. The following migratory insertion is most likely accompanied by a splitting of the η^2-H_2 resulting in a Ir(V) species **II**. After both hydrogens have been transferred to give **III** and free catalyst **IV**, subsequent dihydrogen addition leading to **V** and new substrate coordination close the catalytic cycle[73]. In the mechanistic proposal of Burgess *et al.*, a first H-atom of the axial side-on coordinated H_2 is transferred, followed by the axial hydride of the opposite side[3] (mechanism not shown). However, the mechanistic proposal of Brandt suggests a transfer of the axial hydride followed by an H-atom of the axial side-on H_2 molecule (coordinated on the opposite side)[1] (Fig. 5).

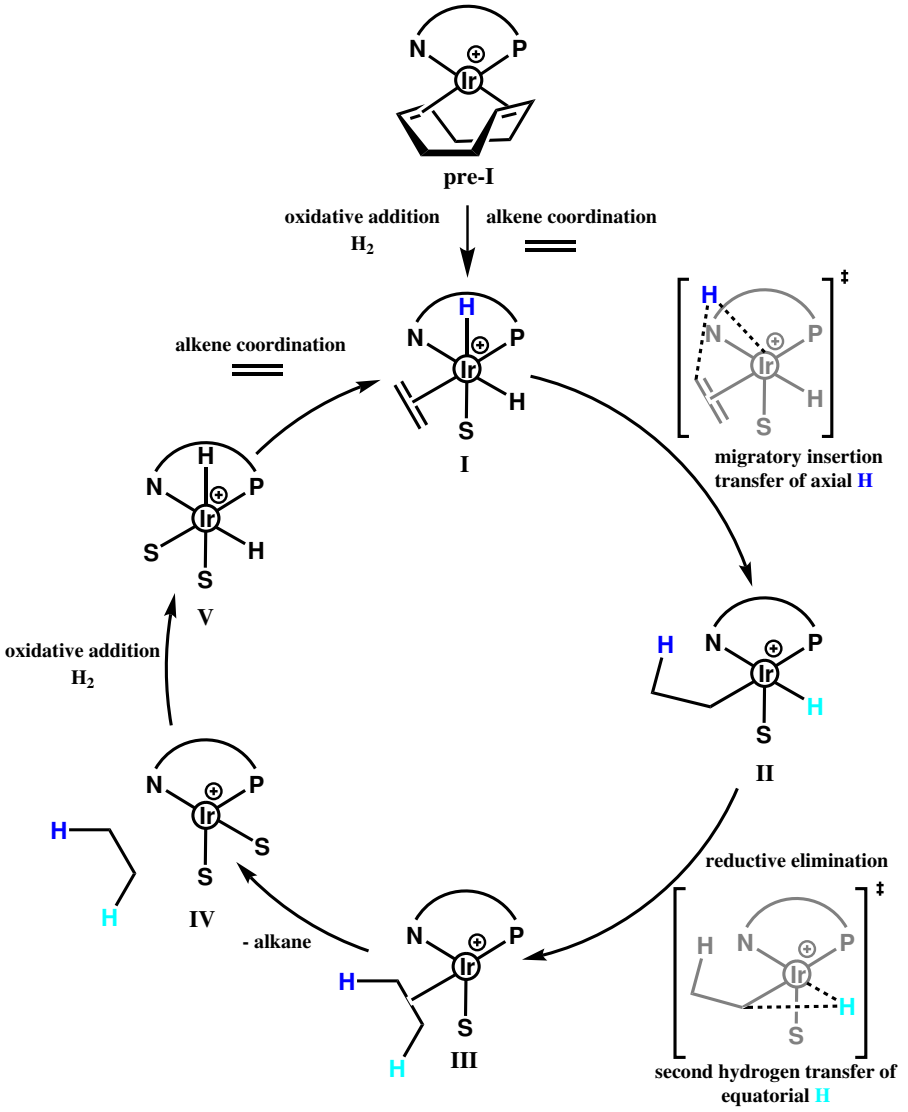

Figure 4.: A catalytic cycle for olefin hydrogenation involving Ir(I)/(III) intermediates.

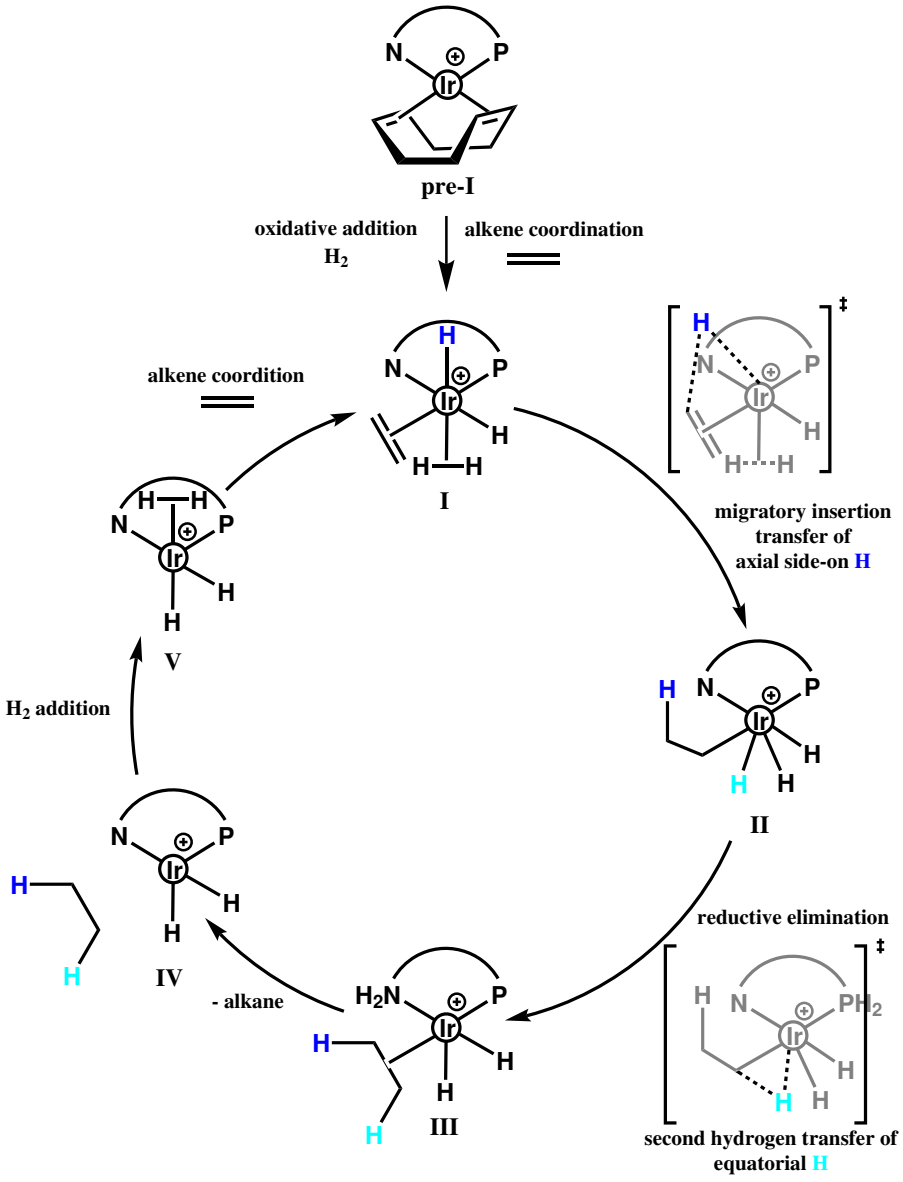

Figure 5.: A catalytic cycle for olefin hydrogenation involving Ir(III)/(V) intermediates.

A recent computational study[76] involved an investigation of all three proposed mechanisms[1,3,5] under identical chemical conditions. A direct comparison revealed that the Ir(I)/(III) mechanism has a feasible energy barrier (19.2 kcal/mol) and may be favored if a coordination of a second dihydrogen is prohibited or if the reaction is under low hydrogen pressure. Concerning the Ir(III)/(V) mechanism, it is demonstrated that Brandt's suggestion provides the lowest reaction barrier of 18.6 kcal/mol while the proposal of Burgess had a 22.7 kcal/mol barrier height. Based on these results, the main steps of the two relevant mechanisms of Dietiker (Ir(I)/(III)) and Brandt (Ir(III)/(V)) are illustrated in Fig. 6.

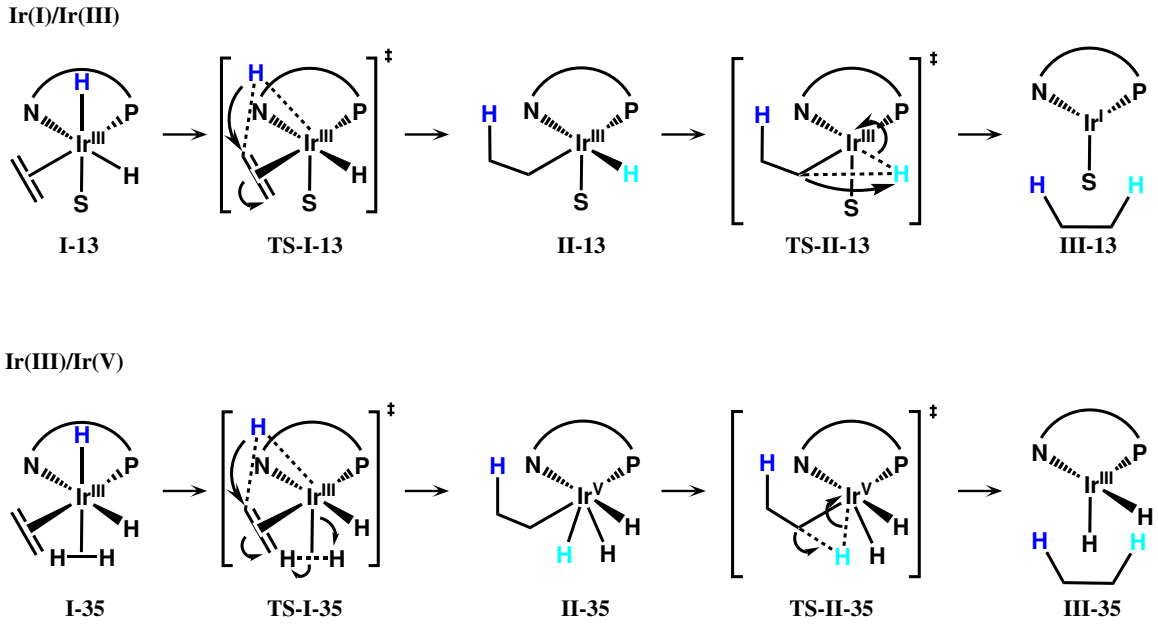

Figure 6.: Relevant steps of the olefin hydrogenation involving Ir(I)/(III) and Ir(III)/(V) species.

The catalyst, the substrate and the specific reaction conditions might have a high impact on the underlying mechanism. None of the three proposed mechanisms can be ruled out but in our investigations, we will only focus on the two mechanisms shown in Fig. 6.

3. Methods

3.1. Computational Details

Applied density functional theory has already supported several mechanistic studies for the qualitative prediction of reaction barriers and relative stabilities[43,76]. Within this purely theoretical study, we also apply the quantum mechanical approach to determine mechanistic details of hydrogenation reactions. All calculations were carried out with Gaussian03[77] in the gas phase, using the B3LYP functional[78,79]. Ligands were computed with the 6-31G(d,p)[80] basis set including polarization functions, and the metal center was treated with the LANL2DZ[81] basis set including an effective core potential. The determination of the relative stabilities of the substrate-catalyst complex were not only carried out in gas phase but also validated using the polarizable continuum model (PCM)[82–84]. Dichloromethane (DCM) was taken as an implicit solvent. Additionally, two explicit DCM molecules were placed beside the substrate-catalyst complex in the optimization process to obtain a more realistic description of the relative stabilities.

DFT can describe different intermediates occuring during a chemical reaction in terms of their electron density. This performance has been proven to be regularly better in line with the experiment than results obtained from Hartree-Fock (HF) calculations at comparable computational cost[85,86]. It supports the description of transition and excited states and other geometrical properties[87]. However, DFT also suffers from many shortcomings which has its origin in the used exchange-correlation functional[88]. One of the main problems concerning the study of reaction pathways is the multi-configuration character of the wave-function. Here, the approximation of the kinetic energy of interacting electrons leads to biased transition state energies[89–91]. In addition, there is a well known deficiency in the description of the dispersion interactions of chemical compounds[92,93] also leading to defective energies. For a more exact description of these and other shortcomings, the reader is referred to Chapter 3. Despite these failures, DFT methods are successful to provide precise description of relative stabilities (thermodynamics) and the determination of reaction rates (kinetics)[43,76].

3.2. Locating Transition States

Global search algorithms are essential to determine transition states between two (local) minima by determining the Hessian matrix. The Hessian matrix consists of second derivatives of the energy in relation to the nuclear motion[94]. For our study, the *quadratic synchronous transit methods*[95,96] QST2/QST3, a simple scan approach, or Berny's optimization algorithm were used for the determination of the Hessian at 0 K. These search algorithms identify the negative transitional degree of freedom (DoF), a frequency which is characteristic for the transition state[97]. The vibration of this frequency reflects the motion of the corresponding reaction. If more negative eigenvalues were obtained from the Hessian during the optimization, the eigenvalue check was turned off with *noeigen*. IRC calculations were carried out to validate obtained transition states, and a second functional, the GGA functional PBE[98], was chosen to confirm energies[99] obtained from B3LYP. In general however, the applied methods are sensitive to initial geometries and bias the result by the proposed mechanism[100]. Therefore, it is inevitable to investigate several mechanisms for the final assignment of the reaction sequence. For more information of locating transition states see Chapter 3.

4. Results

4.1. Alignment of Substrate and Ligands on the Metal Center

Our theoretical investigation examines the effect of an inverted selectivity triggered by small modifications on the periphery of an iridium-PHOX catalyst. The complementary experimental study on this subject was already reported by our group[8]. As a catalyst, an Ir-PHOX species was chosen where the alkene is *trans*-coordinated to the phosphorus, and one hydrogen is *trans* to the nitrogen atom[55,56] (Fig. 7). Using this substrate-catalyst complex, there are four possibilities for the coordination of the olefin species with its ester group pointing towards the metal ion. In all of these four possibilities, the alkene is placed parallel to the P-Ir-N plane (in-plane) (Fig. 7 A). There are additional four possibilities for a perpendicular (out of plane) arrangement of the olefin (Fig. 7 B). However, the arrangement in Fig. 7 B, where the alkene is out of plane, are higher in energy, so that a structural optimization orients the olefin to lie within the P-Ir-N plane, as suggested in Fig. 7 A. Therefore, calculations were only performed for the in-plane reactants, which did not restrict the olefin to exclusively move from

that plane during the reaction process. Furthermore, the energetically favored reactants *o*-tolyl-or (0.00 kcal/mol) and *o*-tolyl-ur (5.18 kcal/mol) were used and the mesityl-or (0.00 kcal/mol) and the mesityl-ur (3.74 kcal/mol) conformations (Fig. 7). Substrate complexes with higher energies *o*-tolyl-ur, *o*-tolyl-ul, and their mesityl-analogs where neglected, as obtained transition states were around 10 kcal/mol higher in energy. The orientation of the *ortho*-methyl groups attached on the phenyl rings of the P-ligand essentially influence the relative stabilities. The arrangements of the *ortho*-methyl groups presented in Fig. 7 are clearly preferred in the gas phase and for implicit solvent calculations in dichloromethane.

The proposed Ir(III)/(V) mechanism cannot be completely applied to the reaction in which we want to explain the inversion of the stereoselectivity. In contrast to other investigated catalyst-substrate complexes, we deal with an ester functionalized olefin where a beneficial coordination of the carbonyl oxygen to the metal center can be formed. Due to this coordination, the only vacant position on the complex is occupied which initially prevents the coordination of a second H_2. The reactant is better stabilized by such a coordination (~ -8.50 kcal/mol) which may also be beneficial to the reaction. However, it is uncertain if the proposed Ir(I)/(III) and Ir(III)/(V) mechanisms can be transferred directly. The ester coordination to the iridium creates more interactions and distortions and may significantly affect the selectivity, which is investigated by analyzing experimental findings in the following[8].

The chosen catalyst in the experimental study of Schneider *et al.* has, an oxazoline moiety bearing an *tert*-butyl group which introduces a *S*-configurated stereocenter in the product. The additional stereocenter in the substrate can influence the stereochemical outcome of the entire reaction disregarding the selected catalyst if the reaction is substrate controlled[4,101]. However, the strong influence of *o*-tolyl and mesityl catalysts which triggers an inversion of the stereochemistry[8] suggests that the reaction is mainly catalyst-controlled which does not exclude strong effects originated by the substrate. As the experimental investigation deals with a chiral substrate and a chiral metal complex, this double stereodifferentiation[101] may cause higher selectivities if the stereocenter in the substrate has a positive effect[102]. Masamune *et al.* reported that the outcome of a reaction, in which two stereocenters are involved, can be determined by dividing the reaction into single reactions, each with one of the chiral compounds. Therefore, it can give either a "mismatch" of the effects caused by the stereocenters or a "match" resulting in an increased selectivity[102]. Furthermore, the two

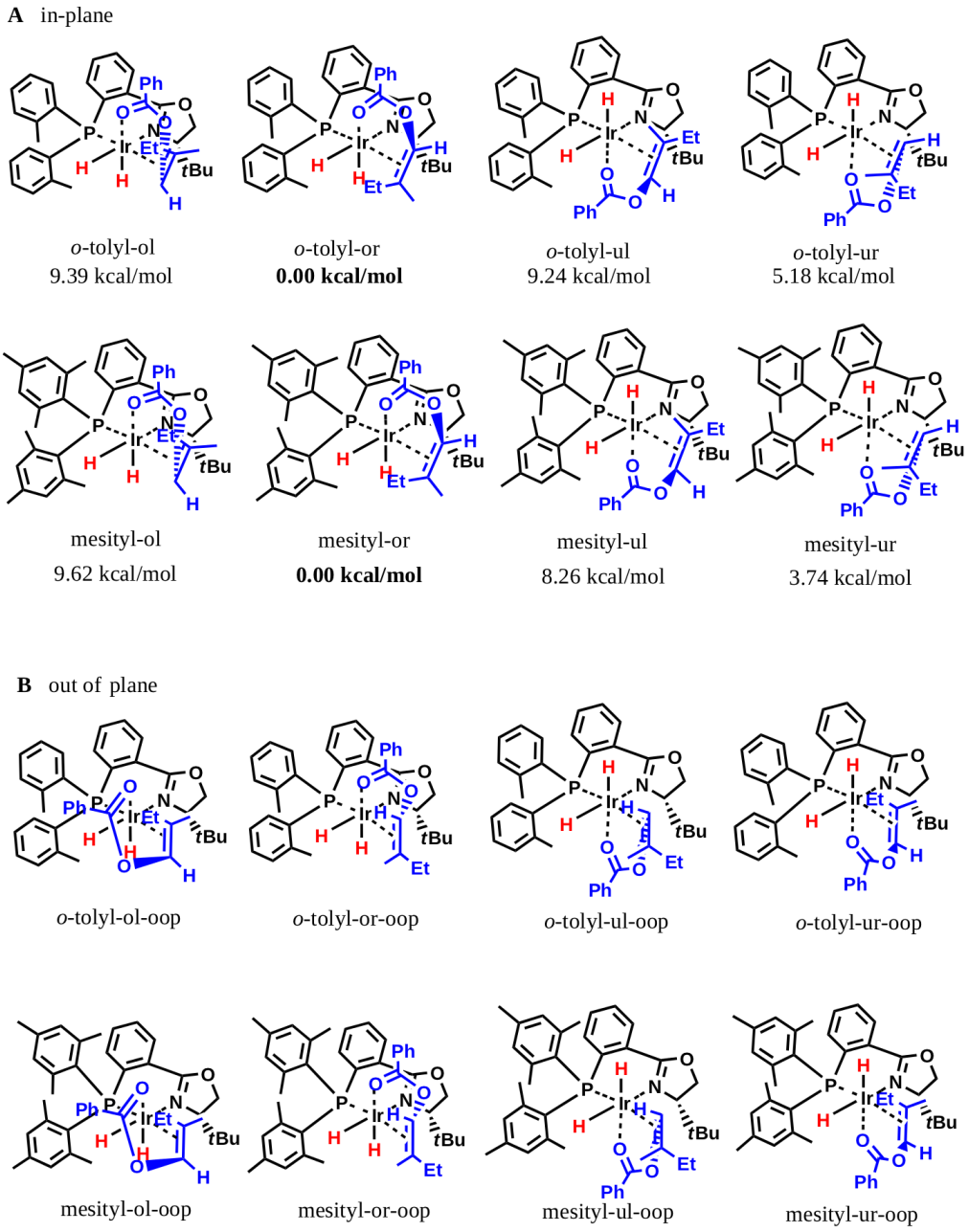

Figure 7.: Ir-PHOX catalysts with *o*-tolyl and mesityl residues. A: Conformations in-plane, B: Conformations out of plane.

stereocenters in the alkyl chain of substrate **2** can cause *syn*-pentane interactions which may have an influence on the amount of substrate-control (*syn*-pentane interactions is marked in orange e.g. in Fig. 10).

The Ir(I)/(III) mechanism of Dietiker *et al.* and the Ir(III)/(V) mechanism according to Brandt *et al.* are taken into account to explain the opposite stereoselectivity[8] in Tab. 1. To deal with the

hydrogenation of two C=C bonds, as it is reported for the experimental reaction, is not trivial with our computational model. The hydrogenation of the terminal C=C bond was modelled to determine reactivities while the C=C bond of the residue chain was kept intact. A subsequent hydrogenation gave the final product. According to a theoretical study[76], the Ir(III)/(V) mechanism of Burgess[44] involves energetically higher transition states compared to Brandt's approach and will not be considered further. As the originally vacant position is occupied by a metal-coordinated ester oxygen in this reaction, a coordination of a second H_2 is only feasible after the first hydrogen transfer. This can be a critical factor in the sense of the chosen mechanism, as the coordination of functional groups play an essential role, especially for iridium catalyzed reactions[103].

4.2. Ir(I)/(III) Mechanism

In a first attempt, Dietiker's Ir(I)/(III) mechanism[5] is investigated with a model compound which is similar to substrate **2** depcited in Fig. 3 but reduced by replacing one alkene substituent by an ethyl-residue (Et-residue). Thus, only the enantioselectivity can be determined but supposedly, it is an indicator for a switch of enantioselectivity between catalyst **3a** and **3b**.

The transition states of the second hydrogen transfer (Fig. 8) are slightly higher in energy, the *o*-tolyl and the mesityl species, therefore this is supposed to be the rate limiting step. For the green pathway leading to a *R*-configuration (Fig. 8, upper panel), the TS (ax-o13-u2r-TS1) for the first H-transfer of the axial hydrogen is at a barrier height of 26.19 kcal/mol and for the second H-transfer of the equatorial hydrogen at 27.67 kcal/mol. Compared with the red pathway leading to a *S*-configuration, the critical second H-transfer is lower in energy by 4.91 kcal/mol (ax-o13-or-TS2), so that the pathway leading to the *S*-configuration is kinetically favored. Concerning the analogous reaction with a mesityl-catalyst (Fig. 8, lower panel), an inverse selectivity as suggested in the experiment is depicted[8]. Here, the rate limiting transition step of the green reaction pathway (ax-m13-ur-TS2) is favored by 0.46 kcal/mol yielding the *R*-configuration. As the preferred transition state is only favored by 0.46 kcal/mol for the mesityl mediated path but 4.91 kcal/mol for the *o*-tolyl mediated path, a destabilization effect of the mesityl TS2, ax-m13-or-TS2 (Fig. 8 lower panel, red path) is found. The effect of a non-coordinating ester group (dashed lines in Fig. 8) was also investigated, as the ester group pointed in an opposite direction of the alkene-metal bond. In some cases, the ester group is coordinating with the hydrogen

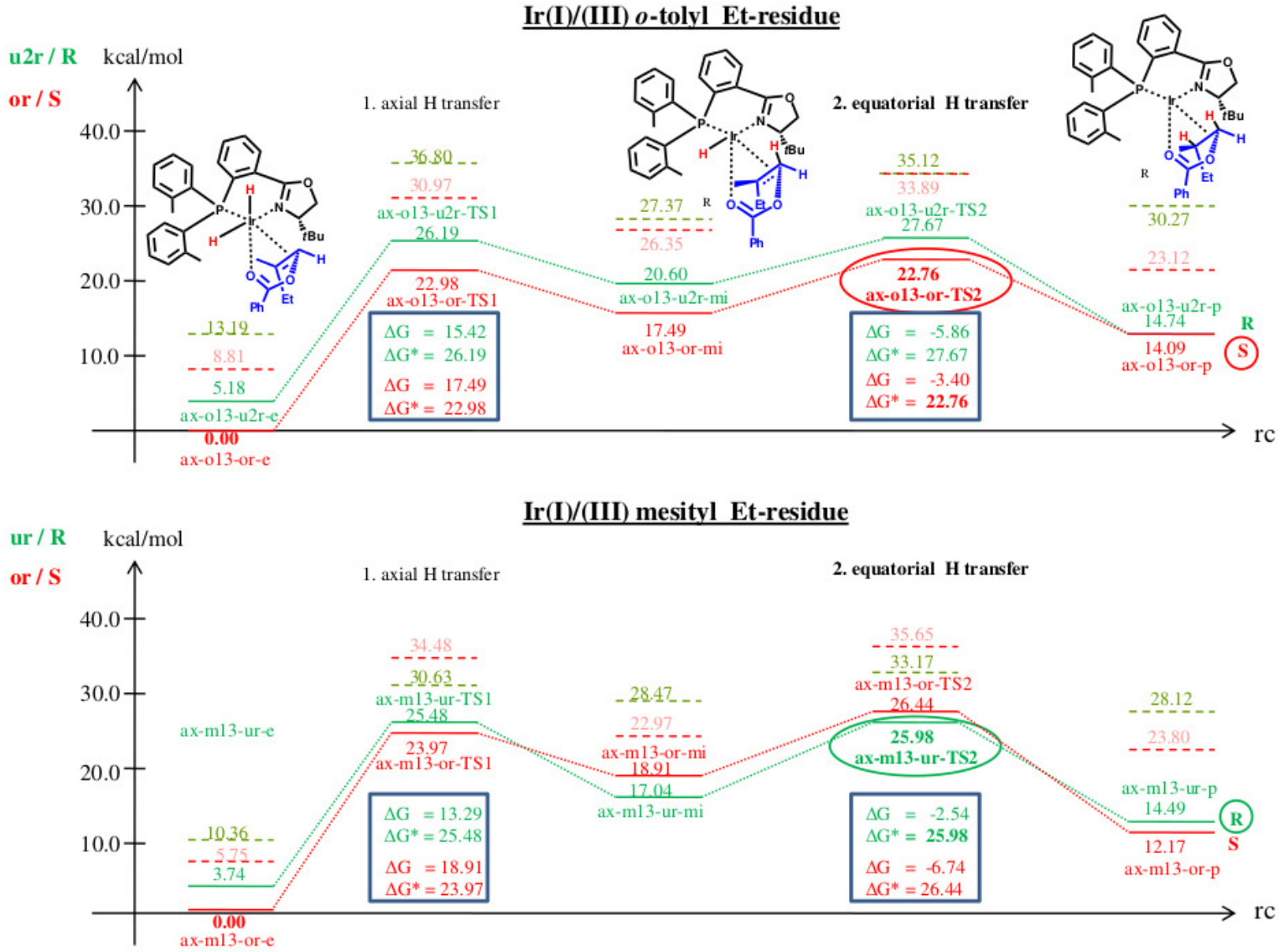

Figure 8.: Hydrogenation reaction with an **Ir(I)/(III)** mechanism, where the axial H is transferred first followed by the equatorial H. Upper panel: *o*-tolyl catalyst with an Et-substituted alkene species yielding a *S*- (red) and *R*- (green) enantiomer. Lower panel: mesityl catalyst with an Et-substituted alkene species yielding a *S*- (red) and *R*- (green) enantiomer. The light red and green dashed lines are the corresponding mechanisms with a non-coordinating ester group.

of the *S*-configurated carbon where the *tert*-butyl (*t*Bu) residue is bound to (Fig. 9). However, an unfavorable interaction arises if the ester oxygen is close to the hydride which has to be transferred to the C=C bond. Depending on the extent of these interactions, the combined interaction can either stabilize or destabilize the transition state.

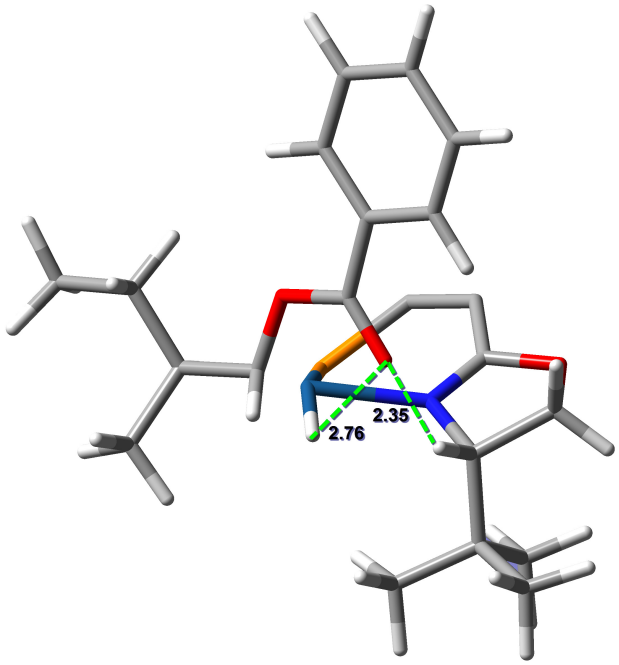

Figure 9.: Schematic representation of a substrate with a non-coordinating ester group during transfer of the second hydrogen. The green dashed lines indicate interactions between the ester oxygen and the transferred hydrogen, as well as with the hydrogen located on the *S*-configured carbon of the oxazoline ring. Atoms at the PHOX moiety are neglected for clarity.

In Fig. 8, the sum of these interactions indicate an unfavorable contribution as the reaction pathways are significantly higher in energy for the non-coordinating species. In agreement with the coordinated species, an inversion of the enantioselectivity is observed.

In the following, substrate **2** is used to verify the inversion of the selectivity (Fig. 10) which was already shown for the model complex in Fig. 8. In Fig. 10 (upper panel), it is illustrated that the *o*-tolyl-mediated reaction has a not significantly better stabilized TS2 (fax-o13-or-TS2) for the reaction pathway by 0.07 kcal/mol, leading to a *syn*-configuration. As a destabilizing *syn*-pentane interaction is observed for the red pathway in Fig. 10 (upper panel), the preference of the *syn*-configuration may be caused by other effects which have an impact on the substrate-control. As there is enough space

for the two methyl groups on the stereocenters, the 1,3-allylic strain can at least partially be avoided leading to a less pronounced *syn*-pentane interaction. The small difference of the TS2 barrier heights between the fax-o13-u2r-TS2 (green) and the fax-o13-or-TS2 (red) was investigated with the PBE functional leading to similar small energy difference. Using the B3PW91 functional however, stabilizes the fax-o13-u2r-TS2 (green) transition state with almost 1 kcal/mol leading to no inversion of the selectivity anymore. This implies a strong dependence of the relative energy levels of the transition states on the used DFT functional. More demanding methods such as MP2 may clarify if the B3LYP or the B3PW91 under or overestimates certain interactions.

For the mesityl-mediated pathway (Fig. 10 lower panel), a *syn*-pentane interaction is also observed in addition to other catalyst-controlled effects which cause a larger energy difference for the rate limiting second transition states. Here, the fax-m13-ur-TS2 is more stable by 4.53 kcal/mol, leading to an *anti*-configuration. The inversion of the stereochemistry, as reported in the literature[8], was found again with substrate **2** where a subsequent hydrogenation of the second olefin in the residue chain led to the correct ratio of diastereomers.

In most of the presented mechanisms, the first hydrogen transfer is supposed to overcome the highest energy barrier[3,4,76]. However, in our studies depicted in Fig. 8 and Fig. 10, the second hydrogen transfer causes the highest kinetic energy barrier. Therefore, it was considered to invert the order of the hydrogen transfer and to start with the equatorial located hydrogen followed by an axial hydrogen transfer. However, the highest energy barrier remained for the second hydrogen transfer.

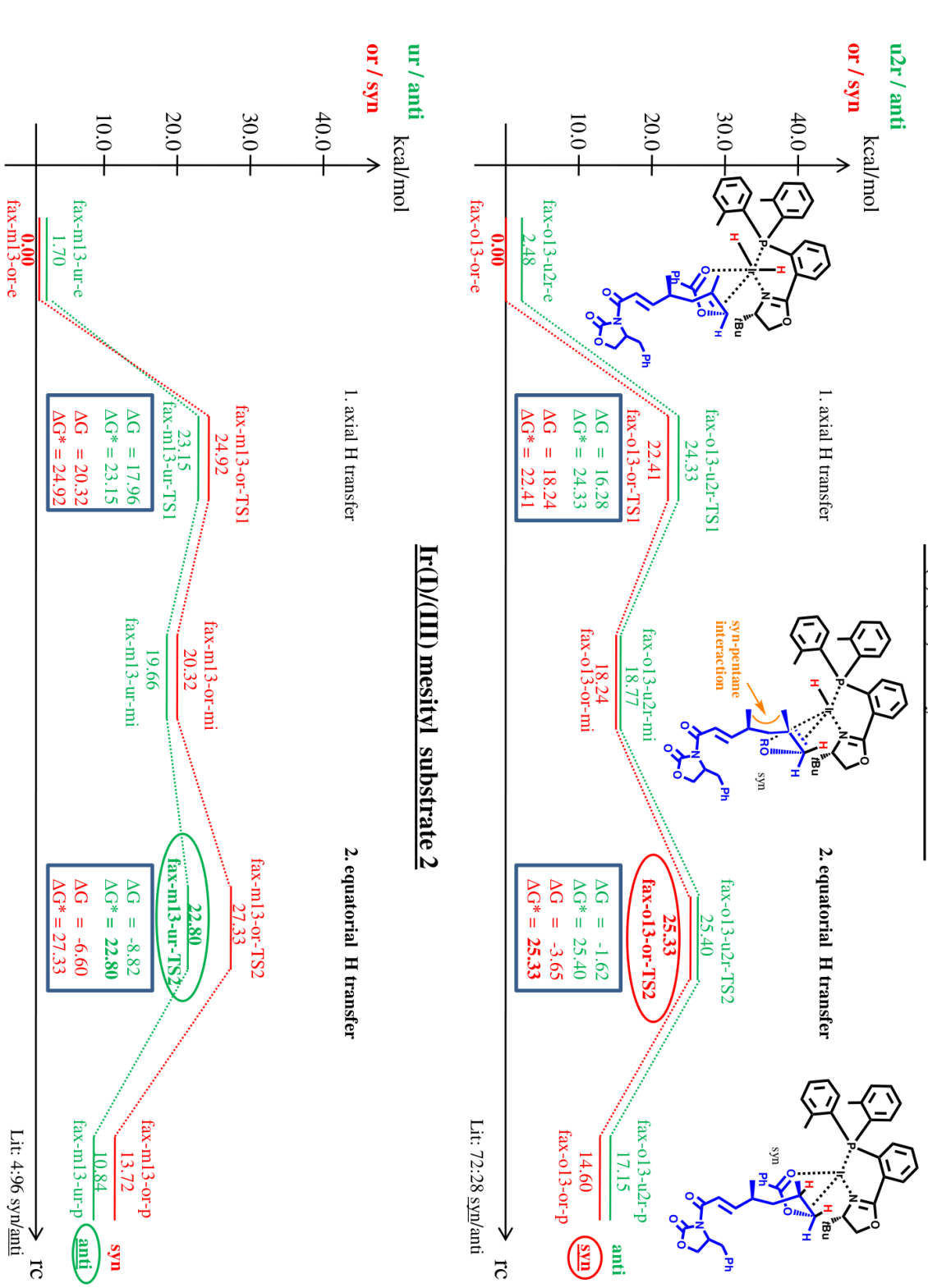

Figure 10.: Hydrogenation reaction with an **Ir(I)/(III)** mechanism, where the axial H is transferred first followed by the equatorial H. Upper panel: *o*-tolyl catalyst with the alkene substrate **2** yielding an *anti*- (green) and *syn*- (red) diastereomer. Lower panel: mesityl catalyst with the alkene substrate **2** yielding an *anti*- (green) and *syn*- (red) diastereomer.

In Fig. 11, the equatorial hydrogen is transferred first. Although the second transfer is now with the axial-located hydrogen, the rate limiting step is still the second TS also yielding a *S*-configuration. Interestingly, the reaction barrier for the *o*-tolyl catalyst (Fig. 11 upper panel, eq-o13-or-TS2) is 21.19 kcal/mol higher for the rate limiting step as reported in Fig. 8 upper panel, ax-o13-or-TS2. The non-coordinating analog (light red dashed lines in Fig. 11, upper panel) which was supposed to be much higher in energy (as reported in Fig. 8) is now more favored by almost 8.60 kcal/mol compared to eq-o13-or-TS2 (Fig. 11). Although the non-coordinated species of the light red transition path in Fig. 8 and Fig. 11 have almost the same barrier height, the coordinated intermediate ax-o13-or-TS2 Fig. 8 is clearly favored. Considering the mesityl-catalyst in Fig. 11 (lower panel), a comparable pattern to the upper panel is shown also in the determined *S*-enantioselectivity. As the energy barriers for the model substrate are much higher and the stereochemistry is not inverted, this mechanism is very unlikely.

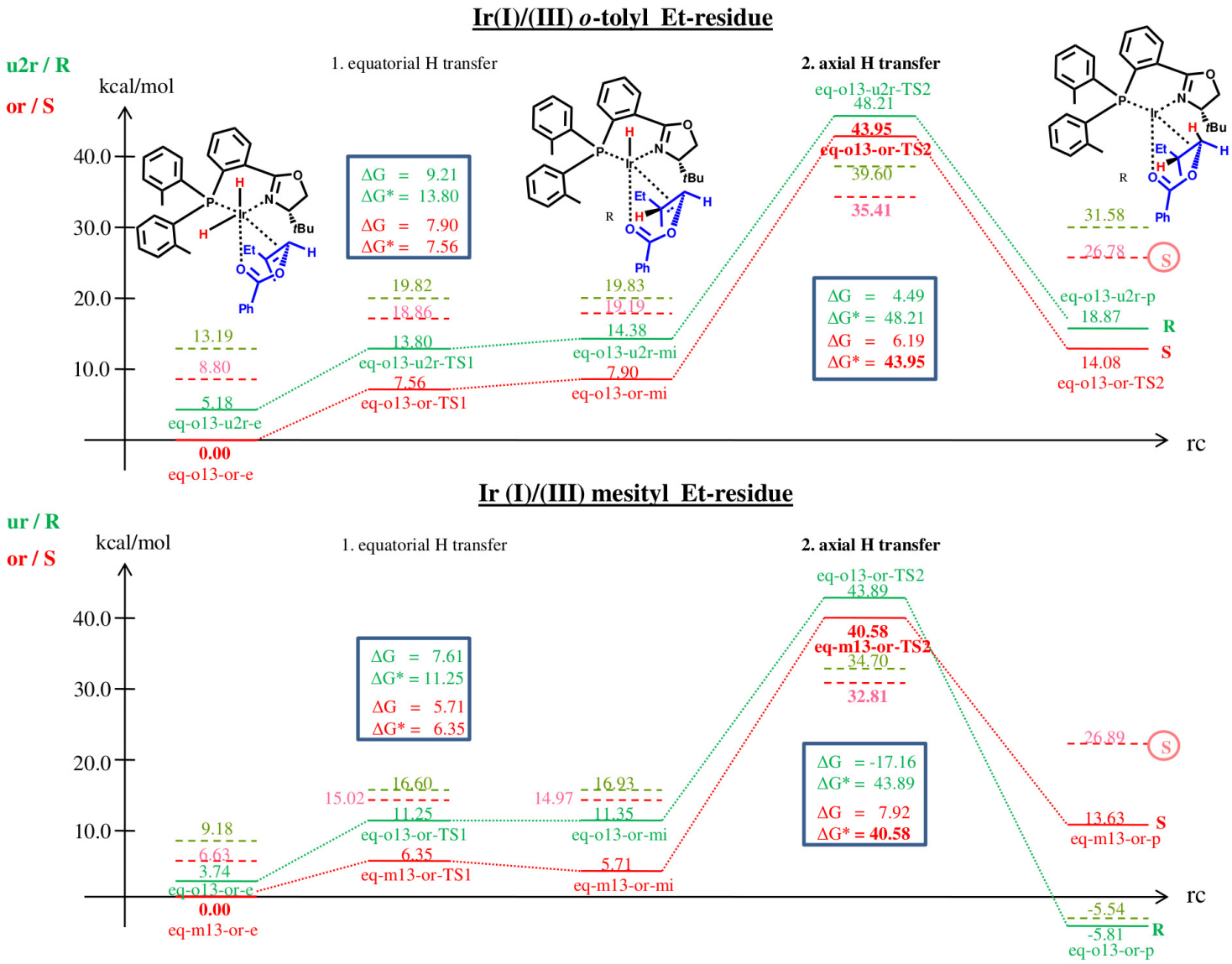

Figure 11.: Hydrogenation reaction with an **Ir(I)/(III)** mechanism, where the equatorial H is transferred first followed by the axial H. Upper panel: *o*-tolyl catalyst with an Et-substituted alkene species yielding a *S*- (red) and *R*- (green) enantiomer. Lower panel: mesityl catalyst with an Et-substituted alkene species yielding a *S*- (red) and *R*- (green) enantiomer. The light red and green dashed lines are the corresponding mechanisms with a non-coordinating ester group.

To examine an alternative mechanism in which an equatorial H is transferred first followed by an H-transfer from an axial position, substrate **2** is taken to enable a comparison with the literature. The literature[8] reported a 72:28 *syn*/*anti* proportion Tab. (1) for the *o*-tolyl catalyst and a 4:96 *syn*/*anti* ratio for the mesityl species.

A steric hindrance of the two methyl groups is obtained again (*syn*-pentane interaction marked in orange in Fig. 12, upper panel), however, the *syn*-configuration is still favored with an energy difference of 6.62 kcal/mol compared to the *anti*-configuration. If the TS2 for the *o*-tolyl mediated path (red) with the substrate **2** is compared to the analogous mechanism with the model complex (Fig. 11, upper panel), a larger difference of 1.52 kcal/mol is found for the two TS2. The mesityl-mediated path (Fig. 12, lower panel) has a reduced energy difference of the TS2 by 0.33 kcal/mol compared to the TS2 of the model complex (Fig. 11, lower panel). This indicates a higher amount of catalyst-control. However, due to high energy barriers and no inversion of the selectivity, the reaction pathways are unlikely.

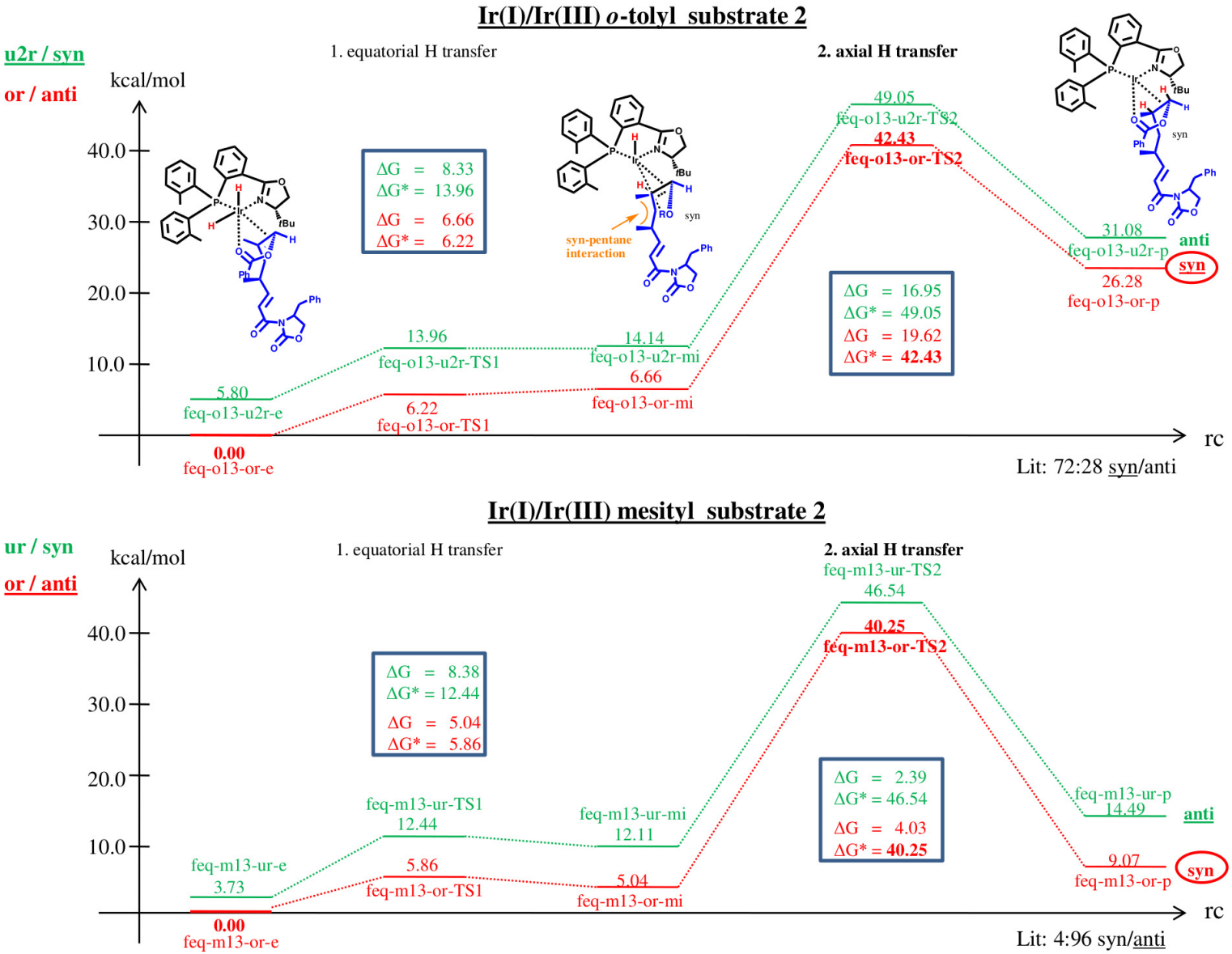

Figure 12.: Hydrogenation reaction with an **Ir(I)/(III)** mechanism, where the equatorial H is transferred first followed by the axial H. Upper panel: *o*-tolyl catalyst with the alkene substrate **2** yielding an *anti*- (green) and *syn*- (red) diastereomer. Lower panel: mesityl catalyst with the alkene substrate **2** yielding an *anti*- (green) and *syn*- (red) diastereomer. The light red and green dashed lines are the corresponding mechanisms with a non-coordinating ester group.

4.3. Ir(III)/(V) Mechanism

The majority of the theoretical studies involving hydrogenation reactions supported an Ir(III)/(V) mechanism[1,7]. In analogy to the Ir(I)/(III) mechanistic study, the transfer of an axial hydrogen followed by an equatorial one was investigated and *vice versa*. Additionally, the order of H-transfer of Brandt's mechanism[1] was applied to study the difference between H-transfer from a coordinated H_2 and an equatorial H-transfer.

The transfer of an axial hydrogen offers a vacant position in the Ir-coordination sphere. This enables an additional axial coordination of an H_2 in a η^2-fashion (Fig. 13), although this raises the energy (in average) by around 5 kcal/mol. Consistent with the Ir(I)/(III) mechanism, in this case, the rate limiting step is the second hydrogen transfer. However, it is surprising that the barrier heights of TS2 for the Ir(III)/(V) mechanism are in a comparable range as the barrier heights of the TS2 for the Ir(I)/(III) mechanism. This is also the case for the intermediates where the transferred hydrogen is one of the H_2-coordinated ligand. The *o*-tolyl catalyst (Fig. 13, upper panel) predicts the transition state of ax-o35-u2r-TS2 (blue) and the corresponding side-on transition state ax-o35-u2r-sideTS2 (turquoise) at a similar barrier height. In contrast, the transition of the path leading to an *S*-configuration, ax-o35-or-TS2 (red), is higher in energy (1.54 kcal/mol) than the side-on transition state ax-o35-or-sideTS2 (deep red). For the mesityl catalyst (Fig. 13, lower panel) a comparable energetic pattern was found. The TS2 of the side-on intermediate (ax-m35-or-sideTS2) leading to a *S*-configuration, is 2.50 kcal/mol lower in energy than ax-m35-or-TS2. But disregarding if the side-on intermediate is favored or not, both yielded the same configuration. Therefore, again no inversion of the selectivity is found. Only the non-coordinating species showed an inversion of the selectivity, but due to the large barriers, this pathway seems to be not feasible.

Figure 13. *(following page)*: Hydrogenation reaction with an **Ir(III)/(V)** mechanism, where the axial H is transferred first followed by the equatorial H or alternatively one of the side-on hydrogen according to Brandt's mechanism. The side-on intermediates are marked as turquoise and deep red narrow dotted lines. The light red and blue dashed lines are the corresponding mechanisms with a non-coordinating ester group. Upper panel: *o*-tolyl catalyst with the Et-substituted alkene yielding an *S*- (red) and *R*- (blue) enantiomer. The yellow inset provides both products, depending on the second H-transfer). Lower panel: mesityl catalyst with the Et-substituted alkene species yielding an *S*- (red) and *R*- (blue) enantiomer.

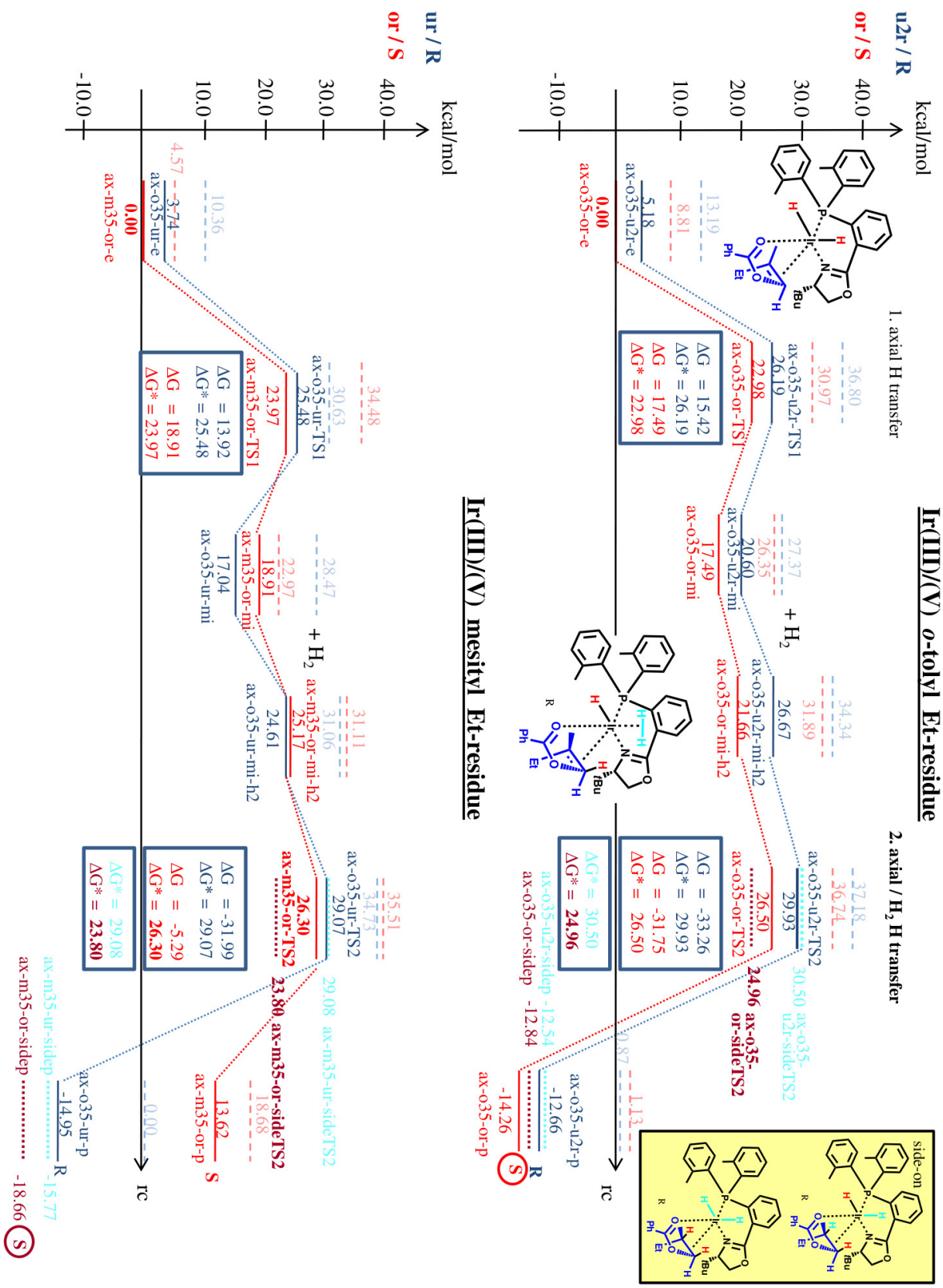
Ir(III)/(V) o-tolyl Et-residue
Ir(III)/(V) mesityl Et-residue
kcal/mol
or / S
u2r / R
ur / R
rc
1. axial H transfer
2. axial / H2 H transfer
+ H2
ax-035-or-e
ax-035-u2r-e
ax-035-u2r-TS1
ax-035-or-TS1
ax-035-u2r-mi
ax-035-or-mi
ax-035-u2r-mi-h2
ax-035-or-mi-h2
ax-035-u2r-TS2
ax-035-or-TS2
ax-035-u2r-sidep
ax-035-or-sidep
ax-035-u2r-p
ax-035-or-p
ax-035-or-sideTS2
ax-035-u2r-sideTS2
24.96 ax-035-or-sideTS2
23.80 ax-m35-or-sideTS2
ax-m35-or-e
ax-035-ur-e
ax-035-ur-TS1
ax-m35-or-TS1
ax-035-ur-mi
ax-m35-or-mi
ax-035-ur-mi-h2
ax-m35-or-mi-h2
ax-035-ur-TS2
ax-m35-or-TS2
ax-035-ur-sidep
ax-m35-or-sidep
ax-035-ur-p
ax-m35-or-p
ax-m35-ur-sideTS2
ax-m35-ur-sidep
side-on
R
S

Curiously, the previous mechanism did not show lower barriers for the TS2. At least for this reaction, it seems to be beneficial to have first a transfer of the equatorial hydrogen followed by the axial one. This may be due to the fact that the addition of a second H_2 in an axial position underlies sterical hindrance. In contrast, if the equatorial H is transferred first, the second H_2 can coordinate in-plane to the metal center, which is found to be favorable.

Fig. 14 depicts the preferred addition of the side-on H_2 in-plane. Here, the energy is reduced by around 3.60 kcal/mol after the dihydrogen addition in an equatorial position. This contrasts the H_2 addition on an axial position as presented in Fig. 13 as the energy is raised by $\sim$ 5 kcal/mol. Thus, the in-plane addition seems to stabilize the second hydrogen transfer by almost 10.0 kcal/mol, leading to barriers between 13.56 and 16.32 kcal/mol. A side-on mechanism is no longer feasible as the distance to the side-on coordinated H_2 is too far. Although the Ir(III)/(V) mechanism in which an equatorial H-transfer is followed by the axial H-transfer is clearly favored, the kinetic results show that no inversion of the stereocenter occurs. However, for the mesityl catalyst, the two intermediate states eq-m35-ur-TS2 and eq-m35-or-TS2 only differ by 1.0 kcal/mol which is not decisive. To lower the possibility that the current method (B3LYP) causes the difference, additional calculations were carried out with the PBE and B3PW91 functionals. However, qualitatively same results were obtained.

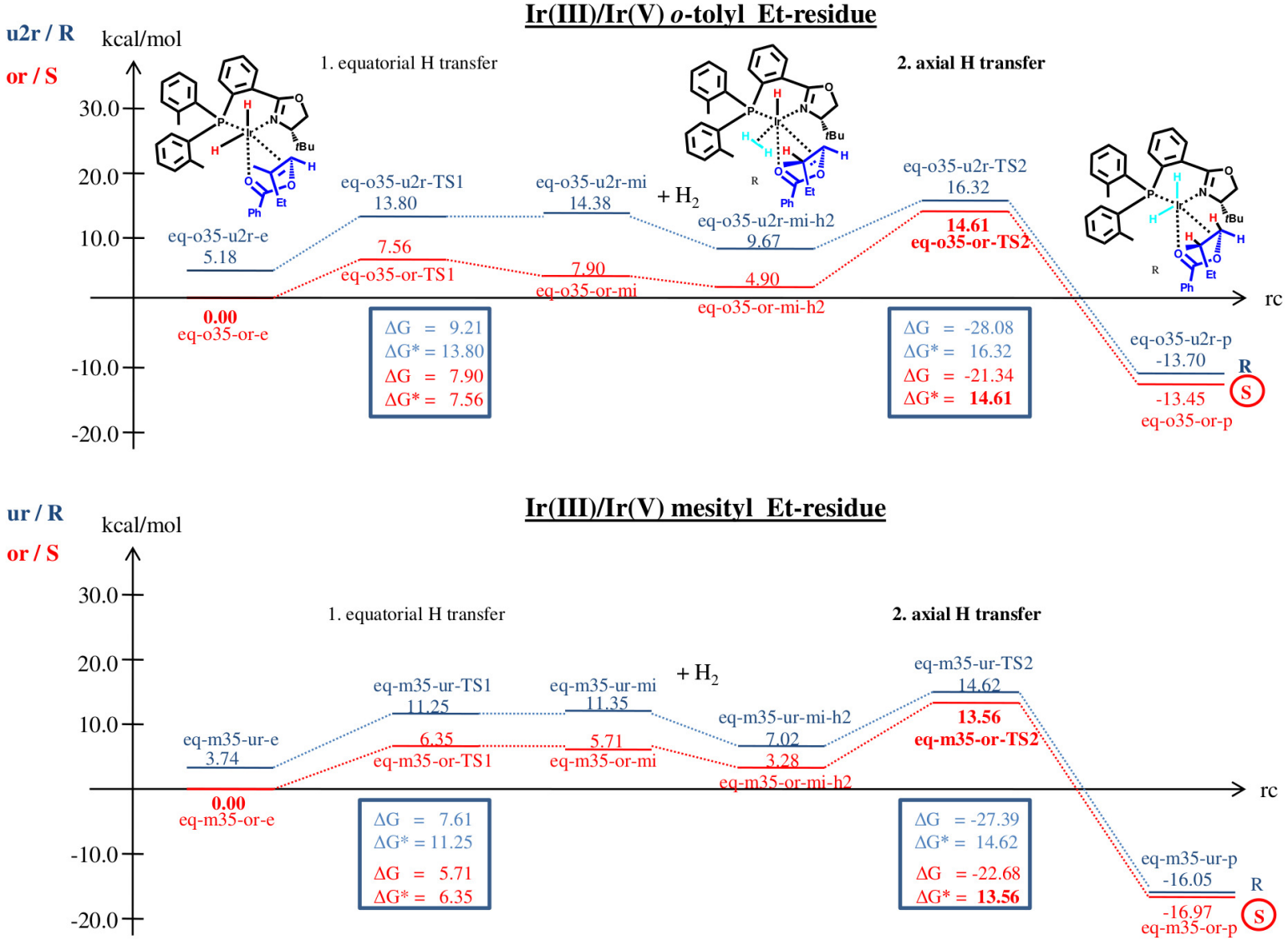

Figure 14.: Hydrogenation reaction with an **Ir(III)/(V)** mechanism. where the equatorial H is transferred first followed by the axial H. Upper panel: *o*-tolyl catalyst with the Et-substituted alkene species yielding an *S*- (red) and *R*- (blue) enantiomer. Lower panel: mesityl catalyst with the Et-substituted alkene species substrate yielding an *S*- (red) and *R*- (blue) enantiomer.

It is worth to investigate this mechanism with substrate **2** to judge the significance of the selectivity seen above. According to the literature[8], the reaction path with the *o*-tolyl catalyst should yield a 72:28 *syn/anti* ratio. The experimentally favored *syn*-product is obtained using the *o*-tolyl catalyst (Fig. 15 upper panel). The TS2 is clearly favored by 4.04 kcal/mol (feq-o35-or-TS2) compared to the TS2 leading to the *anti*-product. The correct prediction of the *anti*-configuration for the pathway involving the mesityl catalyst (Fig. 15 lower panel) was not possible.

The difference of the barrier heights using substrate **2** are more significant than the heights for the model complex. In the reaction of the mesityl catalyst (Fig. 15, lower panel), the TS2 leads to the *syn*-configuration favored by 6.33 kcal/mol. For the *o*-tolyl mediated path there is a difference of 4.04 kcal/mol forming again the *syn*-product. Therefore, no inversion of the selectivity was found.

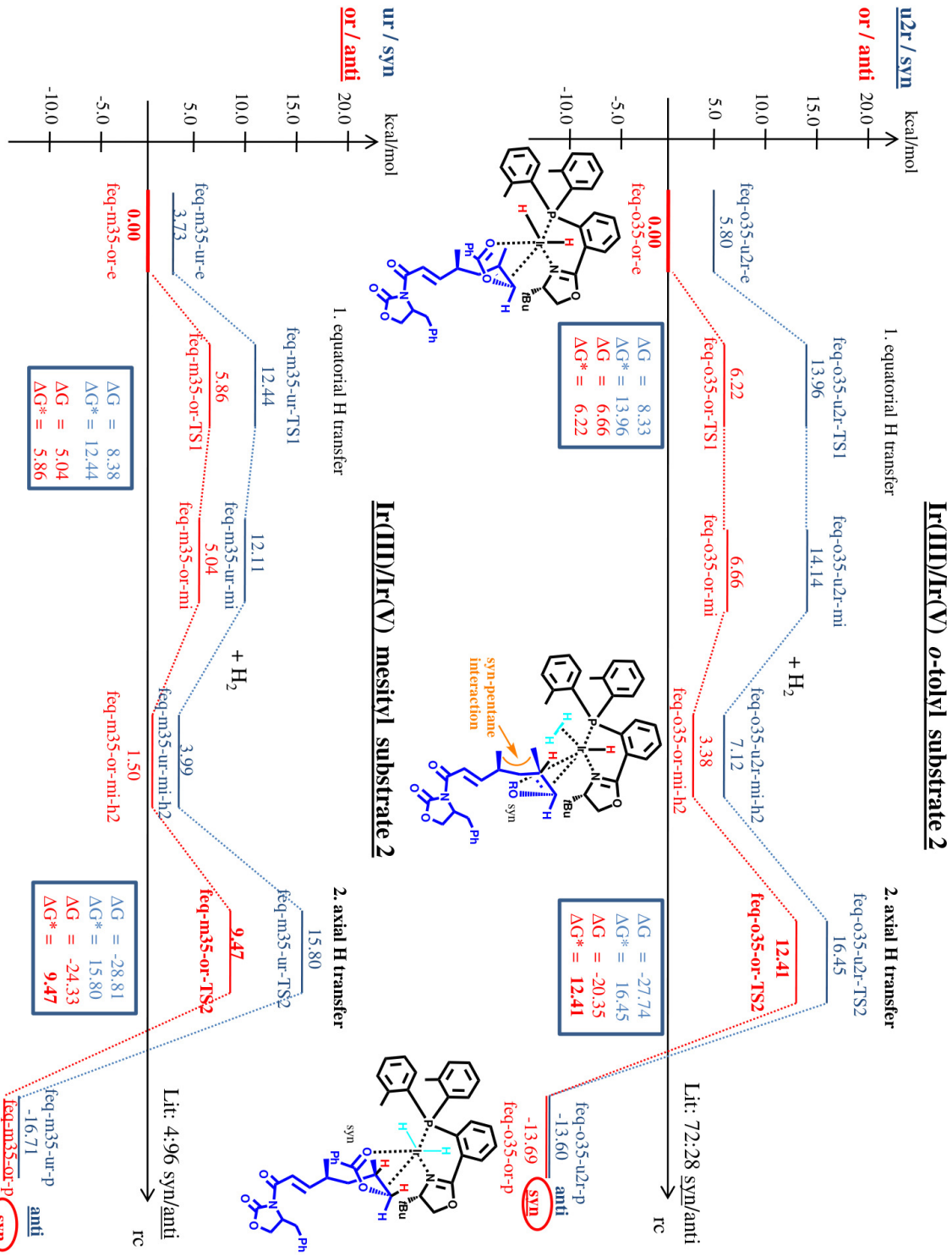

Figure 15.: Hydrogenation reaction with an **Ir(III)/(V)** mechanism, where the equatorial H is transferred first followed by the axial H. Upper panel: *o*-tolyl catalyst with the alkene substrate **2** yielding an *syn*- (red) and *anti*- (blue) diastereomer. Lower panel: mesityl catalyst with the alkene substrate **2** yielding an *syn*- (red) and *anti*- (blue) diastereomer.

4.4. Discussion

The Ir(I)/(III) mechanism suggested by Dietiker *et al.*[5] was the only approach that showed an inversion of the selectivity in accordance with the literature[8]. An overlap of the two transition states for the *o*-tolyl and mesityl catalysts in Fig. 8, ax-o13-u2r-TS2 (colored) and the ax-m13-ur-TS2 (grey) leading to a *R*-product are presented in Fig. 16. The transition states of the second hydrogen transfer, catalyzed by the *o*-tolyl and mesityl species, demonstrate a significant change in their geometrical arrangement. The methyl groups of the mesityl catalyst induce more sterical strain leading to a displacement of the mesityl rings. The Ir-P-C angle (C is the carbon of the mesityl ring (Ph3) whereby Ph3 is *cis* located to the oxazoline nitrogen) is increased from 111.11° (*o*-tolyl) to 117.41° (mesityl) which may cause an influence on the reactivity reported in Fig. 8.

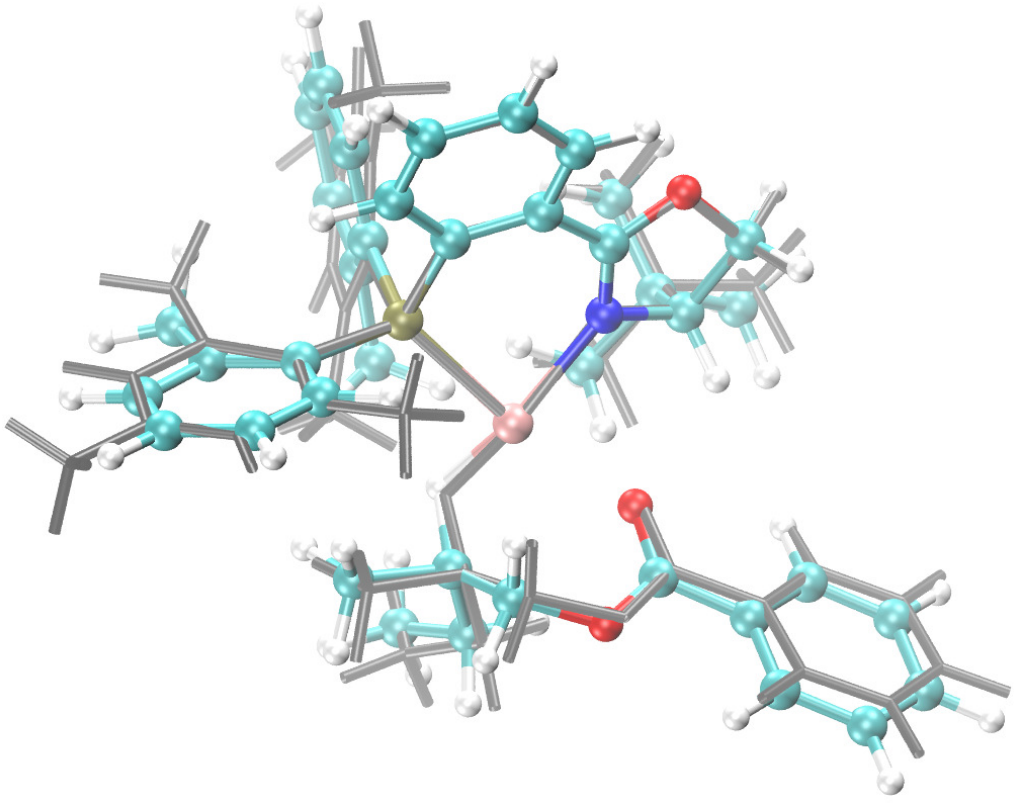

Figure 16.: TS2 overlap of the *o*-tolyl (colored) and mesityl (grey) catalyzed reaction paths in Fig. 8 leading to *R*-configurated enantiomers. The Ir-PHOX plane is aligned with an RMSD of 0.05 Å.

In Fig. 16, the substrate is now located *cis* to the phosphorus, for both the *o*-tolyl and the mesityl substituted catalyst and not *trans* as in the initial catalyst-substrate complex. This can be explained

by the interaction between the *tert*-butyl group with the phenyl group of the substrate depicted in Fig. 17.

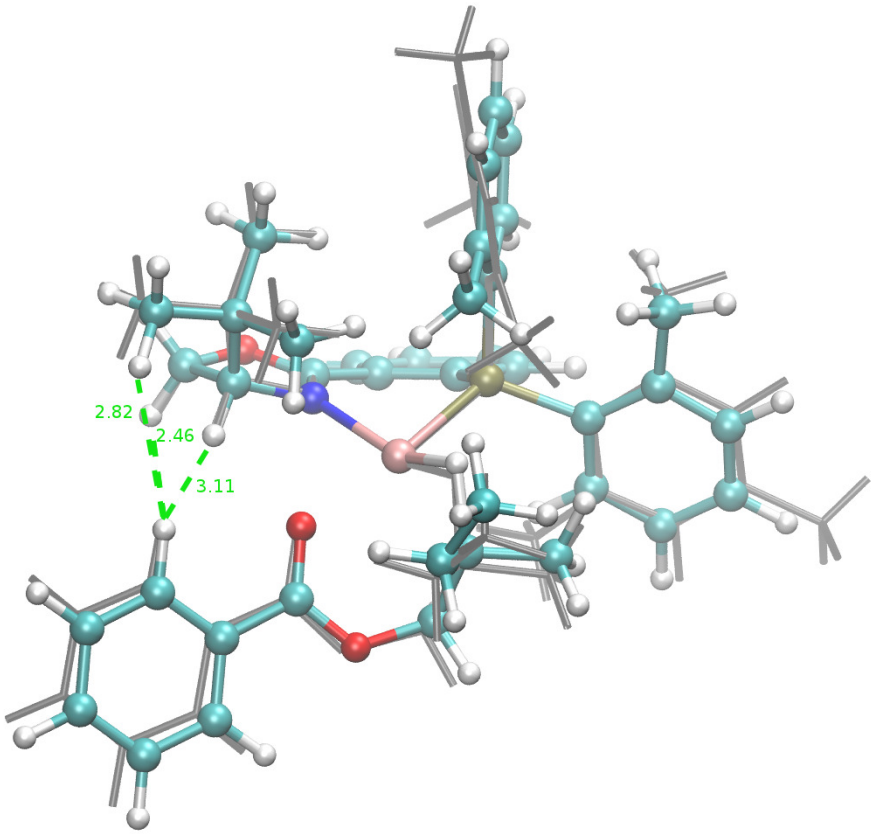

Figure 17.: TS2 overlap of the *o*-tolyl (colored) and mesityl (grey) catalyzed reaction paths in Fig. 8 leading to *R*-configurated enantiomers. The Ir-PHOX plane is aligned with an RMSD of 0.05 Å. The interaction between the *t*Bu and the substrate phenyl is marked with a light green dotted distance line.

A transfer of the first hydrogen from the axial position creates a vacant position. This axial position is then occupied by the second hydrogen as it is reoriented from its equatorial position to the axial one. The new vacant position on the equatorial plane enables the substrate to avoid the unfavorable interaction with the *tert*-butyl group by occupying the vacant position, which is *cis* to the phosphorus atom. Possibly, a smaller substituent as the *t*Bu group would lower this interaction with a beneficial impact on the selectivity.

It is not obvious which interaction is mainly responsible for the inversion of the selectivity, but some structural changes may influence the stereochemical outcome. For example, the distance of the iridium

to the hydrogen on the phenyl group (Ph2) (further away from the oxazoline nitrogen) is 3.46 Å for the *o*-tolyl catalyst and the distance from the metal to the methyl hydrogen (mesityl calalyst) is only 2.71 Å (light green dotted lines in Fig. 18). The methyl hydrogen of the phenyl ring Ph3 (closer to the oxazoline nitrogen) where the distance is 2.73 Å for the *o*-tolyl catalyst (blue dotted lines in Fig. 18) is also close to the metal center. The narrow distance of the methyl hydrogens for the Ph2 and for the Ph3 to the metal center can have a strong energetic influence on the TS.

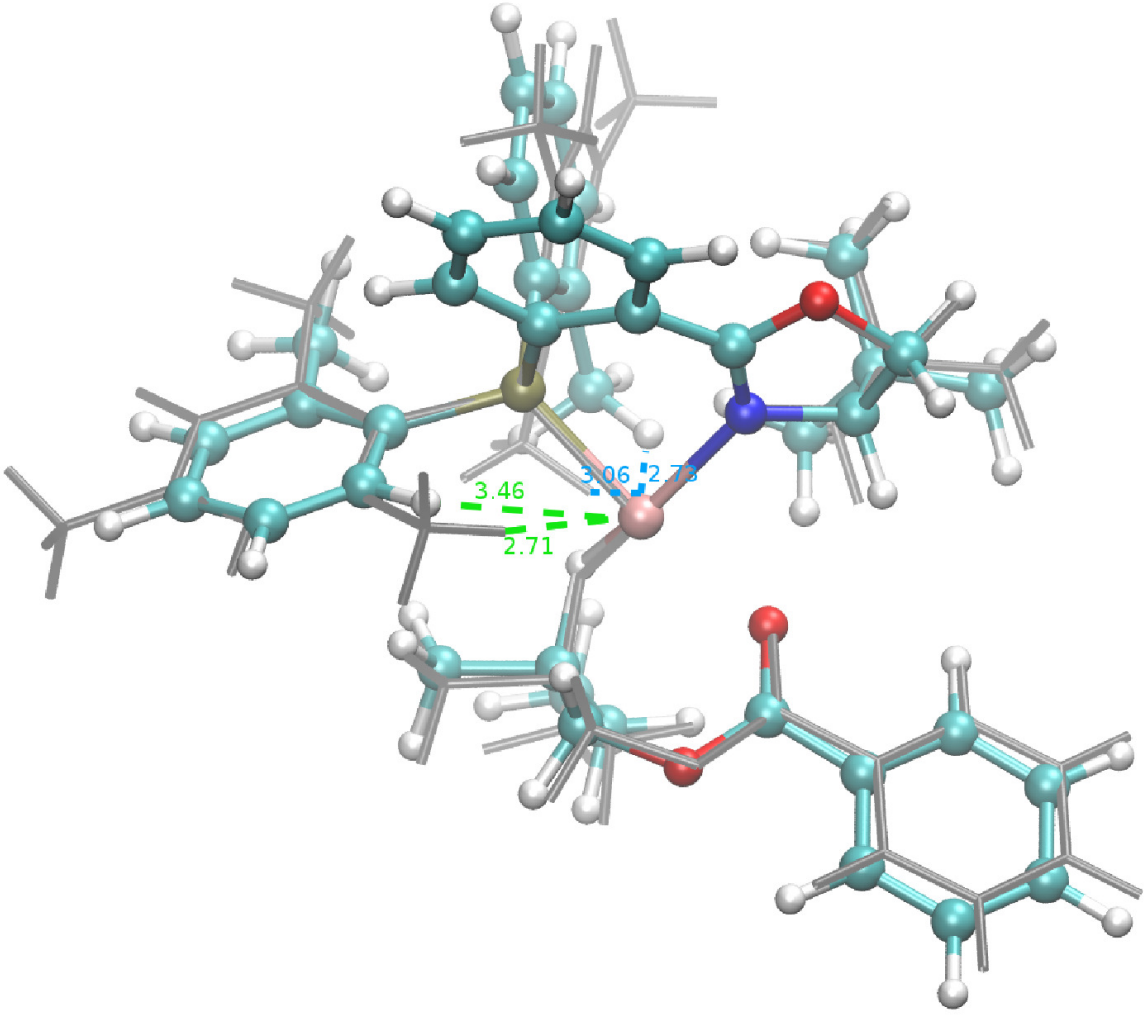

Figure 18.: TS2 overlap of the *o*-tolyl (colored) and mesityl (grey) catalyzed reaction paths in Fig. 8 leading to *R*-configurated enantiomers. The Ir-PHOX plane is aligned with an RMSD of 0.05 Å. The interactions between the phenyl ring hydrogen (Ph2) and the metal center are marked with a light green dotted distance line, and the interactions with the phenyl (Ph3) are in blue.

Minor changes in distances were also found for the Ph2 hydrogen to the substrate (Fig. 19) and for

the Ph3 hydrogen to the hydrogen which has to be transferred (Fig. 20). As in the first case reduction in distance of the Ph2 hydrogens to the substrate changes from 2.66 to 2.42 Å (light green dotted lines); this substituent effect is supposed to be small. However, the reduction in distance between the hydrogen of the Ph3 group and the transferred hydrogen of 0.18 Å (blue dotted lines in Fig. 20) indicates a critical interaction for the pathway, leading to a *R*-configuration. This can be examined by analyzing a molecular dynamics simulation with Gaussian using the atom-centered density matrix propagation (ADMP)[104–106] approach. The DFT-MD simulation was carried out for the TS2 from Fig. 8 (upper panel) at 300 K with an NVE ensemble. Visualizing the snapshots reveals an interaction of the Ph3 methyl group which directs the hydrogen to the substrate as shown in Fig. 20. A minor change in this interaction distance may have a strong influence as the methyl group (Ph3) is directly involved in the transition process.

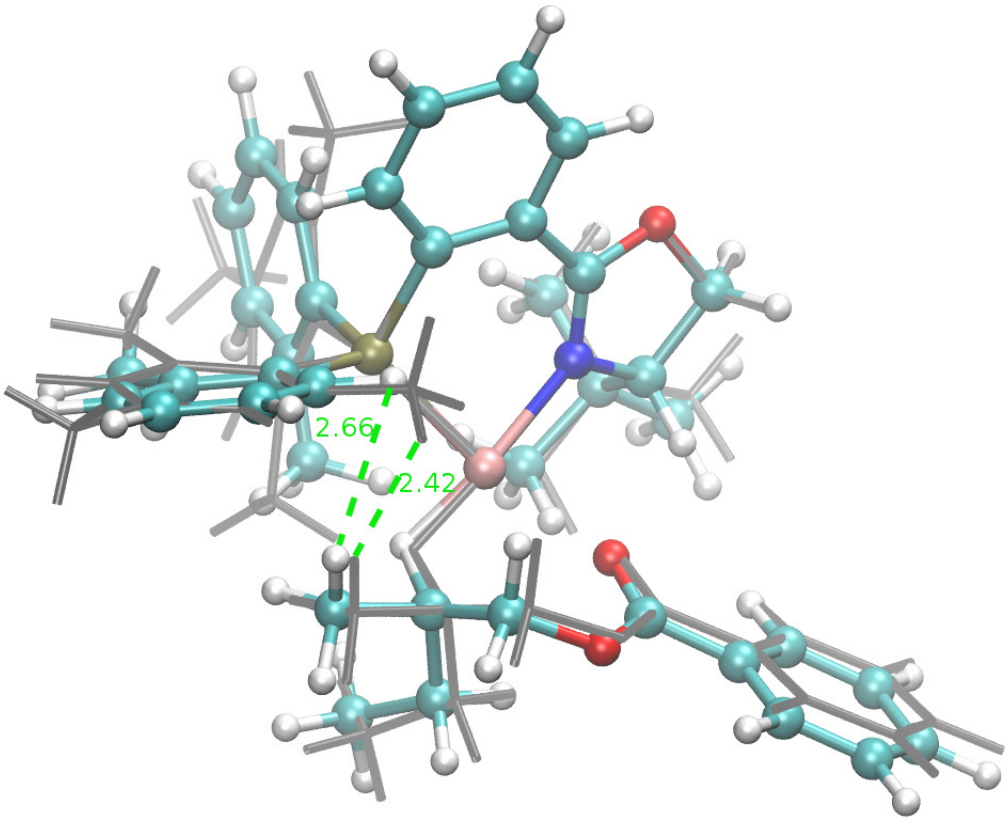

Figure 19.: TS2 overlap of the *o*-tolyl (colored) and mesityl (grey) catalyzed reaction paths in Fig. 8 leading to *R*-configurated enantiomers. The Ir-PHOX plane is aligned with an RMSD of 0.05 Å. The interactions between the phenyl ring hydrogen (Ph2) and the substrate marked with a light green dotted distance line.

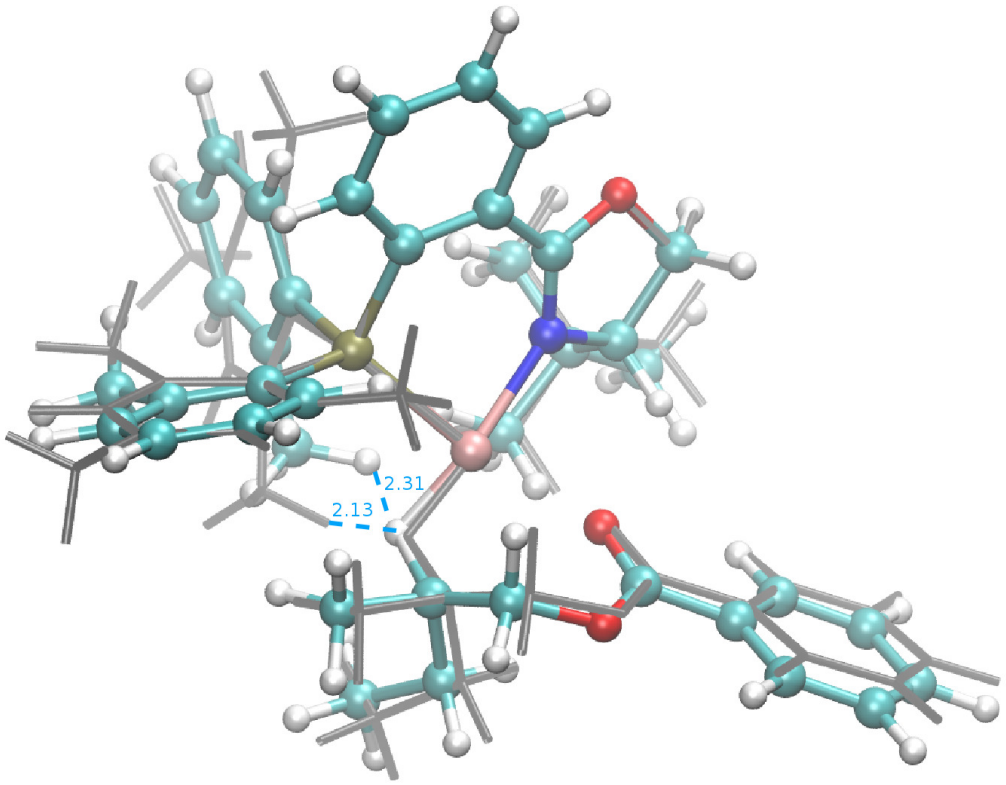

Figure 20.: TS2 overlap of the *o*-tolyl (colored) and mesityl (grey) catalyzed reaction paths in Fig. 8 leading to *R*-configurated enantiomers. The Ir-PHOX plane is aligned with an RMSD of 0.05 Å. The interactions between the hydrogen on the phenyl ring Ph3 and the transferred hydrogen are marked with a blue dotted distance line.

A significant geometrical change was also revealed for the phosphorus residues. For the *o*-tolyl catalyst, the angle between the PHOX-phenyl Ph1, the phosphorus and the phenyl Ph3 is highlighted in Fig. 21. The Ph1-P-Ph3 angle is 107.00° in case of the mesityl catalyst compared to 101.31° for the *o*-tolyl catalyst.

This significant difference implies that one methyl group of the Ph3 is closer to the transferred hydrogen by 0.18 Å which was already shown in Fig. 20. In addition to the change in Ph1-P-Ph3 angle (Fig. 21), the torsional angle over the transferred hydrogen, iridium, phosphorus and the Ph3 carbon is decreased by 0.5° from 81.2° for the *o*-tolyl to 80.7° for the mesityl catalyst.

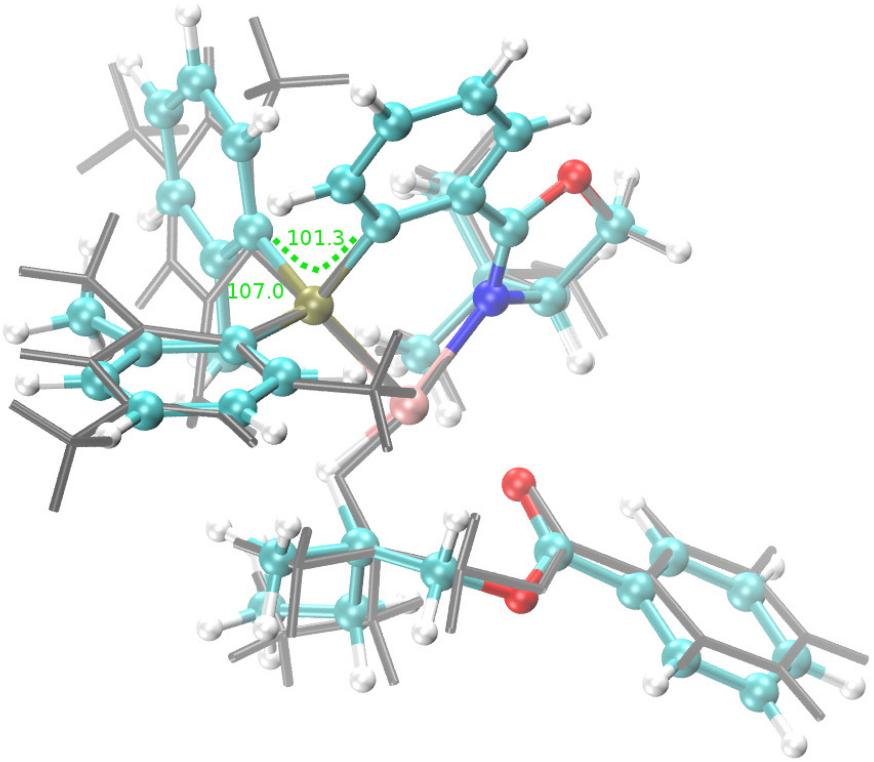

Figure 21.: TS2 overlap of the *o*-tolyl (colored) and mesityl (grey) catalyzed reaction paths in Fig. 8 leading to *R*-configurated enantiomers. The Ir-PHOX plane is aligned with an RMSD of 0.05 Å. The changed angles between the carbon of the PHOX-phenyl Ph1, the phosphorus and the carbon of the phenyl (Ph3) are marked with a light green dotted distance line.

Until now, only the transition states leading to a *R*-configuration were considered. A comparison of all four TS2 reported in Fig. 8 also presents the TS2 leading to a *S*-configuration as it is presented in Fig. 22. For the comparison of the TS2 yielding a *S*-configuration similar effects were found as discussed for the TS2 leading to a *R*-configuration.

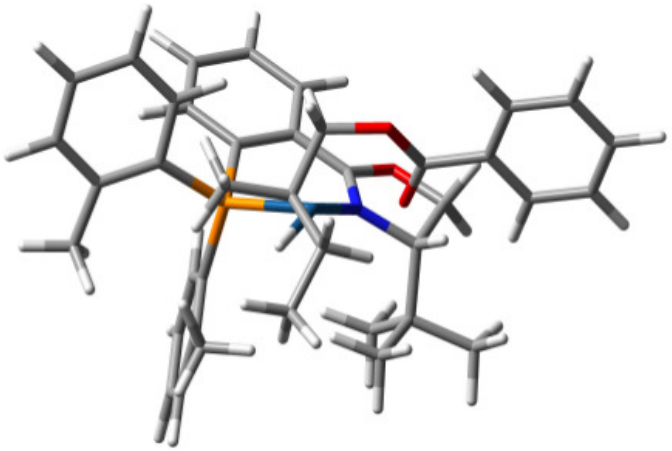

ax-o13-u2r-TS2 (*R*-configuration)
27.67 kcal/mol

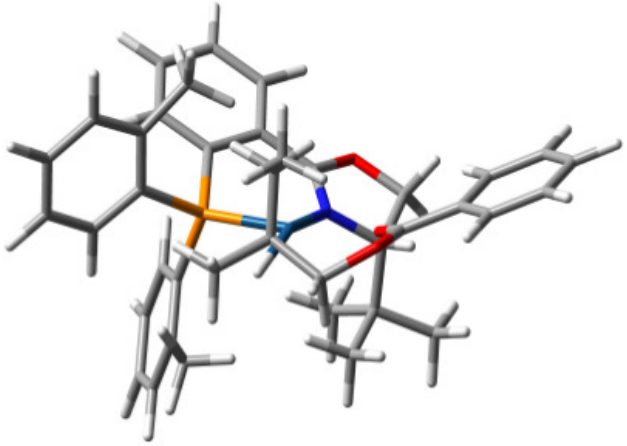

ax-o13-or-TS2 (*S*-configuration)
22.76 kcal/mol

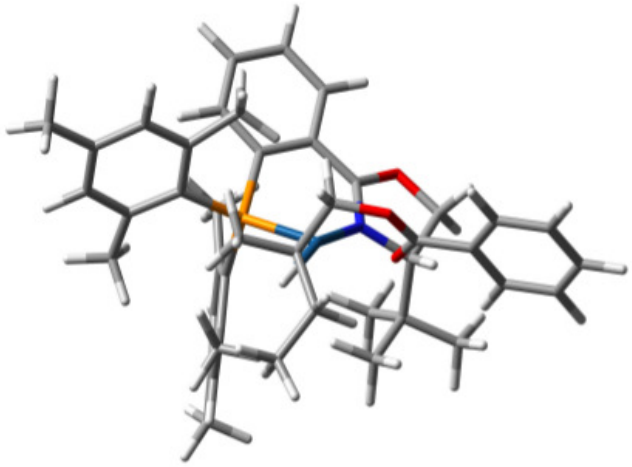

ax-m13-ur-TS2 (*R*-configuration)
25.98 kcal/mol

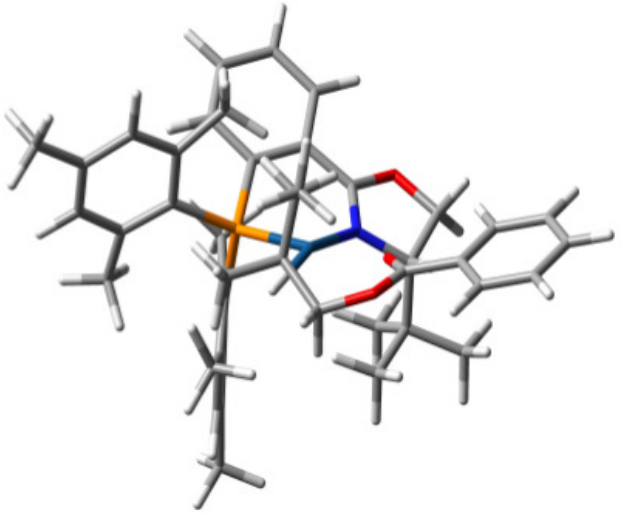

ax-m13-or-TS2 (*S*-configuration)
26.44 kcal/mol

Figure 22.: All second transition states of the Ir(I)/(III) mechanism reported in Fig. 8 are presented.

However, one major interaction occurs for the TS2 leading to a *S*-configuration. The interaction between the mesityl group and the transferred hydrogen is more pronounced than for the *R*-configurated TS2 in Fig. 20. The preferred second transition state for the reaction of the *o*-tolyl catalyst is favored by 4.91 kcal/mol over the TS leading to the opposite enantiomers, while for the mesityl analog the difference is only 0.46 kcal/mol indicating a destabilizing effect of the mesityl TS2, ax-m13-or-TS2 (Fig. 8 lower panel, red path). This repulsive effect arises from one of the methyl groups on the Ph3 which is interacting with the transferred hydrogen as depicted in Fig. 23. The distance to the transferred hydrogen is significantly smaller for the *S*-configurated mesityl-TS2 with 2.05 Å and 2.31 Å compared to the *R*-configurated TS2 (2.13 Å and 2.36 Å in Fig. 20). Therefore, the destabilization of the ax-m13-or-TS2 is most likely the reason for the inversion of the selectivity.

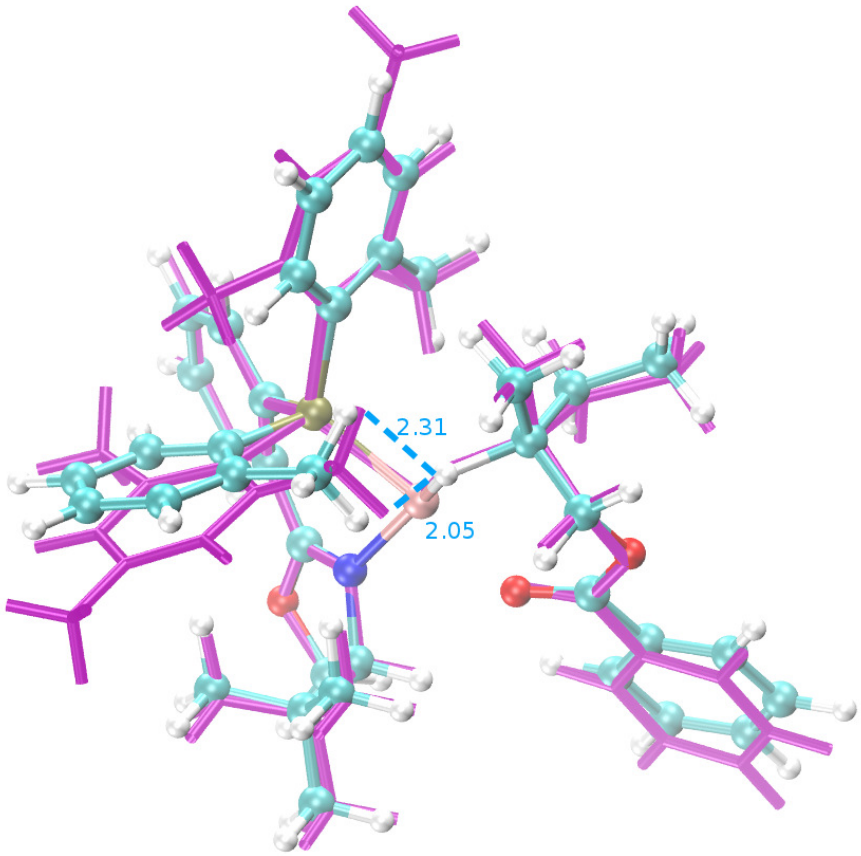

Figure 23.: TS2 overlap of the *o*-tolyl (colored) and mesityl (purple) catalyzed reaction paths in Fig. 8 leading to *S*-configurated enantiomers. The Ir-PHOX plane is aligned with an RMSD of 0.05 Å. The interactions between the methyl group of the phenyl ring (Ph3) and the transferred hydrogen are marked with a blue dotted distance line.

For the (I)/(III)-mediated transition states, the transfer of the axial hydrogen followed by the equatorial one is favored over the reverse sequence. The latter was not only higher in energy but did not predict an inversion of the selectivity either. For the Ir(I)/(III) mechanism where the axial H was transferred first, an inversion of the stereoselectivity was observed (Fig. 10) in accordance to the literature. The reaction was found to be catalyst-controlled but the calculations also indicated a substrate control originating from the *syn*-pentane interaction and the interaction of the substrate phenyl with the *t*Bu group. The transition states involving non-coordinated species were in almost all cases higher in energy, assuming that the unfavorable interaction of the ester oxygen with the hydride is more pronounced than the beneficial interaction with the C-*t*Bu hydrogen (Fig. 9). As the unfavorable interaction destabilizes the TS, the resulting high energies make the mechanism unlikely.

The Ir(III)/(V) mechanism, suggested by Brandt *et al.*[1] showed surprisingly high reaction barriers, which are comparable with the barriers obtained for the Ir(I)/(III) mechanism. Interestingly, a reversed order of the hydrogen transfer (from axial and equatorial to equatorial and axial) resulted in reasonable activation barriers which were approximately 10.0 kcal/mol lower in energy. Thus, for this specific reaction, the order of transferred hydrogen is reversed compared to the order reported in the literature[1,76]. This is most likely due to the fact that the original vacant position on the catalyst-substrate complex is occupied by the coordinating ester oxygen. An addition of a second H_2 is therefore only allowed after the first hydrogen is transferred. Thus, it is essential wheter the axial or the equatorial hydrogen is transferred as the vacant position plays a crucial role for the subsequent coordination of H_2. The coordination of the H_2 in-plane is clearly favored over the coordination at an axial position (10.0 kcal/mol) which provides an explanation for the beneficial reversed hydrogen transfer. However, this mechanism did not reproduce the experimenatlly observed inversion of the selectivity.

5. Conclusions

In conclusion, it can be said that the Ir(I)/(III) mechanism according to Dietiker[5] predicts realistic reactivities and an inversion of the stereoselectivity (Fig. 8 and Fig. 10). An analytically correct ratio of diastereomers (according to literature) could be obtained (Fig. 10) and some critical interactions were identified which may be responsible for the reversal of selectivity. The Ir(III)/(V) mechanistic proposal of Brandt and co-workers turned out to be similar in energy as the Ir(I)/(III) process. However, changing Brandt's order of the hydrogen transfer lowered the barrier heights enormously as the addition of dihydrogen in-plane after the insertion step is more favored. This result suggests a preference for transfer of the equatorial H followed by axial hydrogen over the mechanism postulated by Brandt *et al.*[1] where the axial H is transferred first. Calculations of the Ir(III)/(V) mechanism disagreed with the reported experimetal results, as no inversion of the selectivity was found. Calculations of the Ir(I)/(III)-mediated mechanism not only reproduced an inversion of the stereochemistry, but also the interplay between substrate and catalyst control of the reaction. The Ir(I)/(III) mechanism has a feasible energy barrier and may be favored even more if a coordination of a second dihydrogen is prohibited[76] or the reaction is under low hydrogen pressure[73,74]. If a soluted system can further decrease the barrier heights, this mechanism seems to be plausible. A MM approach may help to

correctly predict the experimental result to perform calculations in explicit solvent. However, although several examples exist where reactions are modelled with force fields[107–109], unfortunately no force field for iridium-mediated hydrogenation reactions was developed until now.

References

Bibliography

[1] P. Brandt, C. Hedberg and P. G. Andersson, *Chem. Eur. J.*, 2003, **9**, 339.

[2] B. F. M. Kimmich, E. Somsook and C. R. Landis, *J. Am. Chem. Soc.*, 1998, **120**, 10115.

[3] Y. Fan, X. Cui, K. Burgess and M. B. Hall, *J. Am. Chem. Soc.*, 2004, **126**, 16688.

[4] J. Zhou, J. W. Olge, Y. Fan, V. Banphavichit, Y. Zhu and K. Burgess, *Chem. Eur. J.*, 2007, **13**, 7162.

[5] R. Dietiker and P. Chen, *Angew. Chem. Int. Ed.*, 2004, **43**, 5513.

[6] L. D. Vazquez-Serrano, B. T. Owens and J. M. Buriak, *Chem. Commun.*, 2002, 2518.

[7] T. L. Church, T. Rasmussen and P. G. Andersson, *Organometallics*, 2010, **29**, 6769.

[8] C. F. Weise, M. Pischl, A. Pfaltz and C. Schneider, *Chem. Commun.*, 2011, **47**, 3248.

[9] J. Halpern and B. M. Trost, *Proc. Natl. Acad. Sci.*, 2004, **101**, 5347.

[10] B. D. Vineyard, W. S. Knowles, M. J. Sabacky, G. L. Bachman and D. J. Weinkauff, *J. Am. Chem. Soc.*, 1977, **99**, 5946.

[11] S. W. Knowles, *Angew. Chem. Int. Ed.*, 2002, **41**, 1998.

[12] A. Cadu and P. G. Andersson, *J. Organomet. Chem.*, 2012, **714**, 3.

[13] A. Pfaltz, J. Blankenstein, R. Hilgrad, E. Hormann, S. McIntyre, F. Menges, M. Schonleber, S. P. Smidt, B. Wuestenberg and N. Zimmermann, *Adv. Synth. Catal.*, 2003, **345**, 33.

[14] A. Aeby, F. Bangerster and G. Consiglio, *Helv. Chim. Acta*, 1998, **81**, 764.

[15] I. Sagasser and G. Helmchen, *Tetrahedron Lett.*, 1998, **39**, 261.

[16] H. Nishiyama, A. Jacobsen, A. Pfaltz and H. Yamamoto, *Comprehensive Asymmetric Catalysis*, Springer, Berlin, 1999.

[17] A. Lightfoot, P. Schnider and A. Pfaltz, *Angew. Chem. Int. Ed.*, 1998, **110**, 3047.

[18] D. G. Blackmond, A. Lightfoot, A. Pfaltz, T. Rosner, P. Schnider and N. Zimmermann, *Chirality*, 2000, **33**, 336.

[19] J. Blankenstein and A. Pfaltz, *Angew. Chem. Int. Ed.*, 2001, **40**, 4445.

[20] G. Helmchen and A. Pfaltz, *Acc. Chem. Res.*, 2000, **12**, 442.

[21] P. Schnider, G. Koch, R. Pretot, G. Wang, F. M. Bohnen, C. Kruger and A. Pfaltz, *Chem. Eur. J.*, 1997, **3**, 887.

[22] K. Kaellstroem, I. Munslow and P. G. Andersson, *Chem. Eur. J.*, 2006, **12**, 3194.

[23] W. J. Drury, N. Zimmermann, M. Keenan, M.Hayashi, S. Kaiser, R. Goddard and A. Pfaltz, *Angew. Chem. Int. Ed.*, 2004, **43**, 70.

[24] D. Rageot and A. Pfaltz, *Helv. Chim. Acta*, 2012, **95**, 2176.

[25] P. G. Cozzi, N. Zimmermann, R. Hilgraf, S. Schaffner and A. Pfaltz, *Adv. Synth. Catal.*, 2001, **343**, 450.

[26] F. Menges and A. Pfaltz, *Adv. Synth. Catal.*, 2002, **344**, 40.

[27] K. Kaellstroem, C. Hedberg, , P. Brandt, A. Bayer and P. G. Andersson, *J. Am. Chem. Soc.*, 2004, **126**, 14308.

[28] R. H. Crabtree, H. Felkin and G. E. Morris, *J. Organomet. Chem.*, 1977, **12**, 205.

[29] R. R. Schrock and J. A. Osborn, *J. Am. Chem. Soc.*, 1971, **9389**, 30.

[30] R. H. Crabtree, *Acc. Chem. Res.*, 1979, **12**, 331.

[31] F. Menges, M. Neuburger and A. Pfaltz, *Org. Lett.*, 2002, **4**, 4713.

[32] D. Liu, W. Tang and X. Zhang, *Org. Lett.*, 2004, **6**, 513.

[33] P. G. Cozzi, N. Zimmermann, R. Hilgraf, S. Schaffner and A. Pfaltz, *Adv. Synth. Catal.*, 2001, **343**, 450.

[34] A. Pfaltz, J. Blankenstein, R. Hilgrad, E. Hormann, S. McIntyre, F. Menges, M. Schonleber, S. P. Smidt, B. Wuestenberg and N. Zimmermann, *Org. Lett.*, 2002, **4**, 4713.

[35] D. Hou, J. H. Reibenspies, T. J. Colacot and K. Burgess, *Chem. Eur. J.*, 2000, **7**, 5391.

[36] M. G. Schrems and A. Pfaltz, *Chem. Commun.*, 2009, **41**, 2610.

[37] G. H. Hou, J. H. Xie, L. X. Wang and Q. L. Zhou, *J. Am. Chem. Soc.*, 2006, **128**, 11774.

[38] S. Bell, B. Wuestenberg, S. Kaiser, F. Menges, T. Netscher and A. Pfaltz, *Science*, 2006, **311**, 642.

[39] S. J. Roseblade and A. Pfaltz, *Acc. Chem. Res.*, 2007, **40**, 1402.

[40] R. Noyori, *Angew. Chem. Int. Ed.*, 2002, **41**, 2008.

[41] S. P. Smidt, A. Pfaltz, E. Martinzez-Viviente, P. S. Pregosin and A. Albinati, *Organometallics*, 2003, **22**, 1000.

[42] S. P. Smidt, N. Zimmermann, M. Studer and A. Pfaltz, *Chem. Eur. J.*, 2004, **10**, 4685.

[43] X. H. Cui and K. Burgess, *Chem. Rev.*, 2005, **105**, 3272.

[44] M. C. Perry, X. Cui, M. T. Powell, D. R. Hou, J. H. Reibenspies and K. Burgess, *J. Am. Chem. Soc.*, 2003, **125**, 113.

[45] S. McIntyre, E. Hoermann, F. Menges, S. P. Smidt and A. Pfaltz, *Adv. Synth. Catal.*, 2005, **347**, 282.

[46] G. Stock and D. E. Kahne, *J. Am. Chem. Soc.*, 1983, **105**, 1072.

[47] I. Dijima, *Pure Appl. Chem.*, 1984, **56**, 99.

[48] Y. Armani and D. Sinou, *J. Mol. Catal.*, 1984, **24**, 231.

[49] H. Lee, T. Jiang, E. D. Stevens and S. P. Nolan, *Organometallics*, 2001, **20**, 1255.

[50] M. M. Taquikahn, B. Taquikahn and S. Begum, *J. Mol. Catal.*, 1986, **34**, 9.

[51] J. Halpern and T. Okamoto, *Inorg. Chim. Acta*, 1984, **114**, 7827.

[52] J. Halpern, *Science*, 1982, **217**, 401.

[53] R. H. Crabtree, P. C. Demou, D. Eden, J. M. Mihelcic, C. A. Parnell, J. M. Quirk and J. M. Morris, *J. Am. Chem. Soc.*, 1982, **104**, 6994.

[54] C. Mazet, S. P. Smidt, M. Meuwly and A. Pfaltz, *J. Am. Chem. Soc.*, 2004, **43**, 14176.

[55] R. H. Crabtree, H. Felkin, T. Fillbeen-Kahn and G. E. Morris, *J. Organomet. Chem.*, 1979, **168**, 183.

[56] R. H. Crabtree and R. Uriarte, *Inorg. Chem.*, 1983, **22**, 4152.

[57] J. Sprinz, M. Kiefer, G. Helmchen, M. Reggelin, G. Huttner, O. Walter and L. Zsolnai, *Tetrahedron*, 1994, **35**, 1523.

[58] C. Breutel, P. S. Pregosin, R. Salzmann and A. Togni, *J. Am. Chem. Soc.*, 1994, **116**, 4067.

[59] J. Sprinz, M. Kiefer and G. Helmchen, *Tetrahedron Lett.*, 1994, **35**, 1523.

[60] H. Steinhagen, M. Reggelin and G. Helmchen, *Angew. Chem. Int. Ed.*, 1997, **36**, 19.

[61] P. E. Ploechl and A. Togni, *Organometallics*, 1996, **15**, 4125.

[62] C. G. Frost and J. M. J. Williams, *Tetrahedron Lett.*, 1993, **4**, 1785.

[63] G. Helmchen, *J. Organomet. Chem.*, 1999, **576**, 203.

[64] T. L. Church and P. G. Andersson, *Coord. Chem. Rev.*, 2008, **252**, 513.

[65] D. H. Woodmansee, M.-A. Mueller, L. Troendlin, E. Hoermann and A. Pfaltz, *Chem. Eur. J.*, 2012, **18**, 13780.

[66] D. H. Woodmansee, M.-A. Mueller, M. Neuburger and A. Pfaltz, *Chem. Sci.*, 2010, **1**, 72.

[67] D. Hou, J. H. Reibenspies and K. Burgess, *J. Org. Chem.*, 2001, **66**, 206.

[68] C. Hedberg, K. Kaellstroem, P. Brandt, L. K. Hansen and P. G. Andersson, *J. Am. Chem. Soc.*, 2006, **128**, 2995.

[69] R. H. Crabtree, H. Felkin and G. E. Morris, *J. Chem. Soc. Chem. Commun.*, 1976, **18**, 716.

[70] T. W. Brauch and C. R. Landis, *Inorg. Chim. Acta*, 1998, **270**, 285.

[71] M. T. Powell, D.-R. Hou, M. C. Perry, X. Cui and K. Burgess, *J. Am. Chem. Soc.*, 2001, **123**, 8878.

[72] X. Cui and K. Burgess, *J. Am. Chem. Soc.*, 2003, **125**, 14212.

[73] S. J. Roseblade and A. Pfaltz, *C. R. Chimie*, 2007, **10**, 178.

[74] M. W. Cook, D. N. Hanson and B. J. Alder, *J. Chem. Phys.*, 1957, **26**, 748.

[75] I. D. Gridnev and T. Imamoto, *J. Comp. Chem.*, 1997, **102**, 252.

[76] K. H. Hopmann and A. Bayer, *Organometallics*, 2011, **30**, 2483.

[77] M. J. Frisch, G. W. Trucks, H. B. Schlegel, G. E. Scuseria, M. A. Robb, J. R. Cheeseman, J. A. Montgomery, Jr., T. Vreven, K. N. Kudin, J. C. Burant, J. M. Millam, S. E. S. Iyengar, J. Tomasi, V. Barone, B. Mennucci, M. Cossi, G. Scalmani, N. Rega, G. A. Petersson, H. Nakatsuji, M. Hada, M. Ehara, K. Toyota, R. Fukuda, J. Hasegawa, M. Ishida, T. Nakajima, Y. Honda, O. Kitao, H. Nakai, M. Klene, X. Li, J. E. Knox, H. P. Hratchian, J. B. Cross, C. Adamo, J. Jaramillo, R. Gomperts, R. E. Stratmann, O. Yazyev, A. J. Austin, R. Cammi, C. Pomelli, J. W. Ochterski, P. Y. Ayala, K. Morokuma, G. A. Voth, P. Salvador, J. J. Dannenberg, V. G. Zakrzewski, S. Dapprich, A. D. Daniels, M. C. Strain, O. Farkas, D. K. Malick, A. D. Rabuck, K. Raghavachari, J. B. F. resman, J. V. Ortiz, Q. Cui, A. G. Baboul, S. Clifford, J. Cioslowski, B. B. Stefanov, G. Liu, A. Liashenko, P. Piskorz, I. Komaromi, R. L. Martin, D. J. Fox, T. Keith, M. A. A. Laham, C. Y. Peng, A. Nanayakkara, M. Challacombe, P. M. W. Gill, B. Johnson, W. Chen, M. W. Wong, C. Gonzalez and J. A. Pople, *Gaussian 03, Revision C.01*, Gaussian, Inc., Wallingford CT, U.S.A., 2004.

[78] A. D. Becke, *J. Chem. Phys.*, 1993, **98**, 5648.

[79] C. Lee, W. Yang and R. G. Parr, *Phys. Rev.*, 1988, **B 37**, 785.

[80] W. J. Hehre, R. Ditchfie and J. A. Pople, *J. Chem. Phys.*, 1972, **56**, 2257.

[81] P. J. Hay and W. R. Wadt, *J. Chem. Phys.*, 1985, **82**, 270.

[82] S. Miertus, E. Scrocco and J. Tomasi, *Chem. Phys.*, 1981, **55**, 117.

[83] J. L. Pascual-Ahuir, E. Silla and I. Tunon, *J. Comp. Chem.*, 1994, **15**, 1127.

[84] J. Tomasi, B. Mennucci and R. Cammi, *Chem. Rev.*, 2005, **105**, 2999.

[85] P. J. Stephens, F. J. Devlin and C. S. Ashvar, *Faraday Discuss.*, 1994, **99**, 103.

[86] K. Burke, *The ABC of DFT*, Burke reasearch group, California, 2000.

[87] K. Burke and L. Wagner, *Int. J. Quant. Chem.*, 2013, **113**, 96.

[88] A. J. Cohen, P. Mori-Sanchez and W. Yang, *Chem. Rev.*, 2012, **112**, 289.

[89] B. J. Lynch, P. L. Fast, M. Harris and D. G. Truhlar, *J. Phys. Chem. A*, 2000, **104**, 4811.

[90] Y. Zhao, B. J. Lynch and D. G. Truhlar, *J. Phys. Chem. A*, 2004, **108**, 2715.

[91] Y. Zhao, N. Gonzalez-Garcia and D. G. Truhlar, *J. Phys. Chem. A*, 2005, **109**, 2012.

[92] S. Kristyan and P. Pulay, *Chem. Phys. Lett.*, 1994, **229**, 175.

[93] A. Milet, T. Korona, R. Moszynski and E. Kochanski, *J. Chem. Phys.*, 1999, **111**, 7727.

[94] A. R. Leach, *Molecular Modelling - Principles and Applications*, Prentice Hall, Edinburgh, 2001.

[95] S. Hirata, M. Nooijen and R. J. Bartlett, *Chem. Phys. Lett.*, 2000, **326**, 292.

[96] S. A. Kucharski, M. Wloch, M. Musial and R. J. Bartlett, *J. Chem. Phys.*, 2001, **115**, 8263.

[97] C. Dykstra, *Theory and Applications of Computational Chemistry: The First Forty Years*, Elsevier, Amsterdam, 2005.

[98] J. P. Perdew, K. Burke and M. Ernzerhof, *Phys. Rev. Lett.*, 1996, **77**, 3865.

[99] J. Paier, M. Marsman and G. Kresse, *J. Chem. Phys.*, 2007, **127**, 024103.

[100] D. C. Young, *Computational Chemistry: A Practical Guide for Applying Techniques to Real-World Problems*, John Wiley and Sons, New York, 2001.

[101] J. Zhu and K. Burgess, *Acc. Chem. Res.*, 2012, **45**, 1623.

[102] S. Masmune, W. Choy, J. S. Petersen and L. R. Sita, *Angew. Chem. Int. Ed.*, 1985, **24**, 1.

[103] A. H. Hoveyda, D. A. Evans and G. C. Fu, *Chem. Rev.*, 1993, **93**, 1307.

[104] D. L. Bunker, *Meth. Comp. Phys.*, 1971, **10**, 287.

[105] H. B. Schlegel, J. M. Millam, S. S. Lyengar, G. A. Voth and A. D. Daniels, *J. Chem. Phys.*, 2001, **114**, 9758.

[106] H. B. Schlegel, S. S. Lyengar, X. Li, J. M. Millam and G. A. Voth, *J. Chem. Phys.*, 2002, **117**, 8694.

[107] F. Jensen, *J. Comp. Chem.*, 1994, **15**, 1199.

[108] J. E. Eksterowics and K. N. Houk, *Chem. Rev.*, 1993, **93**, 2439.

[109] L. Raimondi, F. K. Brown, J. Gonzales and K. N. Houk, *J. Am. Chem. Soc.*, 1992, **114**, 4796.